Structure, Properties, and Chemistry of Iron-Based Superconductors

Simon J. Cassidy

A thesis submitted in part fulfilment of the requirements for the degree of
Doctor of Philosophy at the University of Oxford

St. Catherine's College
University of Oxford
June 2015

Abstract

Structure, Properties, and Chemistry of Iron-Based superconductors

DPhil Thesis Simon J. Cassidy June 2015

This thesis reports the synthesis and characterisation of several layered pnictides, chalcogenides, and oxychalcogenides, with an emphasis on materials that exhibit high temperature superconductivity. High and low temperature techniques have been used to synthesise new materials and modify their properties.

The majority of this work has been focused on the synthesis of superconducting materials with the general formula $A_x(NH_3)_y(NH_2)_zFeSe$, where A is an alkali metal. These materials are formed from a co-intercalation of alkali metals, ammonia, and alkali metal amides into the interlamellar space of pre-formed tetragonal FeSe. There is a remarkable increase in T_c associated with this intercalation, from 8 K in FeSe to a maximum of 46 K in the products. A range of characterisation techniques including neutron and X-ray diffraction, EXAFS, and SQUID magnetometry have been used to identify a variety of crystal structures, compositions, and properties adopted by these materials. The synthesis procedure of these materials where, A = Na and K, has been studied *in-situ* via powder X-ray diffraction at world-class central facilities, revealing new phases, intermediates, and activation energies. The $K_x(NH_3)_y(NH_2)_zFeSe$ phases are found to undergo a topotactic decomposition step to become $K_{x'}Fe_{2-y'}Se_2$ phases on annealing, which has also been studied by *in-situ* powder X-ray diffraction.

Additional studies on $Na_{1-x}Fe_{2-y}As_2$ and CaFeSeO have been performed. $Na_{1-x}Fe_{2-y}As_2$ is the product of a room temperature deintercalation of sodium and iron from NaFeAs, which changes the superconducting properties of the material. XAFS measurements have been used to characterise the local structure of the materials, which supports the conclusion that iron is deintercalated from the parent material and gives new insight into the effect of the iron vacancies on the local structure. CaFeSeO is a newly discovered material that adopts a never-before-seen crystal structure, which has been solved from powder X-ray diffraction data. Intricate vacancy ordering exists in the material, which contributes to a peculiar mixture of magnetic behaviours including signatures of a spin glass, ordered antiferromagnet, and an ordered ferromagnetic component. All of these behaviours however, can be rationalised by the nuclear and magnetic structure of the material that have been refined using powder neutron diffraction.

Acknowledgements

I am immensely grateful for the fantastic supervision of Prof. Simon Clarke and Dr. Silvia Ramos-Perez. They have both been enthusiastic, encouraging, supportive above and beyond expectation, and I have learnt a great deal from them. Thanks also to Prof. Peter Battle, who's been a fountain of knowledge during my entire time in Oxford.

Thanks to the DPhils and Post Docs of the Clarke group that have taught me the research skills I've gained. The DPhils that have passed through the group in my time, the now doctors Mike Pitcher, Alex Corkett, Jack Wright, and Alice Taylor, have been incredibly helpful and always gave up their time, which over the course of my DPhil I've come to appreciate more and more. Thanks to Jack Blandy, who's picking things up impressively quickly. Thanks to Dr. David Free, who got me to grips with Topas back in the early days. Thanks to Dr. Stefan Sedlmaier, who knew an awful lot about a lot of things and whose lab-managing lives on. And thanks to Dr. Daniel Woodruff, who has put an inordinate amount of work in since he joined the group and has been its shoulders this past year.

Thanks to the Part IIs of the group past and present. Thanks to Jacob, Pippa, Fran, and Archie along with Danny and Jack for making this tricky last year an enjoyable one.

Thanks to the hardworking staff on B18: Prof. Andy Dent, who is a fantastic principal beamline scientist, Dr. Giannantonio Cibin and Dr. Stephen Parry, who have ideas for everything, and Phil Robbins, who can build anything.

I am grateful to Prof. Joke Hadermann for performing the electron diffraction work that has benefited this report and Dr. Andrew Jupe for the help performing a background subtraction without which my thesis wouldn't be nearly as colourful.

I am grateful to the beamline scientists at the various facilities for their time and effort. Dr. R. Smith (Polaris and GEM Xpress), Dr. A. Daoud-Aladine (HRPD), Dr. P. Manuel (WISH), Prof. C. Tang, Dr. S. Thompson, Dr. C. Murray, Dr. S. Day, and Dr. A. Baker (I11), and Dr. M. Drakopoulos, Dr. C. Reinhard, and Dr. T. Connolley (I12). Special thanks go to the I12 staff for their help in performing the most exciting and challenging experiment of my DPhil. Thanks also to Dr. P. Wiseman for maintenance of the Powder X-ray diffractometers and SQUID magnetometers in the chemistry department.

Finally, thanks to my family, friends, and to Jenny, who have supported me throughout and kept me going.

Contents

Chapter 1

1. Introduction

1.1 Solid-state chemistry

Solid-state chemistry concerns the synthesis, structure, properties and applications of materials in the solid state. The synthesis, properties, and applications of materials are longstanding areas of study, but it was the experiments of Max von Laue and W.H. and W.L. Bragg in the early 20th century that opened the door to studying the structure of solids and can be said to have transformed solid-state chemistry into its modern form. They investigated the interaction of X-rays with crystals, discovering a method of studying the atomic level structure of a material, which was a turning point in solid-state chemistry because a solid's properties could then be understood in terms of its structure. Building on the structure-property relationship in the solid state has led to the discovery of many of the materials that shape the modern world. Examples of such technologies include the transistors in microchips which are based on doped-silicon, the rechargeable lithium ion battery based on the $LiCoO_2$ cathode[1] and its variants, magnetic storage devices such as hard disks that use ferromagnetic compounds and alloys such as γFe_2O_3 and CoPtCr, light emitting devices such as LEDs and blue lasers that use GaN, heterogeneous catalysis materials based on porous structures such as zeolites and metal organic frameworks, and superconducting magnets used for the generation of large magnetic fields in scientific application such as particle accelerators, NMR spectrometers and SQUID magnetometers, and medical instruments such as MRI scanners, to name only a few.

In many cases, it is possible to predict the properties that a material with a given structure might have. Unfortunately, the largest obstacle in the design of new materials is the relatively low level of control in the synthesis of a targeted structure. In performing a reaction in the solid state, there are huge kinetic barriers to reorganisation of the atoms that must be overcome. The most common way of beating the mobility barrier to a solid-state reaction has always been by use of elevated temperature, often between 500 and 1500 °C in what is known as a 'ceramic' or 'traditional solid-state' synthesis. Ceramic synthesis has always been, and most probably will always be, the foundation of solid-state synthesis, but its core limitation is that it always delivers the most thermodynamically stable product, which may not be the one with the most desirable properties. This is not to say that the number of products available via the ceramic route is entirely limited. The interplay between various enthalpic and entropic forces at high temperatures can be complex, often leading to a range of polymorphs being stable at different temperatures for just one composition, and while cooling slowly will yield the most stable product at room temperature, other polymorphs may be trapped by quenching the material from high temperature.

The traditional ceramic synthesis remains a strong and heavily relied upon tool but will always be fundamentally limited by thermodynamics. ‘Soft chemistry’ is a term used in solid-state chemistry to refer to low temperature methods of achieving kinetically stable products over the thermodynamically favoured ones. Examples of ‘soft’ processes include the aforementioned rechargeable lithium-ion battery, in which Li ions enter the cathode material on discharge and exit when recharging, all reversibly at room temperature. This manipulation of the solid is possible because the layered structure of $LiCoO_2$ lends itself to a low barrier to mobility of small cations from within the interlayer space. The materials studied in this thesis lend themselves well to this type of chemistry since the layered chalcogenides, such as β-FeSe, exhibit weak van der Waals forces between the layers that can often be overcome by a donor atom, pushing the layers apart to provide columbic stabilisation or, in some cases, hydrogen bonding. Equally, deintercalation is also often possible in these systems since the binding energy of a cation to a soft anion will generally be low due to the anion’s low charge density ratio, which provides a low energy barrier to cation removal. Intercalation/deintercalation is often accompanied by a reductive/oxidative process of the host material and is a useful method of tuning the oxidation state of a redox-active transition metal elsewhere in the structure.

1.2 Chemistry of layered chalcogenide, pnictide, and mixed anion compounds

The most explored class of solid-state compounds are the oxides rather than the chalcogenides or pnictides, because the oxides have inherent availability and stability. Synthesis of an oxide can most often be carried out successfully at high temperatures under normal atmospheric (oxidising) conditions and a vast number of products can be formed in a variety of different structures and compositions. Non-oxide and mixed-anion solids are less explored due to their lower natural abundance and lower formation enthalpies than the oxides that often lead to difficulties in avoiding oxidation and/or hydrolysis when forming and storing them. These materials show intriguing structures and properties that compare and contrast well with the oxides.

1.2.1 Common layered crystal structures

In general terms, oxide materials prefer to adopt crystal structures that reflect significant ionic bonding based on “hard” interactions that maximise Coulombic potential. A discerning characteristic of the chalcogenides and pnictides is their relative stability and apparent favourability for “soft” interactions that occur from their polarisability such as the van der Waals force between two polarisable anions, covalency with a metal centre, or covalency with another anion to form dianions.

A large number of known chalcogenide, pnictide, oxychalcogenide and oxypnictide materials adopt 2-dimensional, layered structures in which the layering allows interlayer van der Waal bridging interactions and/or the separation of different anions into different layers to occur. These layered structures can be rationalised in terms of the anion polarisation: the high polarizability of the higher row anions can be best utilised if the anions are in an asymmetric environment; they can then be polarised to screen the repulsion between cations.[2] The tendency towards some level of covalent bonding interaction and relatively large size of the chalcogenides and pnictides often gives a preference for a tetrahedral coordination around a transition metal. Layers of edge sharing tetrahedra such as those found in the PbO structure are widely observed, on their own or as part of a related structure. Three such related structures that represent some of the most widely observed among the pnictides and chalcogenides are shown in Figure 1.1. The $ThCr_2Si_2$ structure consists of $[Cr_2Si_2]^{4-}$ layers separated by a single layer of Th^{4+} in an 8-coordinate site, note that in this structure alternate $[Cr_2Si_2]^{4-}$ layers are shifted relative to PbO such that the structure has body centring. Moving from the $ThCr_2Si_2$ structure to the PbFCl structure a double layer of Cl^- ions in 5-coordinate sites separate the $[PbF]^+$ layers, which have the same relative configuration as PbO. The ZrCuSiAs ($HfCuSi_2$) structure is related to the PbFCl structure by a filling of the tetrahedral vacancies between the double layer of Cl^-, or specifically for ZrCuSiAs, Cu fills the tetrahedral vacancies between As layers.

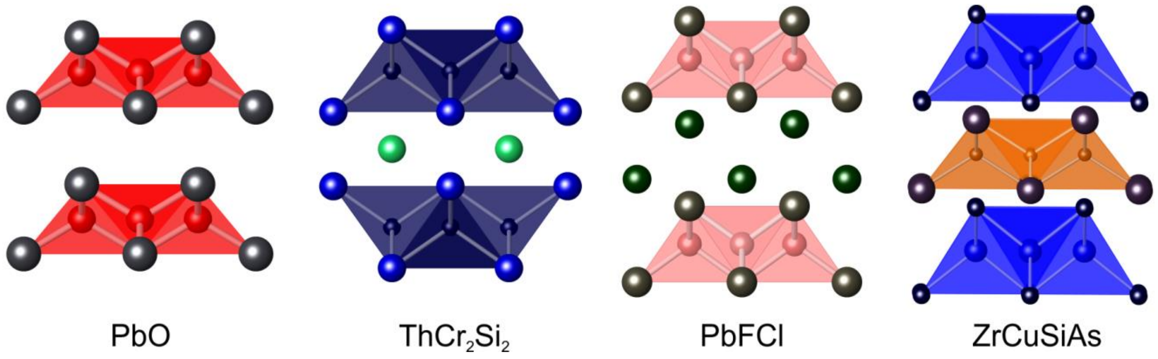

Figure 1.1 Common structures types that are topologically related to one another.

The layered structures described above are each represented by a vast number of compounds that adopt the structure: over 600 examples of the ThCr$_2$Si$_2$,[3] over 200 examples of the PbFCl and equally popular anti-PbFCl structures,[4] and over 150 examples of the ZrCuSiAs structure are known. The versatility of these structures largely comes down to their ability to accommodate different types of bonding interactions, be they highly ionic, highly covalent, anion-anion bridging, or metal-metal bonding in nature. It may be noted that the ThCr$_2$Si$_2$ structure type has the potential for anion-anion bonds that bridge the layers, which are present in many cases, including ThCr$_2$Si$_2$, but are not present in many others such as BaFe$_2$As$_2$. The degree to which anion-anion bonding occurs in the structure is predominantly a function of the filling of the band structure.

As mentioned previously, layered systems such as those shown in Figure 1.1 are prime candidates for intercalation and deintercalation chemistry. Looking again at these four structures, it can reasonably be imagined that the barrier to conversion between them may be relatively low in energy. Several such conversions will be described in chapters 3-5 of this thesis. A conversion between any of the given structure types would be described as topotactic, as it preserves the topology of PbO-type layers.

1.2.2 Topotactic intercalations into layered systems

Topotactic reactions are those that preserve the parent structure in the product and usually occur when a fraction of the ions is inserted or removed but leave most of the structure unchanged. Intercalations into transition metal dichalcogenides are perhaps the most explored examples of topotactic intercalations. TiS$_2$ was the predecessor to the LiCoO$_2$[1] battery cathode material, which not only showed a reversible intercalation of lithium and sodium,[5] but also was shown to undergo intercalations with Lewis bases such as ammonia,[6] as shown in Figure 1.2, and other molecular species rather than exclusively with reductants.

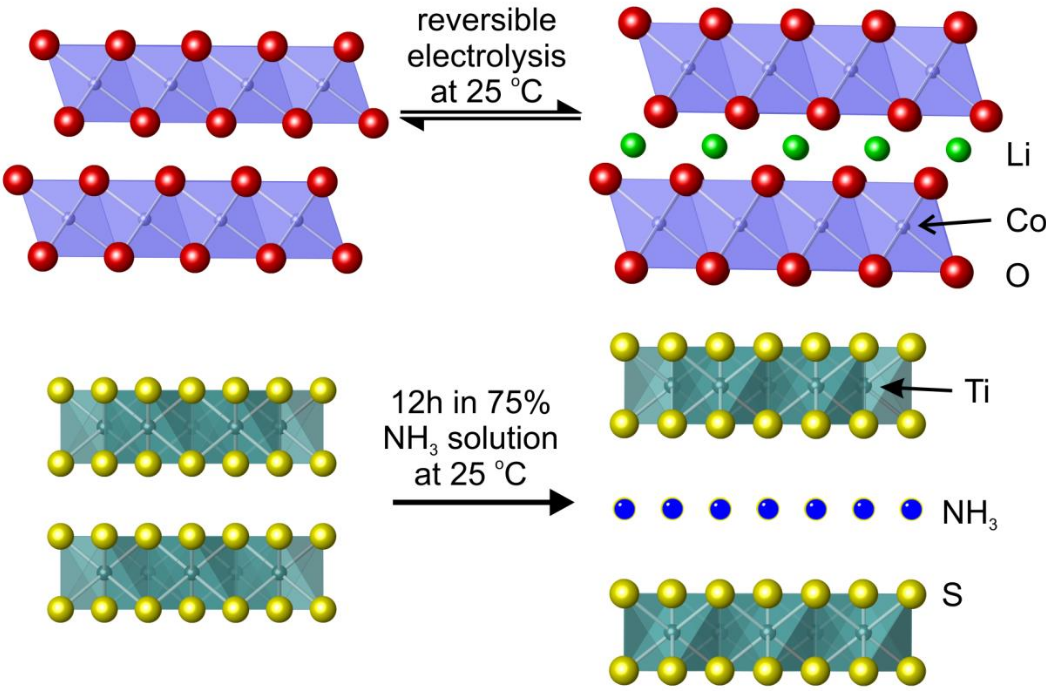

Figure 1.2 Topotactic intercalations of species in the interlamellar space of layered structures.

The intriguing structural flexibility exhibited by such materials and their potential application in the battery field sparked a flurry of research in the late 1960s and 1970s into the many different ions and molecules that could be intercalated into the group IV-VI disulfides and diselenides (MCh_2). Over 30 different molecular species were found to intercalate into TiS_2 alone,[7] with a number of different routes to intercalation including: sealed tube reactions between the MCh_2 species and the anhydrous intercalate,[6] reaction with strong solutions of the intercalate in an appropriate solvent,[8] electrolysis using the corresponding salt in aqueous solution as the electrolyte,[9] and indirect intercalation by first intercalating NH_3 then subsequent substitution with the chosen species.[6]

The intercalation of water molecules in layered systems is an extremely common phenomenon in clay materials. Similar intercalation properties of $Na_{0.3}CoO_2$ drew particular attention in 2003 when a reversible intercalation of water molecules was observed, forming a material that superconducts below a temperature of 5 K with a composition of $Na_{0.3}(H_2O)_{\sim1.3}CoO_2$.[10,11] It was further discovered that the hydration of the material goes through a non-superconducting, partially hydrated intermediate with composition around $Na_{0.3}(H_2O)_{\sim0.6}CoO_2$,[12] a schematic of these processes is given in Figure 1.3.

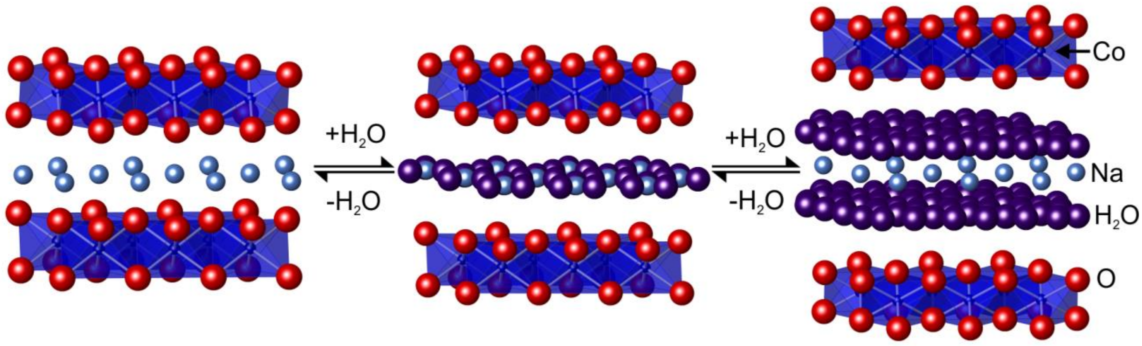

Figure 1.3 The reversible intercalation of H_2O forming the hydrates of $Na_{0.3}CoO_2$.

A few further examples of topotactic intercalations include the group 4 nitride halides, which can accommodate intercalations between the halide-halide van der Waals gaps, such as with lithium in Li_xZrNCl. Li intercalation *n*-type dopes the conduction band forming a metal from a semimetal and the system becomes superconducting with T_c of 12.5 K.[13] Trithiophosphates such $FePS_3$ shows extensive intercalation chemistry of large molecular species such as 4-aminopyride between sulfur bridged layers.[14] Sodium may be intercalated between sulfide layers in MoS_2 to form Na_xMoS_2, which upon exposure to moist air gradually uptakes water to form $Na_x(H_2O)MoS_2$ with water co-intercalated into the interlamellar space in a similar manner to $Na_{0.3}(H_2O)_{\sim 0.6}CoO_2$.[15] Intercalations of this type are described in chapters 4 and 5.

1.3 Common magnetic properties of solids

1.3.1 Diamagnetism

Diamagnetism is an intrinsic repulsion from an applied magnetic field that all materials experience, generated by the interaction of electrons with the magnetic field. As an electron precesses in the applied field it induces a small current, giving an internal magnetic field that opposes the applied field in accordance with Lenz's law.

The strength of the magnetisation generated by inherent diamagnetism is generally several orders of magnitude lower than that of magnetic phenomenon that are associated with unpaired electrons (such as paramagnetism, discussed next) and so is often ignored when considering materials with unpaired electrons. In materials with only paired electrons the diamagnetic response will depend greatly on the number of electrons in the system and can be approximated well as a sum of the diamagnetic magnetisations of the individual elements comprising the material in the appropriate ratio.

1.3.2 Paramagnetism

In materials that contain atoms or ions with unpaired electrons, their spins will tend to align with an applied external magnetic field, generating a magnetisation in the same direction. In order to be classed as a paramagnet, the coupling interactions between different spins must be negligible. Curie paramagnetism is a relatively strong magnetisation effect generated by the alignment of localised spins on magnetically active sites in materials. For a system to be Curie paramagnetic, the localised magnetically active sites need to be dilute in the systems so that they are non-interacting with one another: molecular magnets in solution are a fine example.

1.3.3 Pauli paramagnetism

Pauli paramagnetism is a type of paramagnetic behaviour that occurs when valence electrons are itinerant (*i.e.* in a metallic band) instead of localised. In an applied magnetic field the conduction band, which would usually otherwise contain equal proportions of spin-up and spin-down electrons, loses its degeneracy as one spin state aligned parallel with the field becomes energetically favoured and the other aligned anti-parallel becomes energetically disfavoured. The lower energy spin state is preferentially occupied giving a net positive magnetisation in the direction of the applied field that is proportional to the density of states at the Fermi level.

Pauli paramagnetism is usually several orders of magnitude weaker than paramagnetism from localised spins (Curie paramagnetism), of a similar magnitude to diamagnetism, owing to the fact it occurs only from electrons near the Fermi energy.

1.3.4 Ferromagnetism

Like paramagnetic materials, ferromagnetic materials contain atoms or ions with unpaired electrons that tend to align parallel to an applied magnetic field. Unlike in a paramagnet however, alignment of the spins occurs even in the absence of an applied magnetic field because of a strong coupling interaction between the spins of these materials. The degree of alignment depends on the strength of the coupling interaction and is randomised by thermal energy, k_BT, so above a certain critical temperature known as the Curie temperature, T_C, the coupling is disrupted and paramagnetic behaviour is observed.

A ferromagnetic material will not necessarily exhibit a macroscopic magnetic field itself, even below T_C, because the alignment occurs in domains, which do not align with each other spontaneously. The application of an external magnetic field can promote the alignment of the magnetic domains to give a net positive magnetisation, which will persist even if the field is removed. If a stronger field is applied or the temperature is lowered then more of the domains will align until all are co-aligned, a situation known as saturation. The strength of an internal coupling is typically much stronger than an external coupling to a magnetic field and so the magnetisation of a ferromagnetic material is typically several orders of magnitude greater than that of a paramagnet.

1.3.5 Antiferromagnetism

In an antiferromagnetic system, again there are ions with unpaired electrons that experience a strong coupling interaction with their neighbouring spins, but the coupling is such that nearest neighbour spins align antiparallel rather than parallel. This method of coupling is actually more frequently observed than ferromagnetic coupling. As with ferromagnets, the directions of the coupled spins are randomised by thermal energy such that at a critical temperature, this time known as the Néel temperature, T_N, the antiferromagnetic coupling is broken and paramagnetic behaviour is observed. Below T_N the magnetisation of a sample will decrease and tend towards zero (or more accurately its diamagnetic magnetisation) as the temperature approaches zero. Schematic diagrams of typical magnetisation versus temperature plots for a ferromagnet and antiferromagnet are shown in Figure 1.4.

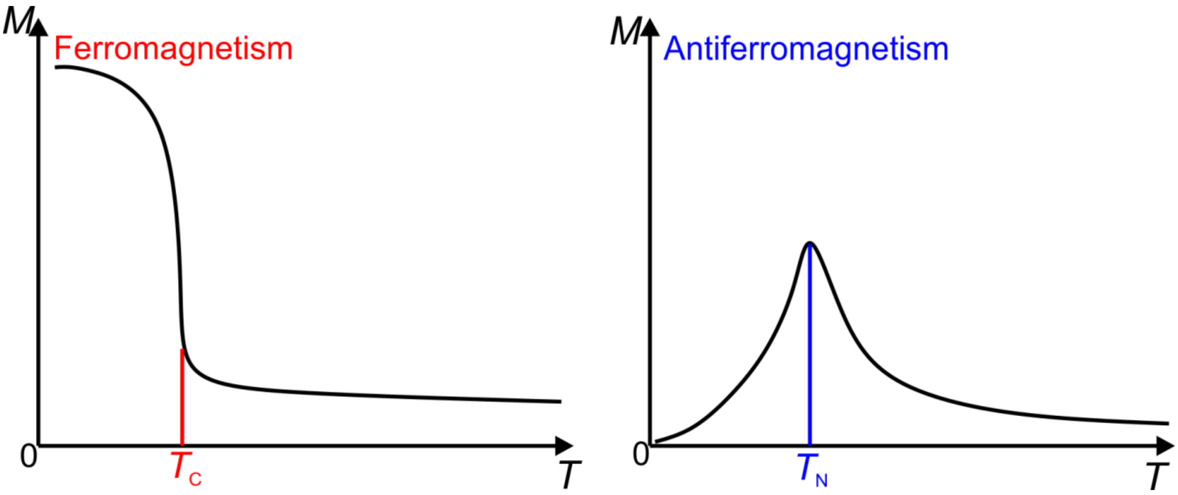

Figure 1.4 Typical Magnetisation (*M*) against temperature (*T*) curves for a ferromagnet and antiferromagnet.

1.3.6 Spin glass behaviour

A spin glass is a type of magnetic material that results from magnetic frustration and disorder. The classic example of a magnetically frustrated system is the triangular antiferromagnet shown in Figure 1.5. In this example, an antiferromagnetic coupling between all three spins is preferred but not achievable; if two spins are aligned antiparallel then whichever choice is made for the third spin, it cannot align antiparallel to both. The system cannot reach an entirely satisfied state but can possess several equal energy unsatisfied states, which leads to a metastability with hysteresis effects (dependence on the sample's magnetic or thermal history) and time dependant relaxation towards equilibrium.

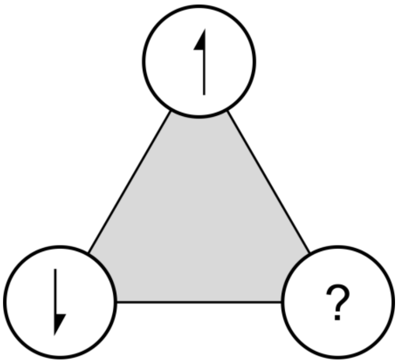

Figure 1.5 Frustrated magnetism in a triangular antiferromagnetic system. The spin of the bottom right point cannot satisfy antiferromagnetic couplings to both of the other sites simultaneously.

A spin glass can be defined as a random, magnetic system with mixed interactions characterised by a random, yet cooperative, freezing of spins at a well-defined freezing temperature, T_f, below which a metastable frozen state appears without the usual magnetic long-range ordering. Randomness in a spin glass material can be caused by a number of different types of disorder, such as disordered vacancies or disordered variation in bond lengths. If the ordered system is frustrated then introducing disorder will lead to a localised lifting of the frustration and domains (clusters) in which magnetic order can take place. Not all the spins in the system will have been relaxed by the disorder; those outside the clusters take part in the interactions between them. As the temperature cools towards T_f, the interactions between clusters and spins gradually becomes more long-range and the system freezes in one of its many ground states. The ground states below T_f appear 'glassy', possessing no long range order, metastability and slow relaxation behaviour; as a consequence spin glasses possess no magnetic Bragg peaks in their neutron diffraction patterns and a divergence between the field cooled and zero field cooled susceptibility below T_f.

1.3.7 The Curie-Weiss law

The Curie law is an equation that may be used to relate the magnetisation of a Curie paramagnet to the effective magnetic moment on the ion. The addition of the Weiss constant is a correction that is necessary when interactions between spins are not negligible and can account for some degree of ferromagnetism or antiferromagnetism in the system.

Curie paramagnetism is a temperature dependant phenomenon because the thermal energy, k_BT, of the system will tend to randomize the spins away from their alignment to the magnetic field. An inverse relationship exists between temperature and magnetic susceptibility, χ, in Curie paramagnetic systems, which is described by the Curie law:

$$\chi = \frac{C}{T} \qquad \textbf{Equation 1.1}$$

in which C is the Curie constant defined as:

$$C = \frac{N_A \mu_{eff}^2 \mu_B^2}{3k_B} \qquad \textbf{Equation 1.2}$$

where N_A is Avogadro's constant, μ_B is the Bohr magneton, μ_{eff} is the effective magnetic moment and k_B is the Boltzmann constant, which may be reduced to $\mu_{eff} \approx 2.84\sqrt{C}$.

Application of the Curie law allows the Curie constant, and hence the effective magnetic moment of the magnetic species, to be experimentally determined by measuring the magnetisation and evaluating the magnetic susceptibility as a function of temperature, plotting $1/\chi$ against T for a gradient of C, as shown in Figure 1.6. Susceptibility in Equations 1.3 and 1.4 is generally handled as a molar susceptibility, χ_{mol}, which is the sample's magnetisation per unit of applied field and per mole of magnetic ions in the sample.

Curie paramagnetism is in fact relatively rare in extended solid systems, magnetic atoms or ions present in the materials tend to experience some interaction with one another, usually showing antiferromagnetism or ferromagnetism. In such cases, the magnetic susceptibility deviates from the Curie law and is often better described by the Curie-Weiss law:

$$\chi = \frac{C}{T-\theta} \qquad \textbf{Equation 1.3}$$

where θ is the Weiss constant, and is obtained as the intercept of the temperature axis in a Curie-Weiss plot. The sign of the Weiss constant tells of the nature of the interaction, positive for a ferromagnetic interaction and negative for an antiferromagnetic interaction. The magnitude of θ gives an indication of the strength of the interaction between localised spins, and is expected to be close to the Curie temperature, T_C, or Néel temperature, $T_{N,}$ for a ferromagnet or antiferromagnet, respectively.

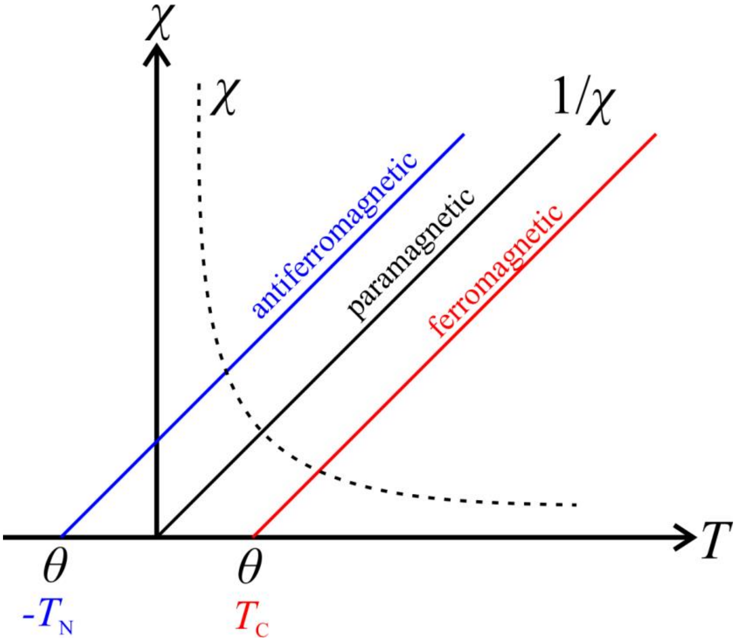

Figure 1.6 Curie-Weiss plot of $1/\chi$ against T demonstrated for paramagnetic, antiferromagnetic and ferromagnetic systems.

Plots of $1/\chi$ against T may break from linearity, particularly in systems that exhibit more complicated magnetic phenomenon or systems with strong coupling interactions when approaching T_C or T_N as the Curie-Weiss law fails to be an accurate description for the susceptibility. In these systems, the Curie-Weiss law only holds at temperatures far exceeding the Weiss temperature.

1.4 Superconductivity

1.4.1 Conventional superconductivity

The discovery of superconductivity has its links to advancement of cryogenic refrigeration techniques in the early 20th century that allowed scientists to cool samples to 4 K (liquid helium temperature). The phenomenon was first identified in 1911 by Heike Kamerlingh Onnes who studied the resistance of solid mercury at low temperatures and observed that its resistance rapidly and discontinuously disappeared below 4.2 K[16] as shown in Figure 1.7. The property was exhibited in further systems and it was later shown to be possible to construct a superconducting circuit from tin or lead, in which current continued to flow even after the external power supply had been removed.[17]

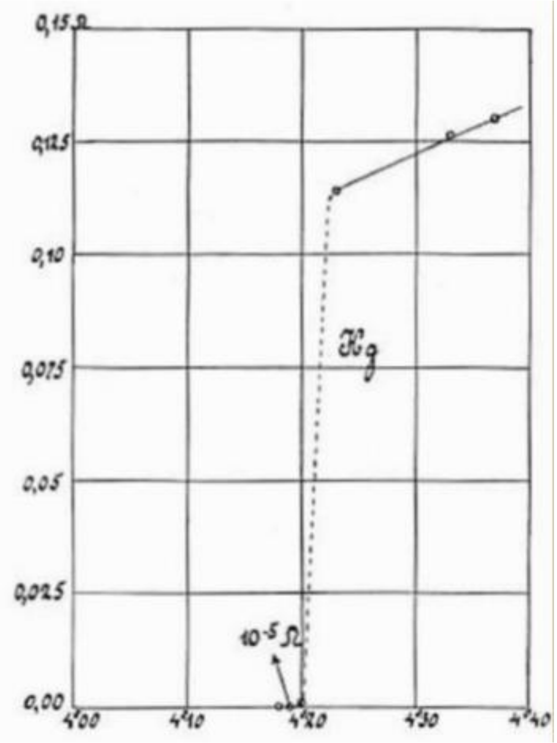

Figure 1.7 Plot of resistance (ohms) versus temperature (kelvin) for mercury from October 1911 showing the superconducting transition at 4.20 K (from reference 18**).**

A second breakthrough discovery in the properties of superconductors was made in 1933, when Meissner and Ochsenfeld showed that the superconducting transition coincides with a remarkable magnetic property. In an applied magnetic field, zero resistance currents near the surface of the superconducting sample generate a magnetic field equal and opposite to the applied field, completely shielding the inside of the sample from the external field. This means that the internal field, *B*, of a superconductor, is always zero (perfect diamagnetism).[19] This second intrinsic property of superconductors was subsequently named the Meissner-Ochsenfeld effect.

The properties of zero resistance and perfect diamagnetism exhibited by these materials could not be explained by any classical theory of conduction. An early theory developed by the brothers Fritz and Heinz London attempted to explain the Meissner effect in terms of superconducting electrons that are condensed into a single macroscopic quantum state.[20] The Ginzburg-Landau theory of 1950 gave further explanation of the macroscopic properties of superconductors, without offering an explanation for the underlying microscopic properties.[21] Also in 1950 Maxwell and Reynolds both discovered a dependence of the superconducting critical temperature (T_c) on the isotopes used in the constituent elements – suggesting that an interaction of the electrons with lattice vibrations (phonons) may play an important role.[22,23] These discoveries and theories laid the groundwork for the Bardeen-Cooper-Schrieffer (BCS) theory, published in 1957 (and awarded the Nobel Prize in Physics in 1972), which was able to explain and predict all of the properties of the known superconductors: zero resistivity, the Meissner-Ochsenfeld effect, and the isotope effect.[24]

1.4.2 Bardeen-Cooper-Schrieffer (BCS) theory

In BCS theory, phonons create a small attractive interaction between conduction electrons in the vicinity of the Fermi level, which below T_c condense into so called 'Cooper pairs' aligned antiparallel to one another. This has the effect of opening an energy gap at the Fermi level, stabilising the superconducting state over the normal state. The gap here corresponds to the energy required to break the alignment of the Cooper pair and is related to T_c at a given temperature T in units of Kelvin by:

$$\boldsymbol{E = 3.52 k_B T_c \sqrt{1 - \frac{T}{T_c}}} \qquad \textbf{Equation 1.4}$$

The equation for this energy gap can be used to derive an expression for the transition temperature as a function of the electron-phonon coupling constant (λ) and the theoretical maximum phonon energy of the crystal, known as the Debye energy ($\hbar\omega_D$), which is in units of Joules:

$$\boldsymbol{k_B T_c = 1.13 \hbar\omega_D \exp(-1/\lambda)} \qquad \textbf{Equation 1. 5}$$

It follows from equation 1.5 that to maximise T_c, both λ and $\hbar\omega_D$ should be maximised, that is, the crystal structure should have high frequency phonons and a strong electron-phonon coupling. An important prediction of this theory is that superconductivity arising from an electron-phonon coupling cannot normally give rise to a bulk transition temperature much above 30-40 K. However, recent theoretical calculations have predicted that extremely high λ and $\hbar\omega_D$ values could be achieved for many hydrides at high pressures, giving rise to very high T_cs,[25,26] and there has been an experimental report of T_c as high as 190 K in a H_2S sample pressurised at 200 GPa.[27]

It should be noted that just as thermal energy can break the antiparallel alignment of Cooper pairs, the application of an external field also opposes the pairing and above a certain critical field, H_c, superconductivity is ceased. Superconductors can be divided into two types based on how the Meissner-Ochsenfeld effect is broken by high fields. Type I superconductors experience the effect up to H_c, (at fixed temperature) at which point there is a discontinuous transition and the material no longer excludes the external field and ceases to be superconducting. For a type II superconductor there is total exclusion of the external field up to a critical field, H_{c1}, then gradual reduction in the extent of field exclusion to zero up to a second critical temperature, H_{c2} after which there is no Meissner-Ochsenfeld effect at all, and superconductivity is ceased.

Superconductivity continued to be discovered in an increasing number of systems, several alloy systems such as Nb_3Sn[28] and NbTi[29] with superconducting transition temperatures (T_c) of 18.3 K and 10 K, respectively are still the frontrunners for most commercial applications of superconducting magnets. MgB_2 was discovered to be a superconductor only in 2001 with a T_c of 39 K, its light element constituents giving rise to high frequency phonons.[30] This is perhaps the highest T_c non-theoretical BCS superconducting material that can be made and is stable at atmospheric pressure, but a number of superconducting materials have been discovered that exhibit properties that are inconsistent with BCS theory and have T_cs that well exceed that of MgB_2.

1.4.3 The cuprate superconductors

While superconductivity was still of interest after 1957, it was labelled as a solved problem with quantifiable limits on the properties of the materials that were made, however in 1986 the discovery of superconductivity at 30 K in the ceramic material $(La_{2-x}Ba_x)_2CuO_4$,[31] an unexpectedly high temperature for such a material, brought new intrigue to the area. A vast surge in research followed and subsequent reports of superconductivity at 36 K in $La_{2-x}Sr_xCuO_4$,[32] 93 K in $YBa_2Cu_3O_{6+x}$,[33] 85 K in $Bi_2Sr_2CaCu_2O_8$,[34] 110 K in $Bi_2Sr_2Ca_2Cu_3O_{10}$,[35] and 125 K in $Tl_2Ba_2Ca_2Cu_3O_{10}$.[36] $YBa_2Cu_3O_{6+x}$ drew particular attention for not only well exceeding the predicted maximum T_c of BCS theory, but also being the first superconductor with a T_c above the boiling point of liquid nitrogen. The highest known T_c at ambient pressure currently stands at 133 K for the compound $HgBa_2Ca_2Cu_3O_{8+\delta}$.

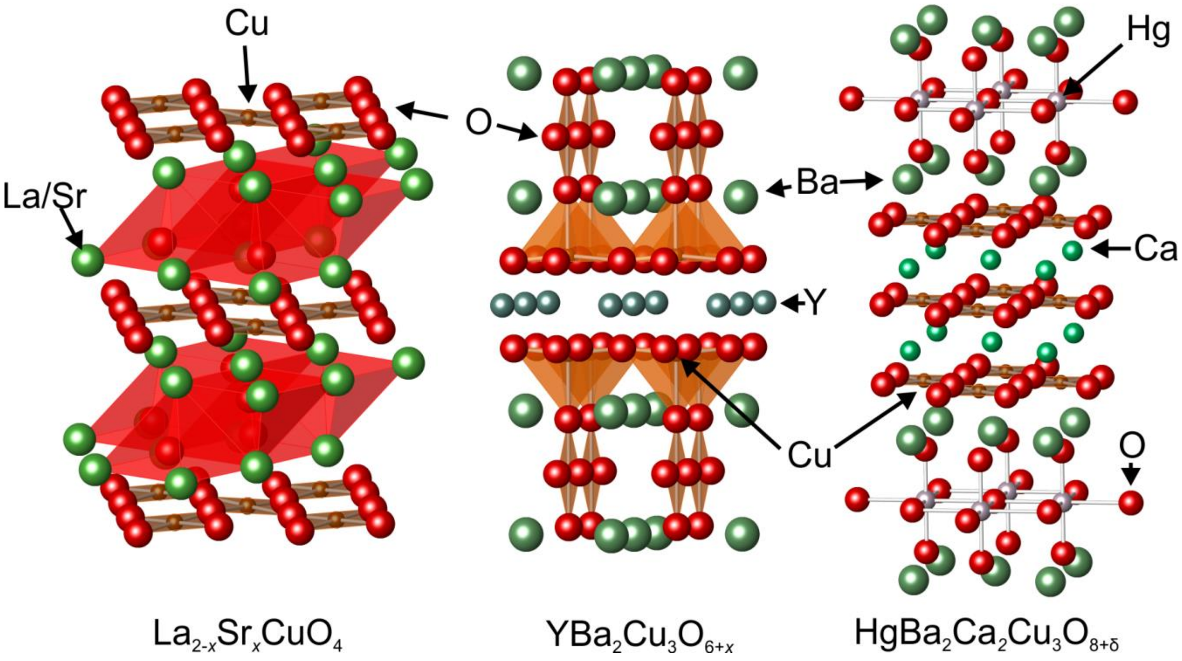

Figure 1.8 Structures of three cuprate superconductors

The common structural feature to all cuprate superconductors is two-dimensional CuO_2 planes formed of corner-sharing, square planar CuO_4 units; a number of different types of layers may separate these. The materials can be described as perovskite-related; some like $La_{2-x}Sr_xCuO_4$ adopt Ruddlesden-Popper phases ($A_{n-1}A'_2B_nX_{3n+1}$, where in this case $n = 1$) like the K_2NiF_4 structure, while others form complex stacks built of perovskite-like layers in which some have reduced coordination about the metal centres due to oxide vacancies. $HgBa_2Ca_2Cu_3O_{8+\delta}$, and the other >100 K superconductors have multiple CuO_2 layers adjacent to one another. The structure of $YBa_2Cu_3O_{6+x}$ (YBCO) contains closely-spaced two-dimensional square based pyramid CuO_2 sheets separated by yttrium ions linked by the oxide vertex at the pyramid tip to one-dimensional chains of corner-linked CuO_4 squares along the crystallographic *b*-direction; here the anion vacancies between the parallel 1-D chains are able to host additional oxide ions.

The versatility of the perovskite based framework structure towards variable oxide occupations such as in YBCO and aliovalent substitution such as in $La_{2-x}Sr_xCuO_4$ allows for considerable control of the oxidation state of copper in the system. In their 'undoped parent' state (*e.g.* La_2CuO_4 or $YBa_2Cu_3O_7$) the cuprates have a nominal copper valency of +2 and are Mott Hubbard insulating antiferromagnets. Suppression of the antiferromagnetism can be achieved by hole or electron doping at the Fermi level (oxidising or reducing copper in the system), both of which can give rise to a metallic cuprate that may become superconducting at low temperatures. The phase diagrams of

$Nd_{2-x}Ce_xCuO_4$ and $La_{2-x}Sr_xCuO_4$ as a function of x are good examples of the effects of hole and electron doping, respectively, these are shown in Figure 1.9.

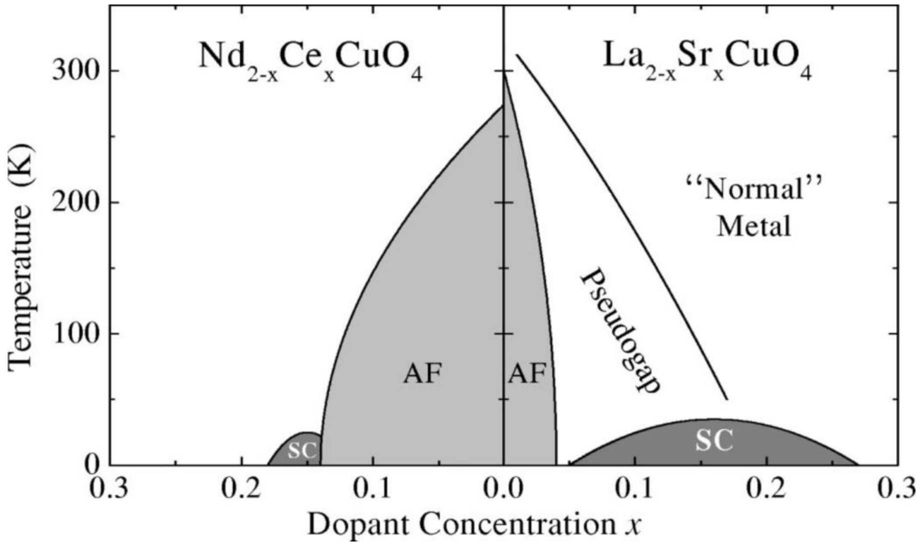

Figure 1.9 Phase diagram of *p*- (left) and *n*- (right) type doping of a cuprate superconductors (figure from reference 37**).**

The unconventional superconducting properties of the cuprates cannot be explained in terms of the BCS theory; their properties differ in several ways to those of the conventional superconductors, showing no phonon dependence and a strong correlation to the Fermi level density of states. Correlations, whereby magnetic "spin wave" interactions between the electron and the magnetic lattice may play a role in the coupling of Cooper pairs, but as yet there is no predictive theory for unconventional superconductors.[38] Despite superior transition temperatures, applications of the cuprate superconductors are limited by the difficulty of making a ceramic into a wire, YBCO based commercial MRI magnet systems are in development and may not be far away, but for the moment, they are not yet widely exploited. Interest in finding new materials that exhibit high temperature superconductivity declined in the late 1990s and early 2000s, but then in 2008 came the discovery of an exciting new class of unconventional superconductors – the iron pnictides – and a resurgence of research began yet again.

1.4.4 The iron pnictide superconductors

1.4.4.1 Structure and observation of superconductivity in the pnictides

The first report of superconductivity in an iron pnictide system was in fact in 2006 from Kamihara *et. al.* in Hosono's group, for the material LaOFeP, with the rather inconspicuous T_c of 3.2 K,[39] which was later shown, could be increased to 7 K on doping of the lanthanum oxide layers with 6 % of F^- ions.[40] Excitement came when a second publication from Kamihara *et. al.* showed that replacement of the pnictide ion from P^{3-} to As^{3-} resulted in an increase in T_c to 26 K for $La(O_{0.95}F_{0.05})FeAs$,[41] which proved that the superconductivity was not due to an impurity that might have accounted for the behaviour of the phosphide. The synthesis of a whole series of isostructural $Ln(O_{1-x}F_x)FeAs$ and compounds followed, and T_c is observed to generally increase with decreasing lanthanide radius, reaching a maximum of 55 K for F-doped SmOFeAs, then decreasing to a maximum of 36 K for F-doped GdOFeAs.[42–44]

Investigation of LaOFeP by McQueen *et al.* indicated superconductivity did not exist in stoichiometrically precise LaOFeP, and therefore attributed observed superconductivity to doping caused by oxygen vacancies of the form $LaO_{1-x}FeP$.[45] Further methods of doping have been explored in the system such as cobalt substitution on the iron site, thorium doping the lanthanide site and hydride doping on the oxide site; each successfully introducing superconductivity to a parent non-superconducting system.[46–48]

LaOFeAs adopts the ZrCuSiAs structure with layers of anti-PbO-type $[Fe_2As_2]^{2-}$ separated by layers of PbO-type $[La_2O_2]^{2+}$. Described in Section 1.2.1 were many known and commonly occurring crystal structures that might readily adopt layers of anti-PbO type $[Fe_2As_2]^{2-}$, and there have been reports of superconductivity in several systems that capitalise on this. The structures for several such reported superconducting parent materials in the iron arsenide family are given in Figure 1.10 and discussed below.

The resistivity of $BaFe_2As_2$, which takes the $ThCr_2Si_2$ structure type, appears rather similar to that of LaFeAsO. This was the initial clue that led to its identification as the first alternative parent compound for iron arsenide superconductors; Rotter *et al.* showed that superconductivity could be induced in the system by aliovalent substitution of Ba for K, giving a T_c of 38 K for the stoichiometry $Ba_{0.6}K_{0.4}Fe_2As_2$.[49] In contrast to the F-doping of LaFeAsO, K substitution in $BaFe_2As_2$ is oxidative, but yields a similar relationship between dopant level and T_c. LiFeAs which takes the anti-PbFCl structure was reported to also show superconductivity below 18 K when stoichiometric,[50,51] and isostructural NaFeAs was found to contain a weak superconducting state below 9 K,[52] which could be enhanced by electron doping such as in $NaFe_{0.975}Co_{0.025}As$ to a completely superconducting state with a T_c of 23 K.[53] Also discovered have been some more structurally complex materials such as Sr_2VO_3FeAs, in which the iron arsenide layers are separated by perovskite-related oxide spacing layers, and $Ca_{10}(Pt_nAs_8)(Fe_2As_2)_5$ (n = 3 or

4)[54] which contain layered blocks of ThCr$_2$Si$_2$-type CaFe$_2$As$_2$ separated by Pt$_3$As$_8$ or Pt$_4$As$_8$ layers based on the skutterudite structure – a common crystal structure among binary pnictides. Sr$_2$VO$_3$FeAs was reported to have a T_c of 37 K (from resistivity measurements) without electronic doping of the FeAs carrier layer, resembling the LiFeAs case.[55] Superconductivity in both Ca$_{10}$(Pt$_n$As$_8$)(Fe$_2$As$_2$)$_5$ phases is induced by electron doping the Fe$_2$As$_2$ layer by substitution of Fe with Pt; a maximum T_c of 26 K is observed in Ca$_{10}$(Pt$_4$As$_8$)(Fe$_{2-x}$Pt$_x$As$_2$)$_5$ and 11 K is observed in Ca$_{10}$(Pt$_3$As$_8$)(Fe$_{2-x}$Pt$_x$As$_2$)$_5$.

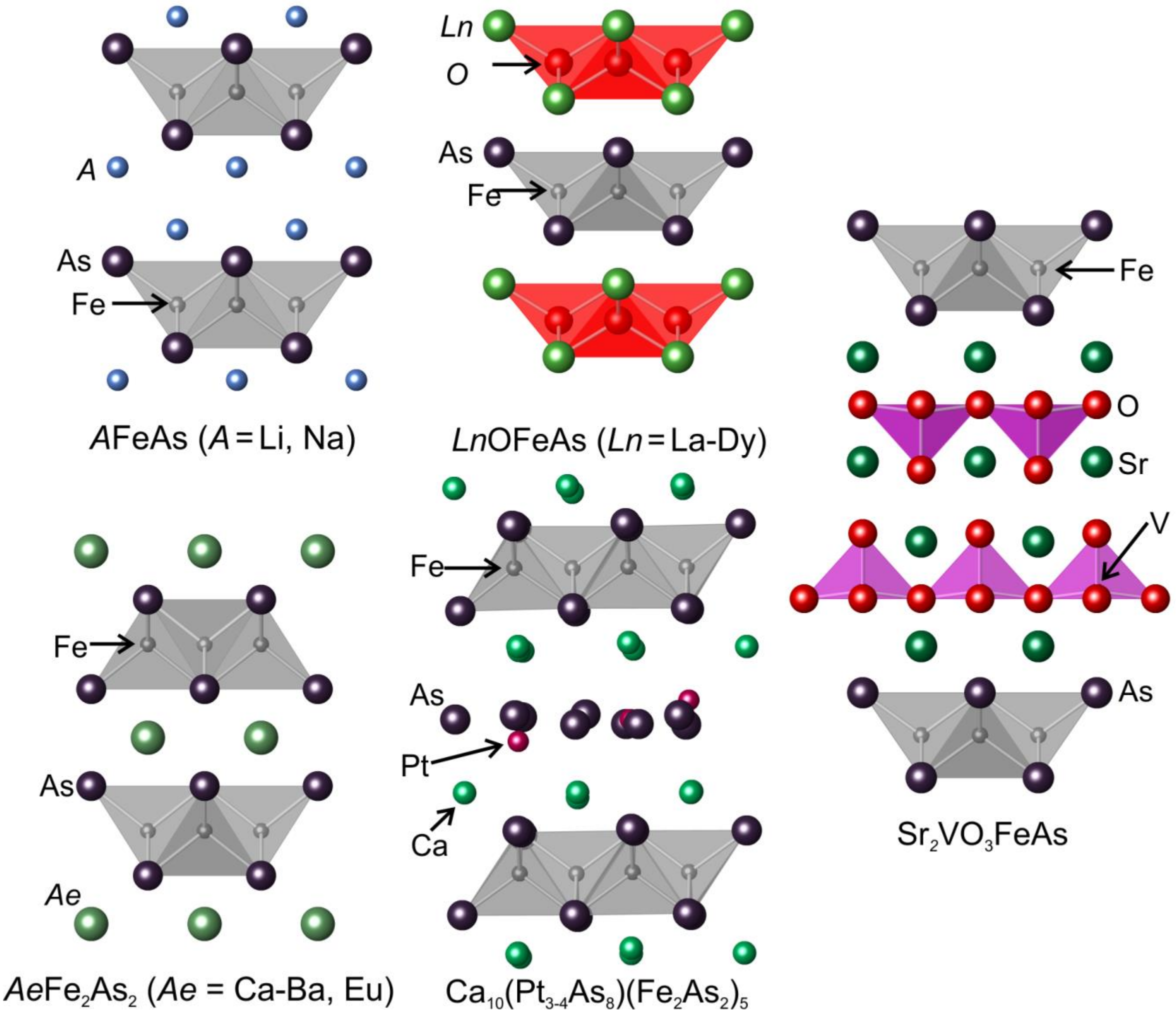

Figure 1.10 Several iron arsenide containing structures that exhibit unconventional superconductivity.

1.4.4.2 Superconducting and magnetic properties of the iron pnictides

Similar to the situation observed in the cuprates, the presence of Fe^{2+} ions in a material often gives rise to magnetic order on cooling. A commonly occurring feature in the iron pnictide superconductor family is the existence of an antiferromagnetic state that closely neighbours the superconducting state. This is exemplified in the undoped *Ln*OFeAs series:

a striped antiferromagnetic arrangement of small Fe moments ($< 1\ \mu_B$) is observed at low temperature following a structural transition from tetragonal symmetry to orthorhombic with an enlarged unit cell. An example of the orthorhombic distortion and antiferromagnetic ordering is shown in Figure 1.11; it may be noted that the magnetic ordering breaks the 4-fold rotation axis of the tetragonal symmetry. Alignment of the spins along the *c*-axis in these systems may be antiparallel (*e.g.* *Ln* = La, Nd) or parallel (*e.g.* *Ln* = Ce, Pr).[56]

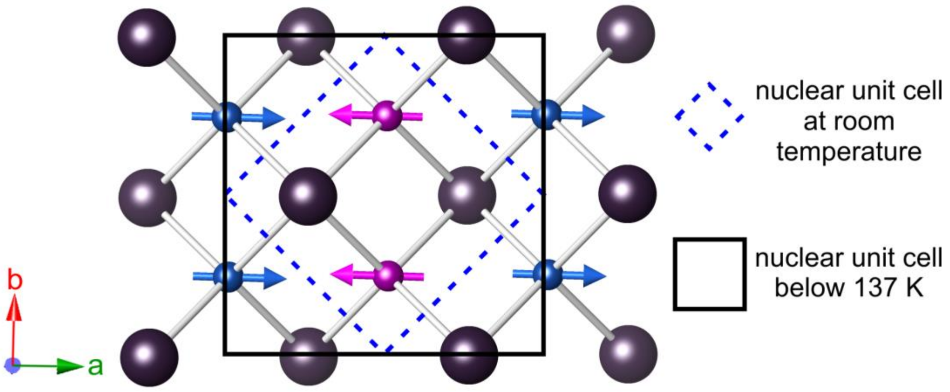

Figure 1.11 Magnetic ordering of Fe^{2+} moments in the $[Fe2As2]^{2+}$ layers of LaOFeAs; Fe = blue/pink, As = purple; the blue/pink colour of the Fe ions relates similar spins.

Superconductivity may be brought on in an iron arsenide parent system by a variety of means. Inspection of the phase diagrams of several systems shows a trend: as the dopant is introduced, the structural and antiferromagnetic transition temperatures are reduced and eventually supressed whilst a superconducting state simultaneously grows in. There is a small region where antiferromagnetism and superconductivity often, but not always,[57] appear to coincide before the system enters a fully superconducting state. Electronic phase diagrams of several systems that exhibit this behaviour are shown in Figure 1.12. LiFeAs appears to be an exception to this general behaviour, exhibiting bulk superconductivity in its stoichiometric ‘undoped’ state;[50] in fact, doping actually serves to supress superconductivity.[58] NaFeAs also exhibits a modicum of superconductivity (~10 % of it volume), however long range antiferromagnetic order is apparent over most of its volume, and bulk superconductivity may be induced by electron doping through the partial substitution of Co or Ni on the Fe crystallographic site.[53] Sr_2VO_3FeAs also exhibits superconductivity in its undoped state and shows no strong evidence for magnetic ordering on the Fe lattice, nor do the isostructural, non-superconducting compounds Sr_2ScO_3FeAs and Sr_2CrO_3FeAs.[59] $Ca_{10}(Pt_nAs_8)(Fe_2As_2)_5$ materials also shows no strong evidence for magnetic ordering of the Fe sites, but the situation is complicated by the possibility of intrinsic platinum doping of the FeAs layers.

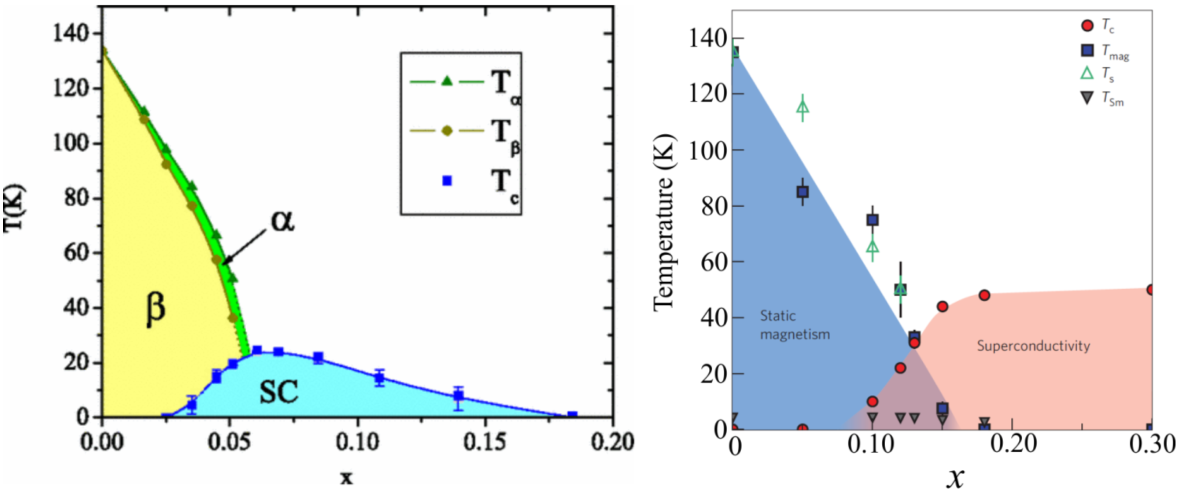

(a) $BaFe_{2-x}Co_xAs_2$ (b) $SmO_{1-x}F_xFeAs$

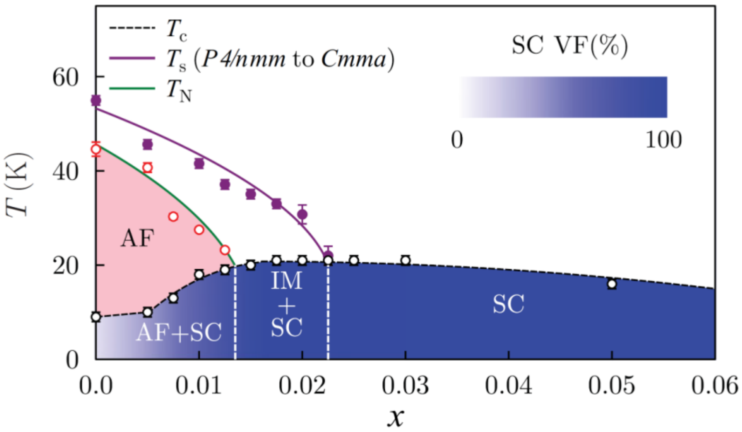

(c) $NaFe_{1-x}Co_xAs$

Figure 1.12 Magnetic phase diagrams taken from the literature showing the effect of electron doping against the magnetic/superconducting properties of three iron arsenide superconductors. (a) is from reference 60 (b) is from reference 61 and (c) is from reference 62.

The reports described so far go to show that carrier doping is an effective means of modifying the Fermi surface and bringing about superconductivity in the iron pnictide parent materials. This method of electronic tuning is well established and has a strong correlation with superconducting properties as shown in Figure 1.12, but slight modifications of the crystal structure without doping can also play an important role in shaping the Fermi surface and determining the T_c of these materials. Superconductivity may be induced in $BaFe_2As_2$ by isovalent substitution of As for P of the form $BaFe_2(As_{1-x}P_x)_2$ which can give a T_c as high as 30 K.[63] The effect of phosphorus in this system appears to be one of chemical pressure, which modifies the bond distances and angles in the structure in a very similar manner to that of applying external physical pressure; as shown by the fact that the two forms of pressure can be used to produce the same phase diagram.[64] The pressure effect in this system has been reported in angle-resolved photoemission spectroscopy (ARPES) studies to influence Fe 3d orbital bands in a similar way to hole doping.[65]

The tetrahedral bond angles in the iron arsenide layer are sometimes correlated to the superconducting transition temperature, as done in the paper by Lee *et al.* shown in Figure 1.13. The authors identify that the closer the tetrahedra is to being regular (α = β = 109.47 °), the higher the T_c of the optimally doped system, *albeit* with a rather selective sample data set.

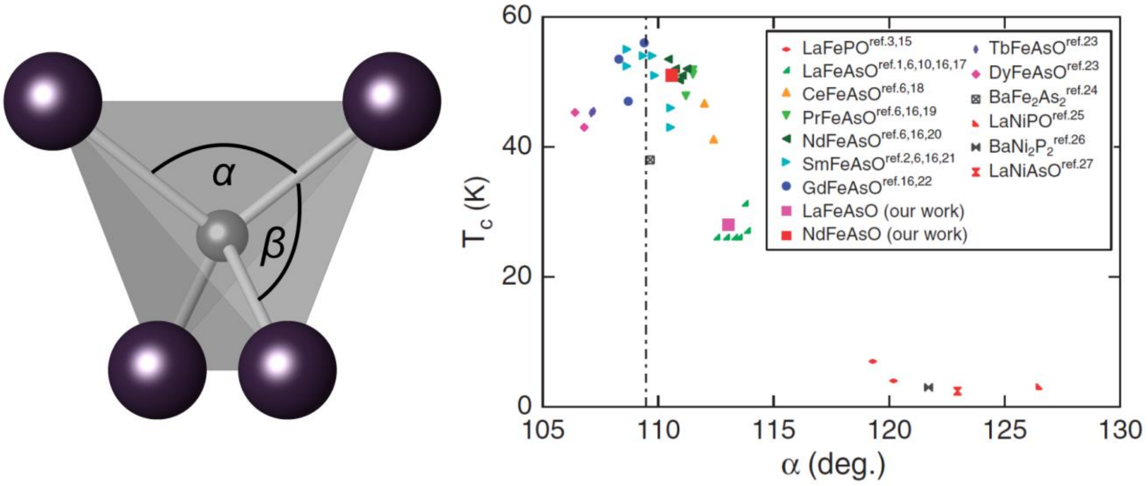

Figure 1.13 T_c vs As–Fe–As bond angle for various pnictide superconductors in their optimally electron doped state (from reference 66).

1.4.5 The iron chalcogenide superconductors

The chalcogenides are an alternative branch of iron-based superconductors that exhibit much the same properties as the pnictides. The first discovery in the area came when, noting the structural similarity between the iron arsenide superconductors and the β polymorph of FeSe, which consists of layers of edge sharing $FeSe_4$ tetrahedra, Hsu *et al.* found it had a superconducting transition at around 8 K.[67]

Superconductivity in β-FeSe is found to be enhanced on the application of external pressure,[68] with a maximum $T_{c(\mathrm{onset})}$ = of 37 K at a pressure of 8.9 GPa.[69] The positive relationship between T_c and pressure in this system is further evidence of it being an unconventional superconductor, since the T_c of a BCS superconductor will lower as pressure is applied. An applied pressure of 8.9 GPa is found to decrease the volume of the unit cell to about 83 % of its original value, but Mössbauer spectroscopy indicates that the local Fe-Se and Fe-Fe bond distances change very little, and it is the collapse of the van der Waals gap between FeSe layers that is responsible for the drop in volume. Isovalent substitution on the selenium site has shown some success in raising the T_c in this system, with a maximum T_c of 15 K observed for $FeSe_{0.5}Te_{0.5}$.[70]

While external and internal pressure effects have been shown to increase T_c in FeSe, charge carrier doping by substitution of iron for cobalt has been shown to supress superconductivity in FeSe[71,72] and $FeSe_{0.5}Te_{0.5,}$[73] with 2.5 % substitution being enough to completely supress superconductivity in the former and 5 % substitution reducing T_c from 15 to 6 K in the latter. It should be noted that in the synthesis of β-FeSe the material is made slightly iron rich $Fe_{1+x}Se$ with x typically being 0.02 so as to stabilise over the α structure. It has been reported that this excess iron which occupies interstitial sites within the interlamellar space of the FeSe layers is detrimental to the superconductivity, quenching superconductivity at $x = 0.03$.[74]

FeSe represents the most structurally simple iron-based superconductor with superconducting layers of anti-PbO type FeSe separated only by a van der Waals gap. While having the advantage of structural simplicity, β-FeSe offers less electronic flexibility than the arsenides, which have modifiable interlamellar species. Related materials in which alkali metals (K, Rb) separate the layers can be synthesised in a high temperature reaction to produce materials with T_c around 31 K.[75,76] Although initially reported as having a nominal composition of $K_{0.8}Fe_2Se_2$,[75] it is widely found that this composition does not exist in the bulk, and that attempting to reduce iron much away from a +2 oxidation state in this manner instead results in large numbers of vacancies on the iron site. The class of materials is defined thusly as $K_{1-x}Fe_{2-y}Se_2$, which are often found to exhibit iron vacancy ordering.[77] Well characterised compositions close to a stoichiometry of $K_{0.8}Fe_{1.6}Se_2$ (or $K_2Fe_4Se_5$) having a formally divalent iron state are most commonly found to exist in the iron vacancy-ordered state, and are also found to show antiferromagnetic order in which the magnetic structure is linked to the vacancy ordering scheme and the localised moment on iron is around 3.5 μ_B.[78] A cursory glance might draw analogy to the antiferromagnetic states exhibited by the parent material of the iron arsenide superconductors such as NaFeAs. An antiferromagnetic state in NaFeAs appears close to the superconducting regime, and may be quenched by electron doping, however the antiferromagnetic state in $K_2Fe_4Se_5$ is not of the same nature as evidenced by a much larger local moment on iron (around 0.1 μ_B in NaFeAs). The literature on the $K_{1-x}Fe_{2-y}Se_2$ is confused by contradictory reports of bulk superconductivity in phases with variously reported compositions which have proved difficult to reproduce.[79] A proposed solution to the origin of superconductivity in compounds of this system is that the materials consist of intergrowths of an antiferromagnetic majority phase, and a superconducting minority phase. There is growing evidence to this effect, an NMR study on superconducting Rb-Fe-Se phases showed evidence of intergrowths of superconducting filaments of a material with a composition of $Rb_{0.3(1)}Fe_2Se_2$ within the bulk which is antiferromagnetic and non-superconducting, of composition $Rb_{0.8}Fe_{1.6}Se_2$.[80] Mössbauer spectroscopy,[81] Optical microscopy, and low-energy muon-spin rotation (µSR) measurements support this model,[82] and ARPES[83] and high resolution powder diffraction[84] measurements have shown evidence for this being the case in superconducting K-Fe-Se systems also. Recent progress has been made on the isolation of the superconducting phase component in the K-Fe-Se system, *in-situ* scanning electron and transmission electron microscopies at elevated temperatures have been used to probe the growth mechanism of the superconducting phase in single crystals.[85,86] High temperature *in-situ* single crystal X-ray diffraction experiments have successfully followed the growth of the superconducting domains in $K_{1-x}Fe_{2-y}Se_2$ single crystals and suggested that there may be ways to enhance the growth of these domains.[87]

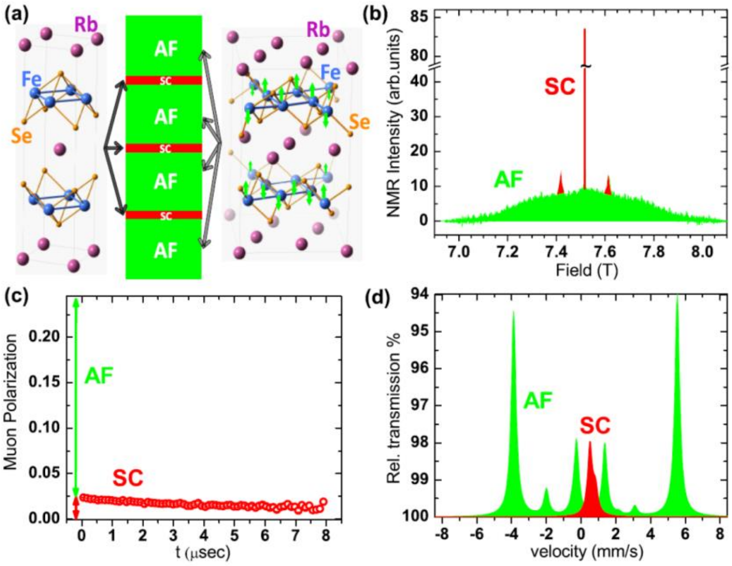

Figure 1.14 Taken from reference 80 **showing (a) the proposed alternate layered arrangement of antiferromagnetic $Rb_{0.8}Fe_{1.6}Se_2$ (green) and superconducting $Rb_{0.3}Fe_2Se_2$ (red) that was suggested from optical microscopy[82] alongside (b) their own NMR data, (c) µSR spectroscopy data from reference** 88 **and (d) Mössbauer spectroscopy data from reference** 81**, to support the proposed model.**

It appears in the systems mentioned thus far that superconductivity occurs in a layered FeSe based system when the iron site in the selenide layer is fully occupied and a higher T_c

is observed when the iron is slightly reduced and the FeSe layers are well separated. The synthesis at high temperature of $K_{1-x}Fe_2Se_2$ introduces vacancies in the iron selenide layer, presumably because the reduction of iron in a selenide system to an average oxidation state lower than +2 is thermodynamically unfavourable with respect to disproportionation at high temperatures. This leads to the question of whether any other synthetic routes can yield a stoichiometric FeSe layer with a slightly reduced iron oxidation state and an increase in the FeSe interlayer space.

As discussed previously in this chapter, compounds with an interlamellar space between relatively polarisable anions are commonly susceptible to topotactic intercalation or deintercalation of species between the layers. This ‘soft’ chemistry provides a promising route to a target compound containing FeSe layers separated by a spacer ion, blocks, or molecules. Successful intercalation into β-FeSe was first achieved by Ying *et al.* by reaction with alkali, alkaline earth, and rare earth metals in liquid ammonia solvent, reporting large increases of the FeSe interlayer space and superconductivity, from 5.52 Å and 8 K in β-FeSe to 8-10.25 Å and 30-46 K in the intercalate depending on the metal used.[89] A similar reaction had been attempted in the research group by Paul Adamson, who reacted β-FeSe with ^{n}butyllithium, but found that the lithiating agent formed Li_2Se with the expulsion of elemental iron.

Lithium solvated in ammonia is expected to have a higher reduction potential than ^{n}butyllithium, so it is surprising that the former could give lithium intercalated between the layers of FeSe with partial reduction of Fe^{2+}, but the latter reduces Fe^{2+} all the way to Fe^{0}. The structure proposed by Ying *et al.* for the intercalates made in liquid ammonia solution was the $ThCr_2Si_2$ structure with the intercalating cation in the Th site, which gives a decent match to powder X-ray diffraction but is chemically unrealistic when comparing the separation between FeSe layers in the intercalates (7.5-10.25 Å) and $K_{0.8}Fe_{1.6}Se_2$ (~7.0 Å). There is also no correlation between interlayer separation and cation size, and the proposed structure would leave an unreasonably long distance between the selenium and the alkali/alkaline earth/rare earth metal in the product structure – particularly notable when lithium is the chosen intercalate. Thorough investigations in the group of the lithium intercalate by Burrard-Lucas *et al.* showed using neutron powder diffraction on a deuterated sample that ammonia / amide moieties were being co-intercalated into the structure along with lithium and refined the structure on the right of Figure 1.15, with a formula of $Li_{0.6(1)}(ND_2)_{0.2(1)}(ND_3)_{0.8(1)}Fe_2Se_2$.[90] The existence of amide in the intercalate structure has important ramifications on the iron oxidation state; the refined composition of the deuterated sample yields an average iron oxidation state of +1.9. Scheidt *et al.* reported that in samples made in low concentrations of lithium ammonia solution, the appearance of amide is avoidable, describing samples of composition $Li_{0.5}(NH_3)_{0.6}Fe_2Se_2$ and $Li_{0.9}(NH_3)_{0.5}Fe_2Se_2$ with which would have iron oxidation states of +1.75 and +1.575, respectively.[91]

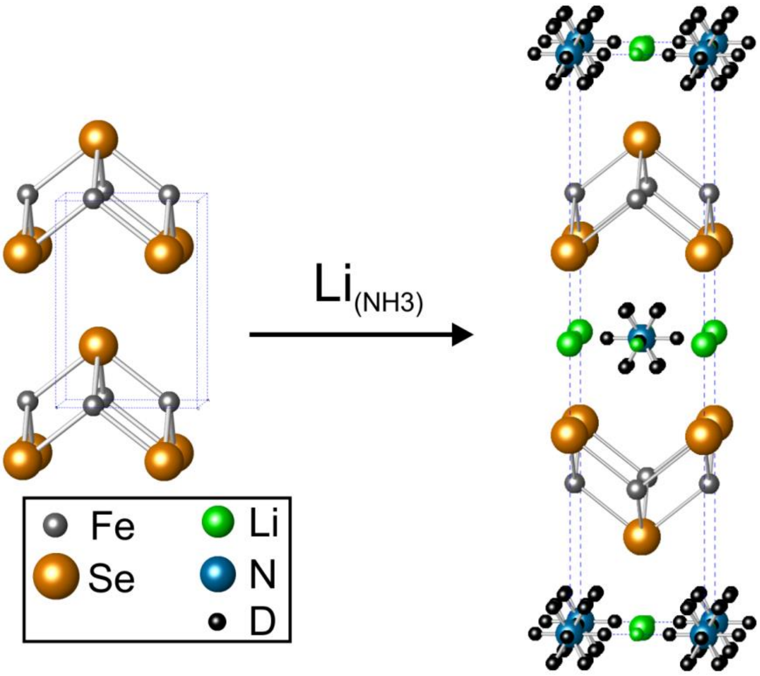

Figure 1.15 Reaction of iron selenide with lithium metal in liquid ammonia solution yields the structure shown with both lithium and ammonia co-intercalated. The deuterium atoms are disordered over sites about nitrogen.

The lithium intercalate has a reported T_c of 43 or 44 K. Ying *et al.* reported a superconducting volume fraction of 32 % form SQUID magnetometry, Burrard-Lucas *et al*. reported a volume fraction of 50 % from SQUID magnetometry and μSR spectroscopy.

1.5 Summary and project aims

Traditional ceramic synthesis of materials at high temperatures is the foundation for the discovery of new materials, but is its products are always driven by thermodynamics. ‘Soft chemistry’ in solid state synthesis generally relies on the high mobility of certain ions in certain crystal structures to make modifications to an existing system that could not be achieved at high temperatures. These methods are particularly useful in the field of iron-based superconductors.

There are several parent structure types in the iron based superconductor family, the common feature that identifies them as members, are anti-PbO type layers of iron pnictide or iron chalcogenide. Superconductivity in these materials is unconventional (not adhering to the BCS theory), originating from Cooper pairs of electrons that are not paired through phonons but seemingly though some magnetic interaction. Correlations of the superconducting transition temperature may be made with the number of electrons at the Fermi surface by *p*- or *n*- type doping the materials, however there is no universal theory to explain or predict the superconducting properties of these materials. The research described in this thesis uses a mixture of high and low temperature synthesis techniques as a means of exploring and expanding the spectrum of phases and chemical systems relating to the iron based superconductors. Various characterisation techniques have been employed using world-class facilities to understand the structure of these systems.

Chapter 3 discusses NaFeAs, which takes the layered anti-PbClF structure and is an archetypal iron arsenide superconductor. Itself an itinerant antiferromagnet, it exhibits a trace fraction of superconductivity, but *n*-type doping the band structure by substituting small amounts of iron for cobalt can bring the material into the bulk-superconducting regime. There have been reports that sodium can be deintercalated from the material by exposure to oxygen or an oxidising solution to give a new superconductor with the nominal composition $NaFe_2As_2$ that adopts the $ThCr_2Si_2$ structure type, akin to KFe_2As_2.[92,93] There has followed a report that suggests iron is deintercalated along with sodium leaving a stoichiometry close to $NaFe_{1.7}As_2$.[94] This work aims to investigate the effect that cobalt substitution carries through to the deintercalated material and further investigate its structure by use of a local probe.

β-FeSe is the most structurally simple iron-based superconductor with superconducting layers of anti-PbO type FeSe separated only by a van der Waals gap. Expanding the number of systems based on iron selenide layers has long been a goal since superconductivity in the system was discovered in 2008.[67] The discovery that alkali metals and ammonia can be co-intercalated between FeSe layers[89,90] brings a wealth of possible target structures, with precedent in similar systems such as the widely explored area of molecular intercalations into transition metal dichalcogenides. Chapters 4 and 5 will explore the remarkable structural chemistry exhibited by these superconducting systems and improve on the reported characterisation of some of these materials, including identification of intermediates formed during their synthesis using state-of-the-art diffraction facilities.

Finally, Chapter 6 will discuss the synthesis, structure and magnetism of the previously unreported material CaFeSeO, which crystallises with a so-far-unique variant of the BaZnSO structure, with an unusual distorted tetrahedral coordination about iron that has two oxide and two selenide vertices. Solution of the previously unknown crystal structure has been carried out from laboratory X-ray powder diffraction data. Further study of the material using electron, Synchrotron X-ray, and neutron diffraction techniques show that the structure has additional complexity, which can be related back to its unusual coordination environment about iron. The magnetism of the system has been characterised by means of SQUID magnetometry and low temperature powder neutron diffraction, showing an interesting combination of spin glass behaviour and antiferromagnetic order.

Chapter 2

2. Experimental techniques

2.1 Synthetic techniques

2.1.1 Ceramic synthesis

As discussed in Chapter 1, the ceramic synthesis is a method of overcoming the mobility barrier to reaction in the solid-state by undertaking said reaction at high temperature. The solid reactants are ground together in an effort to achieve an even distribution of grain boundaries, over which the two or more solids must react. To further improve the proximity of the grain boundaries, the ground reactants are often pressed into a pellet, typically under a 0.1-1 GPa of pressure. The ground powder or pressed pellet is contained within a crucible made from an inert material (alumina is often chosen) and annealed in a furnace at a specific temperature for a prolonged period of time, typically 12+ hours. The method of cooling can have influence on the product formed, rapid cooling can trap a polymorph which is only stable at high temperature, while a very slow cooling rate might be used to favour crystal formation.

2.1.2 Handling of air-sensitive materials

For processes involving air-sensitive reactants or products, it is necessary to use inert atmosphere conditions during the appropriate stages of the synthesis. Handling reactant mixtures in which one or more components were air-sensitive was performed inside an argon-filled dry glovebox. Argon was recirculated through a Dow Chemical copper catalyst and molecular sieve bed to remove any contaminating O_2 and H_2O, respectively that may slowly leak in through the gloves or by other means. The O_2 concentration was monitored by an integrated O_2 sensor, and was kept below 0.5 ppm under normal working conditions. It was necessary to press any pellets outside of the glovebox, and so a protective atmosphere was maintained around the pellet die by tying it inside two polyethylene bags before quickly transporting it to the press, applying pressure, and then returning it to the glovebox for extraction. High temperature reaction of air-sensitive reactants can be achieved by heating under an inert gas flow, but for most reaction mixtures it is more effective to seal them inside an evacuated silica ampoule. All silica tubing was stored in a 100 °C drying oven before use to minimise exposure of the reactant mixture to absorbed surface moisture. In cases where reactants are particularly sensitive to moisture, the tubing was ‘flamed’ – heating it to ~700 °C with a butane/oxygen blowtorch under dynamic vacuum to eliminate further absorbed water.

High temperature reactions with volatile metals involve the production of a corrosive metal vapour, which renders the aforementioned use of silica ampoules unsuitable. For such reactions, it is more suitable and safer to seal the reaction mixture inside a suitable metal ampoule, choosing a metal that is inert to the reaction mixture. Niobium and tantalum are typically well suited to this application due to their ductility, high melting points, and low reactivity outside of oxidising conditions. When using this technique for the synthesis in this thesis, niobium tubes were prepared by crimping the open end of a tube containing the reaction mixture shut, then sealing it under an argon atmosphere using arc-welding apparatus. The metal ampoule must itself be sealed inside a silica ampoule before annealing at high temperature to prevent degradation of the wall integrity by reaction with atmospheric oxygen. For niobium ampoules this final protective step was performed when reaction temperatures exceeded 250 °C.

2.1.3 Solution based manipulation of solids

Topotactic changes to a material can often carry low kinetic barriers and can be achieved at much lower temperatures than those required for ceramic synthesis. If a crystal structure is facile towards intercalation and deintercalation processes, this can often be achieved by stirring the solid in an oxidising or reducing solution of a suitable agent. Redox processes are most often necessary driving forces in intercalations and deintercalations.

The treatment of air-sensitive and moisture-sensitive materials with reductive and oxidative solutions was performed using dry solvents in a dry nitrogen or argon environment. Dry solids were first handled inside the argon-filled, dry glovebox, loading them into sealable reaction vessels before transferring them from the glovebox to an exterior Schlenk line such that standard Schlenk line techniques could be used to handle the transfer of solutions between reaction vessels. After a reaction had been completed the product was isolated by removing any liquid via cannula transfer or evaporation, followed by exposure to dynamic vacuum for an appropriate length of time to ensure no vapour remained before extracting in a dry argon glovebox. Glassware was stored in a 100 °C drying oven before use to remove surface moisture.

2.1.4 Synthesis of precursors

The precursor *β*-FeSe, with an anti-PbO structure, was synthesised via a ceramic method typically on a 5-15 g scale. The iron-selenide binary system exhibits a number of different phases, with *β*-FeSe being stable only in a narrow region as a function of stoichiometry and temperature.[95] The reaction procedure was optimised to minimise impurities arising from competing polymorphs, particularly the *α*-FeSe phase which takes the NiAs structure. Powders of iron (Alfa Aesar, 99.998%) and selenium (Alfa Aesar, 99.999%) were ground together in a 1:0.98 ratio, this small excess of iron can adopt interstitial positions between the layers in *β*-FeSe, promoting its formation. The 5-15 g mixture was sealed in an evacuated silica tube and heated to 700 °C at a slow rate (2 °C min^{-1}) to prevent a high pressure of selenium vapour building up before it reacts with the iron. The reaction was held at 700 °C for 24 hours before being cooled to room temperature. After extracting and regrinding the powder product in the glovebox, the powder was divided into ~3 g portions and each was individually sealed in an evacuated silica ampoule for a second annealing at 700 °C for 38 hours, followed by a final annealing step at 400 °C for 48+ hours. The final annealing temperature favours the *β* phase and the ampoules were quenched in ice water from 400 °C to prevent conversion back to the *α* phase, which may occur on slow cooling.

2.2 Characterisation techniques

2.2.1 Diffraction

The irradiation of liquid, gaseous or amorphous matter causes scattering of the radiation in all directions with a broad and seemingly featureless distribution with respect to the scattering angle. However, when the matter is translationally periodic (crystalline) and the radiation has a wavelength similar to that of the atomic scale, the scattering is highly featured; it scatters strongly at a few distinct angles and very weakly at all others, which is known as diffraction. The diffraction of radiation by a crystal is the foremost technique in studying the structure of crystalline solids, suitable types of radiation include X-rays, neutrons, and electrons.

2.2.2 X-ray diffraction

When X-rays enter a crystalline solid, they can interact with the matter in a number of ways. When a photon interacts with a core electron, the electron enters an excited state, from which a second photon can be emitted in a random direction when a relaxation event occurs. This is known as fluorescence and can be probed in X-ray absorption spectroscopy, but for a diffraction experiment fluorescence contributes to the background signal. Photons may also be scattered by an atom's electrons elastically or inelastically as the oscillating electric field of the photon interacts with the electron in a Coulombic interaction. An elastic scattering event emits an electromagnetic wave with the same energy as the incident photon giving rise to the "Bragg scattering" used in crystallography. Inelastic scattering can be used as a spectroscopy technique (*e.g.* Raman spectroscopy) but in a diffraction experiment inelastic scattering contributes to the background.

The Nobel Prize winning discovery of X-ray diffraction was accomplished by von Laue, with his co-workers Friedrich and Knipping in 1912, who obtained a diffraction pattern of a copper sulphate hydrate single crystal. Laue developed the first theory of X-ray diffraction by crystals, considering them to be three dimensional networks of regularly spaced atoms, but the theory can be illustrated by a one dimensional lattice as shown in Figure 2.1.

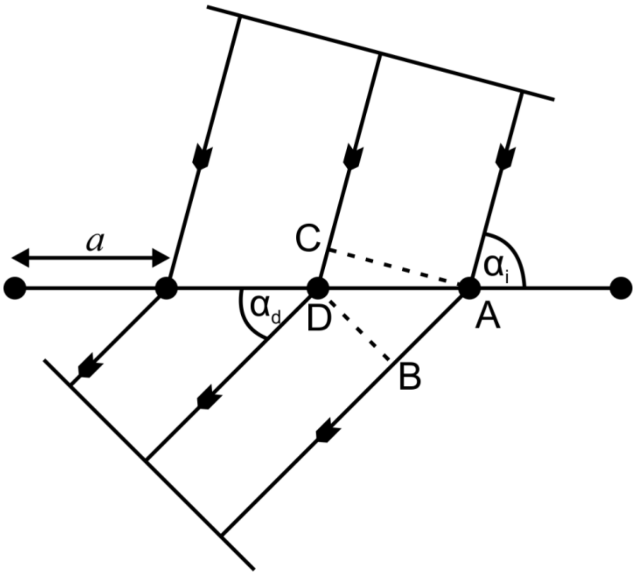

Figure 2.1 Laue scattering of monochromatic radiation by a one-dimensional lattice.

As a parallel, monochromatic beam of X-rays hits the lattice, each atom in the row acts as a point scatterer, producing a secondary source of monochromatic X-rays with a spherical wavefront. Interference occurs between the scattered beams, and the condition for constructive interference from a row of atoms is only satisfied if the path length differs by an integer number (h) of wavelengths (λ):

$$\boldsymbol{AB - CD = a(cos\alpha_d - \ cos\alpha_i) = h\lambda} \qquad \textbf{Equation 2.1}$$

For a three dimensional system there are three Laue equations, corresponding to the orthogonal x, y, and z axes, which must be satisfied simultaneously for constructive interference:

$$\boldsymbol{b(cos\beta_d - cos\beta_i) = k\lambda} \quad \textbf{Equation 2.2}$$

$$\boldsymbol{c(cos\gamma_d - cos\gamma_i) = l\lambda} \quad \textbf{Equation 2.3}$$

This provides a rigorous description of X-ray diffraction, but requires the solution of up to 12 variables, which limits the practical use of these equations in crystallography. An alternative formulation was proposed by W.L. Bragg, who considered instead, diffraction as arising from the reflection of X-rays from planes of atoms within a crystal. These sets of planes, known as Miller planes, are defined by the Miller indices, $h\ k\ l$, which for a unit cell with dimensions $a \times b \times c$ intersect the edges of the unit cell at $\frac{a}{h}$, $\frac{b}{k}$, and $\frac{c}{l}$, respectively. Figure 2.2 shows that constructive interference will occur when the difference in path lengths (2r) equal to an integer number of wavelength $n\lambda$.

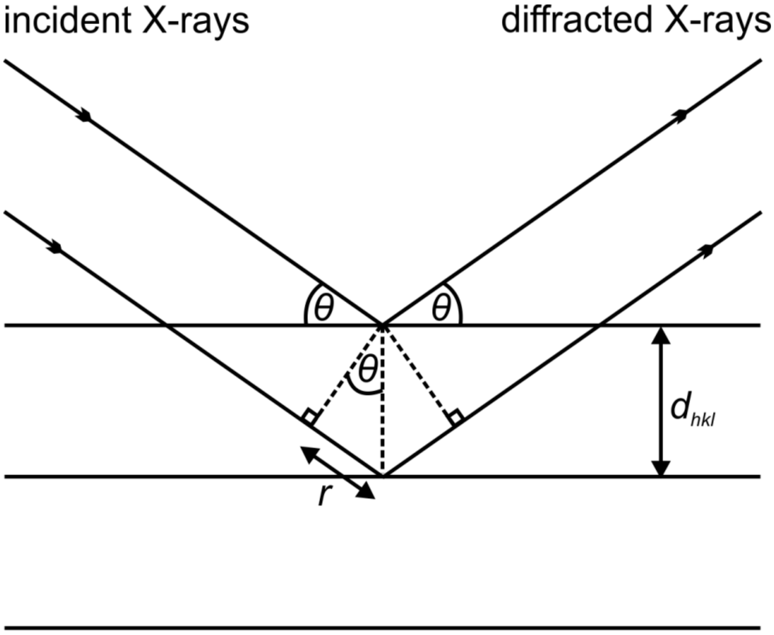

Figure 2.2 Bragg scattering of monochromatic radiation by Miller planes in one dimension.

It follows that for constructive interference, which gives rise to the diffraction spots at an angle of θ from the incident beam, the diffraction angle can be related to the wavelength and spacing between planes (d_{hkl}) by what is known as Bragg's law:

$$\boldsymbol{n\lambda = 2d_{hkl}sin\theta} \quad \textbf{Equation 2.4}$$

In a standard diffraction experiment a monochromatic beam of X-rays is shone on a crystal and the diffracted intensity is monitored as a function of θ. Diffraction intensity is observed at discrete values of θ which satisfy Bragg's law. Information about the size and symmetry of the unit cell can be obtained from the occurrence and positions of the reflections. This is done by assigning Miller indices to each of the observed reflections (known as indexing) to determine the spacing between h, k, and l layers, and since systematic absences of certain reflections are symptoms of the presence of symmetries within the unit cell, a Bravais lattice type may be determined by characterising the conditions for allowed reflections. Information about the contents of the unit cell is available from the intensity of the reflections. Each reflection intensity I_{hkl} is dependent on the structure factor F_{hkl} as well as the Lorentz factor L (instrument geometry), a polarisation correction p if the beam is polarised, a scale factor K depending on the instrument being used to collect the diffraction pattern, and an absorption factor A which accounts for reduced intensity from the competing absorption process:

$$\boldsymbol{I_{hkl} = |F_{hkl}|^2 KLpA} \qquad \textbf{Equation 2.5}$$

The structure factor considers the interference of waves scattered by different atoms and as such is dependent on the positions and identities of atoms in the unit cell of the structure. It may be defined as:

$$\boldsymbol{F_{hkl} = \sum_{n=1}^{N} f_n(\theta)[cos2\pi(hx_n + ky_n + lz_n]q + i\sum_{n=1}^{N} f_n(\theta)\,[sin2\pi(hx_n + ky_n + lz_n)]q}$$

Equation 2.6

where $f_n(\theta)$ is the form factor of atom n, which describes its scattering amplitude, x_n, y_n, and z_n are the coordinates of atom n in the unit cell, q is a Debye-Waller term which accounts for the non-static nature of the atom, and h, k, and l are the Miller indices of the reflection in question. For centrosymmetric structures with identical atoms at $+(x,y,z)$ and $-(x,y,z)$, given that $\sin(-x) = -\sin(x)$, the imaginary component of Equation 2.6 cancels to zero and the structure factor reduces to a real number.

The form factor in X-ray diffraction is given by:

$$\boldsymbol{f_n(\theta) = {}^1\!/_2\,(1 + cos2\theta)\frac{e^2}{mc^2}\int \Psi\Psi^{*} e^{ikr} dT} \qquad \textbf{Equation 2.7}$$

or more simply can be expressed in terms of its dependencies on the scattering angle (θ) and the number of electrons in the atom (Z):

$$\boldsymbol{f_n(\theta) \propto \frac{Z}{2}(1 + cos2\theta)} \qquad \text{Equation 2.8}$$

The dependence of diffraction intensity on Z introduces difficulties in extracting information about light atoms in a structure, it also makes differentiating between atoms of the same or similar electron counts problematic. The angular dependence of diffraction intensity means the higher the scattering angle of the reflection, the more reduced it will be in intensity. This effect arises from the relatively large separation of electrons within the scattering atom when compared to the size of the radiation particle: the atomic radius is of the order of 1 Å, so two photons scattered from different regions of the same atom will emerge with slightly different path lengths, introducing a small degree of destructive interference, which increases with θ.

The Debye-Waller factor q also contributes to the intensities of peaks. Atoms are non-stationary at finite temperatures and so atomic vibrations lead to a dispersion of electron density, which results in a fall off of intensity with θ as destructive interference increases due to a greater phase difference between scattered waves. For isotropic thermal motion q_{iso} can be given by:

$$\boldsymbol{q_{iso} = \, exp\left(\frac{-8\pi^2 U_{iso} sin^2(\theta)}{\lambda^2}\right)} \qquad \text{Equation 2.9}$$

In which U_{iso} is an experimentally-determined isotropic temperature factor, the $8\pi^2$ term may be taken inside the temperature factor by defining $B_{iso} = 8\pi^2 U_{iso}$.

Solution of a given set of structure factors and applying them in Equation 2.6 gives a full picture of the contents of a unit cell of a crystalline material, but only the amplitude and not the phase of F_{hkl} may be directly extracted from the intensities of reflections, since the intensity of a reflection is proportional to the square of the modulus of the structure factor. This is known as the phase problem, and is addressed primarily through computational power by using techniques such as the "Patterson method", "direct methods", or charge-flipping.[96–98]

2.2.2.1 Powder X-ray diffraction

In a diffraction experiment performed on a single crystal, typically a monochromatic beam is shone on single crystal as it is rotated to satisfy Bragg's law for sets of Miller planes. This provides an unambiguous way in which d_{hkl} values can be chosen and the crystal rotated to yield a diffraction event at a single absolute angle. In a polycrystalline powder sample of 1 mm^3 volume, if a similar monochromatic radiation is applied it would illuminate 10^9 1 μm^3 crystallites, which would be randomly distributed in every possible orientation. Statistically, every orientation is represented in the powder, and so for all allowed reflections there are some crystallites that satisfy Bragg's law while the remainder do not diffract. Since more than one absolute orientation of a crystallite can give rise to diffraction from a set of Miller planes, Debye-Scherrer cones of diffracted intensity (Figure 2.3) are generated around the sample.

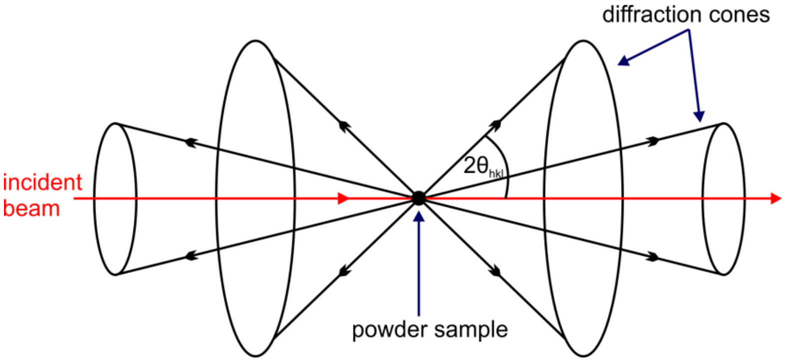

Figure 2.3 Debye-Scherrer cones of diffracted X-rays from the illumination of a crystalline powder sample with X-ray radiation. The diffraction experiment is depicted in transmission mode.

Intercepting the Debye-Scherrer cones and measuring the diffracted intensity as a function of the diffraction angle 2θ gives a two spatial dimension pattern. A loss of information occurs between single crystal and powder experiments as in the powder diffraction pattern, all reflections that have the same d_{hkl}; the (001) and $(00\bar{1})$ for example, are coincident, whereas in a single crystal pattern these reflections would show as separate points in a three axis plot. Structural solution from a powder diffraction pattern is difficult because of this loss of information; the structure factor given in Equation 2.6 must be modified by adding a multiplicity factor to account for the certain reflections being equivalent. A more serious problem arises when reflections overlap in position and are not of the same class such as the (511) and (333) reflections of a cubic crystalline material. When convolution of unrelated reflections occurs; it is not possible to determine accurately their individual contributions to the overall intensity, which is extremely problematic in low symmetry systems, in which a greater number of reflection overlap.

The phase problem and overlapping peak intensity make structural solution difficult, often impossible for powder diffraction data. Direct methods and charge-flipping can be applied to powder diffraction data but may struggle with complicated systems. However powder diffraction is an extremely important and useful technique: the purity of phases may be assigned by “fingerprinting” a collected powder pattern against those of known materials, and although a full solution of an unknown model may be difficult, if a reasonable structural model is known or deduced, then the phase problem is solved and the structure may be refined by minimising the difference between the calculated diffraction pattern and that collected experimentally, known as Rietveld refinement. The application of the Rietveld method described in section 2.2.6, allows for the accurate determination of many structural parameters.

2.2.2.2 Laboratory powder X-ray diffractometers

The typical method of generating X-rays for laboratory diffractometers is firing electrons at the surface of a metal anode, such as Cu or Mo, at a particular energy to cause the emission of X-rays in a divergent beam at characteristic energies. All the laboratory instruments in this thesis use a Cu source, for which the emission profile consists of a K_{α} line, which itself is split into a $K_{\alpha 1}$ and $K_{\alpha 2}$ in a 2:1 ratio, and a higher energy K_{β} line of approximately a fifth the intensity of the K_{α} line. For Cu radiation a Ni filter is used to absorb K_{β}, or a monochromator may be used to eliminate either just K_{β} or both K_{β} and $K_{\alpha 2}$ radiation at a greater cost to intensity. Optical slits are used to focus the beam on the sample and eliminate radiation that is diverging faster (lower energy) than the wanted K_{α} radiation. Soller slits may be are used to collimate the beam, suppressing the axial divergence and improving the instruments resolution. Monochromators are typically crystals that diffract the beam from one specific *hkl* plane at a specific angle to give a specific wavelength. They can either be “narrow-band” and let through only a very specific energy *i.e.* can be used to select only $K_{\alpha 1}$ radiation, or “broad-band” and let through a wider range of energies *i.e.* both K_{α} lines are let through but K_{β} is eliminated. Broad-band monochromators, such as pyrolytic graphite crystals, are typically mounted between the diffracted beam and detector (secondary), which has the advantage of excluding the X-rays arising from fluorescence. Narrow band monochromators, such as Si or Ge crystals, are typically mounted between incident beam and sample (primary) because they are very sensitive to alignment and so cannot be as easily moved with the detector. Secondary monochromators are particularly useful when studying compounds with elements that have only slightly lower proton numbers than the one used as the X-ray source *e.g.* Cr-Co for a Cu source. Details of the laboratory diffractometers that were used to carry out work in this thesis are given in appendix I.

2.2.3 X-ray Absorption Spectroscopy (XAS)

XAS is an electronic spectroscopy technique that can be used to probe the nature of a partially filled highest occupied atomic/molecular orbital and lowest unoccupied atomic/molecular orbital. In addition the fine structure of an X-ray absorption spectrum can be modelled to give information about the structure, atomic number, structural disorder, and thermal motions of atoms that neighbour a targeted element in the material. XAS can be applied to materials that possess little or no long range order, including liquids and even molecular gases, which makes it a very general technique that can be applied to a wide range of disciplines.

For any particular atom the X-ray absorption, as measured by the absorption coefficient, $\mu(E)$, will generally decrease with energy approximately as $1/E^3$ as the X-ray become more penetrating. However, when the energy of the photons is high enough to liberate an electron from a bound state in the atom, a sharp rise in $\mu(E)$ is observed as enough energy is supplied to excite a core electron to the first, selection-rule-allowed, excited state. This event is known as an absorption edge. An element may have several absorption edges, which are labelled according to the principal quantum number of the electron that has been promoted *i.e.* *K*-edge for $n = 1$, *L*-edge for $n = 2$ *etc.*. As photon energy is increased, the bound electron is excited to the continuum and a photoelectron is released, which if there are atoms surrounding the absorber, will be scattered by them creating interference between the outgoing and scattered parts of the photoelectron wavefunction. Whether the interference is constructive or destructive will have an effect on $\mu(E)$ and is dependent on the energy of the photon absorbed creating a modulation. Modulations created by this effect can be quantitatively interpreted to provide structural information.

X-ray absorption by a sample can be expressed by the Beer-Lambert Law:

$$\boldsymbol{I = I_0 e^{-\mu t}} \qquad \textbf{Equation 2.10}$$

where I the intensity of transmitted X-rays, I_0 the intensity of incident X-rays, and t the thickness of the sample. The absorption coefficient $\mu(E)$ for an atom in isolation is given approximately by:

$$\boldsymbol{\mu(E) \approx \frac{\rho Z^4}{AE^3}} \qquad \textbf{Equation 2.11}$$

where ρ is the sample density, Z the atomic number, A the atomic mass, and E the photon energy. In an XAS experiment, $\mu(E)$ can be determined either by measuring the intensity of the X-ray beam before and after the sample and rearranging the Beer-Lambert law to give:

$$\boldsymbol{\mu(E) = t \ln\left(\frac{I_0}{I}\right)} \qquad \textbf{Equation 2.12}$$

or by measuring the fluorescence intensity I_f, which is the number of photons emitted from the sample as the excited state atoms relax, related to $\mu(E)$ by:

$$\boldsymbol{\mu(E) \propto t \frac{I_f}{I_0}} \qquad \textbf{Equation 2.13}$$

In both cases the sample thickness and concentration (for a diluted sample) can be removed from the relation by normalisation. Between measuring in transmission or fluorescence mode, transmission is more often the preferred since “self-absorption” of emitted photons by another atom in the sample leads to an inaccurate measure of I_f, which must be minimised by using a low sample concentration.

An X-ray absorption spectrum may be divided into several parts as shown in Figure 2.4. The pre-edge region is unaffected by the edge event and is typically used in the normalisation of data, although included in this are pre-edge features that arise just before the main edge from orbitally forbidden transitions (Δl must be ± 1), which have become partially allowed by molecular orbital mixing governed by the Laporte selection rule. Pre-edge features may be informative of the local site symmetry, *e.g.* a pre-edge feature in a transition metal absorption spectrum implies there is a partially filled d orbital, and the local coordination environment does not have a centre of inversion. The edge position is informative of the energy separation between the ground and first allowed excited state, which gives information about the oxidation state of the atom. The near-edge region contains characteristic features pertaining to the very local structure about the absorber but is presently most often not modelled (not included in EXAFS modelling). The post-edge region contains the modulations from which structural information can be obtained.

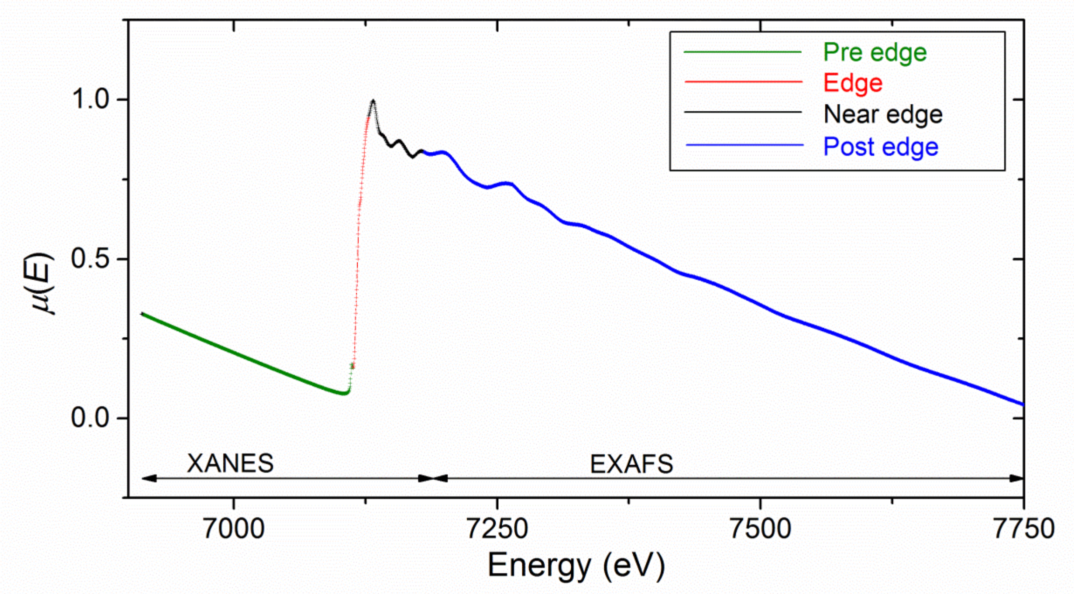

Figure 2.4 A typical iron *K*-edge X-ray absorption spectrum shown divided into components.

When approaching an X-ray absorption spectrum, it is convenient to consider the two regimes: X-ray Absorption Near Edge Spectroscopy (XANES), which includes the electronic and local symmetry information, and Extended X-ray Absorption Fine-Structure spectroscopy (EXAFS), which includes the information about the local structure of the system. Both these regimes may come under the umbrella term X-ray Absorption Fine Structure (XAFS).

2.2.3.1 Analysis of X-ray Absorption Fine Structure (XAFS)

Analysis of XAFS in this thesis was performed using the Athena and Artemis as part of the Demeter software suite, which is a GUI shell for the IFEFFIT interactive analysis program.[99] Normalisation of the X-ray absorption spectrum is performed by modelling lines for the pre-edge and post-edge regions (usually as linear and quadratic lines, respectively), subtracting the pre-edge line from the data then multiplying by the difference between post and pre-edge lines at the edge position in energy (the edge step). From the normalised data the EXAFS function after the absorption edge, $\chi(E)$, can be defined as:

$$\boldsymbol{\chi(E) = \frac{\mu(E)-\mu_0(E)}{\Delta\mu_0(E)}}$$ **Equation 2.14**

where $\mu(E)$ is the measured absorption coefficient, $\mu_0(E)$ the modelled background function which is equivalent to the absorption of the isolated atom, and $\Delta\mu_0$ the edge step. It is useful to convert from units of energy (E) to units of wavenumber (k) in order to have $\chi(k)$ in units of Å^{-1}.

A common scenario in modern EXAFS measurements is for oscillations that are above the noise to be observed at high wavenumbers, but this signal is dwarfed by the oscillations at low wavenumbers (close to the edge). A *k*-weighting is often applied to the data in order to properly weight the signals at high and low wavenumbers, by multiplying the signal by the wavenumber to the power of the weighting, *e.g.* with a *k*-weighting of 2, $\chi(k)$ is multiplied by 4 at a wavenumber of 2 Å^{-1} and 144 at a wavenumber of 12 Å^{-1}. A Fourier transform may be used to convert $\chi(k)$ into real space $\chi(R)$, and fitting can be carried out in either *k*- or *R*-space, and over a particular *k*- and *R*-range allowing for the selective fitting of particular coordination shells. A schematic overview of these data preparation steps is given in Figure 2.5.

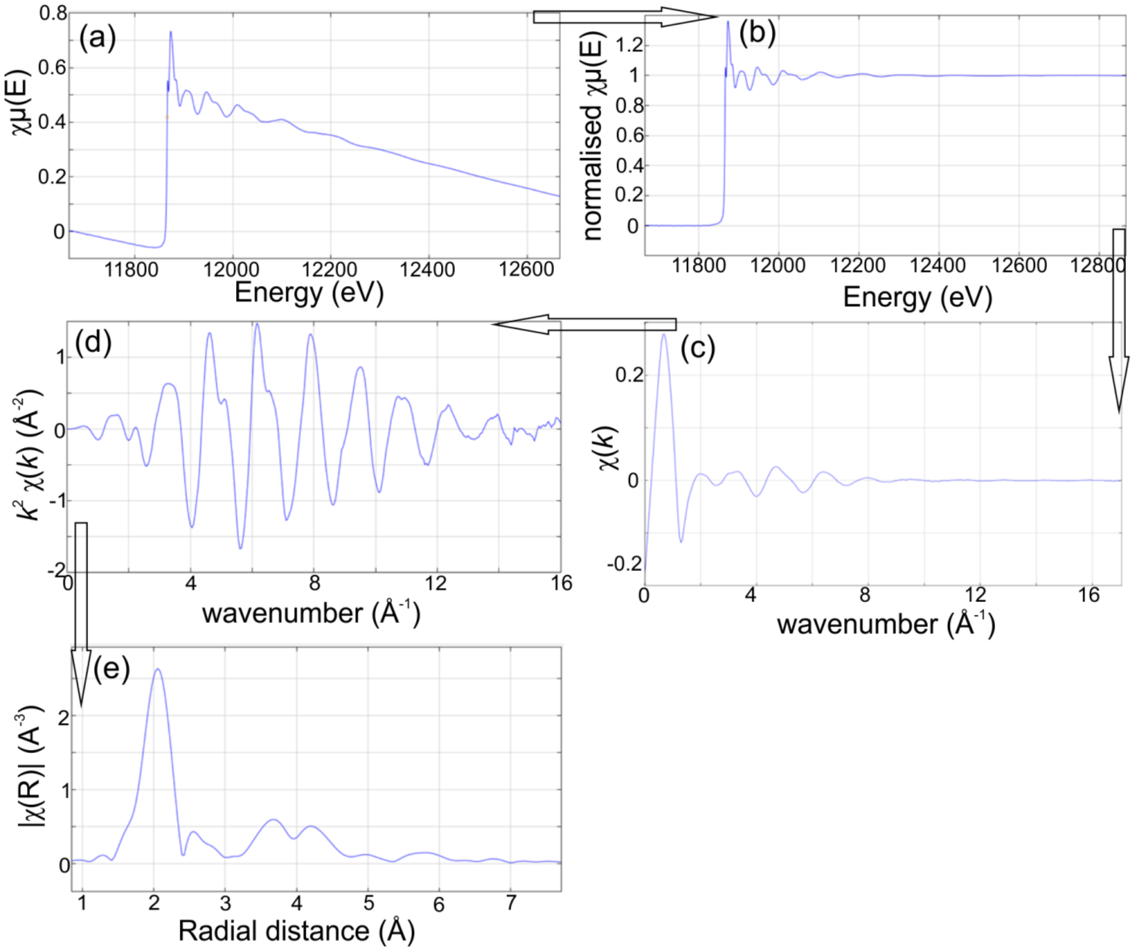

Figure 2.5 The steps involved in the extraction of EXAFS signal from an X-ray absorption spectrum. (a) the X-ray absorption spectrum as a function of energy, (b) the X-ray absorption spectrum normalised by the edge step, (c) the EXAFS signal after the edge, obtained from subtraction of the background from the spectra, and plotting as a function of wavenumber instead of electron volt, (d) the amplified EXAFS spectra with a k weighting of 2, obtained by multiplying the signal at each point by the square of the wavenumber, and (e) the magnitude of the EXAFS Fourier transform from Fourier transform of the (d) to give the EXAFS data in real space.

$\chi(k)$ can be interpreted as the sum of the different frequency waves occurring from the interferences between the outgoing photoelectron and the photoelectrons returning to the absorbing site via different scattering paths. This can be modelled using the EXAFS equation:

$$\boldsymbol{\chi(k) = \sum_j \frac{N_j S_0^2 F_j(k) e^{-2r_j/\lambda(k)} e^{-2k^2\sigma^2}}{kr_j^2} \sin\left(2kr_j + \delta_j(k)\right)} \qquad \textbf{Equation 2.15}$$

where j represents a scattering path from a neighbouring atom, N_j is the number of equivalent paths, $F_j(k)$ is the scattering amplitude expected of the scatterer j, $\lambda(k)$ is the mean-free-path of the photoelectron (mean distance travelled before scattering inelastically or the absorber core-hole is filled), r_j is the distance between the absorber and scatterer, σ^2 is a Debye-Waller term corresponding to the mean-squared-variation in r_j with contributions from both static and thermal disorder, $\delta_j(k)$ is the phase shift in the wavefunction which depends on the absorbing and scattering species (typically 0.5 Å or so), and S_0^2 the amplitude reduction factor which accounts for losses of coherence due to multielectron excitations as well as experimental losses of amplitude from effects such as air absorption and imperfect normalisation. Of these factors, for a given path $F_j(k)$, $\delta_j(k)$, and $\lambda(k)$ can be calculated, which in this work is performed by the FEFF program.[100] The other terms are parameters that are refined in the fitting of the EXAFS; N_j, S_0^2, σ^2, and r_j, as well as an alignment term ΔE_0 to match the energy scale in the fit to that of the data. A photoelectron's scattering path does not need to be direct from the neighbour back to the absorbing site; it can scatter from multiple atoms before returning to the absorbing site, in which case the EXAFS equation can still be applied with r_j equal to half the total path length.

2.2.3.2 Statistical analysis of XAFS

The IFFEFIT fitting routine uses Levenberg-Marquardt non-linear least-squares minimization, a standard χ^2 fitting metric:

$$\boldsymbol{\chi^2 = \frac{N_{idp}}{\epsilon N_{data}} \sum_{i=1}^{N} [\mathrm{Re}(\chi_d(r_i) - \chi_t(r_i))^2 + \mathrm{Im}(\chi_d(r_i) - \chi_t(r_i))^2]} \qquad \textbf{Equation 2.16}$$

χ_d and χ_t are the observed and calculated EXAFS, respectively, ϵ is the measurement uncertainty, N_{data} is the number of points, i, in the fitting range of the data, and N_{idp} is the number of independent variables in the measurement defined by the Nyquist criterion[101] as:

$$\boldsymbol{N_{idp} = \frac{2\Delta k \Delta R}{\pi} + 1} \qquad \textbf{Equation 2.17}$$

where Δk is the range of Fourier transform in $\chi(k)$ and ΔR is the range in R-space where the fit is evaluated. The Nyquist criterion is only accurate if the signal is ideally packed sum of sine waves, error in the fitting parameters is normally distributed, all errors are enumerated, and the theoretical lineshape of the data is known, failure to meet these conditions introduces additional uncertainty and lowers the true N_{idp}. None of these conditions are truly met in an EXAFS experiment, as such the Nyquist criterion represents, at best, an upper bound of the actual number of independent parameters that may be extracted. As a rule of thumb: a number of parameters equal to no more than two thirds of N_{idp} should be used in fitting.

A reduced chi squared, χ_v^2, that takes into account the amount of information modelled and the total possible amount of information available is defined as:

$$\boldsymbol{\chi_v^2 = \frac{\chi^2}{N_{idp} - N_{var}}} \qquad \textbf{Equation 2.18}$$

where N_{var} is the number of variables used in the refinement. Ideally χ_v^2 should approach 1, but is always found to be a large number due to under-predictions in the measurement uncertainty, ϵ, which is modelled as the average in the signal between 15 Å and 25 Å in the Fourier transform: notionally containing no signal above intrinsic noise. This estimation of ϵ does not allow for uncertainty factors such as approximations and errors in the model calculation, sample inhomogeneity, and detector non-linearity. As such, χ_v^2 can be used to compare the quality of two fits to the same $\chi(k$ or $R)$ but is not an absolute indicator of agreement.

Another factor that may be considered is the reliability factor R which describes the absolute misfit between theory and data given by:

$$\boldsymbol{R = \frac{\sum_{i=1}^{N}\left[\mathrm{Re}(\chi_d(r_i) - \chi_t(r_i))^2 + \mathrm{Im}(\chi_d(r_i) - \chi_t(r_i))^2\right]}{\sum_{i=1}^{N}\left[\mathrm{Re}(\chi_d(r_i))^2 + \mathrm{Im}(\chi_d(r_i))^2\right]}} \qquad \textbf{Equation 2.19}$$

which again is limited by systematic errors in the model calculations, but in general a fit with $R \leq 0.04$ might be considered good.

2.2.4 Synchrotron radiation

Synchrotrons are sources of extremely high spectral brightness photons in a wide range of obtainable energies, which lends it to a huge variety of different analytical techniques and offers big advantages over most purpose built laboratory instruments.

Synchrotron radiation relies on the principle that the acceleration of charged particles generates electromagnetic radiation, and when the charged particles are accelerated around a curved path by a magnetic field at speeds approaching the speed of light, this radiation has a range of high frequencies (energies), has a high flux, and can be highly directional.

A synchrotron consists firstly of a typical electron gun as shown in Figure 2.6. A linear accelerator (*linac*) accelerates the electrons to provide a high energy beam, typically in the range of 10^6 to 10^9 eV. The *linac* feeds those electrons a booster ring, which further accelerates them, bridging the gap between the output-MeV electrons produced by the *linac* and the input-GeV electrons necessary to produce the desired radiation. From the booster ring, pulses of electrons are injected into the storage ring, which circulate in discrete bunches, allowing the synchronous feeding of energy to the electron bunches by a radio-frequency generator/cavity to compensate for the loss of energy experienced during emission.

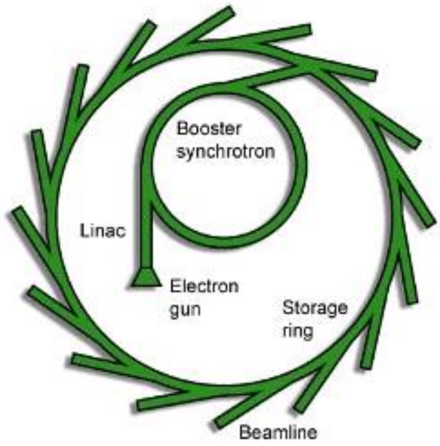

Figure 2.6 Schematic of a synchrotron

The storage ring is not perfectly circular, but in-fact is made up of several straight sections and bends. The targeted spectral emission of photons from electrons circulating in the storage ring is classically achieved at the bends of the storage ring, but can also be achieved along the straight sections using an insertion device (see Figure 2.7). A bending magnet applies a magnetic field **H**, in a direction perpendicular to the direction of electron travel **v**, causing the electron to experience a force **F**, perpendicular to both **v** and **H**. This produces a centripetal acceleration, moving the electron in a circular orbit and generates a horizontally polarised, narrow-angled radiation fan at a tangent to the ring, which can be extracted to an experimental beamline.

Insertion devices are magnet systems which accept and return electrons in the same direction, allowing them to operate along the straight sections of the storage ring as additional photon sources without affecting the operation of the bending magnets. They consist of alternating magnetic poles producing an alternating series of inward and outward electron accelerations, each with a radiation emission. Two basic types exist: undulators and wigglers. In an undulator source, these emissions are in phase and as such the amplitudes of the radiated waves are added, giving a beam intensity that is the square of the sum of the amplitudes. The result is a quasi-monochromatic beam with harmonics, which has very high intensity at energies where the emissions are in phase and low intensity at other energies. A key requirement for the coherent addition of amplitudes is that electron accelerations execute only small angular oscillations, which means that a typical undulator consists of many alternating magnets of relatively low field strength. In a wiggler, the electron beam undergoes a series of circular arcs, turning it left and right with large angular oscillations and emissions that add incoherently. This gives an output spectrum that more closely resembles a bending magnet's, but the high local curvature that is achieved results in the production of very high energy photons ("hard" X-rays).

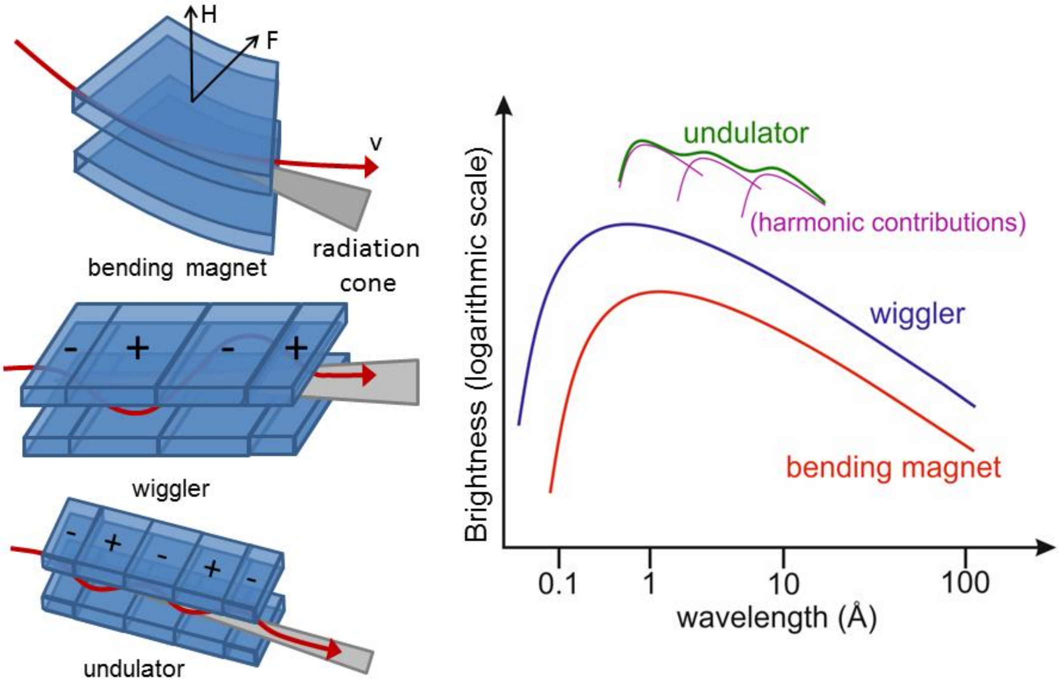

Figure 2.7 Schematic of the emission devices used in a synchrotron with their spectral profile as a function of wavelength on the right.

Bending magnets, wigglers and undulators all provide a white beam of photons with a spectrum of energies, but with different flux versus energy profiles. Each method of generation has advantages and disadvantages, and the primary purpose of the beamline is usually chosen to make best use of the generated radiation.

2.2.4.1 I11 - high resolution powder diffraction at Diamond Light Source

I11 is powder diffraction beamline with an undulator source that produces X-rays ranging from 5-30 keV, with highest flux obtained at medium energies (11-20 keV), with flux decaying quickly beyond 20 keV.[102] Rotation of a double-crystal-monochromator comprising of two Si(111) crystals is used to select the desired beam energy for diffraction. A closed circuit liquid nitrogen cooling system to alleviate the heat load and maintain constant temperature cools the crystals.

The diffractometer itself consists of three coaxial rotary stages; the θ-circle at the centre of the diffractometer upon which the sample is staged, the 2θ-circle which holds and rotates the Multi-Analysing Crystal (MAC) detector above the sample, and the δ-circle which holds and rotates the position sensitive detector (PSD) below the sample. [103]

Typically samples are measured in a glass capillary. Alignment of the capillary is performed by placement through the centre of brass ferrule with as narrow bore as possible and additional centring can be performed using aligned irises to hold the capillary in the centre while it is glued in place. The brass ferrule is screwed into a magnetic base that engages with a precision-engineered spinner pre-aligned with the diffractometer's centre of rotation.

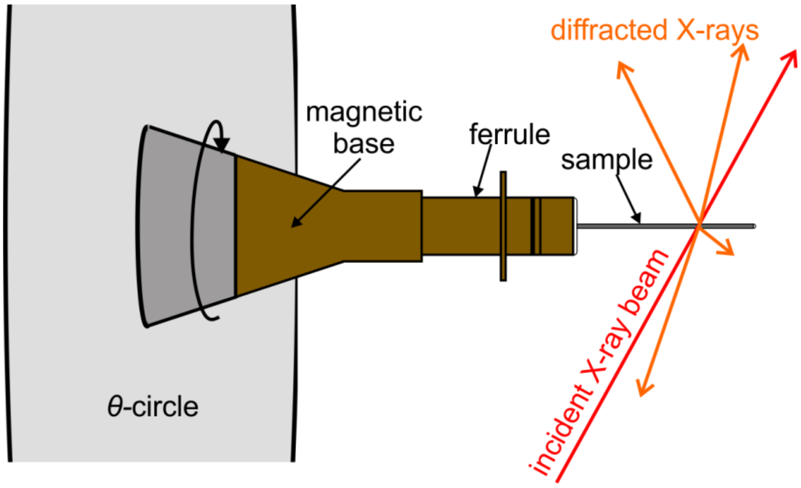

Figure 2.8 Schematic of the typical setup and sample geometry used for collection of powder diffraction patterns on beamline I11 at Diamond Light Source, and most other synchrotrons.

The Multi-Analyser Crystal (MAC) detector consists of 5 identical MAC-arms each containing nine Si(111) analyser crystals and detector combinations such that in a diffraction experiment, 45 2θ scans are collected and merged by correcting the patterns by the angular offset of each detector. Data collection using the MAC detector is performed in a constant trajectory scan, rather than a step scan, with a nominal 2θ interval of 0.0008 °

achieved by gating the detectors at an appropriate frequency. The PSD uses MYTHEN-II (Microstrip system for time-resolved experiments) silicon microstrip technology, providing wide-angle powder diffraction data with resolution of $\Delta d/d \approx 10^{-3}$-$10^{-4}$. The detector comprises of 18 linear Si p-n junction strip detection modules arranged in a 90 ° arc. The detector operates in single-photon counting mode and its efficiency is energy dependant, from ~100 % at 7 keV to ~ 15 % at 25 keV. A ~ 1 mm gap between modules leaves uncollected gaps in the diffraction pattern, which can be accounted for by collecting a second pattern at an interval of 0.25 ° in 2θ and merging the two patterns. Advantages of the MAC detector are its slightly higher resolution than the PSD, a lower background, and lower sensitivity to imperfect sample alignment and preparation, while the PSD offers much faster collection times at a good resolution.

Sample environments available on I11 include a robotic arm and carousel for automated sample changes of up to 200 capillary samples, a nitrogen cryostream providing a 80 - 500 K temperature range, a hot air blower which is capable of heating a capillary to 1000 °C, helium cryostats capable of cooling to 5 K, and furnaces capable of heating to 1500 °C. Capillary gas cells are also available, allowing *in-situ* exposure of a sample to a determined gas or vacuum which were used in the work presented in this thesis (chapter 4).

2.2.4.2 ID31 - high resolution powder diffraction at the ESRF

ID31 was an undulator sourced beamline at the ESRF in Grenoble, optimised for high resolution powder diffraction. Data obtained using ID31 has not been included in this report, but a comparison of the high resolution powder diffraction beamline at the ESRF with I11 at diamond is given in appendix I.

2.2.4.3 I12 - Joint Engineering, Environmental, and Processing at Diamond Light Source

I12 is a multipurpose, multipole wiggler-sourced, high energy X-ray beamline, built to be highly accommodating to a wide variety of experiments. I12 has two in-line experimental hutches, the first is closer to the insertion device and is preferred for a higher intensity beam, the second is further from the insertion device but provides a space for large-scale engineering experiments. A fixed exit, liquid nitrogen cooled, bent double silicon crystal in Laue geometry monochromator is able to select an energy between 50 and 150 keV. Flux decreases approximately linearly from 1.8×10^{12} photons s^{-1} at 50 keV to 9.4×10^{10} photons s^{-1} at 150 keV. Permanent attenuators are used to reduce heat load on the monochromator and other components, to filter low energy X-rays, and to act as vacuum windows, additional movable filters are available for specific experiments.

The detectors available at I12 are capable of collecting data for imaging, tomography, X-ray diffraction, and small angle X-ray scattering (SAXS) experiments. For X-ray diffraction a Thales Pixium RF4343 2D flat plate detector is available, which is a scintillation detector using CsI on amorphous Si substrate. The pixels of the detector are $148\ \mu\text{m} \times 148\ \mu\text{m}$, with $2880\ \text{pixels} \times 2881\ \text{pixels}$ in the $430\ \text{mm} \times 430\ \text{mm}$ active area. When operating at its highest resolution the detector can produce a diffraction pattern in discrete exposure times of 80 ms, 0.5 s, 1 s, 2 s, and 4 s. Faster collections can be achieved at lower resolution by using a larger binning of the pixels. Readout of the taken diffraction pattern from the detector currently requires a minimum of 250 ms. This wait time must be included before the next diffraction pattern can be taken. The combination of a high flux, highly penetrating beam, and a fast collection times make I12 highly suitable for *in-situ* X-ray diffraction experiments.

The sample table in the first experimental hutch is highly mobile, allowing the sample stage to be translated, rotated and tilted in any direction. The flat plate detector is located on a table, which can be translated in the path of the beam so as to increase or decrease the sample to detector distance. Sample environments are not available as standard on I12 due to the diversity of experiments that are performed there. Sample environments are usually user-built for the purpose of the beamtime.

2.2.4.4 B18 core EXAFS at Diamond Light Source

B18 is a spectroscopy beamline, built to be a general-purpose X-ray absorption spectroscopy (XAS) instrument. It has a bending magnet source which provides a wide range of energies (2 to 35 keV) with appreciable flux throughout.[104]

A wide beam fan is provided by the bending magnet, which allows it to be divided in two in the horizontal plane by primary slits. The beam fans first encounter a vertically collimating Si mirror, which is coated with both Cr and Pt stripes to give a Cr branch and a Pt branch such that measurements requiring energies close to the Pt L-edge or Cr *K*-edge can be scanned by choosing the alternative coating. Monochromation of the beam is performed by a fixed-exit, water-cooled double set of Si crystals; two sets of these Si crystals, Si(111) and Si(311), are available as to allow lower and higher energy ranges to be accessed, respectively. The beam’s two branches are focused both horizontally and vertically by a double toroidal focusing mirror, again coated with Cr and Pt. Finally a pair of harmonic rejection mirrors with two coatings (Ni and Pt) can be inserted into the beam path when low energies, which have significant 3rd harmonic flux in the white beam, are used (<11 keV).

X-ray absorption of the sample can be measured in either transmission or fluorescence. In transmission mode three ion chamber detectors sat along the beam's path are used to give a measure of the beam intensity before the sample, after the sample, and after the reference foil/sample. The ion chambers are filled with a mixture of helium and nitrogen, argon, or krypton to a ratio of gases that gives appropriate ionisation for the energy range that is to be measured. In fluorescence mode a 9 element monolithic Ge solid-state detector sits perpendicular to the beam at the sample, a 4 element Si drift detector can be used for fluorescence and electron yield measurements in vacuum with soft X-rays.

For experiments using soft X-rays (looking at Ca or below) a soft X-ray vessel is installed before the ionisation chambers such that samples might be measured in high vacuum using fluorescence or electron yield. The experimental table is built of a small stage with high movement flexibility upon which standard samples and small sample environments can be installed and a large table with minimal movement flexibility for larger sample environments. Liquid nitrogen and He-pulse tube cryostats are available for low temperature measurements down to 77 K and 1.5 K, respectively and a 1000 °C furnace capable of holding pelletised samples is available for high temperature measurements.

Sample stage design

During the course of this work, a sample environment for the measurement of air-sensitive samples on beamline B18 was designed, built, and tested. The previous standard method for handling air-sensitive samples on B18 was to press the sample between two pieces of Kapton® tape, which provides adequate protection from the air for most samples, but aerial degradation of the sample will eventually occur. A new sample environment, which is now available for use on B18, was designed in order to provide excellent protection from the air and control of the atmosphere surrounding the sample when measuring, and leaves the door open to future modifications such as variable temperature heating and cooling. The samples can be prepared in a local glovebox and mounted in a sample loader as shown in Figure 2.9. The sample loader can be transported to the beamline and mounted in the sample environment shown in Figure 2.10, which is based around a six-way cross: a stainless-steel shell built of three orthogonally intersecting cylinders with the option to add doors, windows, and other connecting ports to the ends of each of the six openings (see figure).

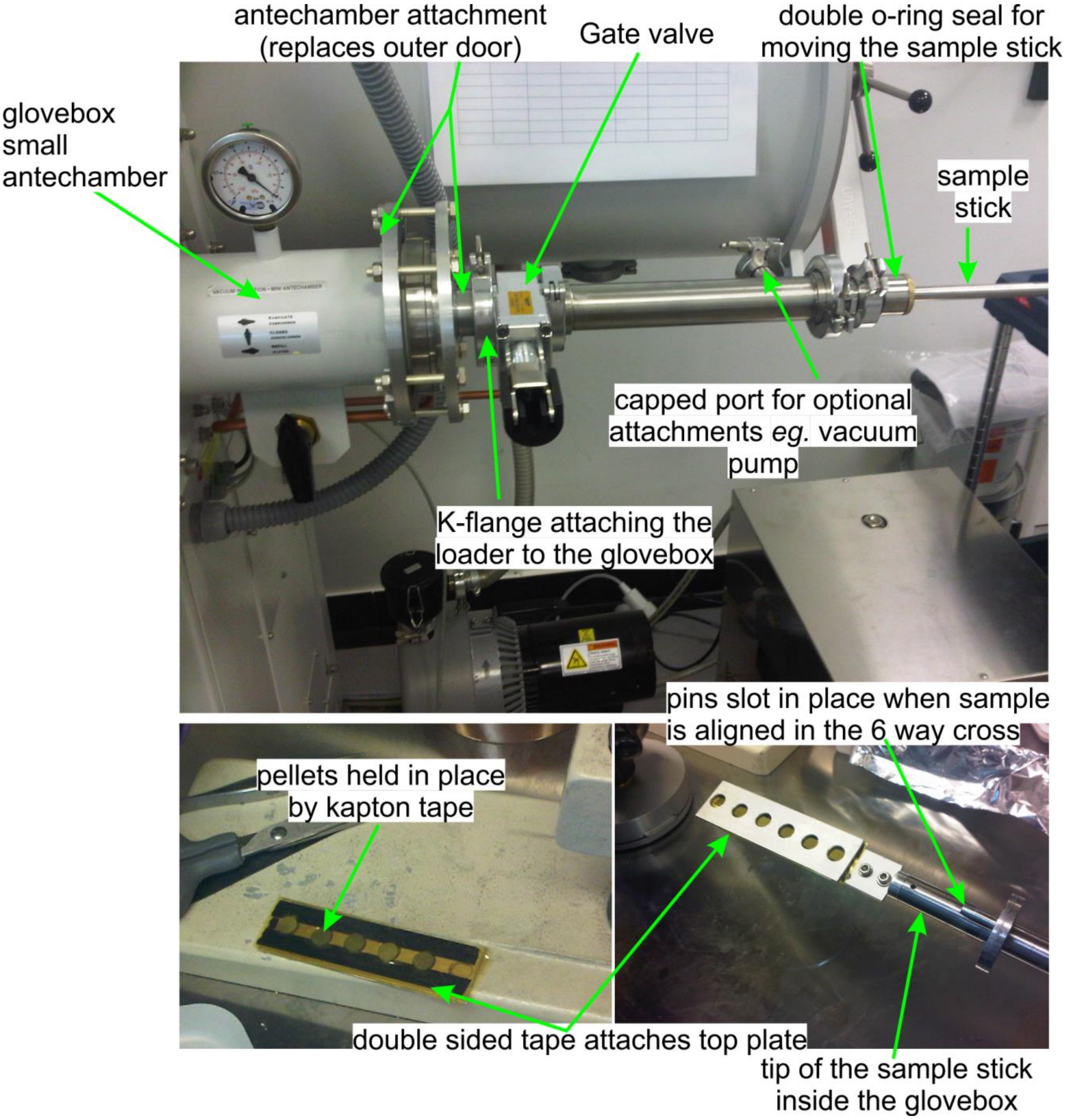

Figure 2.9 Apparatus for the loading of air sensitive samples from inside an argon-filled glovebox directly into a sealable, detachable vessel. See text for a description of the sample loading procedure.

To load the samples: with the inner door of the glove box antechamber closed, the sample loader is connected to the glovebox by clamping against the K-flange of the antechamber attachment with a pressed O-ring to create a seal. With the gate-valve open, the loader and antechamber are evacuated and filled with argon several times. Once the sample loader is under an argon atmosphere, the inner door of the antechamber can be opened, and the sample rod pushed in so that the samples can be mounted on its tip. Once the samples are attached, the stick is retracted and the antechamber inner door is closed. The samples are retracted past the gate-valve, the gate-valve is closed, and the sample loader detached from the glovebox antechamber.

With the samples contained in the sample loader, it can then be attached to the six-way cross at another K-flange at its top as shown in Figure 2.10. The six-way cross is then evacuated and filled with helium before opening the gate-valve on the sample loader and lowering the sample stick into position. The sample stick is kept straight by an internal guide and the tip of the sample stick has pins that slot into the base of the guide when the samples are aligned. Appropriate markings on the top of the loader help with this alignment, which can also be checked through a window on the side of the six-way cross. The six-way cross can, if necessary, be evacuated so as to minimise the gas scattering/ absorption along the beam-path, which is particularly useful when using low energy (‘soft’) X-rays. A remote-controlled mechanical bellows can vertically translate the sample stick, loader, and guide by 10 cm, which allows several samples to be measured from one loading (six in the current set-up).

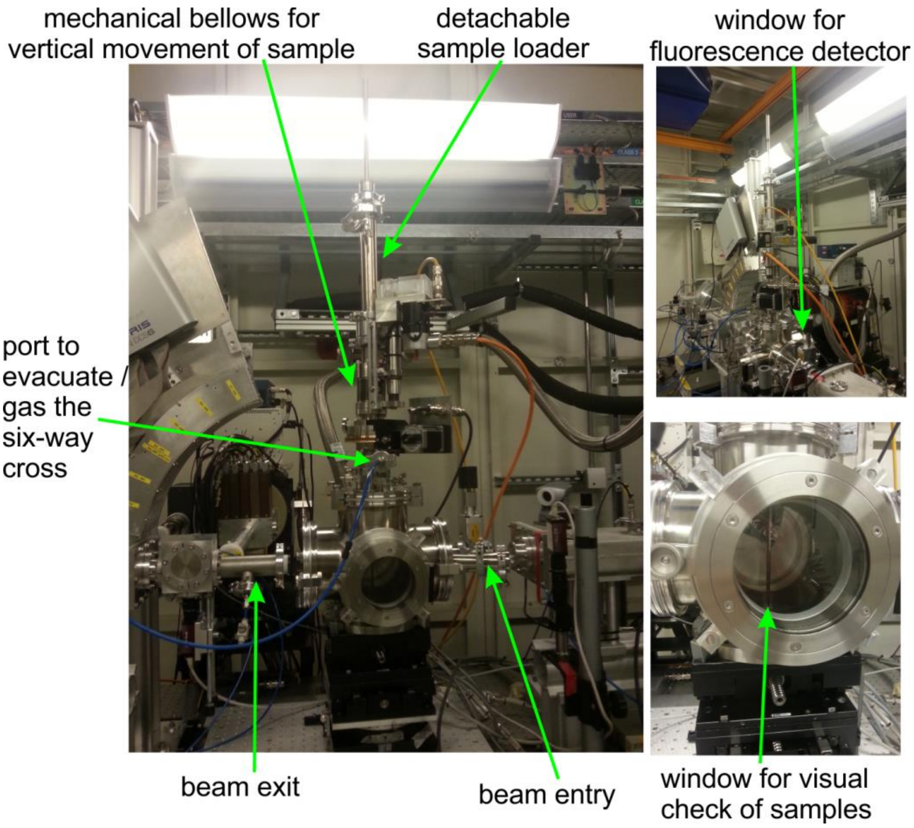

Figure 2.10 Sample environment, designed for measurement of air-sensitive samples on beamline B18.

The design is very versatile towards future modification, for example; the guide could carry liquid nitrogen to a cooling coil at the sample position for low temperature measurements and/or a resistive heater and thermocouple could be attached to allow the sample to be heated.

2.2.5 Neutron diffraction

Having a similar typical wavelength to the atomic scale, neutrons are an alternative to X-rays as a suitable type of radiation for diffraction. In contrast to a photon, a neutron is scattered by the nucleus of an atom, rather than the electron cloud, and so the neutron scattering form factor is not proportional to the atomic number, but instead is proportional to the coherent scattering length of the atom, which shows almost random variation with atomic number. In fact each isotope has its own coherent scattering length, which may take a range between ~ -5 fm to ~ +16 fm. This often allows different isotopes or atoms with very similar electron counts to be distinguished from one another, which can be very useful in mixed transition metal compounds. It can also be the case that light elements, which do not make significant contribution to X-ray diffraction, have significant coherent scattering lengths and are 'visible' to neutrons. Another consequence of neutron diffraction occurring from the atomic nuclei is that the neutron form factor does not decrease with angle in the same way the X-ray form factor does, since the size of the scatterer (nucleus) is not large compared to the size of the radiation (neutron). Scattering lengths of the atoms found in the solids studied by neutron diffraction in this thesis are given in Table 2.1.

Table 2.1 Bound coherent neutron scattering lengths for the elements and isotopes used that form the materials studied in this thesis (values taken from International Tables for Crystallography)[105]

Element	Scattering length / fm	Element	Scattering length / fm
H	-3.739(1)	K	3.67(2)
D	6.671(4)	Fe	9.45(2)
N	9.36(2)	Se	7.970(9)
Li	-1.90(2)	O	5.803(4)
Na	3.63(2)	Ca	4.70(2)

A further useful characteristic of neutrons is that they are spin-½ particles, meaning they interact with the magnetic moments of atoms. In an ordered magnetic material, neutrons can be diffracted by the magnetic lattice to a degree that is proportional to the square of the magnitude of the ordered moment. This interaction occurs with the outmost unpaired electrons of the atoms and effectively forms a second diffraction pattern with comparable intensity to the nuclear scattering as a superimposed component of the diffraction pattern. As with X-ray diffraction, the magnetic neutron scattering form factor has an angular dependence, which actually falls off faster with θ since scattering only occurs from the outer electron shell introducing a large amount of destructive interference.

2.2.5.1 Generation of neutrons

The generation of a neutron beam for diffraction is a difficult and expensive undertaking, and as such neutron diffraction experiments are carried out at specialised central facilities. Generation of neutrons may be achieved by a nuclear reactor source; which take advantage of the output of neutrons from the fission process, or a spallation source; which accelerates pulses of high-energy particles at a heavy metal target to produce neutrons.

The Institut Laue-Langevin (ILL) in Grenoble, France, is a reactor source using the fission of ^{235}U to provide neutrons with an extremely high intensity. The neutrons are equilibrated by a heavy-water moderator, which determines the character of the incident flux available by slowing down the neutrons when they collide with H/D nuclei, which allows the fission process to be maintained and generates a thermal beam with a maximum flux at 1.2 Å. This white beam is typically monochromated at the beamline, for some applications it is further moderated to obtain a different distribution of energies.

The ISIS facility, situated at the Rutherford Appleton laboratory, UK, generates a pulsed neutron beam by firing high energy protons at a tungsten target. The process is achieved by accelerating hydride ions into a synchrotron, which ionises them to protons on entry and fires them in bunches at the target, doing so continuously such that the proton bunches have a 50 Hz frequency. ISIS has two target stations, which the proton bunches are divided between. 4/5 of the proton bunches go to target station one (TS1) and 1/5 go to target station two (TS2). Intense neutron pulses are generated in this way, with only modest heat production. The neutrons are moderated to slower speeds by an array of various hydrogenous moderators surrounding the target, which then direct the neutrons with suitable velocity distributions towards the various neutron instruments. The moderated white beam then illuminates the sample with regular discrete pulses and time-of-flight (ToF) diffraction experiments are carried out in an energy dispersive mode with detectors (usually several) at fixed scattering angles around the sample. The time of flight over a known distance can be related to their wavelength through the de Broglie relation:

$$\boldsymbol{\lambda = \frac{h}{p} = \frac{h}{m_n v}} \qquad \textbf{Equation 2.20}$$

Where h is the Planck constant, p is momentum, m_n is the mass of the neutron and v is its velocity. In energy dispersive mode λ is used as the variable in the Bragg equation (Equation 2.4) with θ constant (fixed detector angle) in order to probe d_{hkl}. Operating in this mode is available for a pulsed beam and makes maximum use of the white beam. In order to obtain as much data as possible, instruments are designed to cover as much of the possible 4π steradians surrounding the sample with detectors.

For a constant wavelength diffractometer the resolution is described as the variation of the full width at half maximum (FWHM) of a Bragg reflection with scattering angle, according to the Cagliotti function:[106]

$$\boldsymbol{\sigma^2 = \frac{FWHM^2}{8ln2} = U\, tan^2\theta + V \tan\theta + W} \qquad \textbf{Equation 2.21}$$

Many instrumental factors, such as monochromator geometry, beam collimation, and the sample’s structure contribute to the parameters U, V, and W.

For a ToF diffractometer the resolution of a detector is described by the width of a reflection Δd over its position in d-space, and is dependent on the uncertainty in time-of-flight (Δt), the uncertainty in path-length over which the neutron has travelled, ΔL, and the uncertainty in the diffracted angle, $\Delta\theta$:[107]

$$\boldsymbol{R(d) = \frac{\Delta d}{d} = \sqrt{\Delta\theta^2 cot^2\theta + \left(\frac{\Delta t}{t}\right)^2 + \left(\frac{\Delta L}{L}\right)^2}} \qquad \textbf{Equation 2.22}$$

The uncertainty in the flight-path, ΔL, is due to the finite depths of the moderator, sample, and detector. ΔL may be minimised by increasing the length of the flight-path, which also maximises the time-of-flight, reducing uncertainty in both (at the cost of flux and overlap of consecutive neutron pulses). The angle dependant term arises because the finite angular widths of the moderator, sample and detector allow a range of wavelengths to satisfy the Bragg condition for each reflection. This term dominates at low angles (large cotθ), the maximum resolution may be obtained by placing the detector in the “backscattering” region, as close as possible to 2θ = 180° (cotθ = 0), without interrupting the incident beam path. A detector bank is usually located at 90° which provides a good compromise between d-spacing range and resolution, helps to improve statistics, and makes scattering from parts of the sample environment that are very close to the sample easier to avoid. In contrast to constant wavelength diffraction, for a given detector, resolution is effectively a constant across the complete *d*-spacing range, which minimises peak overlap at low *d*-spacings.

2.2.5.2 Neutron diffractometers

Polaris (ISIS-TS1)

The Polaris instrument at ISIS is a high intensity, medium-high resolution powder diffractometer, allowing for measurements on small samples, or with short counting times, opening the door to kinetic experiments. Polaris receives a white beam of neutrons through an ambient temperature water moderator, with a wavelength distribution of ~0.1 – 6.5 Å.[108] The maximum beam dimensions on the sample are 40 mm high × 20 mm wide, which can be reduced by motor driven collimators in the incident beam path, to match the sample size and minimise the background. In 2011-2012 Polaris underwent a major upgrade, and was used in its new configuration for the work presented in this thesis. Polaris now has a primary flight path of 14 m to the sample, around which 40 detector modules covering a total of ~44 % of the maximum possible 4π steradians are contained within a large vacuum vessel. The detector modules, each containing a number of scintillator detectors are spread among now 6 banks at fixed angles (previously 4 banks) of 9, 26, 48, 90, 139, and 155 ° in around the sample. The upgrade provided increased count rates, particularly in the low angle banks, and increased $\Delta d/d$ resolution, particularly in the high angle banks. The total coverage in *d* space between the five currently operational banks is ~0.25-20 Å with a maximum resolution in the back scattering bank of 0.3 % $\Delta d/d$, comparable to that of GEM and the 90 ° bank of HRPD.

GEM (ISIS-TS1)

GEM is the GEneral Materials powder diffraction instrument at the ISIS, neutron facility.[109,110] Designed to provide short collection times by maximising the angular coverage of the detectors and very good resolution, the detector array has 7270 scintillator elements in 86 modules, divided between 8 detector banks, which cover an angular range of 1.1 to 169.3 ° around the sample. Banks 0 and 7 are currently not in use, reducing this coverage slightly to 5.6-149.2 °. The six detector banks are at mean angles of 9, 17, 35, 62, 92, and 146 ° around the sample, and give a total reliable *d*-spacing coverage of ~0.4 - 25 Å, with a maximum resolution of 0.3 % $\Delta d/d$. GEM is sourced through a poisoned liquid methane moderator, without any beam optics other than a series of motorised jaws, which define a maximum beam size of 40 mm high × 20 mm wide to a minimum of about 1 × 1 mm, the primary path length to the sample is 17 m.

HRPD (ISIS-TS1)

HRPD, was named and built to be a high-resolution (time-of-flight) powder diffractometer. The heightened resolution is obtained by maximising the path length from the 90 K liquid methane moderator, which at 100 m makes the $\Delta L/L$ in Equation 2.22 (page 53) very small. Flux intensity would normally follow an inverse-square fall-off with distance and so to compensate for the long flight path, a Ni plated glass neutron guide is employed, along which neutrons travel by total external reflection from the inside walls. The flux transmitted by the neutron guide is related to the wavelength of the neutrons, such that short wavelengths are disfavoured. In the flux versus wavelength curve; a minimum wavelength of ~0.5 Å arrives at the sample, the flux rises with wavelength to a maximum of around 2.4 Å, and then drops off rapidly with the decreasing flux from the moderator source. Although an appreciable portion of flux from the source reaches the sample, over such a long flight path with a pulsed neutron source, slower neutrons from a first pulse are caught up with by faster energy neutrons from successive pulses, known as frame overlap. Two choppers situated at 6 and 9 m from the moderator are used to combat frame overlap, which as a consequence also restricts the wavelength range. In the highest flux operating mode the HRPD choppers select neutrons with a time of flight between 30 and 130 ms which allows 1 in 5 pulses from the source. Restricting the time of flight to 30 - 130 ms allows only neutrons with wavelength in the range ~1.2-5 Å to be used, which limits the maximum observable *d*-spacing to ~10 Å. Alternatively, the choppers can select neutrons with a 30 – 230 ms time of flight, increasing the maximum observable *d*-spacing to ~ 16.5 Å, but only 1 in 10 pulses from the source may be used in this operating mode.

The diffracted neutron beam on HRPD is detected by three fixed angle banks; one backscattering at 168 °, one at 90°, and a low angle bank at 30 °. Maximum resolution attainable in the back scattering bank is a $\Delta d/d$ of 0.04 %, an order of magnitude greater than that on GEM or Polaris. HRPD requires longer collection times and offers a relatively narrow *d*-spacing region to be collected, but returns extremely high resolution for a neutron powder diffractometer.

WISH (ISIS-TS2)

WISH (WIde angle in a Single Histogram) is a long-wavelength diffractometer, primarily designed for powder diffraction at long *d*-spacings, which is useful in systems with large nuclear or magnetic unit cells. Its key advantage over other instruments at ISIS is a very high resolution at high *d*-spacings, which allows the maximum amount of information to be extracted from this region and prevents weak peaks at high *d*-spacings from being lost by broadening into the background.

WISH is sourced through a solid methane moderator at 50 K that favours the generation of long wavelength neutrons with a maximum flux peak occurring around 4 Å and can provides neutrons with incident wavelengths of up to 15 Å, notably higher than GEM or Polaris. A 40 m primary flight path with a sophisticated ballistic supermirror beamguide provides WISH with a high resolution (low $\Delta L/L$) while maintaining a 8 Å maximum bandwidth that can be employed whilst avoiding frame overlap. Three choppers can be phased to avoid frame overlap and select the range of incident wavelengths, which are available from 1.5 to 15 Å. The choppers, together with several collimating slits that limit beam divergence, can be used to select the best compromise between resolution and flux, and focus the beam on single crystals or small samples.

WISH has a single detector manifold, which provides uninterrupted coverage of scattering angles from 10 to 170 °. The resolution function changes with θ, so the detector manifold is divided into 5 portions on each side giving 10 banks. Banks 1 and 10, 2 and 9, *etc.* are situated at equivalent angles on opposite faces surrounding the sample and as such, the diffraction patterns from each pair of banks are often merged in the data handling. A high resolution is attainable over a *d*-spacing range of 0.7-17 Å using the WISH instrument, with a total *d*-spacing coverage of up to 50 Å giving it a near unique coverage and resolution profile.

D2B (ILL)

D2B is a high resolution constant wavelength diffractometer at the ILL reactor source in Grenoble, France. The work presented in this thesis does not make use of D2B, but a comparison of the constant wavelength powder neutron diffractometer with the time of flight diffractometers described previously is available in appendix I.

2.2.6 Rietveld refinement

The Rietveld method is a means of side-stepping the phase problem for solving the structure of a material from a powder diffraction pattern. Rather than being a method of structural solution, it allows a starting structural model close to that of the real structure to be refined in order to match the observed pattern. The method was developed by H. M. Rietveld in the late 1960s. As computer power was becoming available he decided to treat each point of data (rather than each peak) as an individual observation, which allowed overlapping reflections to be treated separately.[111,112] For a given point I in the pattern, the intensity y_{ci} is calculated by combining all the contributions of the Bragg reflections within a fixed range:

$$\boldsymbol{y_{ci} = s \sum_{hkl} L_{hkl} |F_{hkl}|^2 \phi(2\theta_i - 2\theta_{hkl}) P_{hkl} A + y_{bi}} \qquad \textbf{Equation 2.23}$$

where s is the scale factor, L_{hkl} is the Lorentz polarisation factor, F_{hkl} is the structure factor, ϕ is the reflection profile function that describes the peak shape, P_{hkl} is the preferred orientation function, A is the absorption factor and y_{bi} is the background intensity at point i. The calculated intensities from the sum are compared with the observed intensities from the pattern to give the residual, S_y:

$$\boldsymbol{S_y = \sum_i w_i (y_i - y_{ci})^2} \qquad \textbf{Equation 2.24}$$

where y_i is the observed intensity at point i and w_i is a weighting factor equal to $\frac{1}{y_i}$ which means that each point contributes equally to the refinement. S_y is minimised by a least squares method; user defined parameters are perturbed to reduce the residual, which if successful feeds the refined parameters back into the starting model and the cycle is repeated until the model is no longer improved and a stable solution is reached. The user of this method must use some judgement to choose which parameters to refine at what time, and interpret whether the refined structure corresponds to a true global minimum in the residual rather than a local one.

The quality of the refinement is assessed by reported statistical parameters, known as R-factors which provide a numerical measure of the quality of the fit, and by visual inspection of the match between the calculated and observed patterns. The R-structure factor (R_F) is based on the fit of the Bragg intensities of the calculated peaks, disregarding any peaks that are not close to those calculated:

$$\boldsymbol{R_F} = \frac{\sum_K \left| I_{K_{obs}}{}^{1/2} - I_{K_{calc}}{}^{1/2} \right|}{\sum_K I_{K_{obs}}{}^{1/2}} \qquad \text{Equation 2.25}$$

where $I_{K_{obs}}$is the intensity of an observed reflection *K*, and $I_{K_{calc}}$is the calculated intensity of reflection *K*. R_F can be useful as an indicator of how good the model is without other considerations such as the background modelling and presence of impurity phase peaks, but factors that describe the full pattern fitting are often more useful. The profile *R* value (R_p) and the weighted profile *R* value ($R_{wp)}$ are the most commonly used full-pattern fitting parameters:

$$\boldsymbol{R_p} = \frac{\sum_i |y_i - y_{ci}|}{\sum_i y_i} \qquad \text{Equation 2.26}$$

$$\boldsymbol{R_{wp}} = \sqrt{\frac{\sum_i w_i (y_i - y_{ci})^2}{\sum_i w_i y_i{}^2}} = \sqrt{\frac{S_y}{\sum_i w_i y_i}} \qquad \text{Equation 2.27}$$

of which the weighted R-factor, R_{wp}, is arguable the most meaningful gauge of the least-squares refinement process from a mathematical standpoint, since it includes the residual function, S_y, in the numerator. The final R_{wp} should approach the statistically expected *R* value, R_{exp}:

$$\boldsymbol{R_{exp}} = \sqrt{\frac{N_{obs} - N_{var}}{\sum_i w_i y_i{}^2}} \qquad \text{Equation 2.28}$$

where N_{obs} and N_{var} are the number of observables and the number of refined parameters, respectively. For a typical powder experiment N_{obs} ~ 2000, so we expect $N_{obs} \gg N_{var}$. In a perfectly matched model and pattern with differences only arising from statistical fluctuations, R_{wp} will be equal to R_{exp}, hence a “goodness-of-fit” parameter, χ, can be defined in terms of these two *R*-factors:

$$\boldsymbol{\chi} = \frac{R_{wp}}{R_{exp}} = \sqrt{\frac{S_y}{N_{obs} - N_{var}}} \qquad \text{Equation 2.29}$$

It is generally true that the smaller these values are, the better the fit. Typically a good fit is achieved if $\chi^2 < 2$ and $R_{wp} < 0.05$ (sometimes written as 5 %), large values of R_{exp} can be caused by insufficient counting time or the refinement of too many variables which give a misleadingly low χ^2 (in some cases < 1). Likewise, a well-fitted high background can give values of R_{wp} that are much smaller than we might expect for a well-fitting model alone. It is also possible to obtain anomalously high values of χ, for example, if too many points are collected or collection times are very long, then R_{exp} values can become very small. In this work Rietveld refinement has been carried out using TOPAS academic version 5 refinement software.[113]

2.2.7 Pawley refinement

Pawley refinement is a structure-independent method of fitting a powder diffraction pattern based on a starting model for only the unit cell of the material.[114] The refinement is carried out by assigning an arbitrary intensity to each *hkl* reflection of the unit cell, then refining those intensities and the unit cell parameters in a least-squares minimisation procedure. The parameters for the diffraction profile which enter the least-squares refinement are: $I(hkl)$ – the intensity of each reflection with indices *hkl*, a, b, c, α, β, and γ – the unit cell parameters, $2\theta_{\text{zero}}$ – an instrumental zero error correction, and U, V, W, z *etc.* - the peak width and shape profile parameters. A space group may also be supplied to inform which reflections should be given intensity. Since a Pawley fit is not constrained by the accuracy of a structural model, it is a useful method of fitting a diffraction pattern when a structural model is not the objective. For example, the method is very useful for comparing different space group assignments; performing a Pawley fit to two possible space groups may indicate which the better choice is. Pawley refinements were also performed in TOPAS academic version.[113]

2.2.8 DC SQUID magnetometry

A Superconducting QUantum Interference Device (SQUID) is a highly sensitive component of a magnetometer that offers a means of measuring the magnetisation of a sample at various temperatures, fields and timescales. A Quantum Design MPMS SQUID magnetometer was used for magnetic susceptibility measurements in this thesis. The key component in a SQUID magnetometer is a closed superconducting loop intersected by two thin strips of insulating material, forming two Josephson junctions. The application of a small current across the junction causes Cooper pairs of electrons to tunnel through the insulation barrier with no resistance. This fragile superconducting state across the insulating barriers can be lost if the applied current exceeds a critical current, and a quantifiable voltage will be established in the device with a finite resistance. The presence of an external magnetic field affects the critical current that is required, and so by monitoring changes in the voltage across the junction, variations in the applied magnetic field may be measured.

The SQUID unit is housed behind a superconducting shield in order to protect it from fluctuating external fields from both the environment and the sample. The sample is mounted within an induction coil and magnetised by a He-cooled superconducting magnet. Once magnetised, vertical translation of the sample induces a current in the induction coil which is coupled indirectly to the SQUID, this generates an output voltage that is proportional to the magnetic moment of the sample.

The superconducting magnet in the Quantum Design MPMS SQUID can generate fields in the range $-5\ \mathrm{T} \leq H \leq 5\ \mathrm{T}$. The sample is kept under a reduced helium atmosphere and can be cooled to a minimum temperature of 2 K so the magnetisation can be measured as a function of both temperature and field strength.

2.2.8.1 Magnetic measurements of superconducting samples

The magnetic susceptibility of a superconducting material is distinguished by the onset of a strong diamagnetic signal below a certain, sample dependent, critical temperature T_c. The diamagnetic signal is due to the Meissner effect: all lines of magnetic flux from within the superconductor are expelled as a state of perfect diamagnetism is reached. The magnitude of the diamagnetic response may be used to assess the bulk superconducting properties of the sample. A sample in a non-superconducting state will have internal flux density:

$$\boldsymbol{B_i = \mu_0(H + M) = B + \mu_0 M}$$ **Equation 2.30**

where $\mu_0 M$ is the contribution from the sample and B the applied flux density. In a superconducting sample the internal flux density $B_i = 0$ and so:

$$\boldsymbol{M = \frac{-B}{\mu_0} = -H}$$ **Equation 2.31**

and a dimensionless volume magnetic susceptibility for a superconductor, χ_{vol}, can be written:

$$\boldsymbol{\chi_{vol} = \frac{M}{H} = -1}$$ **Equation 2.32**

which is the case if all of the sample is superconducting. When plotting the susceptibility of a superconductor, it is convenient to use χ_{vol} since this informs of the fraction of the sample that is superconducting. The Quantum Design MPMS SQUID records a longitudinal magnetic moment (parallel to the applied field) from the sample, which is dependent on the sample mass, concentration, and the applied field, in cgs units. The magnetisation can be expressed in terms of a χ_{vol} as:

$$\boldsymbol{\chi_{vol} = \frac{4\pi\, M_l\, \rho}{H\, m}}$$ **Equation 2.33**

where M_l is the longitudinal moment, ρ the crystallographic density, and m the sample mass. A superconducting volume fraction can be calculated by considering the total drop in χ_{vol} from above the transition temperature to the lowest temperature measured (2 K in this thesis) and dividing by -1; the maximum expected drop. This value is very much an estimate as it requires a number of assumptions. It assumes the sample shape to be spherical which it is not, and neglects grain boundary effects that can affect magnetism. The error introduced into χ_{vol} by these factors should be quite systematic for a series of similar compounds, and so the relative values of χ_{vol} should be quite robust.

For superconducting compounds, magnetisation was measured as a function of temperature in the region $2 \leq T \leq 60$ K in a small applied field (usually 20 Oe) that is lower than the critical field of the sample. The superconducting transition temperature, T_c, was generally taken to be the temperature at which the onset of the transition is observed. Alternatively, T_c may be obtained by extrapolating the steepest section of the superconducting transition and finding the intersection with the extrapolated normal-state curve.

2.2.9 Studying solid-state reaction kinetics with diffraction

The modelling of reaction kinetics in the solid state is well established, the earliest review of the field was *Chemistry of the Solid State*, edited by W. E. Garner, in which Jacobs and Tomkinson covered theories and derivations of nucleation and nuclei growth models.[115] There have been several reviews since.[116–118] In recent years, the rise of high intensity central facility radiation sources has opened up new doors in the study of materials as it is possible to examine a sample at incredible speed. At Diamond Light Source, appreciable intensity and resolution diffraction patterns can be obtained in the sub-second time scale, and there are examples of pump-probe techniques performed on specialised instruments that are able to directly manipulate and measure atomic-scale magnetic structures with the electric field of light on a sub-picosecond time scale.[119,120]

Chapter 4 of this thesis reports the reaction kinetics of the intercalation of sodium and ammonia into iron selenide using *in-situ* powder X-ray diffraction at Diamond Light Source. A description of Avrami-Erofe’ev theory, which has been used for the kinetic modelling of these solid-state reactions, is provided in the introduction to chapter 4 (page 86).

Chapter 3

3. Deintercalation chemistry of NaFeAs

3.1 Chapter introduction

The subject of iron-based superconductors was discussed in chapter one, in which NaFeAs featured as an archetype of one of the structural systems found to exhibit unconventional superconductivity. The structure of NaFeAs consists of anti-PbO type FeAs layers, characteristic to the iron-based superconductors, separated by a double layer of sodium ions. NaFeAs is itself an itinerant antiferromagnet with a trace fraction of superconductivity, but chemical substitution of 2-10 % of the iron with cobalt or 1-5 % nickel can be used to *n*-type dope the band structure and brings the material into the bulk superconducting regime. The T_c can be driven to a maximum of 25 K and a superconducting volume fraction of 100 % in $NaFe_{0.975}Co_{0.025}As$, which is optimally doped.[53]

In the related compound $BaFe_2As_2$, which is also antiferromagnetic at low temperatures and consists of Fe^{2+} in anti PbO type FeAs layers, a similar picture is arrived at by *p*-type doping of the band structure by chemical substitution of Ba by K, $Ba_{1-x}K_xFe_2As_2$ with superconductivity persisting over the range $0.3 < x < 1$.[49] These syntheses are carried out by reaction of the elements at high temperatures, giving only the most thermodynamic stable product. Substitution of the kind $A_{1-x}Na_xFe_2As_2$ can also be performed with A = Ba or Sr, but two investigations conclude that the phase field is limited to the range $0 < x < 0.6$[121] or $0 < x < 0.7$[122] with impurity phases stated to appear when higher values of x are attempted. $NaFe_2As_2$, which represents the $x = 1$ limit of the $A_{1-x}Na_xFe_2As_2$ system, cannot be made by this synthesis procedure since the size mismatch between the 8-coordinate site between FeAs layers and the Na^+ ion prevents it from being the most stable phase at high temperature.

Low temperature strategies have been adopted to target $NaFe_2As_2$ by oxidative deintercalation of sodium from NaFeAs, which has yielded mixed reports of superconductivity between 10 and 25 K. Gooch *et al.* describe reaction of NaFeAs with an unspecified ionic liquid to produce $NaFe_2As_2$, the magnetisation of which shows an onset of T_c at 25 K followed by a larger drop in the susceptibility below 10 K.[92] Todorov *et al.*

describe reaction with air and with water. Their tentative conclusion is that reaction with air produced $NaFe_2As_2$ with T_c of 12 K, but reaction with moisture produced a material of the type $Na_{1-x}FeAs$ with a T_c of 25 K, in which Na vacancies have been introduced without moving to the $ThCr_2Si_2$ structure.[93] In the only reliable report published prior to this work, Friederichs *et al.* used an iodine solution to produce the $NaFe_2As_2$ type material with T_c of 11 K, however concluded through diffraction data and EDX, that both sodium and iron were being deintercalated from the sample, the two techniques giving stoichiometries $Na_{0.99(4)}Fe_{1.67(2)}As_2$ and $Na_{0.9(0.2)}Fe_{1.7(2)}As_2$, respectively.[94]

The products of deintercalation reactions of NaFeAs are relatively poorly crystalline as judged by diffraction methods, and here we use local probes: X-ray Absorption Spectroscopy at the Fe and As *K*-edges to describe a structural model for this deintercalated, make comparison with related materials, and explore whether *n*-type doping of $NaFe_{1.67}As_2$ using Co substitution on the iron site can be used to enhance T_c.

3.2 Synthesis of precursors

Polycrystalline samples of $NaFe_{1-z}Co_zAs$, with z =0, 0.02, 0.05, and 0.12, were prepared by reaction of the elements inside sealed niobium tubes. Handling of the air-sensitive starting materials and products was performed inside an argon-filled, dry glovebox. Iron (Alfa Aesar, 99.998%), cobalt (Alfa Aesar, 99.998%) and arsenic (Alfa Aesar, 99.999%) powders were ground together and combined inside a niobium tube with pieces of sodium (Alfa Aesar, 99.95%), freshly cut from lumps to remove the oxidised surface. The niobium tube was transferred to an arc welding rig, in which the tube was sealed. The sample sealed in the niobium tube was heated to 250 °C for 48-72 hours; the initial product was extracted in a glovebox, ground thoroughly using an agate pestle and mortar, pelletized, and sealed in another niobium tube following the same procedure. The second niobium tube was then heated to 750 °C after first itself being sealed in an evacuated silica ampoule in order to prevent the aerial oxidation of niobium. The final products were extracted in the glovebox. Initial characterisation was performed by laboratory powder X-ray diffraction, and SQUID magnetometry.

A KFe_2As_2 sample, used as a standard for X-ray absorption spectroscopy was synthesised in a similar fashion to the $NaFe_{1-z}Co_zAs$ samples by reaction of the elements in a sealed niobium tube. The purity of KFe_2As_2 was assessed by powder X-ray diffraction.

3.3 Deintercalation of NaFeAs and initial characterisation

Samples of $Na_{1-x}(Fe_{1-z}Co_z)_{2-y}As_2$ were prepared at ambient temperature by topotactic deintercalation of the metals from $NaFe_{1-z}Co_zAs$ precursors. The precursors were reacted with iodine in THF solution, using a 2 : 1 ratio of $NaFe_{1-z}Co_zAs$ to I_2, typically in a 0.05 mol dm^{-3} solution for 20 hours. Standard Schlenk line techniques were adopted to handle the air-sensitive samples. From the diffraction data (Figure 3.1) it can be observed that crystallinity is substantially reduced on deintercalation, and so several reaction conditions were trialled in an attempt to improve the crystallinity of the final product. The reaction was repeated under near-duplicate conditions but; changing the solvent from THF to acetonitrile, modifying the concentration of iodine solution between 0.03 and 0.1 mol dm^{-3}, altering the molar ratio of $NaFe_{1-z}Co_zAs$: I_2 between 1 : 4 and 4 : 1, performing the reaction at 0 °C, and using a reaction time between 4 hours and 7 days. None of these factors were found to improve the crystallinity of the product, and using a molar ratio of 4 : 1 produced an incomplete reaction with some starting material remaining.

3.3.1 Powder X-ray diffraction

The synthesised materials were initially characterised by Rietveld refinement against Laboratory X-ray powder diffraction patterns, as shown in Figure 3.1. $NaFe_{1-z}Co_zAs$ samples were measured in an air-sensitive manner using purpose-built aluminium containers, housing a glass slide on which the powder was placed, with exposure to the X-ray beam through a Mylar® window. Air exposure did not appear to affect the diffraction patterns of the $Na_{1-x}(Fe_{1-z}Co_z)_{2-y}As_2$ samples and so the patterns showed in Figure 3.1and Figure 3.2 were collected under air. $NaFe_{1-z}Co_zAs$ samples were found to adopt the published structure (anti-PbClF type), with no impurities observed. Upon deintercalation the structure type changes to $ThCr_2Si_2$ in agreement with the literature.[92–94] In undergoing this structural transformation there has been a shift of alternative FeAs layers by ½ ½ 0, along with removal of half the sodium, and a shift of the remainder into the new 8 coordinate site at the origin of the unit cell.

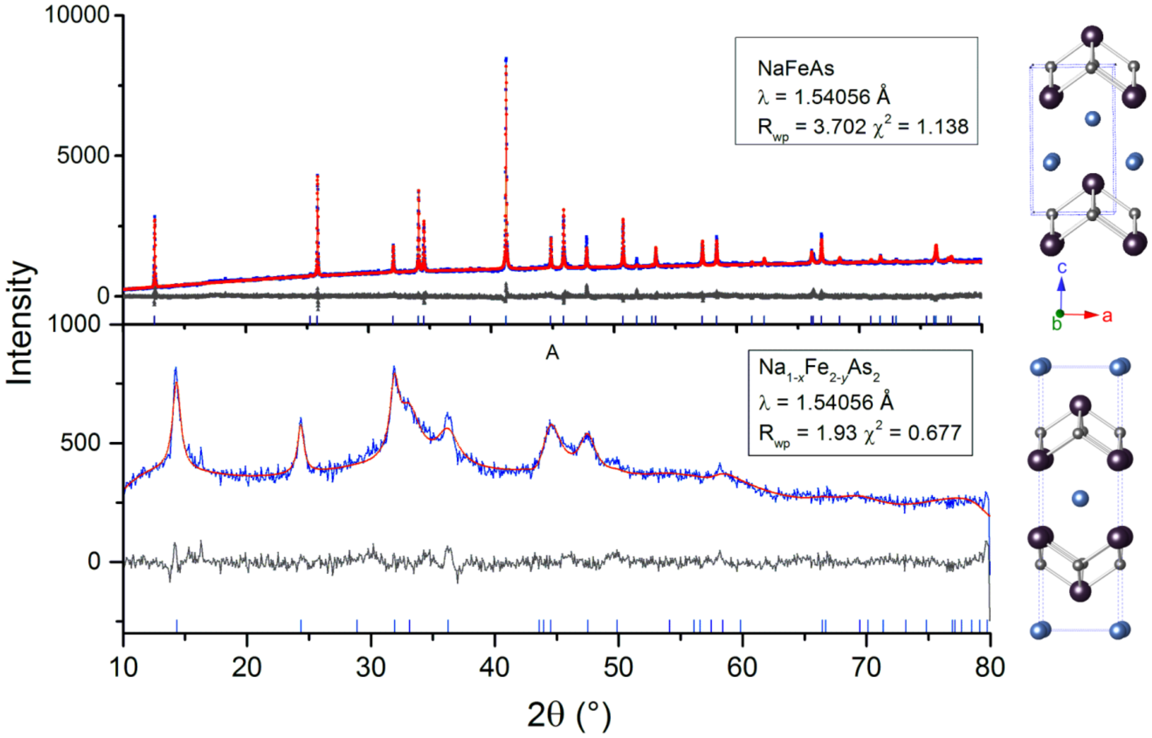

Figure 3.1 Rietveld refinement against laboratory powder X-ray diffraction patterns for NaFeAs (top) and $Na_{1-x}Fe_{2-y}As_2$ (bottom). Blue line = observed diffraction pattern, red line = calculated diffraction pattern, grey line = difference curve (observed – calculated), vertical lines = phase peak markers.

The poor crystallinity of the final product presents a difficulty in obtaining accurately refined structural parameters; the χ^2 has dropped below one indicating the model used to produce a good visual fit has been over-parameterised. The extractable information through traditional diffraction techniques is limited for this compound by the poor resolution of its peaks, inherent to its crystallinity.

Pawley refinements against the diffraction patterns of further $Na_{1-x}(Fe_{1-z}Co_z)_{2-y}As_2$ samples are given in Figure 3.2. Each compound was found to adopt a $ThCr_2Si_2$ type structure with varying degrees of crystallinity.

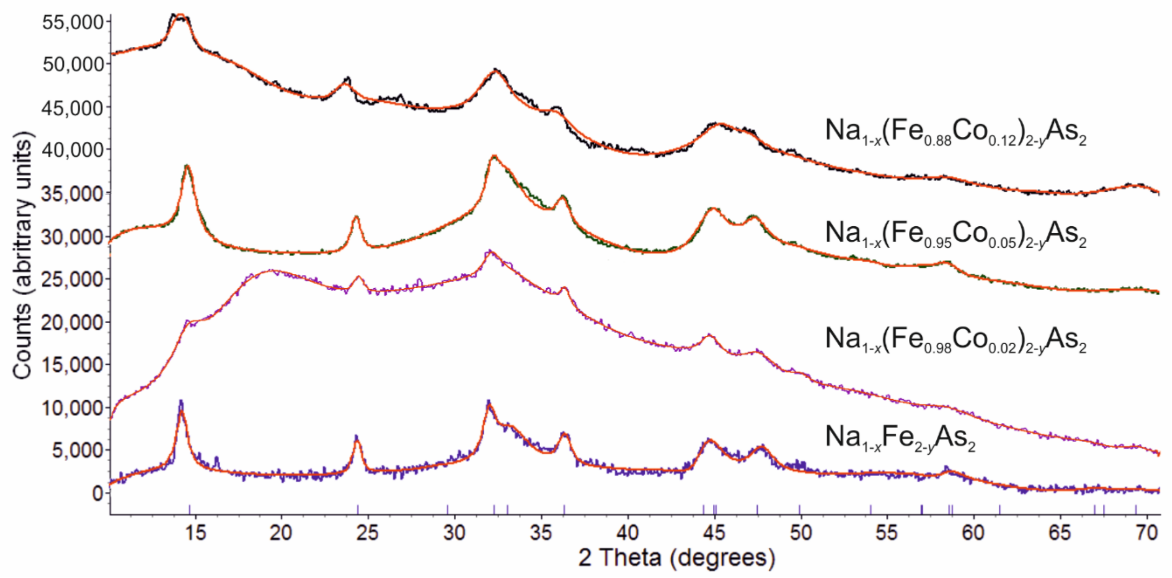

Figure 3.2 Pawley refinement against Laboratory X-ray diffraction patterns (λ = 1.54056 Å) of various $Na_{1\text{-}x}(Fe_{1\text{-}z}Co_z)_{2\text{-}y}As_2$ samples, showing that each adopts the $ThCr_2Si_2$ structure type.

3.3.2 Magnetometry

Characterisation of the magnetic properties of these materials was carried out by SQUID magnetometry. NaFeAs itself typically exhibits a minor superconducting transition at around 10 K with a superconducting volume fraction of 10-20 %. Superconductivity in NaFeAs is observed in several reports[52,93,123] and even in single crystal samples,[124] however the origin of this superconducting transition remains unclear as muon-spin rotation spectroscopy[52,62] and neutron diffraction experiments[125] have shown that stoichiometric NaFeAs is an itinerant antiferromagnet with a small localised moment on Fe (*ca.* 0.1 μ_B). $Na_{1\text{-}x}Fe_{2\text{-}y}As_2$ was also found to exhibit a broad superconducting transition with $T_{c(\text{onset})}$ = 10 K and a superconducting volume fraction of about 7 %, in line with other reports which assign this transition temperature to the deintercalated $Na_{1\text{-}x}Fe_{2\text{-}y}As_2$ species.[52,92,93] In performing the deintercalation, the iron oxidation state has been significantly raised, and so in order to explore the effects of counterbalancing the effect of removing electrons from the Fermi level by deintercalation, the synthesis was repeated using the more electron-rich cobalt substituted $NaFe_{1-z}Co_zAs$, (z = 0.02, 0.05, 0.12) as the starting material. While the parent materials exhibit a positive response even towards very low concentrations of cobalt substitution, the results of magnetometry reveal in the case of the products $Na_{1\text{-}x}(Fe_{1\text{-}z}Co_z)_{2\text{-}y}As_2$, 2% Co substitution is sufficient to completely suppress superconductivity.

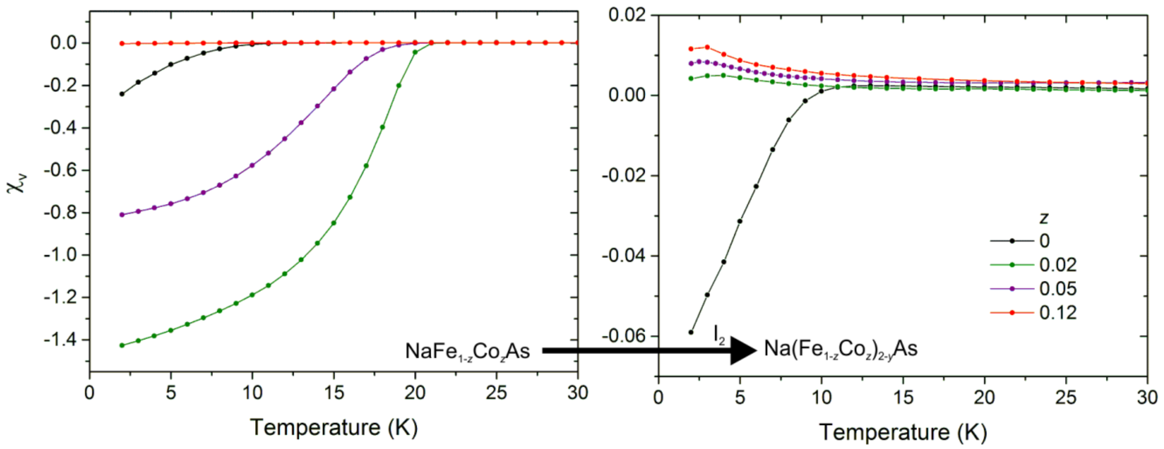

Figure 3.3 Volume susceptibility magnetisation plotted against temperature for parent (left) and daughter (right) cobalt substituted sodium iron arsenide samples.

It should be noted that since the ratio of iron to cobalt being removed in the deintercalation cannot be determined and may not be equal, the nominal stoichiometries have an additional margin of error such that z = 0.020(4), 0.050(9), 0.12(2).

3.4 X-ray absorption spectroscopy

As a technique for structure modelling that is not dependent on high crystallinity, EXAFS presents a promising method for further characterisation of $Na_{1-x}Fe_{2-y}As_2$. Fe and As K-edge absorption spectra of NaFeAs and $Na_{1-x}Fe_{2-y}As_2$ were using beamline B18 at Diamond Light Source.[104]

The samples were measured at room temperature in transmission mode with either an iron or arsenic pellet as a reference material in place after the sample for energy calibration. Preparation of NaFeAs samples for XAS measurements was performed in an argon-filled, dry glovebox. NaFeAs was diluted with cellulose and pressed into a thin, 13 mm diameter pellet under a 1 tonne force. The pellets were sealed between two pieces of Kapton® tape, and transported to the beamline in heat sealed aluminized polythene bags. The pellets were removed from their polyethene bags before measurement, still between Kapton® tape to protect them from the atmosphere, and the spectra were collected over 30 minutes. A second 10 minute scan was performed on the same pellet 4 hours later to assess any degradation of the sample in which no shift in the XANES or change in the EXAFS was observed. The samples of the oxidized product $Na_{1-x}Fe_{2-y}As_2$ were handled in two ways: in the original experiment it was diluted with cellulose and treated as air-stable, then at a later date a portion of the same sample was treated as air sensitive, and boron nitride was used as the supporting material. The follow-up measurement confirmed that the deintercalated products were not affected by air exposure, nor by any interaction with cellulose. XANES and EXAFS results for the follow-up measurement are given in appendix II.

3.4.1 XANES

Figure 3.4 shows the Fe *K*-edge absorption of the crystalline standards NaFeAs and KFe_2As_2, and the deintercalated product $Na_{1-x}Fe_{2-y}As_2$ (green). The Fe *K*-edge consists of a pre-edge feature corresponding to the ionisation 1s to 3d around 7111 eV, with the main edge corresponding to the fully allowed 1s to 4p transition located around 7117 eV. The appearance of a pre-edge feature at 7111 eV is a consequence of the non-centrosymmetric local coordination environment about iron, which is a slightly distorted tetrahedral coordination of arsenide ions. The $\Delta l = \pm 1$ atomic selection rule for optical transitions is partially relaxed for the 1s → 3d transition that forms the pre-edge feature because the "3d" orbitals in a tetrahedral or distorted tetrahedral arrangement will mix with the 4p making the transition partially allowed. Pre-edge features are highly sensitive towards local symmetry: the lack of variation in the position and shape of the feature at 7111 eV between the three samples shows the symmetry and nature of the first coordination shell of Fe remains intact upon deintercalation. The deintercalated product exhibits a clear oxidative shift in the main Fe *K*-edge position relative to the NaFeAs parent, and the 1st and 2nd derivative plots also show $Na_{1-x}Fe_{2-y}As_2$ to be in a higher oxidation state than KFe_2As_2. The centre of the main peak in the first derivative of the edge spectrum lies at 7116.66, 7117.15, and 7117.72 eV, and the zero crossing of the second derivative comes at 7116.73, 7117.26, and 7117.70 eV for NaFeAs, KFe_2As_2, and $Na_{1-x}Fe_{2-y}As_2$, respectively. The increase in edge position by ~0.5 eV in the order NaFeAs (Fe 2+), KFe_2As_2 (Fe 2.5+) and $Na_{1-x}Fe_{2-y}As_2$ indicates that the iron absorbers in $Na_{1-x}Fe_{2-y}As_2$ have an oxidation state of approximately +3, corresponding to a composition of $NaFe_{1.67}As_2$, as deduced by Friederichs *et al.*[94] for compounds prepared by similar means.

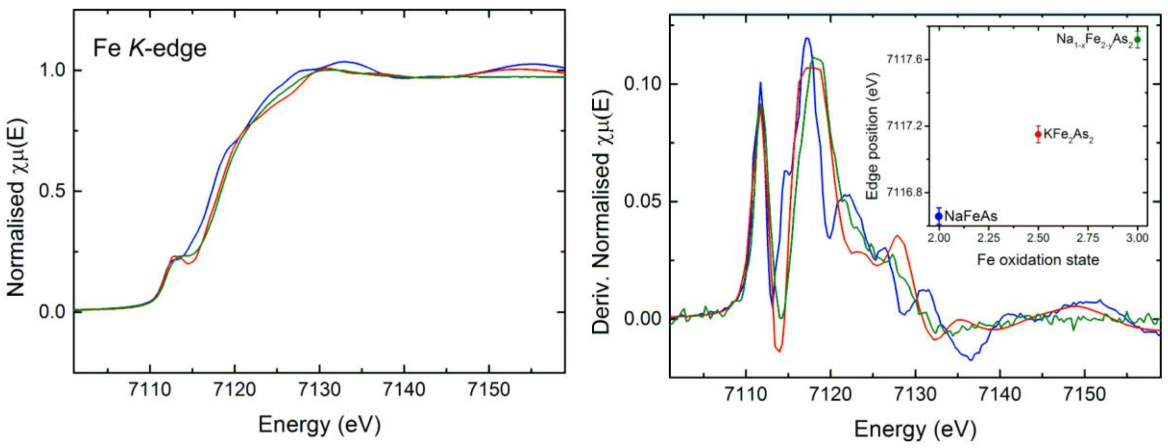

Figure 3.4 Left: Normalised Fe *K*-edge XANES spectra for NaFeAs (blue), its deintercalation product (green) and KFe_2As_2 (red). Right: The corresponding derivative spectra. The inset shows the linear shift of the edge position as judged by the peak in the first derivative plotted against oxidation state, supporting the composition $NaFe_{1.7}As_2$ (Fe^{3+}).

Figure 3.5 shows that the shape of the arsenic *K*-edge XANES spectrum changes significantly on deintercalation. This is indicative of a significant change in coordination environment and is consistent with the removal of some of its neighbouring sodium ions. The onset of the arsenic *K*-edge absorptions overlap for NaFeAs and $Na_{1-x}Fe_{2-y}As_2$, indicating little change in the oxidation state of arsenic, however, the significant change in the shape of the XANES between NaFeAs and $Na_{1-x}Fe_{2-y}As_2$ makes precise comparison of As *K*-edge positions difficult. A shift in the Fe *K*-edge and a lack of any apparent shift in the As *K*-edge matches calculations,[126] and angle resolved photo emission spectroscopy (ARPES) measurements[127] which show that the states at the Fermi surface are predominately of Fe-3d orbital character.

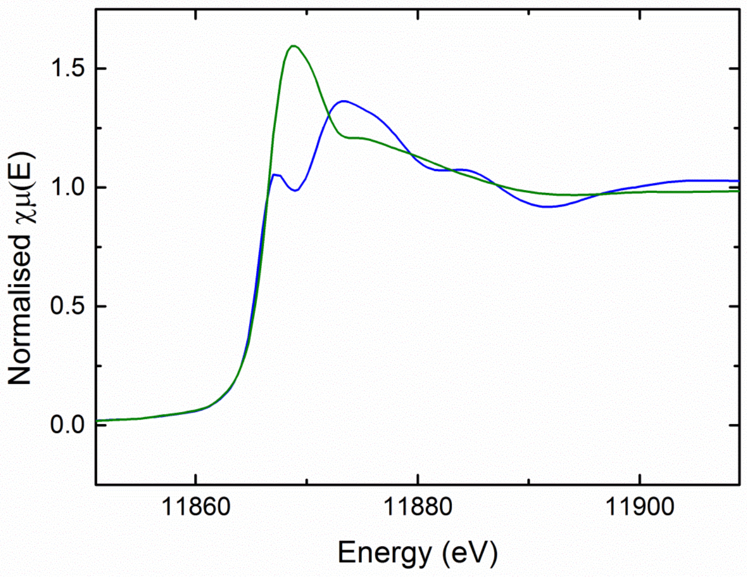

Figure 3.5 Evolution of the normalised As *K*-edge spectra for NaFeAs (blue) and its oxidised deintercalated derivative (green).

3.4.2 EXAFS

Along with the loss of long range order evident in the diffraction pattern, the EXAFS spectra reveal that the local structures about the Fe and As centres of $Na_{1-x}Fe_{2-y}As_2$ become much more disordered relative to the case in the NaFeAs parent material. This is evident from the comparison in Figure 3.6 which shows the loss of well-defined scattering paths beyond a radial distance of 3 Å in the EXAFS of $Na_{1-x}Fe_{2-y}As_2$ as compared with the starting material NaFeAs, and the suppression of the feature in the EXAFS spectrum at a radial distance of 2.5 Å which corresponds to the Fe−Fe nearest neighbour scattering pathway.

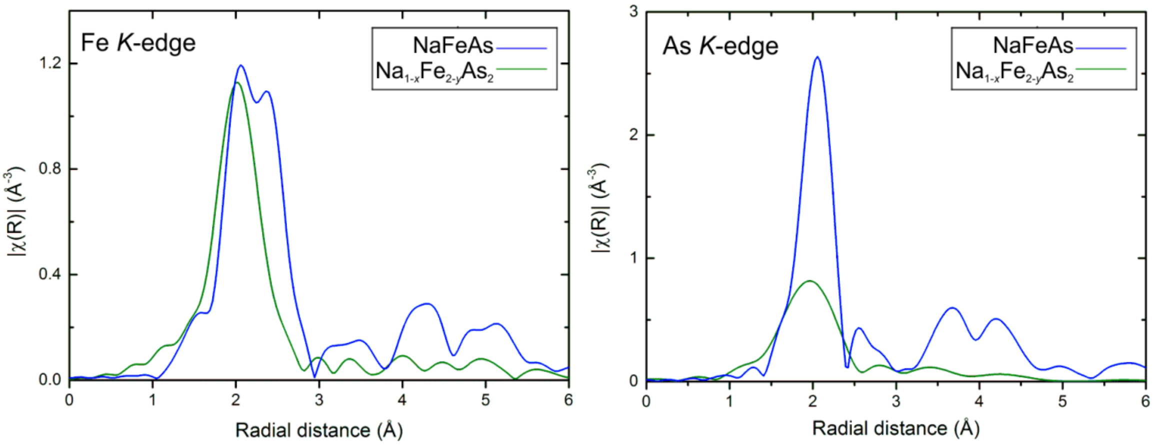

Figure 3.6 Comparison of the Fe *K*-edge and As *K*-edge EXAFS Fourier transform in real space for NaFeAs (blue) and its oxidised deintercalated derivative (green).

The loss of order is similar to that reported to occur in the related system $K_{0.8}Fe_{1.6}Se_2$ compared with β-FeSe from which it is formally derived via an intercalation of potassium and compensating de-intercalation of iron.[128,129] In the latter system, the comparison of FeSe and $K_{0.8}Fe_{1.6}Se_2$ at the Fe *K*-edge is very similar to that shown in Figure 3.6, showing that the introduction of vacancies in the anti-PbO type iron selenide layers leads to a loss of well-resolved scattering paths outside the first coordination shell. This is evident in the EXAFS of $K_{0.8}Fe_{1.6}Se_2$ despite the long-range ordering of vacancies and significantly greater long range structural order in the system as probed by diffraction methods[75] relative to the semi amorphous nature of the $Na_{1-x}Fe_{2-y}As_2$ system (Figure 3.1 and ref. [92]). This loss of order in the local structure around iron is also observed to be a gradual loss as more vacancies are introduced. Figure 3.7 plots the EXAFS spectra of various samples of composition $Li_{1-x}Fe_x(OH)Fe_{1-y}Se$, where $x \approx 0.2$ and $0.85 \leq y \leq 1$, synthesised by group members Hualei Sun and Genevieve Allcroft, alongside a sample of $K_{0.8}Fe_{1.6}Se_2$ synthesised by Dr David Free and a sample of FeSe for reference.[130] The first feature seen in all samples at ~2 Å in the figure is dominated by the Fe-Se 1st nearest neighbour single scattering path. The Fe-Fe 1st nearest neighbour single scattering path at ~2.4 Å and further single and multiple scattering paths out to ~6 Å are gradually more resolved in samples that have been synthesised with a lower number of iron vacancies. Quantitative fitting of the EXAFS of the $Li_{1-x}Fe_x(OH)Fe_{1-y}Se$ samples has been performed and is available in appendix III

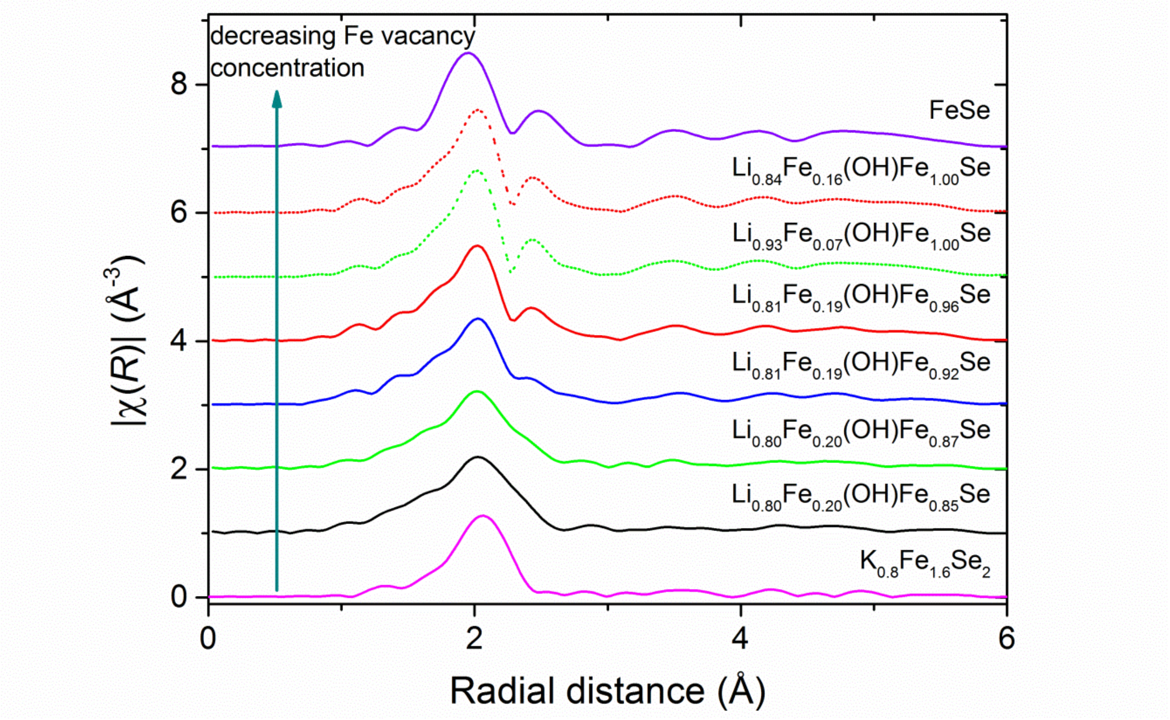

Figure 3.7 The iron *K*-edge EXAFS Fourier transform for several systems that include anti PbO type $Fe_{1-x}Se$ layers. In systems with iron vacancies, the local structure is observed to become highly disordered.

Measurements performed on the $Li_{1-x}Fe_x(OH)Fe_{1-y}Se$ samples were performed on beamline B18 in transmission mode using the air-sensitive sample loader, the design of which is detailed in chapter 2.2.4.4. The samples were prepared in an argon-filled, dry glovebox by grinding together ~5 mg of sample with cellulose in order to make thin, 7 mm diameter pellets, which were pressed inside the glovebox.

3.4.2.1 Modelling the EXAFS of NaFeAs

For the parent material NaFeAs, strong features from direct and multiple scattering paths out to 6 Å away from the absorbing site can be modelled in the EXAFS. A good fit to the data was achieved starting with a model obtained from the diffraction data and refining this model against both the Fe *K*-edge and As *K*-edge EXAFS simultaneously, constraining equivalent path distances and Debye-Waller terms in each data set to the same value. There is strong agreement between the PXRD and EXAFS models with very low variation in refined interatomic distances and the agreement is good even at high R values, which indicate the sample is well ordered on the length scale probed by EXAFS. The sum of all relevant single and multiple scattering path contributions to the EXAFS of NaFeAs are shown in Figure 3.8 fitted against the EXAFS data. For the iron edge, an R-range of 1.5 – 5.6 Å, and k-range of 2.2 – 13 Å^{-1} were used. For the arsenic edge an R-range of 1.4 – 4.7 Å, and k-range of 2.3 – 13.7 Å^{-1} were used. Fitting was carried out in R space with k weightings of 1, 2 and 3, using 27 of 52 possible independent variables in total. These fits have a combined R-factor of 0.011. A representation of the scattering paths used in the fitting is given in Figure 3.9 and the refined parameters for those scattering paths are given in Table 3.1.

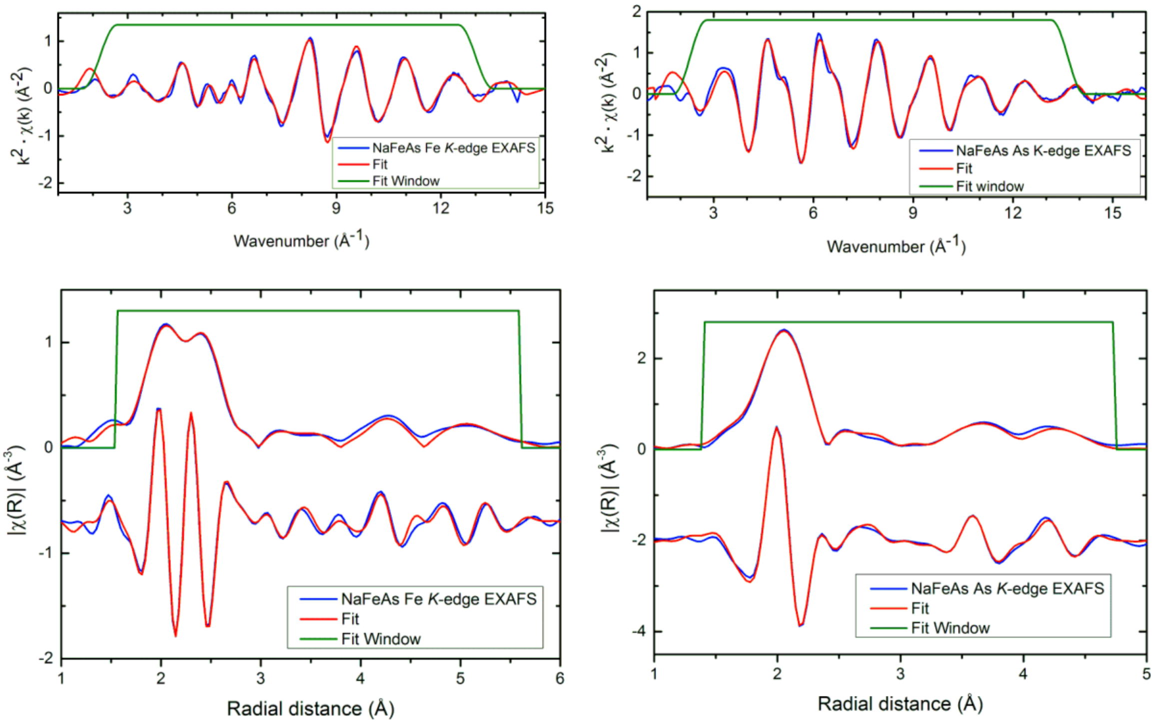

Figure 3.8 Fits to the iron (left two) and arsenic (right two) *K*-edge EXAFS of NaFeAs in k-space (top) and R-space (bottom)

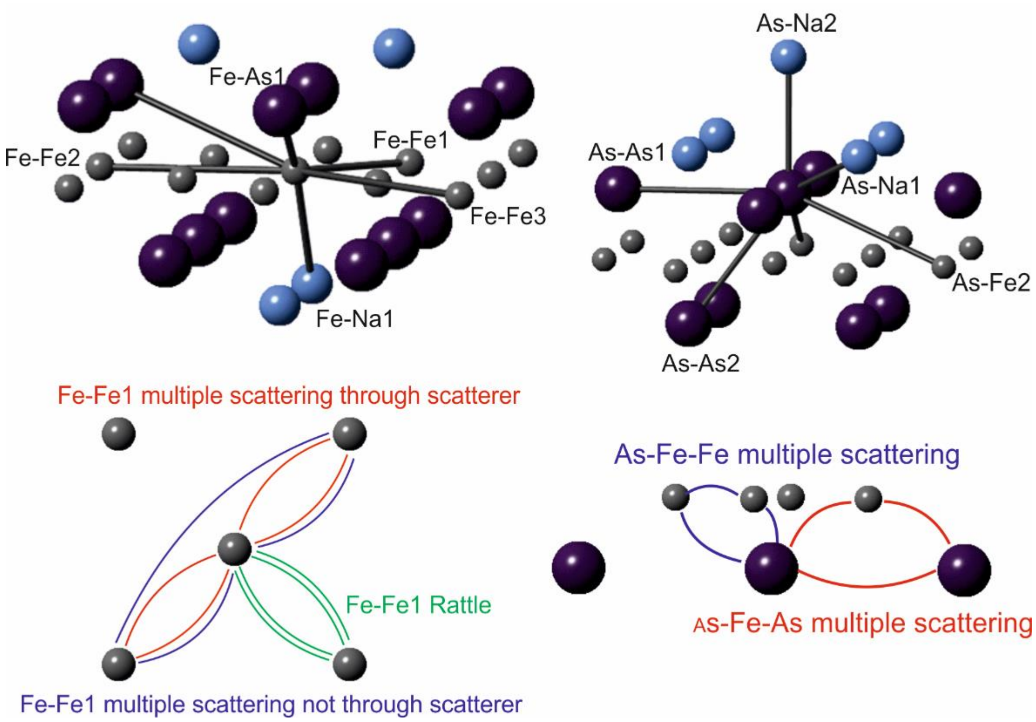

Figure 3.9 Representation of the single and multiple scattering paths included in the fitting of the Fe (left) and As (right) EXAFS for NaFeAs.

Table 3.1 Refined parameters from the EXAFS fitting of NaFeAs Fe and As *K*-edges, alongside the value obtained from Rietveld refinement against the powder X-ray diffraction (PXRD) pattern of the same sample.

Parameter	EXAFS refined value	PXRD refined value
S_0^2 Fe	0.67(4)	-
S_0^2 As	1.000(2)	-
R Fe-As1 (Å)	2.417(2)	2.456(2)
σ^2Fe-As1 (Å^2)	0.0057(2)	-
R Fe-Fe1 (Å)	2.773(6)	2.7950(1)
σ^2Fe-Fe1 (Å^2)	0.0091(10)	-
R As-Na1 (Å)	3.05(2)	2.958(4)
σ^2As-Na1 (Å^2)	0.021(6)	-
R As-Na2 (Å)	3.020(3)	3.161(5)
σ^2As-Na2 (Å^2)	0.007(7)	-
R As-As1 (Å)	3.97(3)	3.9531(2)
σ^2As-As1 (Å^2)	0.006(2)	-
R Fe-Fe2 (Å)	3.941(15)	3.9531(2)
σ^2Fe-Fe2 (Å^2)	0.010(5)	-
R Fe-Na1 (Å)	3.18(3)	3.130(4)
σ^2Fe-Na1 (Å^2)	0.020(7)	-
R As-As2 (Å)	3.88(3)	4.040(3)

σ^2As-As2 (Å^2)	0.010(4)	-
R Fe-As2 (Å)	4.640(11)	4.6537(6)
σ^2Fe-As2 (Å^2)	0.0123(15)	-
R As-Fe-Fe (Å)	= R As-Fe1 + 1/2(R Fe-Fe1)	-
σ^2As-Fe-Fe (Å^2)	0.002(5)	-
R As-Fe-As (Å)	= R As-Fe1 + 1/2(R As-As1)	-
σ^2As-Fe-As (Å^2)	0.004(4)	-
R Fe-Fe3 (Å)	= 2(R Fe-Fe)	= 2(R Fe-Fe)
σ^2Fe-Fe3 (Å^2)	= 2(σ^2Fe-Fe1)	-
R Fe-Fe-Fe (double scattering) (Å)	= 2(R Fe-Fe)	= 2(R Fe-Fe)
σ^2Fe-Fe-Fe (double scattering) (Å^2)	= 4(σ^2Fe-Fe1)	-
R Fe-Fe-Fe (rattle) (Å)	= 2(R Fe-Fe)	= 2(R Fe-Fe)
σ^2Fe-Fe-Fe (rattle) (Å^2)	= 8(σ^2Fe-Fe1)	-

3.4.2.2 Modelling the EXAFS of KFe_2As_2

A similar picture emerges for the Fe *K*-edge EXAFS fitting of KFe_2As_2. Like NaFeAs, this stoichiometric compound shows good local order. Refinement against the Fe *K*-edge EXAFS of KFe_2As_2 was carried out starting with a model obtained from Rietveld analysis of the powder diffraction data. The EXAFS of Fe absorbers was modelled using direct and multiple scattering paths extending to 5.7 Å from the absorbing site, using the scattering paths represented in Figure 3.11, giving the fit shown Figure 3.10, which has an R-factor of 0.010. KFe_2As_2 exhibits good agreement between the diffraction and EXAFS models with a comparison of the refined parameters from both given in Table 3.2. Fitting was carried out in R space over the range of 1-5.7 Å, and k-range of 3-14 Å^{-1}, refining against the EXAFS with k weightings of 1, 2 and 3. 18 of 32 independent variables were used for the refinement.

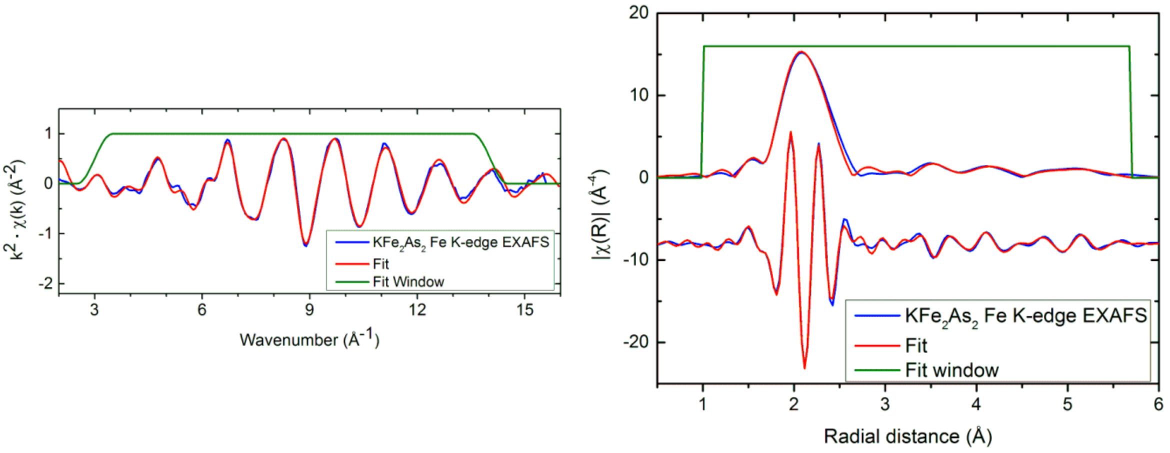

Figure 3.10 Fit to the iron edge EXAFS of KFe_2As_2 shown in k-space (left) and R-space (right).

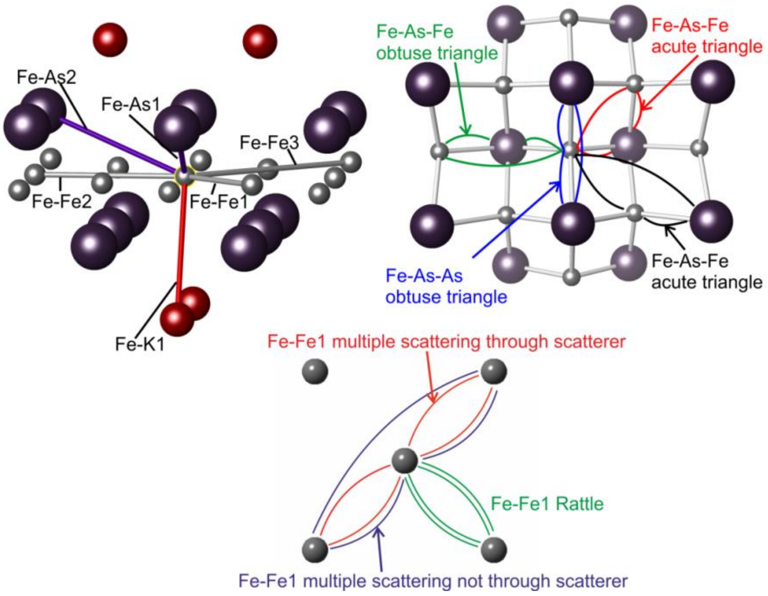

Figure 3.11 Representation of direct and multiple scattering paths that have been included in the fitting of the iron absorber environment in KFe_2As_2.

Table 3.2 Refined parameters from the EXAFS fitting of the KFe_2As_2 Fe *K*-edge, alongside the value obtained from Rietveld refinement against the powder X-ray diffraction pattern of the same sample.

Parameter	EXAFS refined value	PXRD refined value
S_0^2 Fe	0.68(5)	
R Fe-As1 (Å)	2.381(3)	2.388(1)
σ^2 Fe-As1 (Å^2)	0.0042(4)	
R Fe-Fe1 (Å)	2.714(6)	2.7221(3)
σ^2 Fe-Fe1 (Å^2)	0.0127(8)	
R Fe-As-Fe (acute triangle) (Å)	3.76(3)	3.749(1)
σ^2 Fe-As-Fe (acute triangle) (Å^2)	0.010(6)	
R Fe-Fe2 (Å)	3.87(2)	3.8493(5)

σ^2Fe-Fe2 (Å^2)	0.015(2)	
R Fe-K1 (Å)	3.982(2)	3.9673(3)
σ^2Fe-K1 (Å^2)	0.035(2)	
R Fe-As-As (obtuse triangle)and R Fe-As-Fe (obtuse triangle) (Å)	4.32(4)	4.313(1)
σ^2 Fe-As-As (obtuse triangle) and σ^2 Fe-As-Fe (obtuse triangle) (Å^2)	0.002(4)	
R Fe-As2 (Å)	4.624(2)	4.5299(6)
σ^2Fe-As2 (Å^2)	0.011(5)	
R Fe-As-Fe (acute triangle) (Å)	4.74(3)	4.815(2)
σ^2 Fe-As-Fe (acute triangle) (Å^2)	0.003(4)	
R Fe-Fe3 (Å)	5.433	5.4436(7)
σ^2Fe-Fe3 (Å^2)	0.005(1)	
R Fe-Fe-Fe (double scattering) (Å)	= R Fe-Fe3	
σ^2 Fe-Fe-Fe (double scattering) (Å^2)	= 2(σ^2Fe-Fe3)	
R Fe-Fe-Fe (rattle) (Å)	= R Fe-Fe3	
σ^2 Fe-Fe-Fe (rattle) (Å^2)	= 4(σ^2Fe-Fe3)	

3.4.2.3 Modelling the EXAFS of Na$_{1-x}$Fe$_{2-y}$As$_2$

Modelling of the EXAFS for the daughter material Na$_{1-x}$Fe$_{2-y}$As$_2$ was first attempted using a model derived from the diffraction data in which a stoichiometric ThCr$_2$Si$_2$ structure (like that of KFe$_2$As$_2$) was used (*i.e.* $x = y = 0$), using a protocol similar to that used for NaFeAs. The model was refined against both the As *K*-edge and Fe *K*-edge EXAFS simultaneously, fixing the path length and Debye-Waller terms to be the same for equivalent paths in both spectra. The constraint of requiring path lengths to be the same in both edges, as they would be if all sites were fully occupied, produces a poor fit as shown in the left hand panels of Figure 3.13. This shows that the local coordination environments about iron and arsenic in the oxidised deintercalated product are not well described by a stoichiometric NaFe$_2$As$_2$ model. The reason for this is that the EXAFS of As and Fe are heavily influenced by the presence or absence of nearby iron vacancies. A vacancy adapted model for $Na_{1-x}Fe_{2-y}As_2$ was constructed by including two different environments for As.

In one of the two As environments, Fe fills all four nearest-neighbour sites, defined as Fe-As (N = 4), and in the other site, one of the four neighbouring sites is vacant: Fe-As (N = 3) (Figure 3.12). Further environments in which two or more nearest neighbour Fe sites are vacant were neglected in the fit due to their lower statistical probability and unfavourable thermodynamic stability. The distance and Debye-Waller terms for the two Fe–As direct scattering paths: Fe–As (N = 4) and Fe–As (N = 3) were refined independently because they correspond to distinct chemical environments. Further consideration of the effect of a neighbouring iron vacancy on the second coordination shell of As–As scattering paths was not included in the model since the influence of the vacancy is expected to be much smaller for this secondary distortion and the signal from the scattering paths in the second coordination shell is very weak, meaning inclusion of parameters to fit this proposed distortion over-models the available data.

Similar considerations for the effect of vacancies on the local coordination environment of Fe must be made if both sets of data are to be fitted with one model. Since there are no arsenic vacancies, the first nearest neighbours for iron in the analysis of the Fe *K*-edge EXAFS are four arsenide ions. The iron to nearest neighbour arsenic scattering path was modelled with the same distance and Debye-Waller terms as the Fe–As (N = 4) path in the arsenic edge data, this path was refined simultaneously against both data sets. The Fe–Fe scattering path, which contributes to the Fe *K*-edge spectrum will be effected by the iron vacancies, and so was given split amplitude between N = 3 and N = 4 (i.e. each Fe having 3 or 4 Fe neighbours in the plane). These two Fe-Fe paths were constrained to have the same lengths and Debye-Waller terms in order not to over-parameterize the model. The simplification of this part of the structure in the model gives rise to the comparably large Debye-Waller value for this contribution in the fit.

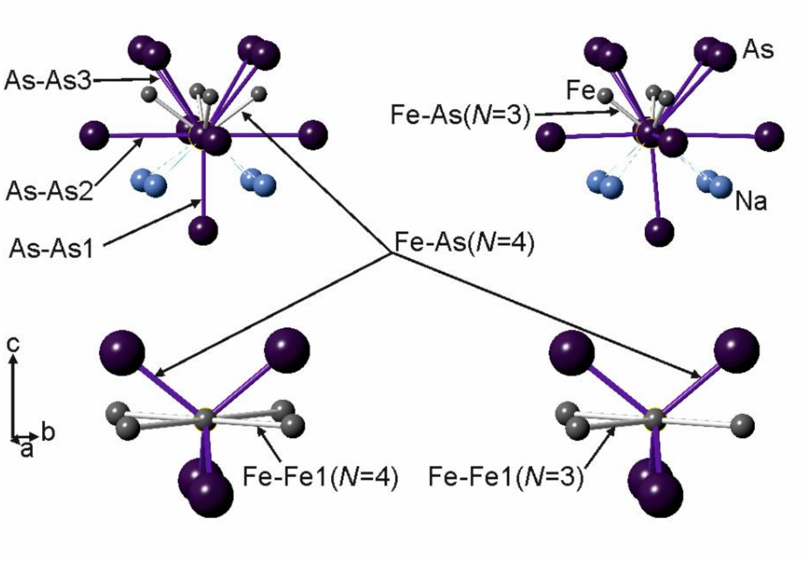

Figure 3.12 Representation of the scattering paths (direct only) included in the modelling of the iron and arsenic *K*-edge EXAFS of NaFe$_{2-y}$As$_2$.

Due to the high structural disorder in the sample, scattering paths to sodium do not contribute significantly to the EXAFS and so are not included in the fit. The model used gives a dramatic improvement over the stoichiometric ThCr$_2$Si$_2$ type model as seen by comparing the fits with (right hand panels) and without (left hand panels) Fe site vacancies in Figure 3.13.

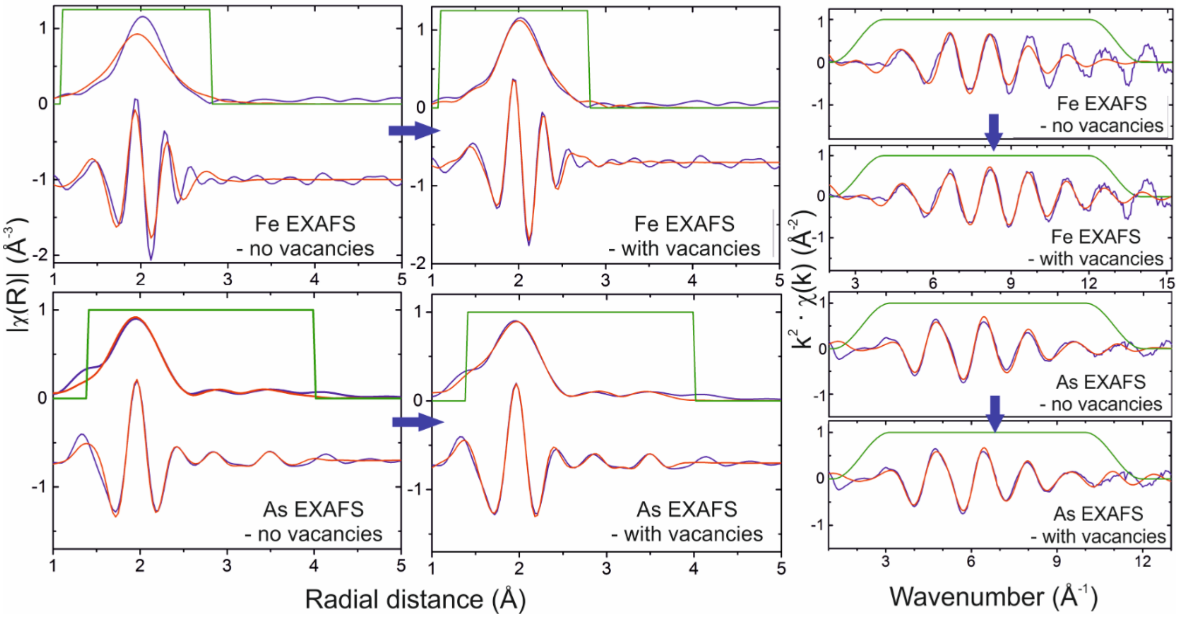

Figure 3.13 Comparison of fitting to EXAFS data of NaFe$_{2-y}$As$_2$ with and without the inclusion of vacancies. Following the blue arrows shows the change in the fit with the introduction of vacancies into the model.

The *R*-factor improved from 0.0911 to 0.0237 when Fe site vacancies were included in the model. Refinement of the composition of the Fe$_{2-y}$As$_2$ layers was carried out by refining the relative numbers of the Fe–As (N = 4) and Fe–As (N = 3) paths in the As *K*-edge EXAFS and the relative numbers of the Fe–Fe (N = 4) and Fe–Fe (N = 3) paths in the Fe *K*-edge EXAFS using a single compositional model. A scale was applied in the model by weighting the amplitude reduction factor S_0^2 for Fe–As (N = 4) by a refinable parameter, w, ($0 \leq w \leq 1$) and the S_0^2 for Fe–As (N = 3) by $1-w$. The weighting parameter, w, refined to 0.59(14) which produces a composition $Fe_{1.7(4)}As_2$ in the iron arsenide layers. This composition has a large uncertainty, since the value is determined by refining the relative contributions of two very similar scattering paths, but is consistent with the composition $NaFe_{1.67}As_2$ derived by Friederichs *et al.*[94] by diffraction methods on a material that was more crystalline than that presented herein. This composition, in which the eight coordinate site is fully occupied by Na (*i.e.* $x = 0$ in the general formula $Na_{1-x}Fe_{2-y}As_2$) and the Fe site is deficient, is consistent with the oxidation state of +3 for iron deduced from the XANES results.

The evaluated parameters return chemically sensible values, given in Table 3.3. S_0^2 parameters are similar to those evaluated for NaFeAs. The Fe–As bond length is shown to shorten on deintercalation, consistent with Fe oxidation, and the Debye-Waller term to increase due to the presence of vacancies.

Table 3.3 Refined parameters from the EXAFS fitting of $NaFe_{1.7(4)}As_2$ Fe and As *K*-edges, alongside values from EXAFS fitting of the parent material NaFeAs and equivalent values obtained from Rietveld refinement against the powder X-ray diffraction (PXRD) pattern of the same sample.

	EXAFS		X-Ray Diffraction	
Parameter	$Na_{1-x}Fe_{2-y}As_2$	NaFeAs	$Na_{1-x}Fe_{2-y}As_2$	NaFeAs
S_0^2As	1.00000(2)	1.000(2)	-	-
S_0^2Fe	0.68(7)	0.67(4)	-	-
Lattice parameter *a* (Å)	-	-	3.818(4)	3.95273(4)
Lattice parameter *c* (Å)	-	-	12.34(3)	7.04717(1)
RFe-As (*N*=4) (Å)	2.38(1)	2.417(2)	2.38(4)	2.456(1)
σ^2Fe-As (*N*=4) (Å^2)	0.006(1)	0.0056(2)		
RFe-As (*N*=3) (Å)	2.24(2)	-	-	-
σ^2Fe-As (*N*=3) (Å^2)	0.010(2)	-	-	-
R As-As1 (Å)	3.17(4)	-	3.3(1)	4.987(3)
σ^2As-As1 (Å^2)	0.011(4)	-	-	-
R As-As2 (Å)	3.7(2)	3.88(3)	3.818(4)	3.95273(4)
σ^2As-As2 (Å^2)	0.04(6)	0.010(4)	-	-
R As-As3 (Å)	3.80(7)	3.96(3)	3.93(9)	4.040(3)
σ^2As-As3 (Å^2)	0.021(8)	0.006(2)		
R Fe-Fe1 (Å)	2.70(3)	2.773(6)	2.700(2)	2.7950(1)
σ^2Fe-Fe1 (Å^2)	0.016(4)	0.009(1)	-	-
As-Fe-As bond angle × 2 (°)	102(4) [a]	106.8(5) [a]	107(2)	107.15(7)
As-Fe-As bond angle × 4 (°)	106(2) [a]	110.0(5) [a]	111(2)	110.65(4)
R As-Na (Å)	3.2(2) [a]	3.05(3) and 3.12(4)	3.17(3)	2.958(2) and 3.161(5)

[a] Marked values are not modelled directly by EXAFS, but inferred from the relevant scattering path lengths, and crystallographic unit cell.

3.5 Discussion and conclusions

Oxidative deintercalation of sodium from NaFeAs using iodine in a dry THF solution produces rather poorly crystalline materials as a consequence of the poor size match between the small sodium cation and the eight-coordinate site of the $ThCr_2Si_2$ structure type which the product material adopts. The results of EXAFS measurements at the Fe and As *K*-edges can only be interpreted using a structural model in which significant amounts of Fe are also deintercalated from NaFeAs so that approximately 40% of the As atoms are surrounded by 3 Fe atoms instead of 4. This is consistent with the XANES measurements at the Fe *K*-edge which show oxidation of Fe to the +3 oxidation state and the analysis by Friederichs *et al.*[94] who used Rietveld refinement against X-ray powder diffraction data and energy dispersive X-ray analysis to deduce a composition $NaFe_{1.67}As_2$ for the products of deintercalation obtained using a similar synthetic method.

Analogues of this deficient $ThCr_2Si_2$-type system are afforded by the $A_{1-x}Fe_{2-y}Se_2$ series (A = K, Rb, Cs; $x \approx 0.2$; $y \approx 0.4$) and EXAFS measurements of some of these materials reveal comparable behaviour to that of $NaFe_{2-y}As_2$ presented herein.[128,129] Measurement of the Fe *K*-edge EXAFS on a related series of compounds of composition $Li_{1-x}Fe_x(OH)Fe_{1-y}Se$, synthesised by Hualei Sun and Genevieve Allcroft, has been able to show that the degree of disorder in the local coordination environment scales with the degree of iron vacancies in the anti-PbO FeSe layer. The level of disorder in the local coordination environment about iron observed in $NaFe_{2-y}As_2$ closely resembles that in $K_{0.8}Fe_{1.6}Se_2$, which is further qualitative evidence that the number of iron vacancies on $NaFe_{2-y}As_2$ is large.

This deintercalate synthesized by oxidation with iodine solution has a much higher oxidation state for iron than other iron-based superconductors, where typically the iron valence ranges between extremes of +1.5 and +2.5 and known examples of optimal doping are typically around +1.9 for electron-doped materials (*e.g.* for $LaFeAsO_{0.88}F_{0.12}$[41]) and +2.2 for the hole-doped materials (*e.g.* for $K_{0.4}Ba_{0.6}Fe_2As_2$).[49]

While $NaFe_{1.67}As_2$ would appear to lie outside the range of superconductivity, the sample studied in this work derived from stoichiometric NaFeAs, like that of Friederichs *et al.*,[94] does exhibit superconductivity but with a superconducting volume fraction derived from the ZFC susceptibility measurement of only 7 % (Friederichs *et al.* reported a volume fraction of about 20%).[94] The investigation of the substitution of Fe by Co shows that this suppresses the superconductivity altogether in the deintercalated products. The complete suppression of superconductivity on cobalt doping may be a consequence of introducing further disorder in these systems.

In the better-investigated $K_{1-x}Fe_{2-y}Se_2$ series ($x \approx 0.2$; $y \approx 0.4$), and analogues with Rb, Cs in place of K, an inhomogeneous phase distribution is well established, with some samples exhibiting superconductivity[84] and some not.[79] Several investigations[80,84,131–134] have shown that a portion of the material with a composition around $A_{0.3}Fe_2Se_2$ (A = K, Rb, Cs) is responsible for the superconducting properties of the samples. A similar scenario may explain the appearance of superconductivity with a small, and variable, volume fraction in these $NaFe_{2-y}As_2$ analogues: regions of the sample where $y \approx 0$ and the Fe oxidation state is lower than average may be the superconducting regions. X-ray absorption spectroscopy and X-ray diffraction both primarily characterise the most numerous environments in the sample, hence it cannot be ruled out that superconductivity only occurs in small domains that have not been resolved by these measurements.

Work by other groups suggests that other deintercalate products with stoichiometries closer to $NaFe_2As_2$ can be synthesised by oxidative deintercalation. Gooch *et al.*[92] used an unspecified ionic liquid to produce a product described as $NaFe_2As_2$ with an onset of superconductivity at 25 K. Todorov *et al.*[93] describe the 25 K superconductor as arising from a $Na_{1-x}FeAs$ phase which still has the anti-PbFCl structure and which forms prior to the $NaFe_2As_2$ phase when oxidation is performed using water. These are evidently different from the samples described here which resemble those prepared by Friederichs *et al.*,[94] and further investigation of the phase field is required.

Chapter 4

4. Sodium and ammonia intercalated iron selenide superconductors

4.1 Chapter introduction

At first glance, sodium and ammonia intercalated iron selenide is quite similar to its lithium cousin described in section 1.4.5, page 24: it has a similar *I*4*/mmm* unit cell with the slightly larger volume of 250 Å^3 versus 243 Å^3 and the material typically exhibits slightly higher T_c of 45(1) K *vs.* 43(1) K. However, further structural defects lead to a more complicated system, and to understand the sodium and ammonia intercalates of iron selenide, it is convenient to first compare with the lithium and ammonia intercalated phases.

4.1.1 Lithium and ammonia intercalation into iron selenide

In an effort to understand the mechanism of the intercalation of lithium and ammonia into iron selenide and identify any intermediate phases that may occur, an experiment on beamline I12 at Diamond Light Source was devised to probe the products as they form by performing powder X-ray diffraction *in-situ* during the reaction.[135] The experiment schematic is shown in Figure 4.1, the penetrating high energy X-rays available on I12 allow appreciable diffraction intensity to be obtained through the thick walled amorphous glass reaction vessel and liquid coolant.

In an argon-filled, dry glovebox, ~ 4 mg of Li were placed at the bottom of an 18 mm *o.d.*, 14 mm *i.d.* Pyrex ampoule. ~150 mg of FeSe were loaded into the side arm not in contact with the lithium metal, and the ampoule was sealed with a High Performance Rotaflo® Teflon valve. Connected to an exterior Schlenk line, the bottom of the Pyrex ampoule was placed in liquid nitrogen and ~3-5 ml of NH_3 were condensed onto the alkali metal. Once the required volume of NH_3 was condensed, the ampoule was sealed at the Teflon tap and the solid NH_3 was allowed to melt at -78 °C in a CO_2-isopropanol cooling bath. The sealed ampoule was transported to the beamline, keeping the solution separate from the solid FeSe. The ampoule was clamped to a remote-controlled rotation stage, such that the FeSe in the side arm could be tipped into the solution remotely. With the Li/NH_3 solution stirring, the solution was exposed to a monochromatic ~80 keV X-ray beam and diffraction patterns were collected continuously as the FeSe in the side arm was tipped into the solution.

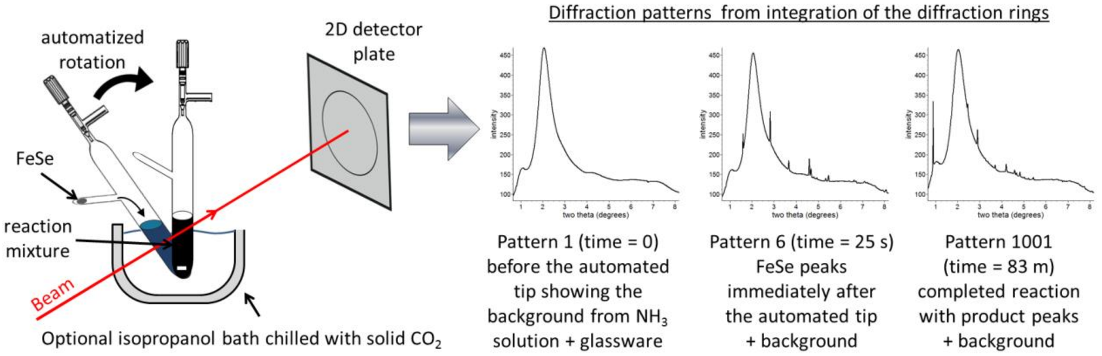

Figure 4.1 Experimental set up for measuring the intercalation of alkali metals and ammonia into iron selenide *in-situ* using powder X-ray diffraction conducted on I12 at Diamond Light Source.

The reaction was performed both at room temperature and with a -78 °C isopropanol-dry ice cooling bath in a borosilicate dewar. When the reaction was performed at -78 °C the reaction proceeded over the course of about 3 hours and no crystalline intermediate peaks were observed. It was found that the total intensity observed during a halfway point of the reaction is lower than would expected if there were a straight forward conversion indicating the presence of a non-crystalline intermediate. This was followed by mapping the integrated intensity of the starting material and product (001) peaks as a proportion of their maxima in the reaction over the course of the reaction, defining the level of conversion from the starting material to product, α, as:

$$\boldsymbol{\alpha(t) = \frac{I_t}{I_{max}}} \qquad \textbf{Equation 4.1}$$

In a reaction involving a straight conversion from one crystalline phase to another the starting material and product $\alpha(t)$ will cross when both $\alpha = 0.5$.[136] When the reaction was performed at room temperature, it took only around 3 minutes. Two unindexed peaks from neither the starting material nor product appeared over the course of the room temperature reaction, indicating the presence of a crystalline intermediate, but two peaks alone were insufficient to characterise the phase.

Rietveld refinement of the final product in the *in-situ* powder X-ray diffraction experiment revealed that the lithium- ammonia- intercalates of FeSe also exist in ‘ammonia-rich’ materials containing an additional ammonia moiety between the iron selenide layers whilst in an ammonia solution. The materials previously described as the products of the reaction[89–91] are in-fact ‘ammonia-poor’ phases, which are the decomposition product of the ammonia-rich phases, obtained in the normal course of removal of the ammonia solvent to produce dry solid products. The absorption and desorption of ammonia from the lithium- ammonia- intercalate was shown to be a reversible process by exposing an ammonia-poor phase to NH_3 vapour, forming the ammonia-rich phase, followed by exposure to a dynamic vacuum returning the ammonia-poor phase, shown in Figure 4.2. This cycling was followed using *in-situ* powder neutron diffraction of a deuterated sample performed on the WISH diffractometer at ISIS and by absorption isotherm at 260 K using an automated gas sorption analyser. The deuterated ammonia-rich lithium intercalate was refined to have the formula $Li_{0.6(1)}(ND_{2.7(1)})_{1.7(1)}Fe_2Se_2$.

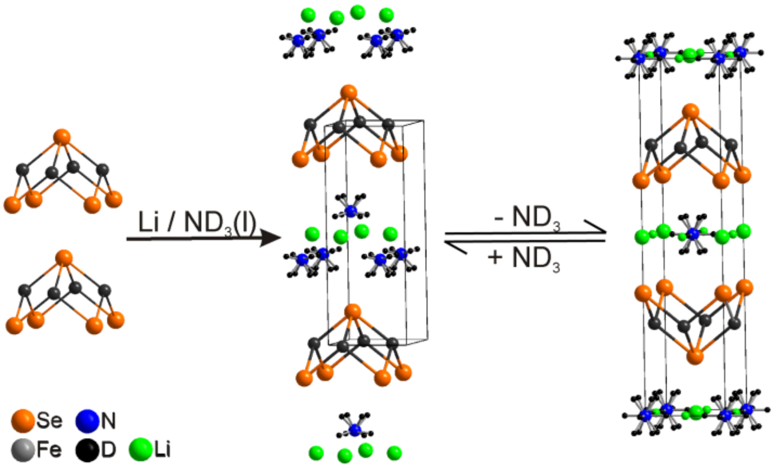

Figure 4.2 Schematic for the intercalation of lithium and ammonia into iron selenide and reversible conversion between the ammonia-rich and ammonia-poor phases, Figure is taken from reference 135**.**

4.1.2 Sodium and ammonia intercalates of iron selenide

The sodium-ammonia intercalate of iron selenide was reported with a T_c of 46 K, the highest of the series.[89] Guo *et al.* studied the intercalation of Na and NH_3 into a series of sulphur substituted compounds $FeSe_{1-z}S_z$, and were able to identify not only an ammonia-rich and ammonia-poor intercalate phases, but also apparently an ammonia-free phase containing only sodium in the FeSe interlayer space.[137] Guo *et al.* were able to perform Rietveld refinement against laboratory powder X-ray diffraction patterns to solve the structures of the ammonia-free and ammonia-poor phases, but were unable to stabilise a phase pure or majority phase ammonia-rich structure for a diffraction experiment. For the pure selenide samples: the three phases were reported with interlayer separations of 6.83, 8.71, and 11.07 Å, in order of increasing ammonia content. Compositions were given for these phases as $Na_{0.65(1)}Fe_{1.93(1)}Se_2$ for the NH_3-free phase, $Na_{0.80(4)}(NH_3)_{0.6(1)}Fe_{1.86(1)}Se_2$ for the NH_3-poor phase, and an undetermined composition for the NH_3-rich phase, assigning T_cs to these phases of 37 K, 45 K, and 42 K, respectively. Sulphur substitution on the selenium site in the intercalates $Na_x(NH_3)_yFeSe_{1-z}S_z$ was found to steadily lower T_c as z is raised for both the ammonia-free and ammonia-poor phases, in line with the observation that the iron sulphides are not known to show high T_c superconductivity.

The lithium and ammonia intercalated phase diagram is clear cut: under partial pressure of ammonia there is a sharp transition to the ammonia-rich phase and on application of a dynamic vacuum there is an equally sharp transition to the ammonia-poor phase. As the work described in this chapter shows, however the sodium and ammonia intercalated phase diagram is complicated by the appearance of one or more competing phases along with the ammonia-poor phase on application of dynamic vacuum to obtain the dry product. Isolation of the pure 45 K superconducting ammonia-poor phase relies on striking a balance to avoid the formation of phases with differing amounts of ammonia intercalated.

4.1.3 Studying solid-state reaction kinetics with diffraction

The reaction kinetics of the intercalation of sodium and ammonia into iron selenide has been studied in this chapter and have been characterised using the following theory. The rates of most solid-state reactions are generally described by an Arrhenius type equation:

$$\frac{\mathrm{d}\alpha}{\mathrm{d}t} = Ae^{-(E_a/RT)}f(\alpha) \qquad \text{Equation 4.2}$$

where A is the pre-exponential factor, E_a the activation energy, R the gas constant, T the absolute temperature, $f(\alpha)$ is some reaction model, α the conversion fraction, and t the time. There are many different reaction kinetic models, which may be grouped on the graphical shape of their isothermal curves (α *vs.* t) into acceleratory, decelerator, linear, or sigmoidal models. Most reactions in the solid-state follow a sigmoidal (bell shaped α *vs.* t curve) with a general formula:

$$f(\alpha) = \frac{1}{1+e^{-\alpha}} \qquad \text{Equation 4.3}$$

and the model proposed by Avrami and Erofe'ev, presented below is the most widely applied.

4.1.3.1 Avrami-Erofe'ev kinetics

Nucleation is the formation of a new product phase at the reactive points (nucleation sites) in the lattice of the reactant. The growth rate is the rate of growth of the radius of the product nuclei. Avrami's work uses the power law $\alpha = kt^n$, which implies that the nucleation rate will grow continuously to some power and nucleus growth is constant with time. However, two factors may lead to a reduction in the conversion: coalescence, which is the loss of reaction interface when two or more growing nuclei merge; and ingestion, the potential nucleation sites are blocked by another growing nucleus. To deal with this issue Avrami's work considers $\alpha' = kt^n$, where α' is the extended conversion fraction that neglects these factors which may be related to the true conversion fraction by:

$$\boldsymbol{\alpha' = -\ln(1-\alpha)} \qquad \textbf{Equation 4.4}$$

Substitution of the power law into, and rearrangement of this equation gives:

$$\boldsymbol{[-\ln(1-\alpha)]^{1/n} = k(t-t_0)} \qquad \textbf{Equation 4.5}$$

where t_0 is an optional term that accounts for a time zero-error.

Erofe'ev independently derived a special case for Equation 4.5 where $n = 3$ by following a different approach, hence Equation 4.5 was attributed to both Avrami and Erofe'ev. This equation has been successfully applied to a variety of solid-state processes including decompositions,[138,139] phase transformations,[140,141] crystallisations,[142] and intercalation reactions.[143] For these systems it is generally found to be most applicable in the range $0.15 < \alpha < 0.5$.

The exponent, n, is the sum of the number of steps involved in the formation of the nucleus, β (usually 0 or 1 with the former implying instantaneous nucleation), and the number of dimensions in which the nuclei grow, λ.

Incorporation of a diffusion term in nucleation and growth reaction models was proposed by Hulbert.[144] The overall rate expressions have the same format as the Avrami-Erofe'ev equation:

$$\boldsymbol{[-\ln(1-\alpha)]^{1/m} = k(t-t_0)} \qquad \textbf{Equation 4.6}$$

with $m = \beta + \lambda/2$. It is not always possible to identify m in a kinetic model as different values of β and λ can give the same result as below shown in Table 4.1.

Table 4.1 Nuclei growth models for solid-state reactions based on the Avrami-Erofe'ev equation. These models are also known as the JMAEK models which stands for Johnson, Mehl, Avrami, Erofe'ev, and Kholmogrov, referring to the researchers who contributed to their development.

Dimension of growth (λ)	Nucleation rate (β)	Exponent value	
		Phase Boundary controlled (n)	Diffusion controlled (m)
1	instantaneous	1	0.5
	decelerator	1-2	0.5-1.5
	constant	2	1.5
2	instantaneous	2	1
	decelerator	2-3	1-2
	constant	3	2
3	instantaneous	3	1.5
	decelerator	3-4	1.5-2.5
	constant	4	2.5

The value of the exponent is most accurately obtained from a straight line plot, known as a Sharp-Hancock plot, rather than from the α-curve and involves plotting ln(-ln(1-α)) *vs.* ln(t) as

$$\boldsymbol{ln}[-\boldsymbol{ln}(\mathbf{1}-\boldsymbol{\alpha})] = \boldsymbol{n}\ln \boldsymbol{t} + \boldsymbol{n}\ln \boldsymbol{k} \qquad \text{Equation 4.7}$$

This plot has gradient equal to *n* and *y*-intercept equal to *n*ln*k*. The linearity of the plot demonstrates the validity of the model against the experimental data.

4.2 Ammonia-rich sodium intercalated iron selenide

4.2.1 Studying the reaction *in-situ* using powder X-ray diffraction

Following the discovery of the ammonia-rich lithium intercalate of iron selenide, a follow-up experiment on beamline I12 at Diamond Light Source was scheduled to investigate the sodium, potassium, and other alkali and alkaline earth intercalates. The experimental setup was largely the same as described in the introduction to this chapter (section 4.1.1), with the addition of a chiller coil replacing dry ice as the coolant for the isopropanol bath, this allowed more precise control and stability in the temperature of the solution. In order to accommodate the chiller coil, the borosilicate dewar vessel had to be replaced by a larger plastic container. In the experimental setup, the centre of the beam was set to pass through the top of a stirring solution of sodium in ammonia (~0.3 mol dm^{-3}) in the Schlenk flask, whilst the iron selenide powder waited in the side arm. Diffraction pattern collection was started in an appropriate time step for the expected speed of the reaction, collecting one pattern every 0.5-5 seconds. A mechanical rotation tipped 150 mg of FeSe into the stirring Na/NH$_3$ solution, and the subsequent reaction could be observed through the changing diffraction pattern. This process was successfully repeated at reaction temperatures of -53, -45, -20, -10, 0, and 25 °C, a stoichiometric ratio of 1 Na : 2 FeSe was used in each of these reactions. Post reaction the Schlenk tube was moved to a Schlenk line in the fume hood and the ammonia solution was allowed to evaporate under a flow of argon gas. Once no more liquid ammonia was present, the product was placed under dynamic vacuum before extraction in an argon-filled, dry glovebox.

The data were collected using a Pixium® image plate detector. The diffraction rings in the collected data were integrated to produce a one dimensional pattern using the software suite FIT2D.[145] A CeO_2 standard was used to calibrate the wavelength, detector distance, and detector deviation from vertical alignment (yaw and roll). An additional background subtraction was performed on a copy of the integrated data using a program written by Dr Andrew Jupe, which runs the Bruckner background removal procedure.[146] The background subtracted data will be used in this thesis for graphical representation of the data only, Rietveld refinement and peak fitting of the integrated diffraction patterns was performed on the uncorrected data using the refinement program TOPAS version 5.[113]

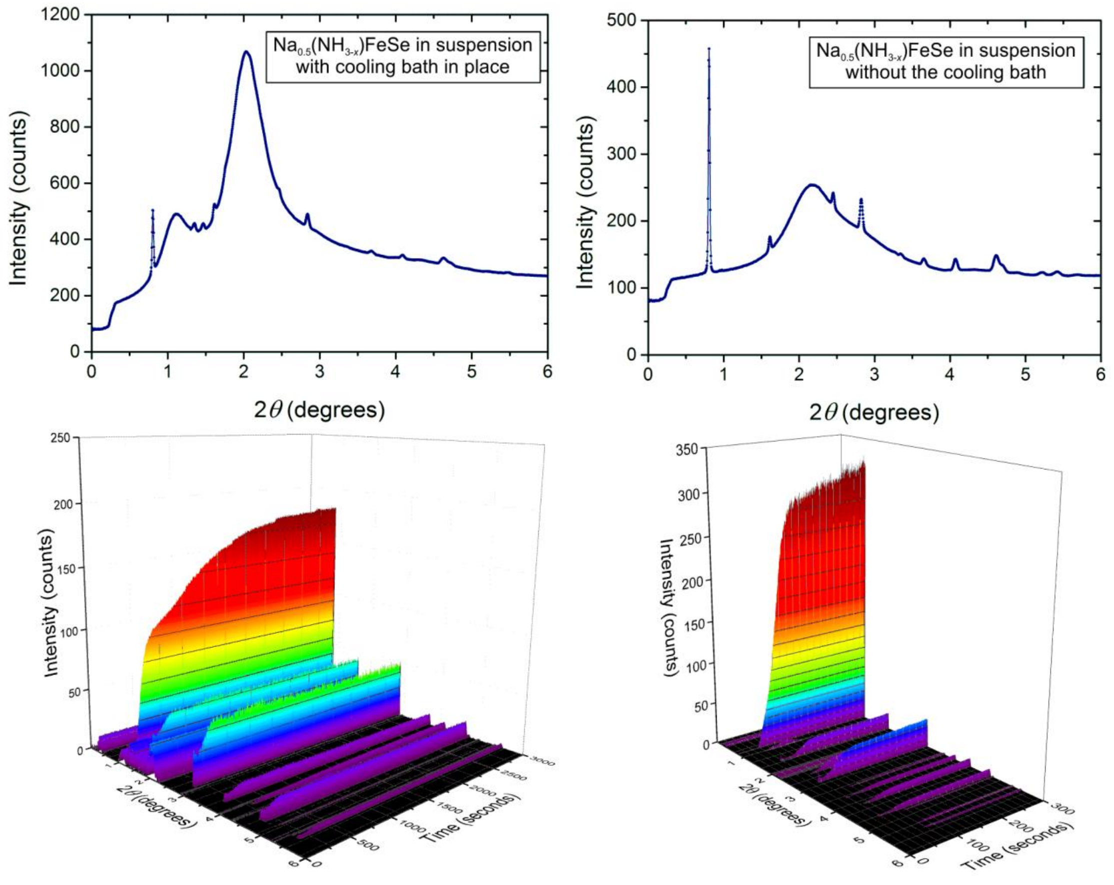

Figure 4.3 Above: typical diffraction patterns of the final product of the sodium intercalation in solution with (left) and without (right) the cooling bath, showing the difference in background and peak intensity. Below are surface plots of the background subtracted powder patterns for each case.

The reaction rate was observed to scale with reaction temperature (see section 4.2.1.1). At each temperature the observed final product was the same, having a *P4/nmm* unit cell with dimensions of around 3.80 × 3.80 × 11 Å, slightly larger than for the corresponding ammonia-rich lithium intercalate. In the synthesis at room temperature, a single additional peak at 8.65 Å in *d*-spacing was observed which corresponds to the (002) reflection of the ammonia-poor phase, this was not observed at lower temperature, although may have been obscured by the higher background. No other intermediate peaks were observed.

Rietveld refinement against the final diffraction pattern of the reaction of Na and NH_3 with FeSe at room temperature is shown in Figure 4.4. The background has been refined using 15 parameters: A lognormal distribution curve which uses three parameters (the mean and the standard deviation of the distribution, and a scaling parameter) that approximates the large broad feature with its maximum at 2.1 ° and tail at higher angles, and a 12th order Chebyshev polynomial to account for the additional curvature. Peakshapes were modelled with two Gaussian and two Lorentzian parameters, thermal displacements were refined isotropically with those of sodium and nitrogen refined to be the same as those of Se. Hydrogen atoms were omitted. A good fit is achieved to using the model shown, which is structurally similar to that of the ammonia-rich lithium intercalate.[135]

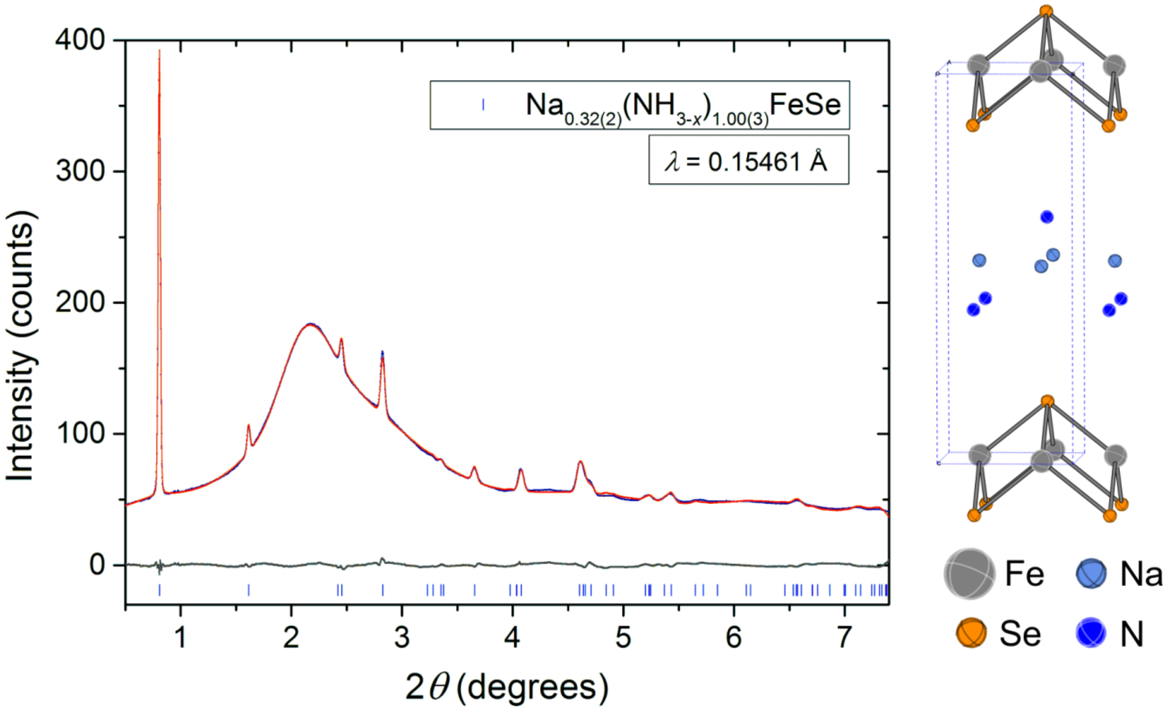

Figure 4.4 Rietveld refinement of the ammonia-rich structure against the final diffraction pattern of a reaction of Na and ammonia with FeSe at room temperature, *Rwp (%)* = 0.727. the unit cell is *I4/mmm* with lattice parameters of 3.822(3) and 10.9770(4) Å for *a* and *c*, respectively.

4.2.1.1 Kinetic modelling of the reaction rate

An unfortunate coincidence largely inhibits the amount of information that can be extracted from the variable temperature *in-situ* experiment: the iron selenide starting material has a unit cell with *P4/nmm* symmetry with an *a* cell parameter (3.774 Å) that is similar to that of the product and a *c* cell parameter that is almost exactly half (5.51 Å). The result of this coincidence is that only the (001) reflection of the product has a unique position in the entire pattern, all other peaks from the product overlap in position with reflections from the starting material, which itself has no unique peaks in the pattern.

With the restrictions on available information from peak overlap, the reaction conversion may still be followed by modelling the intensity of the (001) peak as a function of time, and estimating the ratio of conversion to the product at a given time, α(t), to be equal to the product (001) peak intensity at that time divided by the intensity of the (001) at the end of the reaction (Equation 4.1). Peak intensities were modelled for each diffraction pattern in a batch mode operation using a total of 6 parameters: a 3rd order Chebyshev polynomial to model the background and a parameter each for the peak position, intensity, and full-width-half-maximum. The peakshape could be modelled with a single Gaussian term for all temperatures. Integrated intensities against time are given for the reaction at each temperature in Figure 4.5.

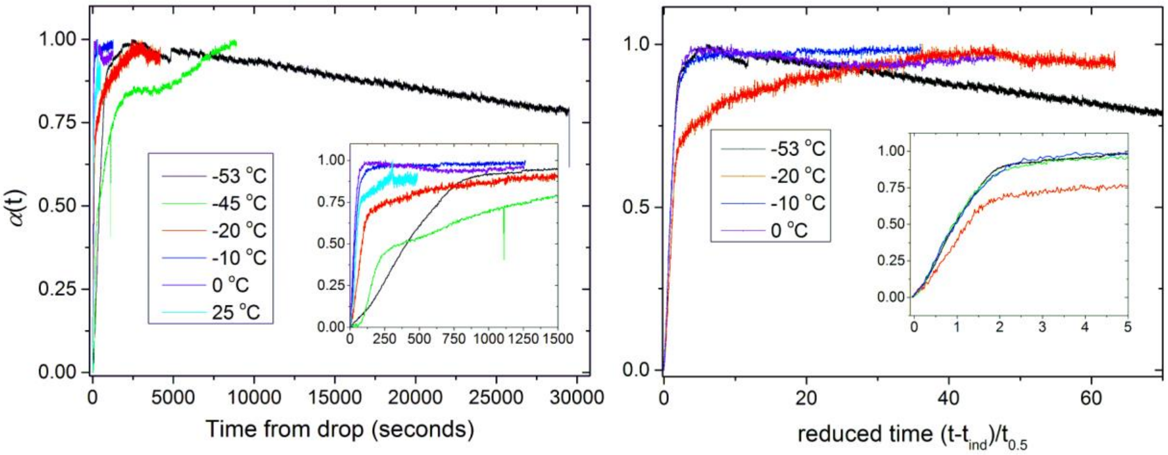

Figure 4.5 Plots of *α vs.* time (left) and *α vs.* reduced time (right) for the intercalation of sodium and ammonia into iron selenide at various temperatures. Insets in the bottom right corner of each plot show the profiles at the start of the reaction.

Anomalous results are observed at room temperature and -45 °C .The reaction at room temperature was performed outside of the isopropanol bath, as such was under different conditions and may not have had time to thermalize completely, the reaction at -45 °C has a very different profile to the other reactions, A plausible explanation is that the tipping of the iron selenide into the solution did not proceed smoothly and some powder stuck to the side of the tube, washing down slowly into the solution.

The parameter "reduced time" can be defined using the following formula:

$$\textbf{Reduced time} = \frac{t-t_{ind}}{t_{0.5}} \qquad \textbf{Equation 4.8}$$

Where t_{ind} is the time taken for the reaction to begin and $t_{0.5}$ is the time at $\alpha = 0.5$. If plots of reduced time *vs.* α at different temperatures are superimposable it is a strong indicator that the reaction proceeds via the same mechanism (assuming all other parameters controlling the reaction rate are constant). In the inset of Figure 4.5 it can be seen that the plots α *vs.* reduced time for reactions at -53, -10, and 0 °C are superimposable up until the point where $\alpha = 1$, however the reaction at -20 °C proceeds more slowly to the maximum in α which may again be due to a non-instantaneous addition of all the FeSe to the solution. In each case after the reaction has seemingly completed ($\alpha = 1$) the reaction profiles diverge as the (001) reflection of the "ammonia-rich" phase continues to develop differently at different temperatures.

As described in section 4.1.3.1, the Avarmi-Erofe'ev model for the kinetics of solid state reactions is a widely applied consideration of reaction rate and nucleation growth mechanism, using equation 4.5: $([-\ln(1-\alpha)]^{1/n} = kt)$. The power exponent in this equation, n, is the sum of the number of steps involved in forming the nucleus, β, and the number of dimensions in which the nuclei grow, λ. The exponent, n, and the rate constant k can be extracted from equation 4.7 using a Sharp-Hancock plot of $\ln\left[-\ln\left(1-\alpha\right)\right]$ against $\ln t$ as shown in Figure 4.6, which gives a gradient of n and a y-intercept of $n \ln k$.

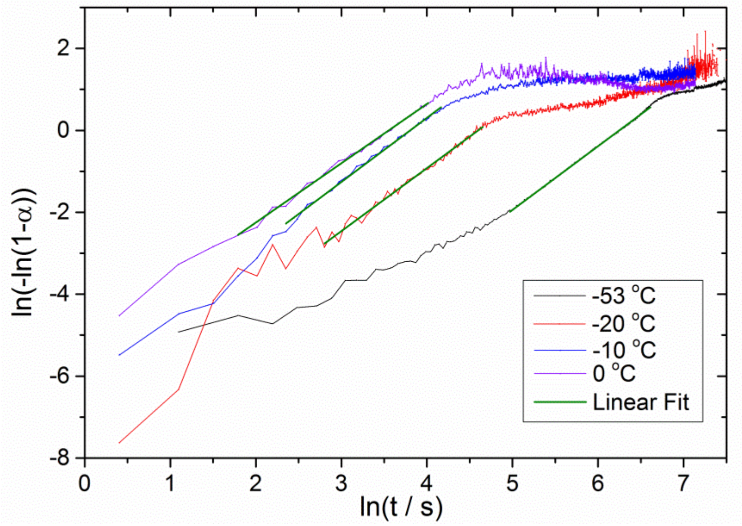

Figure 4.6 Sharp-Hancock plots to the linear region of the intercalation of sodium and ammonia into iron selenide at various temperatures. The lines are least-squares fits to ln(-ln(1- α)) = $n$ln(k) + $n$ln(t).

Table 4.2 Kinetic parameters for the fitting of the reaction conversion ratio, *α*, to a refinable rate constant, *k*, at four temperatures, using equation 4.7.

Temperature / °C	n	k / × 10^{-2} s^{-1}
0	1.45(1)	2.9(1)
-10	1.56(2)	2.2(1)
-20	1.54(2)	1.01(8)
-53	1.39(1)	0.18(1)

The value of the pre-exponent, n, is ambiguous in the Avarmi-Erofe'ev model, because different values of β and λ can give rise to the same exponent value, and are affected by whether the reaction rate is phase boundary controlled or diffusion controlled (see Table 4.2). A pre-exponent value of ~1.5 is indicative of nuclei growth in one or two dimensions.

The temperature dependence of the reaction rate has been used to calculate the activation energy for the reaction using the Arrhenius equation:

$$\boldsymbol{k = Ae^{\frac{-E_a}{RT}}}$$ **Equation 4. 9**

An activation energy for the reaction can be evaluated as 26.3 ± 1.6 kJ mol^{-1} from a plot of ln(k) against 1/T is given in Figure 4.7.

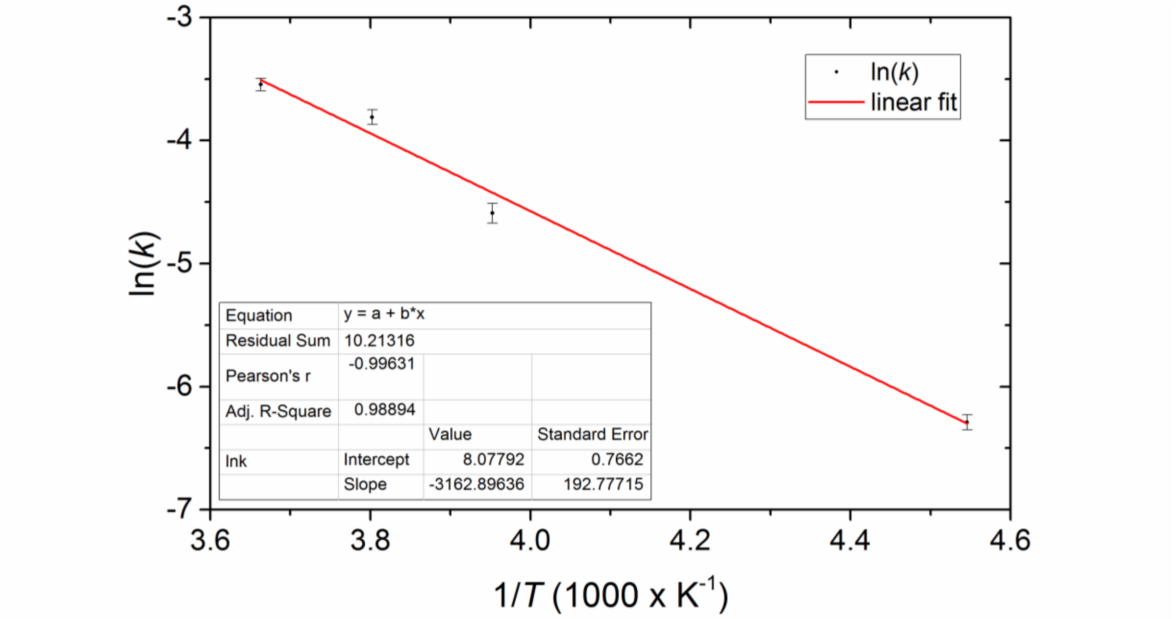

Figure 4.7 Arrhenius plot showing the relationship between the rate constant *k* and temperature for the formation of ammonia-rich sodium intercalated iron selenide from the iron selenide starting material.

4.2.1.2 Post-synthesis sample development

The reaction of Na and NH_3 with FeSe performed at -53 °C was allowed to proceed for 8 hours overnight, over which time it was observed that the maximum in α was achieved after ~1 hour, after which time the peak continued to develop in intensity and position.

Figure 4.8 shows the integrated intensity of the peak slowly lessens by ~20 % over 7 hours, the full-width-half-maximum broadens by ~11%, and the position shifts to lower angle as the interlayer FeSe spacing increases by ~0.1 Å. Comparing the patterns just after completion and 7 hours on we see that the background in both patterns is close to identical indicating that the effect is not arising from a slow un-tuning of the monochromator nor other instrument or beam effect.

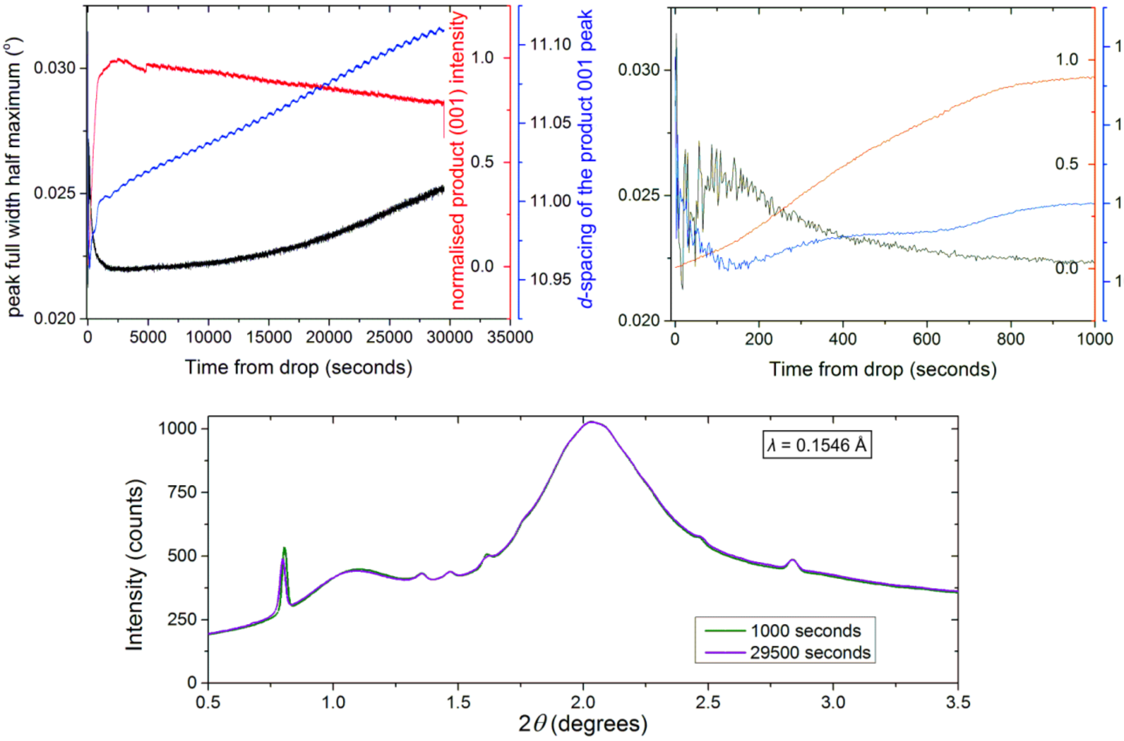

Figure 4.8 Top: modelling of the (001) reflection from the ammonia-rich product from the reaction at -53 °C, plotting normalised intensity (red), *d*-spacing (blue) and full-width-half-maximum (black) as a function of reaction time, with a close up of the first 1000 seconds on plotted on the right. Bottom: overlay of diffraction patterns of the ammonia-rich product phase after 30 minutes and 8 hours stirring in solution at -53 °C.

A rise in the interlayer FeSe spacing is indicative of a further intercalation of either Na or NH_3 into the interlayer. The structure factor, F_{001}, for the ammonia-rich structure described later in section 4.2.2 is given by:

$$\boldsymbol{F_{001} = f_{Fe}\cos(0) + f_{Se}\cos 2\pi(0.131) + f_N \cos 2\pi(0.384) + f_{Na}\cos 2\pi(0.5)}$$

Equation 4.10

which reduces to:

$$\boldsymbol{F_{001} = f_{Fe} + 0.68 f_{Se} - 0.75 f_N - f_{Na}}$$

Equation 4.11

Since the minor scatterers N and Na are both out of phase with the major scatterers, an increase in the occupancy of either will lower the intensity of the (001). Neutron refinement of the nitrogen occupancy in the ammonia-rich phase described later in section 4.2.2 returns a value of 0.89 for a phase with *c* lattice parameter of 10.99 Å, similar to that observed in the initial product here. Figure 4.9 shows that increasing only the nitrogen occupancy to a value of 1 has only a minor effect on the intensity of the (001), not enough to explain the observed 20 % drop in intensity. Enough sodium is supplied in the reaction to form a product with sodium site occupancy of 0.5 and so an increase in sodium content may be observed in this system. This analysis suggests that additional Na is entering the system, with or without additional NH_3. This explanation is not conclusive; an alternative could be a slow redox process occurring with the iron in the interlayer space of the ammonia-rich phase that could cause a change in the Fe-Fe and Fe-Se distances, and Se-Fe-Se bond angles such that the thickness of the iron selenide layer is raised. This observation requires further investigation.

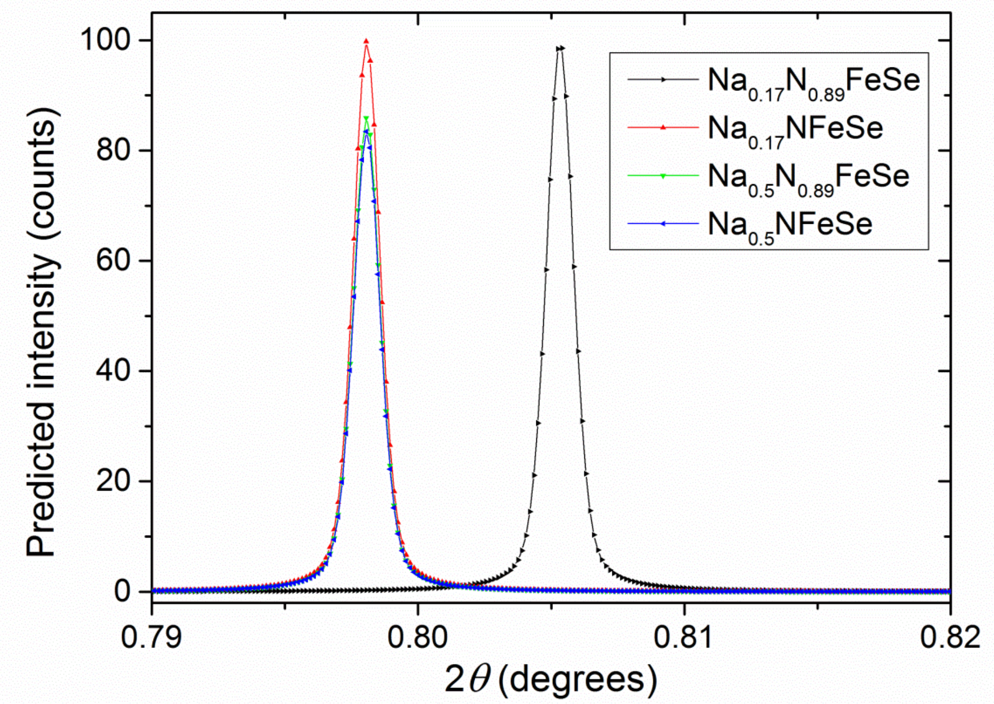

Figure 4.9 Simulated X-ray powder diffraction patterns (λ = 0.1546 Å) for the ammonia-rich intercalate based on the model given later in Table 4.3, with varied sodium and nitrogen content showing the effect of the occupancy of these site on the intensity of the (001) of the ammonia-rich phase.

4.2.2 Neutron powder diffraction

In order to determine the complete structure of the ammonia-rich intercalate, a neutron diffraction experiment was needed to identify the hydrogen atom positions and differentiate between isoelectronic Na^+ and N^{3-}. A high background is often obtained when using hydrogen containing samples due to hydrogen's large incoherent scattering length, and so a deuterated sample (SXC090) was prepared. Pieces of Na (Alfa Aesar, 99.95 %)

were cut from lumps to remove the oxidised surface, inside an argon-filled, dry glovebox. The Na pieces were combined with iron selenide powder in a 1:2 ratio and placed in the bottom of a Schlenk tube with a Teflon coated stirrer bar, both of which had been stored in a 100 °C drying oven before use to remove surface bound moisture. The Schlenk tube was capped and sealed with a Young's tap, before transporting to a Schlenk line inside a fume hood. The Schlenk tube and an ND_3 cylinder were connected to the Schlenk line, then the line, connection tubing, and Schlenk tube were all evacuated. The Schlenk tube was chilled to -78 °C using a dry ice-isopropanol cooling bath, then the tap to the vacuum pump was closed and leaving the system under a static vacuum. With the tap to the vacuum closed, the ND_3 cylinder gradually opened, allowing ammonia to condense in the Schlenk tube. The pressure was followed using a mercury manometer, which also provided a potential escape for the ammonia in the case of pressure build up. Once around 50 ml of ND_3 were condensed, the ammonia cylinder was closed and the reaction was stirred for 2-5 hours before recapturing the ND_3 by cooling the ND_3 cylinder and warming the reaction vessel. Once all the liquid ND_3 had left the reaction vessel the ND_3 storage cylinder was closed and when the sample had reached room temperature, the Schlenk tube was evacuated under dynamic vacuum for 3 minutes before returning it to the glovebox.

In order to trap the ammonia-rich phase, the ammonia-poor dry product was re-exposed to an ND_3 atmosphere whilst inside a vanadium container before quickly sealing the can in a manner shown in Figure 4.10.

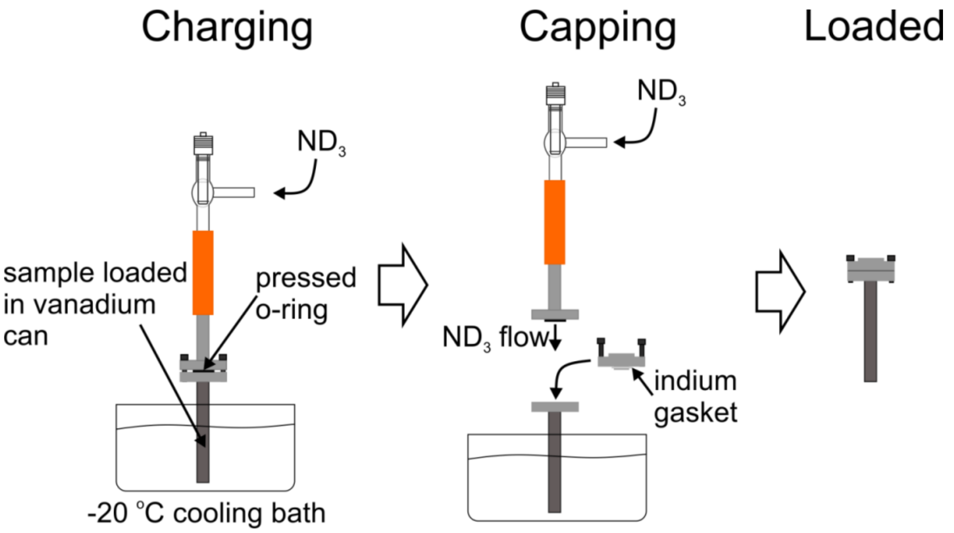

Figure 4.10 Schematic of charging of an ammonia-poor intercalate with ND_3 inside and a vanadium can for powder neutron diffraction. The loading setup was prepared in a glove box, sealed by means of a Young's tap and transferred to Schlenk line outside the glovebox. The sample is cooled to approximately -20 °C by adding small amounts of dry ice to an isopropanol bath in a controlled manner. The sample was exposed to ND_3 for approximately 2 hours before sealing the container.

Powder neutron diffraction was carried out on the HRPD diffractometer at ISIS neutron source. The sample was kept cold from loading to measurement: it was transported to the neutron facility in 0 °C container and transferred straight to a He-cooled cryostat at -20 °C. The sample was measured for 4 hours (160 μA) using the 30-130 ms window range, which provides the maximum flux and a total coverage between the three banks of reflections in a *d*-spacing range around 0.7 - 9 Å.

Rietveld refinement of the neutron powder diffraction pattern was carried out against all three detector banks (30 °, 90 °, 168 °) together. Refined structural parameters are given in and displays of the refinements are shown in Figure 4.11. The sample was modelled with three phases, the minority phases being the unreacted starting ammonia-poor intercalate at 3.1 % and elemental Fe at 2.3 % molar percent of the sample, vanadium peaks are also observed from the sample holder, these are fitted with a Pawley (structure independent) model. The structural parameters for the ammonia-poor phase were given strict limits based on the values given in section 4.3.1.

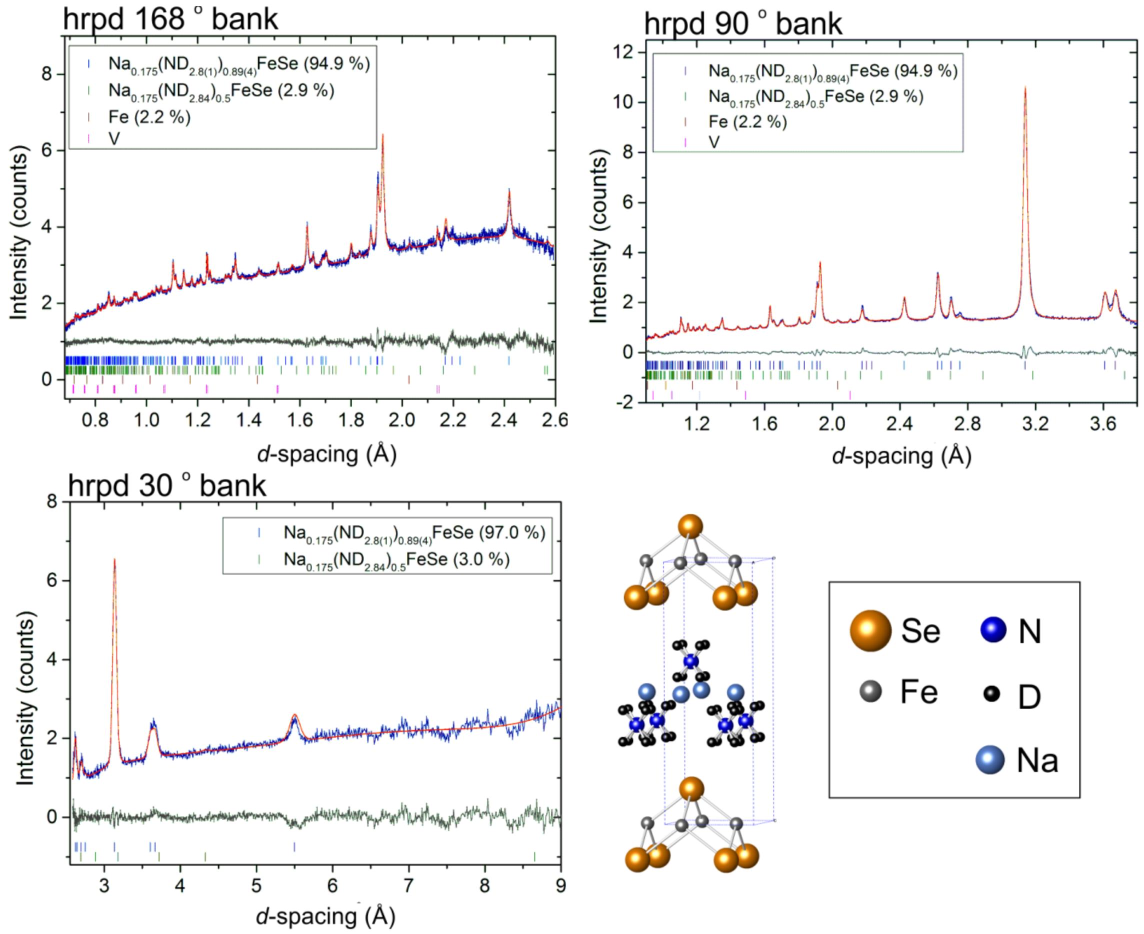

Figure 4.11 Rietveld refinement of the ammonia-rich phase of iron selenide against neutron powder diffraction patterns from HRPD's three detector banks with the refined structure presented at the bottom right.

Table 4.3 Rietveld refinement parameters for the ammonia-rich sodium intercalate of iron selenide corresponding to the fit of the powder neutron diffraction data from HRPD shown in Figure 4.11.

Temperature / K	250	***a* / Å**	3.8128(7)
Space group	*P4/nmm*	***c* / Å**	10.993(2)
origin choice	2		
R_{wp} / %	2.00	**V / Å^3**	159.82(7)
N-D1 distance / Å	0.971(9)	**N-D2 distance / Å**	0.94(1)
Fe-Se distance / Å	2.391(2)	**Se-Fe-Se (α) angle / °**	105.76(9)
D1-Se distance / Å	2.890(8)	**Se-Fe-Se (β) angle / °**	111.36(5)

atom	**site**	**x**	**y**	**z**	**Occupancy**	**U_{11} / Å^2 × 100**	**U_{33} / Å^2 × 100**
Fe	2*a*	0.750	0.250	0	1	0.00(4)	3.8(1)
Se	2*c*	0.250	0.250	0.1312(2)	1	1.08(7)	1.2(1)
N	2*c*	0.750	0.750	0.3827(5)	0.89(4)	9.5(3)[a]	
D1	8*j*	0.878(2)	0.878(2)	0.320(2)	0.373(9)	9.5(3)[a]	
D2	8*j*	0.878(2)	0.878(2)	0.441(2)	0.245(8)	9.5(3)[a]	
Na	2*b*	0.750	0.250	0.5	0.175(11)[b]	9.5(3)[a]	

[a] **These Debye-Waller terms were refined as a single value.**

[b] **constrained to a minimum value of 0.175 corresponding to the sodium occupancy observed later in Figure 4.13.**

Unconstrained refinement of the sodium content in this model gives an occupancy of 0.03(1), with an improvement of R_{wp} by 0.05 % relative to the reported value. The low dependence on the agreement factor with the sodium content arises from the relatively low scattering length of Na and correlations with the thermal displacement parameters. An interlamellar space of 11.0 Å is observed in this refinement, which is larger than that of the ammonia-rich lithium intercalate (10.5 Å). For comparison, this has a lithium occupancy of around 0.3 on the equivalent site. Although it is counter intuitive to suggest that this site being nearly vacant would cause an increased expansion in the interlayer, it is plausible that having less alkali metal causes the bonding in the interlayer to have more van der Waals character, which in turn is gives a larger interlayer space.

With such a small dependence of the agreement factor on sodium content, it is not possible to determine this accurately. A minimum limit on the sodium occupancy of 0.175 was applied to the refinement, which corresponds to the refined occupancy of an ammonia-poor intercalate described in the next section. Refined nitrogen and deuterium contents give a N : D ratio of 1 : 2.8(1), which indicates a mixture of ammonia and amide.

4.3 Ammonia-poor sodium intercalated iron selenide

4.3.1 The ammonia-rich to ammonia-poor phase transition

Following the *in-situ* measurements of the intercalation process on beamline I12, the reaction ampoule was moved to a fume hood and the ammonia solution was allowed to evaporate under a flow of argon gas. Once no more liquid ammonia was present the product was placed under dynamic vacuum for between one minute and one hour. Between these steps, the Schlenk tube was returned to the beamline and a single snapshot was taken of the product at that stage, to probe the process of de-ammoniation in these materials. The de-ammoniation process for one product under argon and after one minute of dynamic vacuum is shown in Figure 4.12, refinement parameters for the Rietveld fit are given in appendix IV, and several snapshot diffraction patterns following the de-ammoniation process over longer evacuation times on further samples are given in appendix VI. After removal of the liquid ammonia under an argon flow, the sample appears mostly converted to the ammonia-poor phase. All observed peaks in this diffraction pattern are predicted either from the poor or rich phases, however there are some mismatches in intensity, particularly the peak(s) around 2.80 ° (the 013 of the poor phase which overlaps with the 012 peak of the rich) and a satisfactory fit to the intensity cannot be made with a reasonable model for these two phases alone. Further degradation of the sample occurs upon exposure to vacuum: the peak at 0.81 ° (the 001 of the ammonia-rich phase) is no longer observed corresponding to the complete loss of the ammonia-rich phase. Along with this loss, the relative intensities of several peaks change, notably the peak at 2.80 ° becomes more intense with respect to the peak at 1.02 ° (the 002 of the ammonia-poor phase) which would be disproportionate if the pattern were simply to be interpreted as arising from the ammonia-poor phase. An additional peak at 1.30 ° (*d*-spacing of 6.85 Å) also appears, which is not predicted in the model.

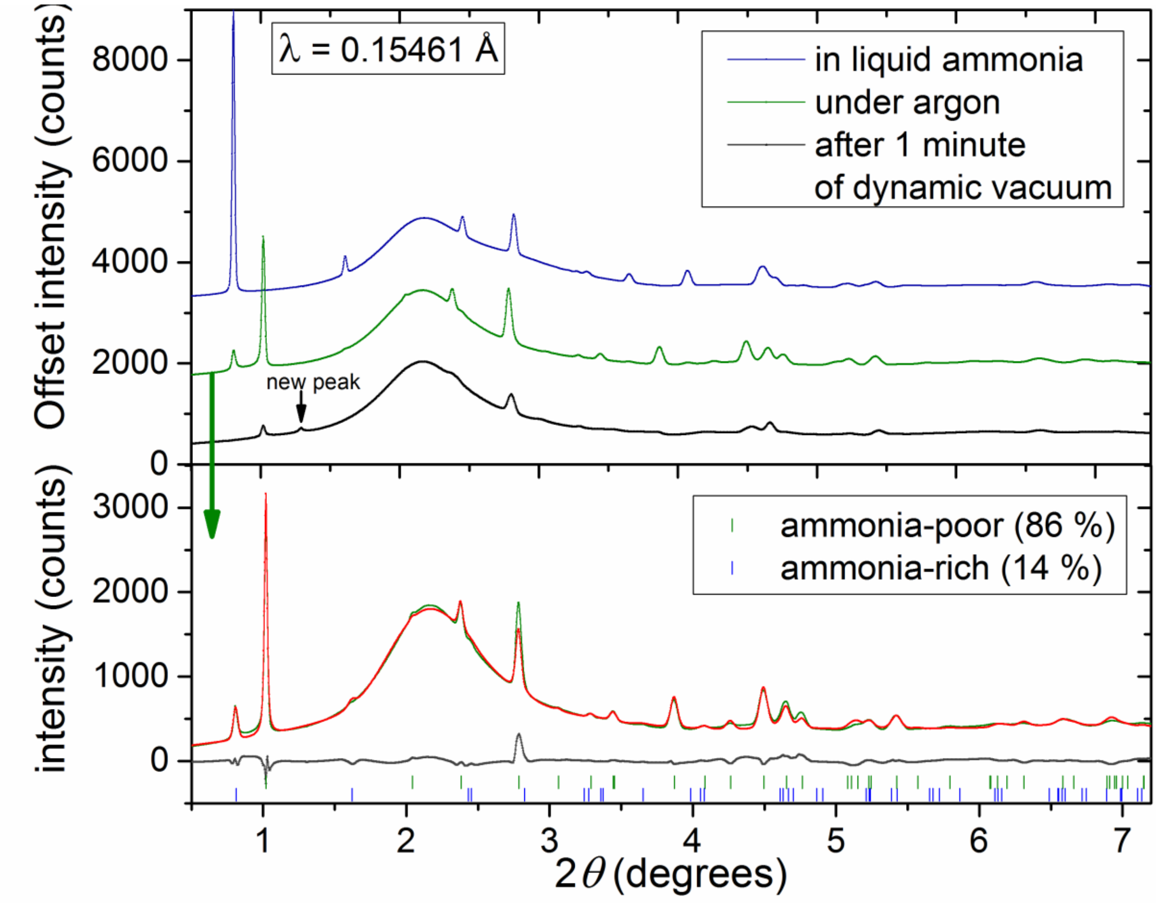

Figure 4.12 Top: diffraction patterns taken of a sodium-ammonia intercalated iron selenide in three environments. Bottom: Rietveld refinement against the sample under an argon atmosphere, having never been exposed to vacuum.

The conclusion from using X-ray diffraction to observe the post-reaction loss of ammonia from a sodium-ammonia intercalate of iron selenide is that upon replacement of the ammonia atmosphere with argon the ammonia-poor phase is formed along with a small amount of an unidentified phase, the strongest peak of which is located at 2.80 ° (*d*-spacing of 3.16 Å) accounting for the unmodelled intensity in the Rietveld refinement in Figure 4.12. When the product under argon is exposed to vacuum the ammonia-poor phase is further lost, and the unaccounted for minor phase becomes a larger contributor. A small additional peak at 1.30 ° (6.85 Å) also grows in under vacuum: this could be the (002) reflection of the ammonia-free phase as reported by Guo *et al.* or a peak from the unidentified phase. The peak at 2.80 °, however, where there appears to be unaccounted for intensity, is not a predicted reflection for the ammonia-free phase and so the pattern cannot be explained as a mixture of the ammonia-rich, ammonia-poor, and ammonia-free phases.

Fortuitously, from the reaction vessel that had been run at -53 °C once warmed to room temperature the ~4 ml of liquid ammonia evaporated slowly over the course ~10 hours through an imperfect seal at the lid. Once all the liquid ammonia had evaporated a diffraction pattern of the product was taken and showed a near perfect ammonia-poor phase, the result of which is shown in Figure 4.13, refined structural parameters are given in Table 4.4.

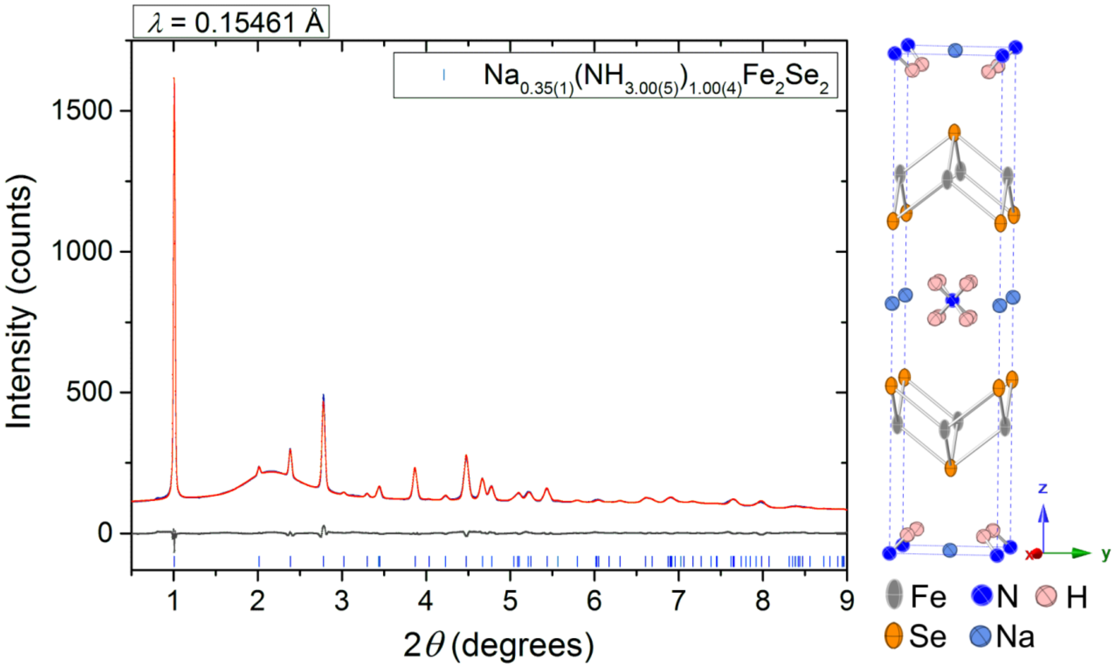

Figure 4.13 Rietveld refinement of the ammonia-poor intercalate of sodium iron selenide structure shown aside. Atoms are plotted with their refined thermal ellipsoids. The background was refined with a lognormal distribution curve which roughly covers the large broad feature with its peak at 2.1 ° and a 12th order Chebyshev polynomial to account for the additional curvature, peak-shapes were modelled with two Gaussian and two Lorentzian parameters.

The peak at 2.80 ° in Figure 4.13 is very slightly under-predicted indicating that the unidentified phase could be present, but only in a very low concentration. Hydrogen is a very weak scatterer of X-rays, and so it could not be refined in the structure, but does improve the fit when included at a chemically sensible position and occupancy in the unit cell (position in Table 4.4). The low scattering power of hydrogen and large correlations with nitrogen site occupancy lead to an unreliable determination of the ratio of ammonia and amide in the system, however correlations between refined structural parameters and the sodium occupancy are all below 16%, indicating that the sodium content has been reliably refined.

Upon exposure to air the sodium-intercalated iron selenide phases decompose to a poorly crystalline form of iron selenide as is shown in appendix V, therefore the leak at the Schlenk tube lid must have been enough to allow the high pressure out but not enough to let any appreciable amount of air in. Upon exposure of this sample to a vacuum, there is further development of the diffraction pattern producing asymmetric broadening of the peaks shown in appendix VI. These observations show that it is possible to form the ammonia-poor intercalate phase pure, however there is a facile transformation to one or more new phases if exposed to vacuum, or even if the conditions during the removal of liquid ammonia are not optimal.

Table 4.4 Rietveld refinement parameters for the ammonia-poor phase shown in Figure 4.13.

Space group	*I*4/*mmm*	**V / Å^3**	253.20(4)
a **/ Å**	3.7956(1)	**R_{wp} / %**	1.68
c **/ Å**	17.475(2)	**χ^2**	0.198
Fe-Se distance / Å	2.419(1)	**Se-Fe-Se (α) angle / °**	103.37(8)
Na-Se distance / Å	2.894(2)	**Se-Fe-Se (β) angle / °**	112.61(4)

atom	**site**	**x**	**y**	**z**	**Occupancy**	**U_{11} / Å^2 × 100**	**U_{33} / Å^2 × 100**
Fe	4*d*	0	0.5	0.25	1	1.7(1)	5.6(3)
Se	4*e*	0	0	0.3363(2)	1	2.05(9)	4.1(2)
N	2*a*	0	0	0	1.00(4)[a]	2.8(4)[b]	
Na	2*b*	0	0	0.5	0.350(9)	2.8(4)[b]	
H	16*m*	0.14[c]	0.14[c]	0.0379[c]	0.38(5)[a]	2.8(4)[b]	

[a] nitrogen occupancy limited to a maximum of 1 and hydrogen occupancy limited to not exceed more than 3 hydrogen per nitrogen in the unit cell

[b] parameters fixed to a weighted average of the iron and selenium total thermal ellipsoids.

[c] hydrogen site position was fixed to have a near linear N-$\hat{\mathrm{H}}$-Se angle such that H is 1.00 Å from the N and the distance to Se is minimised to 2.947 Å.

4.3.2 Variation in laboratory synthesised $Na_{0.5-x}(NH_{3-y})_{0.5-z}FeSe$ samples

Several samples of Na-intercalated FeSe have been made using a similar method as described in Section 4.2.2 using NH_3 in place of ND_3 and allowing the ammonia to evaporate through the Schlenk line instead of recapturing it. Synchrotron powder X-ray diffraction was performed on several of these samples on beamline I11 at Diamond Light Source. Samples were loaded into 0.5 mm diameter borosilicate capillaries in an argon-filled, dry glovebox, the open end of each capillary was filled with grease and fixed against a test tube bung. A test tube was placed over the bung with the capillary inside, removed from the glovebox and taken to a butane-oxygen blowtorch, where the tube was opened and the capillary (still with vacuum grease in the open end and stuck to the bung) was quickly sealed. Figure 4.14 plots the predicted X-ray diffraction patterns of the ammonia-free and ammonia-poor phases alongside the real diffraction patterns of several samples collected using the curved position sensitive detector (mythen) to demonstrate the different phase separation in samples. Whilst several samples contain the ammonia-poor phase, the ammonia-free phase reported by Guo *et al.*[137] does not clearly correspond to the additional reflections in the pattern: there is a reflection around 7.0 ° that coincides with the (002) of the reported ammonia-free phase, but all the other reflections of that phase are absent. The additional reflections in the patterns are likely to arise from a Na/NH_3 intercalated iron-selenide phase, since they do not match any possible impurity and are shown later, in section 4.3.4, to be affected by the application of an ammonia atmosphere in the same way that the ammonia-poor phase peaks are.

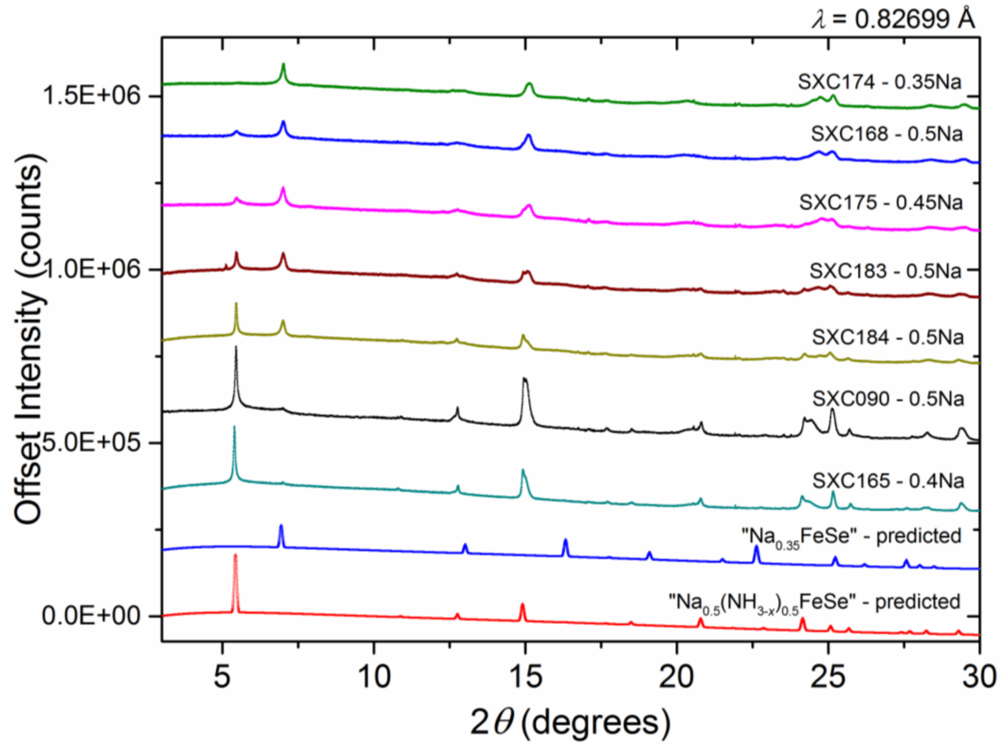

Figure 4.14 Synchrotron powder X-ray diffraction patterns of several $Na(NH_{3-x})_yFe_2Se_2$ samples demonstrating the variation in composition. Each pattern is labelled with an amount of sodium which is the molar ratio of sodium used in the synthesis relative to one FeSe. The bottom two patterns are theoretical patterns of the ammonia-free "$NaFe_2Se_2$" reported by Guo *et al.*[137] and ammonia-poor "$NaNH_{3-x}Fe_2Se_2$", for comparison.

Several variations in the synthesis conditions were trialled in order to find the controlling parameter in the formation of the additional peaks, with a target of forming only the equivalent phase to the ammonia-poor lithium intercalate. Adjusting the stoichiometric ratio of Na : FeSe used in the synthesis did not produce any consistent variation in the phase purity of the final product. Na : FeSe ratios of 0.15, 0.25, 0.3, 0.35, 0.45, 0.5, and 1 : 1 were used with no clear correlation to the products formed. A ratio of 0.15 : 1 was found to be insufficient to consume all the FeSe starting material, suggesting that there is a lower compositional boundary, consistent with the refinement in Table 4.4. All other ratios consumed all the FeSe and gave similar products. Changing the solution concentration is reported by Guo *et al*. to be the controlling factor in the formation of ammonia-poor and ammonia-free phases,[137] however similar products were obtained for the samples synthesised on I12 (0.2 - 0.4 mol dm^{-3} Na in NH_3) and in the laboratory synthesis (0.025 - 0.075 mol dm^{-3} Na in NH_3). Reaction time and reaction temperature profile also did not produce any significant correlation to the appearance of additional phases, SXC184 and SXC183 were made in a parallel synthesis, NH_3 was condensed into both simultaneously, the two were then isolated from one another and SXC183 was kept at -78 °C for 3 hours while SXC184 was kept at -40 ± 5 °C for 3 hours, the NH_3 was then boiled off from both simultaneously, and they present similar diffraction patterns.

SXC174 appears to contain none of the ammonia-poor phase and aside from the peak at 7.0 ° does not show the expected peaks for the ammonia-free phase either. The pattern cannot be indexed to a single unit cell of reasonable size, however this phase does appear to convert to the ammonia-rich phase on exposure to ammonia and so is clearly a related structure, it has undergone some deformation from the ammonia-poor structure upon exposure to vacuum.

To summarise a complex situation: the ammonia-rich and ammonia-poor phases have been observed and characterised in this work. An ammonia-free phase has been reported by another group,[137] but this phase has not been clearly observed in any diffraction pattern of any sodium- ammonia- intercalated iron selenide sample synthesised in this work, including those synthesised using high concentrations of sodium in ammonia solution which are reported to favour the ammonia-free phase. These three phases are shown in Figure 4.15. When exposed to ammonia vapour or solution, Na- NH_3- intercalated iron selenide forms a single ammonia-rich phase. When ammonia was removed very slowly from a freshly synthesised ammonia-rich phase, the ammonia-poor phase formed in a single-phase form that can be well modelled. When exposed to a vacuum, the ammonia-poor phase is formed, but a so far uncharacterised set of peaks are present in nearly all diffraction patterns. The diffraction patterns for the ammonia-poor phase reported both the papers by Ying *et al*.[89] and Guo *et al.*[137] also show these peaks similar to those of SXC165 in Figure 4.9, which are not accounted for in their refinements.

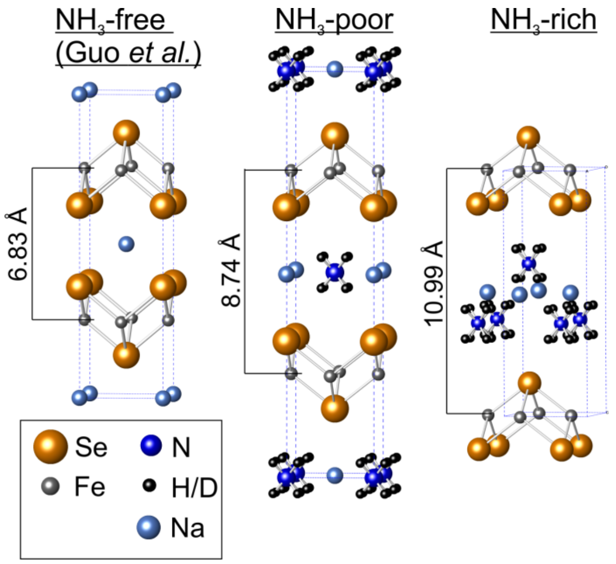

Figure 4.15 Comparison of the ammonia-free sodium intercalated iron selenide phase reported by Guo *et al.* in reference 137 **with the ammonia-poor and ammonia-rich structures reported in this thesis.**

4.3.3 Stacking fault interpretation

A possible solution to the identity of the unidentified component in the complex diffraction patterns of the ammonia-poor phases may be that a partial loss of ammonia has occurred leaving a structure with ammonia in some but not all interlayer spaces. To test this theory a stacking fault model was applied using the functionality built into TOPAS v5,[113] which uses the supercell approach to stacking fault modelling. In the model a tetragonal supercell is built of two layers, **A** and **B**, defined at the base of the supercell, each with a refinable length l_a and l_b corresponding to the layer height. The two layers are then stacked along the *c* axis by a set number of **A** and **B** layers, n_a and n_b, in an ordering that is also set. The **A** layer was chosen to be that of an ammonia-poor intercalate ($Na_{0.5}(NH_3)_{0.5}FeSe$) with l_a of 8.7 Å, the **B** layer was trialled as both an ammonia-free layer ($Na_{0.5}FeSe$) with l_b of 6.8 Å, and an FeSe layer (FeSe) with l_b of 5.5 Å.

In a model with two types of layers stacked in a supercell, the total number of **A** and **B** layers determine the predicted reflection positions, while the stacking order of the layers determines the relative intensities of the peaks when layer contents are fixed. For a $Na_{0.5}FeSe$ **B**-layer the calculated reflection positions did not match those found experimentally for all combinations of $n_a + n_b \leq 16$ when modelled against the X-ray powder diffraction pattern of SXC168 obtained on I11. No larger number of layers was attempted since the number of possible orderings of the layers rises as a factorial function with the total number of layers, making finding the correct ordering difficult. For an FeSe type **B**-layer a reasonable fit to the peak positions was achieved using a $n_a = 6$ and $n_b = 8$.

With 6 **A** and 8 **B** there are 3003 $\left(\frac{14!}{6!\,8!}\right)$ ways of arranging those layers. Since there will certainly be a point at which **A** and **B** meet, the first two layers can be set as **A** and **B**, reducing the number of arrangements to 792. Each of the possible 792 orderings was tried in turn in a Rietveld refinement using a batch mode operation, reporting the R_{wp} in each case. Figure 4.16 shows how the ordering of the A and B layers affects the agreement with the pattern, showing that the orderings that give the best fit are relatively few in number and are quite similar to one another.

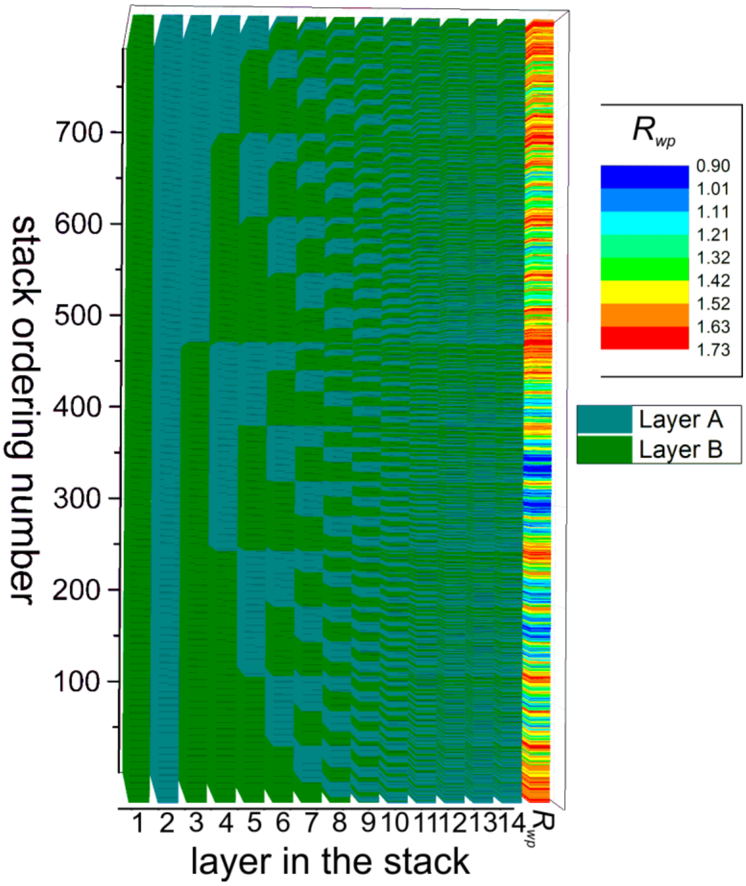

Figure 4.16 Agreement between stacked model described in the text the X-ray diffraction data as a function of the ordering of how the two types of layers are configured along the stacking axis.

Figure 4.17 shows a stacking arrangement that reports a good agreement with the data with refinement parameters used given in. A contribution to the pattern from the high quality ammonia-poor phase of Table 4.4 is included, for which the lattice parameters were allowed to refine and the structural coordinates and occupancies were constrained to be close to the structure observed in Figure 4.13. This model in which stacking disorder is introduced provides a marked improvement over attempts to model the pattern as a mixture of the reported ammonia-poor and ammonia-free phases,[137] a refinement to this effect is shown for comparison.

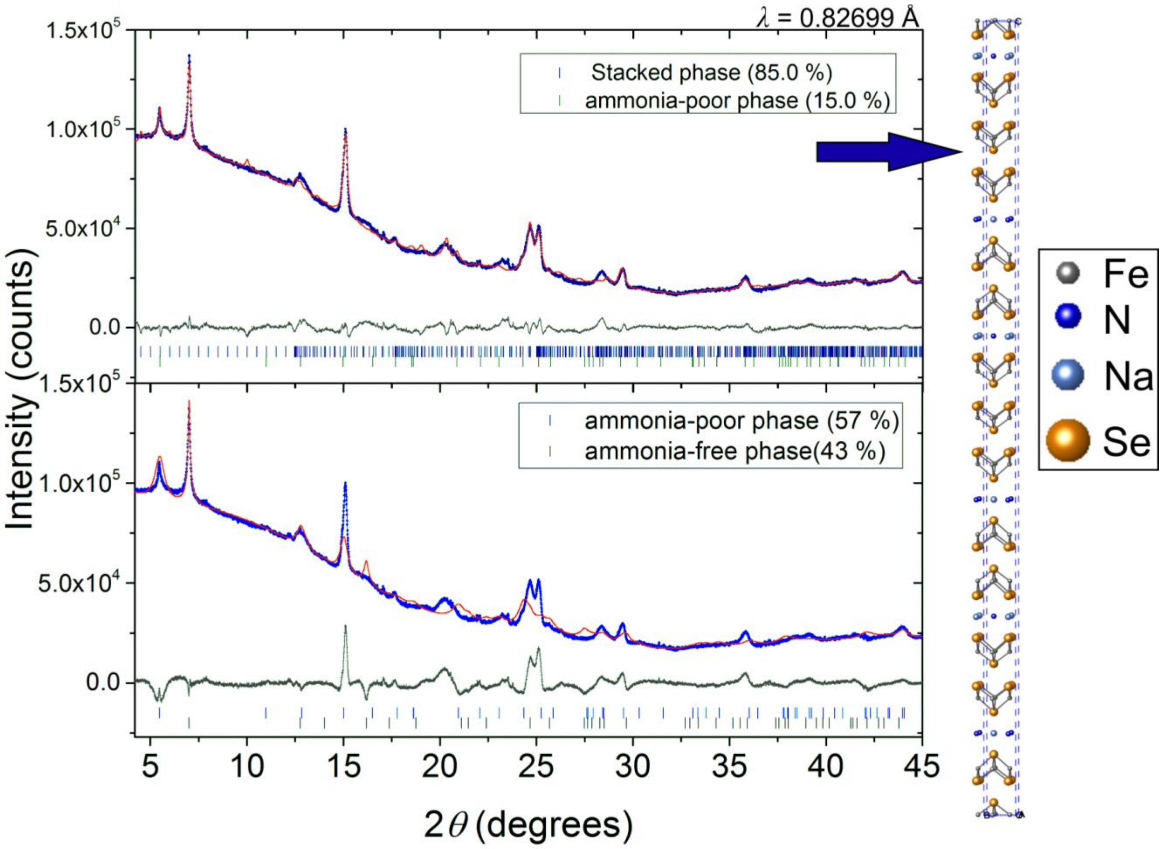

Figure 4.17 Rietveld refinement against synchrotron powder X-ray diffraction pattern of SXC168 taken on beamline I11 at Diamond, UK. Top: The pattern is modelled as two sodium intercalate of iron selenide phases: the ammonia-poor phase given in Figure 4.13 and the stacked structure shown on the right. Phase ratios are given as mass percentages rather than molar percentages. Bottom: the pattern is modelled using the ammonia-poor phase shown in Figure 4.13 and the ammonia-free phase reported by Guo *et al.* in reference 137**.**

Table 4.5 Refined parameters from the Rietveld refinement shown in the top panel of Figure 4.17. The model consists of two types of layers, A and B, with the same dimensions in the *ab* plane, but different lengths along the *c* axis (l_a and l_b), which are stacked in a defined order. Although refined in *P*1, the atomic coordinates of sites in layers A and B were constrained to obey the symmetry operations of the ammonia-poor intercalate and FeSe parent structures, respectively. Atomic *z* coordinates are defined as a fraction of l_a or l_b, for atoms in layers A and B respectively. Debye-Waller factors were constrained to refine to a single value for all atoms.

n_a	6	**a(,b) / Å**	3.8075(5)	**Fe-Se distance in layer A / Å**	2.52(1)
n_b	8	**c / Å (total)**	94.8(2)	**Fe-Se distance in layer B / Å**	2.331(8)
l_a / Å	8.43(2)	**Se z coordinate (along l_a)**	0.197(2)	**Na-Se distance / Å**	2.55(2)
l_b / Å	5.53(1)	**Se z coordinate (along l_b)**	0.243(3)	**Space Group**	*P*1
R_{wp} / %	1.01	χ^2	3.82	**Layer ordering**	*BABABAB-BABABBA*

Site	**x**	**Y**	**Z**	**occupancy**	**U_{eq} / Å^2 × 100**	**layer**
Fe1	0.25	0.75	0	1	1.2(4)	A
Fe2	0.75	0.25	0	1	1.2(4)	A
Se1	0.75	0.75	0.197(2)	1	1.2(4)	A
N1	0.25	0.25	0.5	0.5	1.2(4)	A
Na1	0.25	0.75	0.5	0.35	1.2(4)	A
Se2	0.75	0.75	0.803(2)	1	1.2(4)	A
Fe3	0.25	0.75	0	1	1.2(4)	B
Fe4	0.75	0.25	0	1	1.2(4)	B
Se3	0.75	0.75	0.243(3)	1	1.2(4)	B
Se4	0.25	0.25	0.757(3)	1	1.2(4)	B

This method of modelling provides a plausible description of the structure, but to further test its validity it was applied to high resolution neutron powder diffraction data, in which a far greater number of reflections may be observed. When the deuterated sample SXC090 used in chapter 4.2.2 was first synthesised it was measured on the Polaris instrument at the ISIS neutron facility before, in a separate beam allocation, conducting a re-ammoniation to study the ammonia-rich structure on HRPD. Refinement of the ammonia-poor structure alone produced a moderate quality fit to the data but returned an unreasonably low deuterium content per nitrogen of 1.5(2), an iron occupancy of 0.80(1) Fe per Se, failed to account for several broad features in the pattern, and had a poor fit to the peaks at low *d*-spacing in the backscattering detector bank (bank 5); fits to all detector banks and full refinement and structural parameters with this model are given in appendix VII. Applying the stacking fault model approach used to model the X-ray powder diffraction pattern in Figure 4.17 to the neutron powder diffraction patterns from Polaris gives a similar structure with $n_a = 6$ and $n_b = 8$, with a different ordering of the layers (these are different samples). Figure 4.18 shows the comparison of fits to bank 3 and bank 5 obtained with and without the inclusion of the stacked phase, notably the diffuse features at 4.6 Å in bank 3 and 2.4 Å in banks 3 and 5 are modelled well by the stacked phase. Reflections at low *d*-spacing in bank 5 are also fitted far more accurately by inclusion of the stacked phase, the R_{wp} for the refinement is improved from 3.71 to 2.65 %, and more sensible deuterium occupancies are returned giving a chemically much more sensible N : D ratio of 1 : 2.5, up from 1 : 1.5.

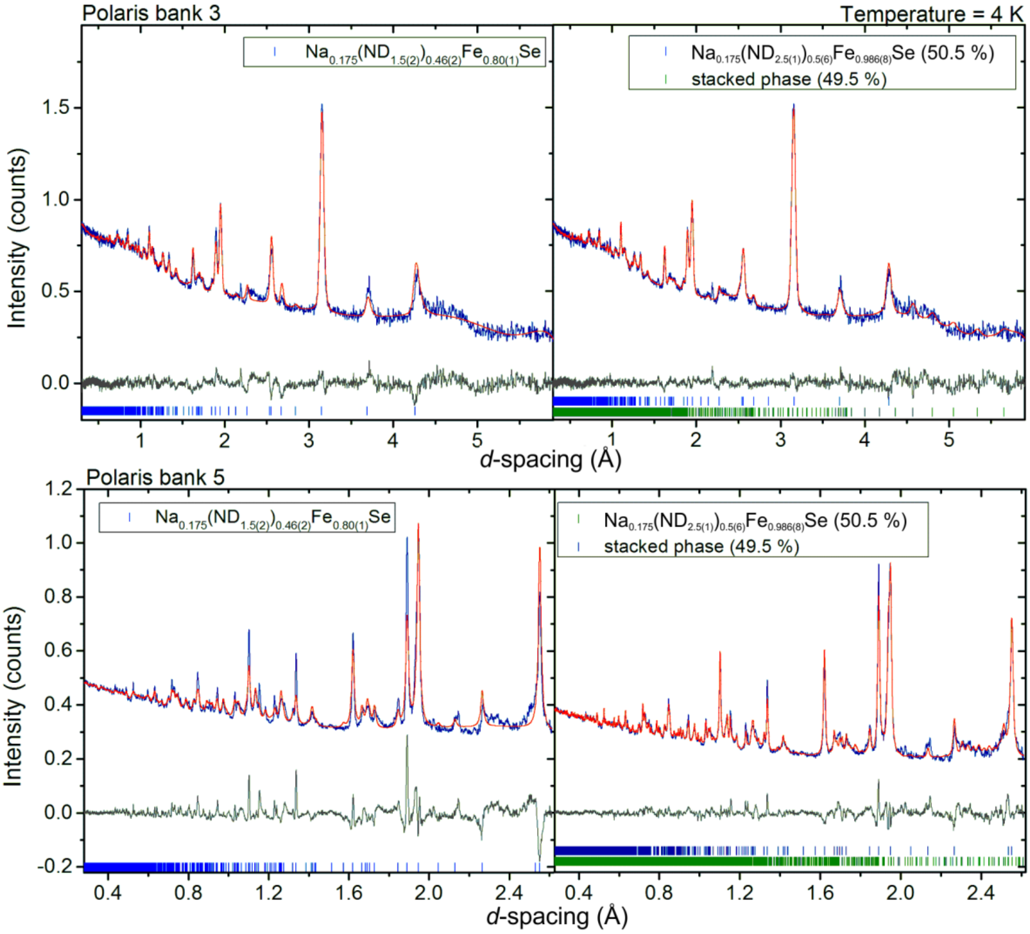

Figure 4.18 Comparison of Rietveld refinements against neutron powder diffraction data obtained for the deuterated ammonia-poor sodium intercalate SXC090 on the POLARIS instrument at ISIS, UK. One the left the pattern is modelled with an ammonia-poor structure, on the right the pattern is modelled with both the ammonia-poor phase and a stacking fault phase.

The stacked phase uses only 9 independent parameters for the refinement of the unit cell: 3 for the lattice parameters with *a* and *b* refined as one value and l_a and l_b being refined separately, 2 for the *z* coordinate of the selenium atoms in each layer, 3 for the occupancies of nitrogen, deuterium, and sodium, and a single value was used to refine the thermal displacement parameters of all sites in order to constrain them to sensible values. Deuterium sites were confined to have the same occupancy and be in a square prismatic arrangement around nitrogen with reasonable D-N and D-Se distances. Sodium has a relatively short coherent scattering length for neutrons compared to the other scattering species, meaning that refinement of its occupancy in a complex model such as this was unreliable. As such the occupancy of sodium was constrained to a minimum value of 0.175 per FeSe. Banks 1, 3, 4, and 5 were refined against simultaneously, only 4 banks including bank 1 could be refined at once, inclusion of all 5 banks introduced too many predicted reflections into the refinement for the software to handle. The same stacking arrangement obtained from the refinement against the neutron data was then applied to synchrotron powder X-ray diffraction data of the same sample in order to test the model against both techniques, fits for both of which are given in Figure 4.19, a comparison of the refined model from I11 and Polaris is given in Table 4.6, structural parameters for the stacked phase from the neutron refinement are given in Table 4.7, and structural parameters for the ammonia-poor phase are given in appendix VII.

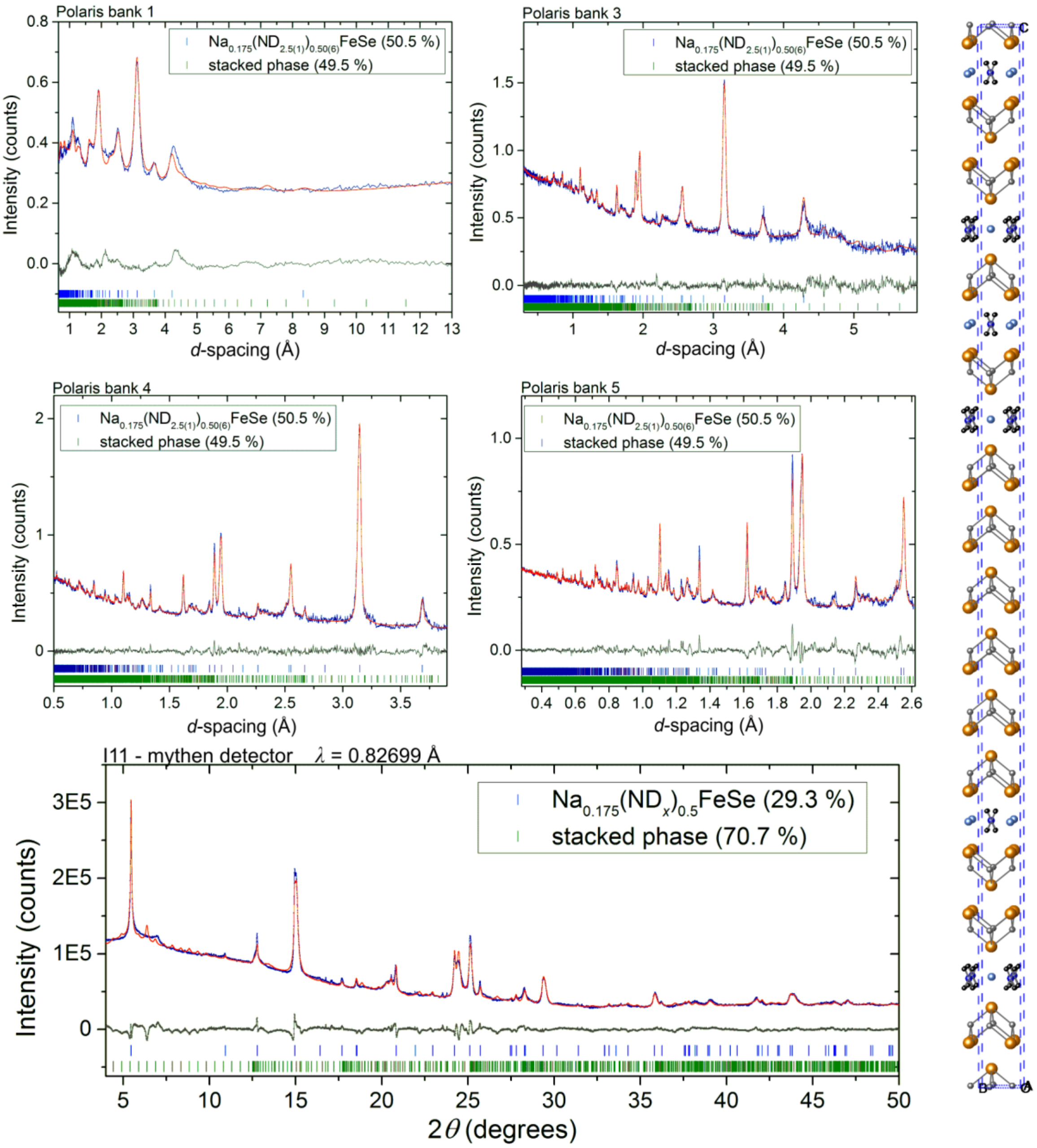

Figure 4.19 Rietveld refinement of the ammonia-poor sodium intercalate and stacked phase shown on the right against neutron powder diffraction patterns of SXC090 obtained on POLARIS at ISIS, UK and synchrotron X-ray powder diffraction pattern of the same sample measured on I11 at Diamond, UK. Phase percentages are given by mass in this figure.

Table 4.6 Comparison of the refined model for the stacking fault structure from X-ray and neutron Rietveld refinement shown in Figure 4.19. The parameter marked [a] was given a constraint to limit its maximum value to 0.20 in order to prevent an unreasonably long Fe-Se distance.

	POLARIS	**I11**		**POLARIS**	**I11**
Temperature / K	4	298	**layer ordering**	*BABABBBBBAAABA*	
Space group	*P*1		**Se z coordinate (along la)**	0.178(2)	0.200(2)[a]
***a, b* / Å**	3.7826(3)	3.7974(3)	**Se z coordinate (along lb)**	0.279(2)	0.269(2)
***c* / Å (total)**	95.82(4)	96.64(5)	**Fe-Se length in layer A / Å**	2.443(7)	2.58(1)
n_a	6		**Fe-Se length in layer B / Å**	2.42(1)	2.410(8)
n_b	8		**Na-Se length / Å**	2.79(2)	2.63(2)
l_a / Å	8.605(5)	8.750(5)	**N-D length / Å**	1.01	*n.a.*
l_b / Å	5.523(4)	5.510(4)[a]	**Se-D length / Å**	2.771(7)	*n.a.*

Table 4.7 Refined structural parameters for the stacked phase from Rietveld refinement against neutron powder diffraction data of SXC090, POLARIS banks 1, 3, 4, and 5. The sodium occupancy marked [a] was given a lower limit of 0.35, to which it refined.

Site	**x**	**y**	**Z (along l_a or l_b)**	**occupancy**	**U_{eq} / Å^2 × 100**	**layer**
Fe1	0.25	0.75	0	1	0.20(4)	A
Fe2	0.75	0.25	0	1	0.20(4)	A
Se1	0.75	0.75	0.178(2)	1	0.20(4)	A
Na1	0.25	0.25	0.5	0.35(5)[a]	0.20(4)	A
N1	0.25	0.75	0.5	0.45(4)	0.20(4)	A
D1	0.35	0.35	0.60	0.222(8)	0.20(4)	A
D2	0.15	0.35	0.60	0.222(8)	0.20(4)	A
D3	0.35	0.15	0.60	0.222(8)	0.20(4)	A
D4	0.15	0.15	0.60	0.222(8)	0.20(4)	A
D5	0.35	0.35	0.40	0.222(8)	0.20(4)	A
D6	0.15	0.35	0.40	0.222(8)	0.20(4)	A
D7	0.35	0.15	0.40	0.222(8)	0.20(4)	A
D8	0.15	0.15	0.40	0.222(8)	0.20(4)	A
Se2	0.75	0.75	0.803(2)	1	0.20(4)	A
Fe3	0.25	0.75	0	1	0.20(4)	B
Fe4	0.75	0.25	0	1	0.20(4)	B
Se3	0.75	0.75	0.243(3)	1	0.20(4)	B
Se4	0.25	0.25	0.757(3)	1	0.20(4)	B

4.3.3.1 Summary of the stacking model

Upon introduction of the stacked model as a contributing phase to the dry product of the sodium-ammonia intercalation of FeSe, both fits to the X-ray and neutron diffraction are greatly improved. SXC090 and SXC168 have been modelled using different stacking arrangements, which is reasonable since they are different samples. A single stacking arrangement is suitable for modelling both the X-ray and neutron powder diffraction data of SXC090. Comparing the fits we see the fit to the neutron powder diffraction produces the most reasonable interatomic distances when compared to those in Na_2Se and β-FeSe in which the Na-Se and Fe-Se distances are 2.93 and 2.39 Å, respectively. A more reasonable interlayer spacing is also obtained in the fit to the neutron data for the Na and NH_3 intercalated FeSe layer which is typically in the region of 8.60-8.78 Å for samples measured at room temperature. Refinement against the I11 data for SXC090 produces lattice parameters consistent with the neutron powder diffraction data (at lower temperature), the Na-Se distance could not be refined to a reasonable value in this case due to the Se *z* coordinate in layer **A** needing to restrained.

The ammonia-rich phase of the sodium intercalate always appears single phase when synthesised on I12, and sample SXC090, which seems to include the stacked phase along with the ammonia-poor phase in the dried product under argon, appears to reform a single ammonia-rich phase when exposed to ammonia, within the resolution of the HRPD instrument. A key criticism of the stacked model’s validity arises from this observation, since it implies that the intercalated sodium is evenly distributed in the ammonia-rich phase but on exposure to vacuum, the sodium becomes unevenly distributed in parts of the sample causing a phase separation. However, it should be noted that the occupancy of the sodium site in the ammonia-rich phase could not be refined reliably and had little quantitative impact on the agreement of the fit, and so it is entirely possible that it is not evenly distributed in the ammonia-rich phase. It is also possible that a migration of the sodium could occur, as movement of small ions between layers is observed in the related layered $Li_{\sim0.8}Fe_{\sim0.2}(OH)Fe_{1-x}Se$ system.[130]

The formation of sodium amide in the intercalate may play a role in the formation of the ammonia-poor and stacked phases: if both sodium amide and ammonia were in the intercalate structure, which is the indication from neutron diffraction experiments described in this report, it is sensible to suggest that application of vacuum could remove ammonia but not sodium amide.

The phase separation that occurs when forming the ammonia-poor and stacked phases from the ammonia-rich could be rooted in a pre-existing phase separation in the ammonia-rich phase, outside the resolution of HRPD. It could also potentially be caused by an encapsulation effect, if the ammonia is lost only from the surface of the crystallite forming the stacked phase but was maintained in the core leaving the ammonia-poor phase. If crystallite size were the controlling factor in the formation of the stacked phase this would also explain the disparity in the relative abundance of the two phases between various samples synthesised under similar conditions.

The stacking model presented provides a sensible description of the system, and fits the data well however it is impossible to say with certainty from the current data that the proposed structure is an entirely accurate one, since there are many possible perturbations and improvements that could be made such as multiplying the number of **A** and **B** layers such that new stack orderings are available and the introduction of a third type of layer into the model containing only sodium and no ammonia. It can be concluded with certainty however, that a deformation of the sodium and ammonia/amide intercalated iron selenide crystallites occurs on removal of the ammonia atmosphere by vacuum, which prevents the system from being described with a small, high symmetry unit cell. The deformation involves partial loss of ammonia giving layers of FeSe separated by more than one type of species in the same crystallite and this deformation is sample dependant.

4.3.4 Cycling of ammonia absorption into sodium- and ammonia- intercalated iron selenide

4.3.4.1 *In-situ* powder neutron diffraction

After the measurement of the deuterated ammonia-rich sodium iron selenide sample on the HRPD instrument described in section 4.2.2 the extra intercalated ammonia was removed from the sample by exposure to dynamic vacuum for ~5 minutes and returning the sample to the helium filled glove box at ISIS neutron source. Once the sample was recovered, it was loaded into a steel can for use in an ammonia cycling experiment and was studied *in-situ* using powder neutron diffraction. The sample (~1.5 g) was loaded into a 6 mm diameter, 50 mm length steel container and topped with a small amount of glass wool. The container lid, capped with a needle valve for attachment to a gas panel, was attached to the steel container with a pressed indium gasket. The sample container was attached to the

Toxic Gas Panel available at ISIS as shown schematically in Figure 4.20. Once the line from the gas panel was connect to the sample holder, valves **A**, **B**, and **D** were opened, then the needle valve to the sample (**E**) was slowly opened, exposing the sample to dynamic vacuum. The sample was loaded into the He-cryostat and cooled to 250 K. Needle valve **A** was closed leaving the sample under a static vacuum with a 500 cc buffer volume.

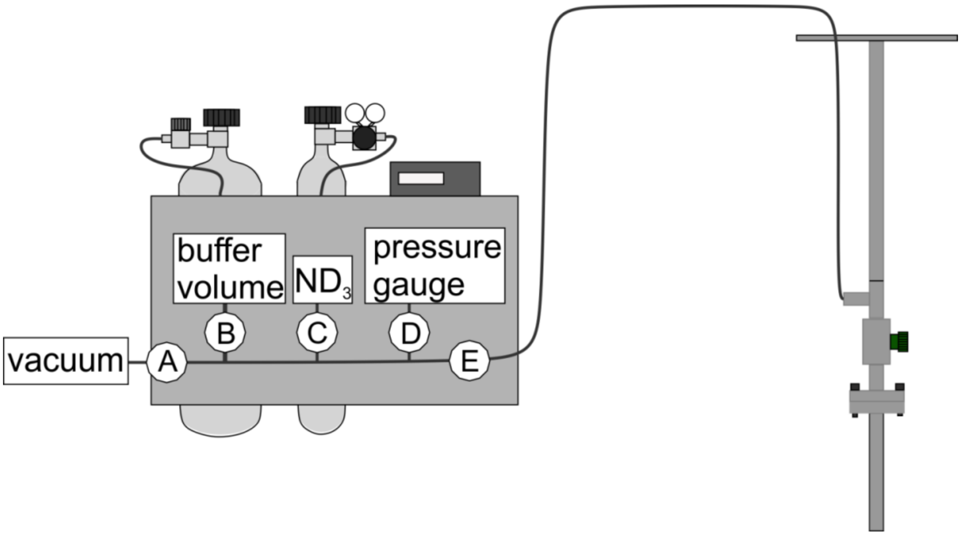

Figure 4.20 Experimental setup used to expose ~1.5 g of deuterated sodium-ammonia intercalated iron selenide to deuterated ammonia, and then vacuum to cycle the ammonia absorption whilst performing *in-situ* powder neutron diffraction

During a scheduled period with no beam, 800 mbar of ND_3 was introduced into the system, leaving the volume of gas to absorb. The pressure dropped quickly at first as ND_3 was absorbed by the sample, the rate of absorption then slowed as the pressure dropped until the pressure in the system reached a minimum of 130 mbar, at which point a second filling of ammonia was introduced and again the pressure dropped quickly as the sample absorbed. This cycle was repeated several times until as absorption slowed to a minimum and eventually the pressure was allowed to be maintained at around 950 mbar by a regulator valve on the ammonia cylinder. When the beam was restored repeated fifteen minute (10 μA) scans were performed as the sample continued to slowly convert from the poor to the rich phase. The rate of conversion was slower than expected from the experience of ammoniating the sample offline, it was likely that a blockage in the pipe was preventing the ND_3 from reaching the bottom of the sample. At around 50 % conversion to the ammonia-rich phase, the desorption was begun by first warming to 265 K and applying a static vacuum by closing the cell to the gas panel, opening the valve to the vacuum to evacuate the buffer volume, closing the vacuum valve, and reopening the cell to the now evacuated line, the pressure in the line rose but little change was observed in the diffraction pattern. The sample was warmed to 273 K, then the pressure in the system lowered by closing the valve to the sample (**E**), evacuating the buffer volume by reopening the valve to the vacuum (**A**), then closing valve **A** and reopening valve **E**. A dynamic vacuum was then slowly applied at 273 K, and once the pressure dropped from 450 mbar down to 85 mbar there was a rapid rise to 600 mbar as ammonia was quickly expelled from the sample. After this event, which occurred during the grey diffraction pattern labelled *AL* in Figure 4.21's collection, the pressure in the system continued to fall smoothly down to base pressure indicating a sharp and total transition back to the ammonia-poor phase had occurred.

These results show that the ammonia-rich phase is relatively stable under an ammonia atmosphere until at least 0 °C, even under a reduced partial pressure. Upon exposure to a dynamic vacuum at 0 °C the loss of ammonia to form the ammonia-poor phase is a rapid process.

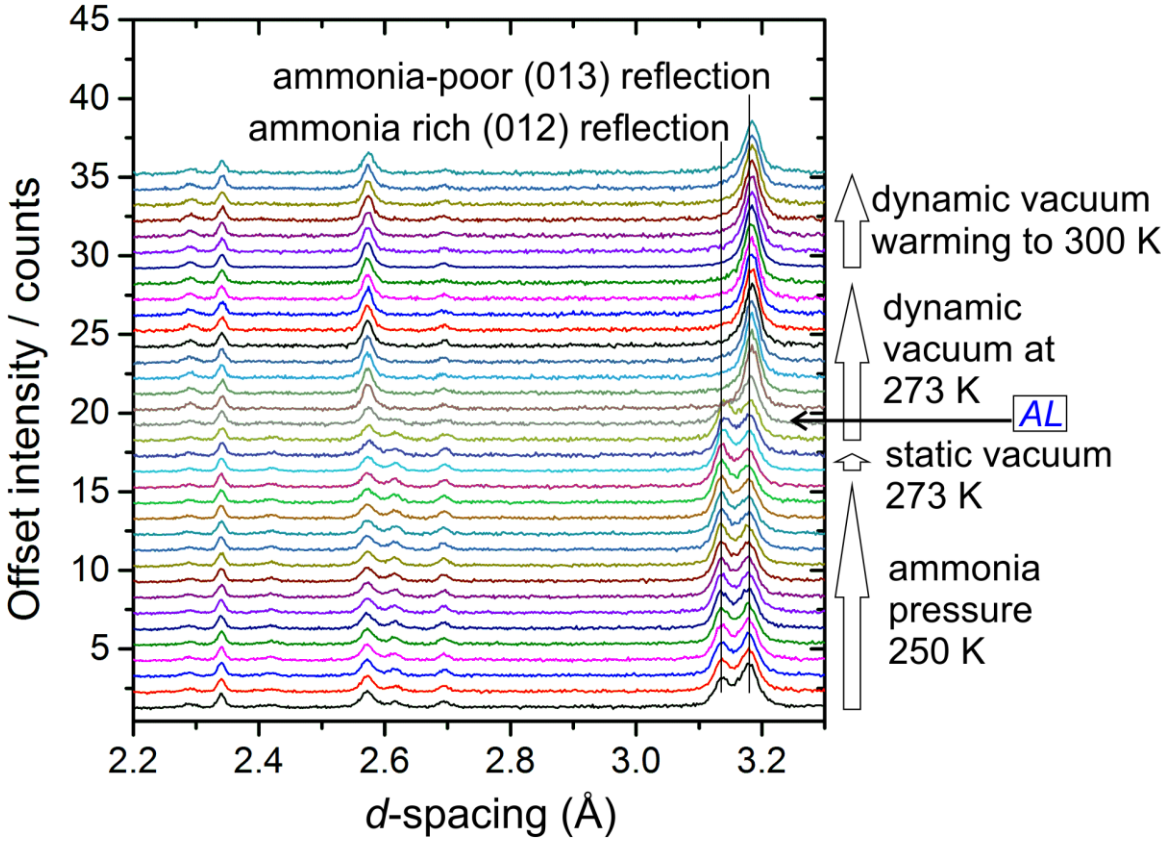

Figure 4.21 ***In-situ*** **powder neutron diffraction collimation of the beam significantly lowers the observed intensity of the steel diffraction peaks.**

In an attempt to observe the appearance of the ammonia-free phase reported by Guo *et al.*[137] the sample was gradually warmed under dynamic vacuum up to 300 K. No additional peaks were observed however a small decrease in the intensity of the (013) peak of the ammonia-poor phase as shown in Figure 4.22, along with a slight asymmetric broadening towards lower *d*-spacing, where often the most intense peak of the stacked phase is observed. There are a no predicted peaks for the ammonia-poor phase in this region.

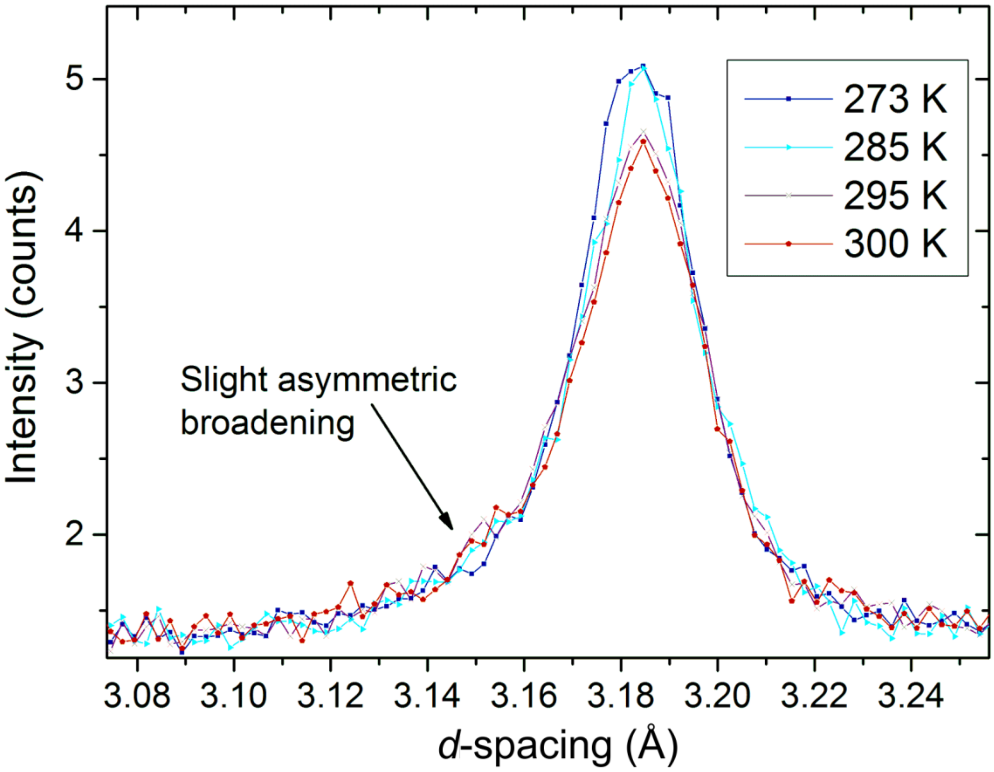

Figure 4.22 (013) reflection of the ammonia-poor sodium intercalate phase of iron selenide on warming under a dynamic vacuum.

The sample was further evacuated for 1 hour after the measurement before being extracted in the glovebox. Finally the sample was returned to a vanadium can and measured once again on HRPD for 4 hours (160 μA). Rietveld refinement against the product of this treatment using only the ammonia-poor phase as a model is shown in Figure 4.23, which displays further asymmetric broadening of the peaks from prolonged exposure to vacuum along with the appearance of a few peaks unaccounted for by the model. Resulting in a very similar pattern to the initially observed neutron diffraction pattern taken on POLARIS shown previously in Figure 4.18, the patterns of the two back scattering banks are very similar indicating the stacked phase has emerged once again, as shown in the overlay of these two patterns.

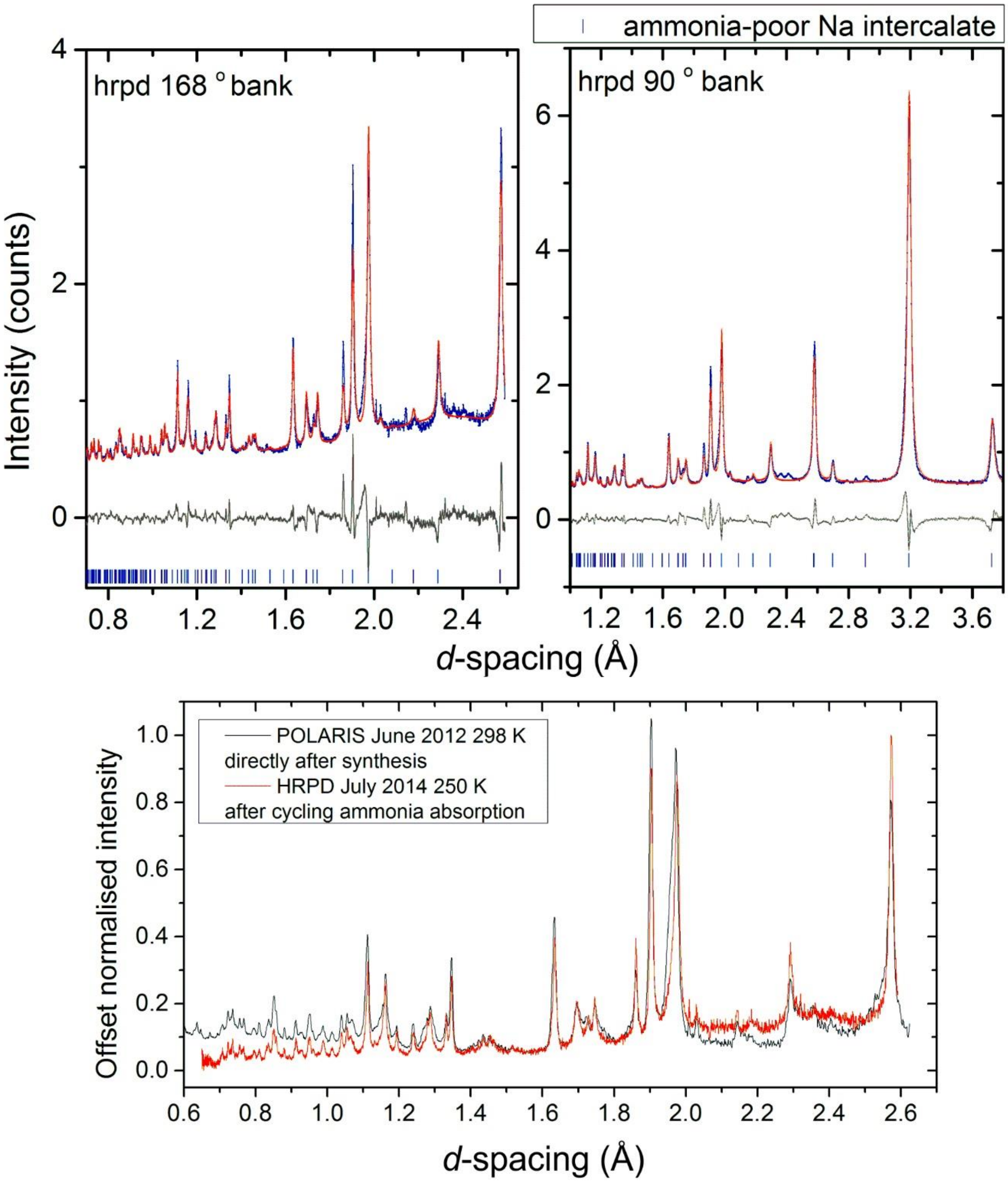

Figure 4.23 Rietveld refinement of the ammonia-poor sodium intercalated iron selenide structure against HRPD's backscattering and 90 ° detector banks, after the sample had been exposed to ammonia at 250 K and then to vacuum at 300 K. discrepancies in the fit arise and model arise from the appearance of the stacked phase on prolonged exposure to vacuum.

These results show there is a reversible equilibrium between the ammonia-rich, ammonia-poor, and stacked phases of Na/NH_3 intercalated iron selenide. Exposure to an atmosphere of ammonia at 250 K will convert both the stacked and ammonia-poor intercalate phases into an ammonia-rich structure, which appears single phase within the resolution of HRPD, as evidenced by the formation of the ammonia-rich phase performed *ex-situ* described in section 4.2.2. Exposure of the sample to a dynamic vacuum at 273 K will remove ammonia from the ammonia-rich phase within 15 minutes, as observed by diffraction, probably almost instantaneously as observed by the rapid increase in pressure in the line during the gradual application of the vacuum. The stacked phase is also reformed as a contributing second phase upon exposure to vacuum, it is intrinsic to all samples synthesised for this work when ammonia pressure is removed and grows in phase percentage as the system is raised towards room temperature.

4.3.4.2 *In-situ* powder X-ray diffraction

Following the partial success of the *in-situ* powder neutron diffraction investigation a follow-up experiment conducted on beamline I11 at Diamond Light Source. Synchrotron radiation holds two key advantages over neutron radiation in this regard: faster collection times due to the higher flux, and the ability to use a smaller sample size, which should provide a more complete conversion. The same samples that were synthesised on I12 and the deuterated sample from HRPD were used for this experiment. 0.5, 0.7 and 1.0 mm diameter borosilicate capillaries of sodium intercalated iron selenide were loaded in an argon-filled, dry glovebox. The open end of the capillary was shortened to just above the sample and the capillary was glued inside a hollow brass ferrule, blocking one of the ferrule's ends. The other end of the brass ferrule was connected to the T-piece shown in Figure 4.24 using a standard Swagelok® fitting. The T-piece was removed from the glovebox and transported to the beamline where it was mounted on a goniometer head, and a Swagelok® quick connection was used to connect the T-piece to a gas panel under dynamic vacuum. A cryostream was used to cool the capillary to 250 K, the vacuum to the sample was closed and ammonia pressure up to 1 bar was introduced into the line. 4 × 10 second measurements were collected using the PSD detector while ammonia was absorbed, moving the detector by 0.25 ° between 10 second collections to cover the blind spots in the detector bank. The sample could not be spun using this setup. A wavelength of 0.82699 Å was used in this experiment.

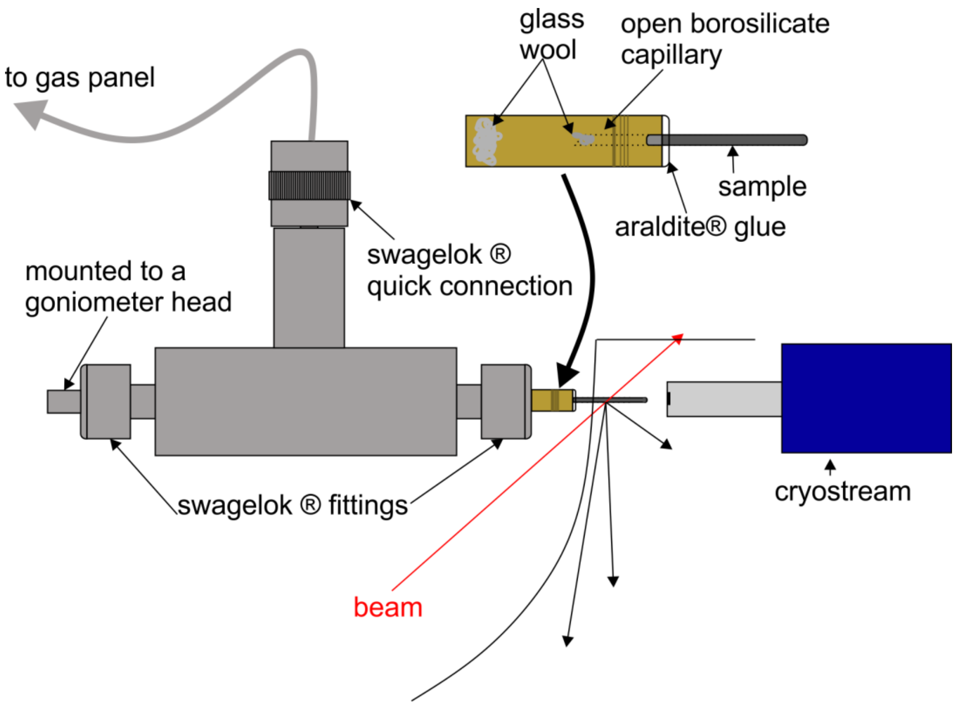

Figure 4.24 Schematic of the set up for an *in-situ* powder X-ray diffraction measurement on beamline I11 at Diamond, UK.

No ammonia absorption was observed when using a 0.5 mm capillary, most likely due to a blockage. When using a 1.0 mm capillary, no scattering was observed due to the sample being too absorbing. Two samples in 0.7 mm capillaries were used, the sample synthesised at room temperature on I12, and the deuterated sample measured after being measured on HRPD SXC090 (NH_3 was used as the absorption gas in both cases). The absorption of ammonia into SXC090 is shown Figure 4.25, a peculiar shift in the (001) peak of the ammonia-rich phase between 4.2 and 4.7 ° is observed over the course of the absorption. Initially the peak position of the ammonia-rich appears at a *d*-spacing around 11.0 Å, as expected from previous Rietveld refinement of the ammonia-rich phase. However, with no change in the temperature or sample environment, as time passes the peak slightly lowers in intensity and shifts to higher angle (lower *d*-spacing). Modelling the total peak intensity was performed using 2 peaks: one with a mainly Gaussian shape and another with a mainly Lorentzian, the normalised (001) intensity shown in Figure 4.25 is the sum of the two intensities and the peak position is an average of the two positions weighted by their intensities.

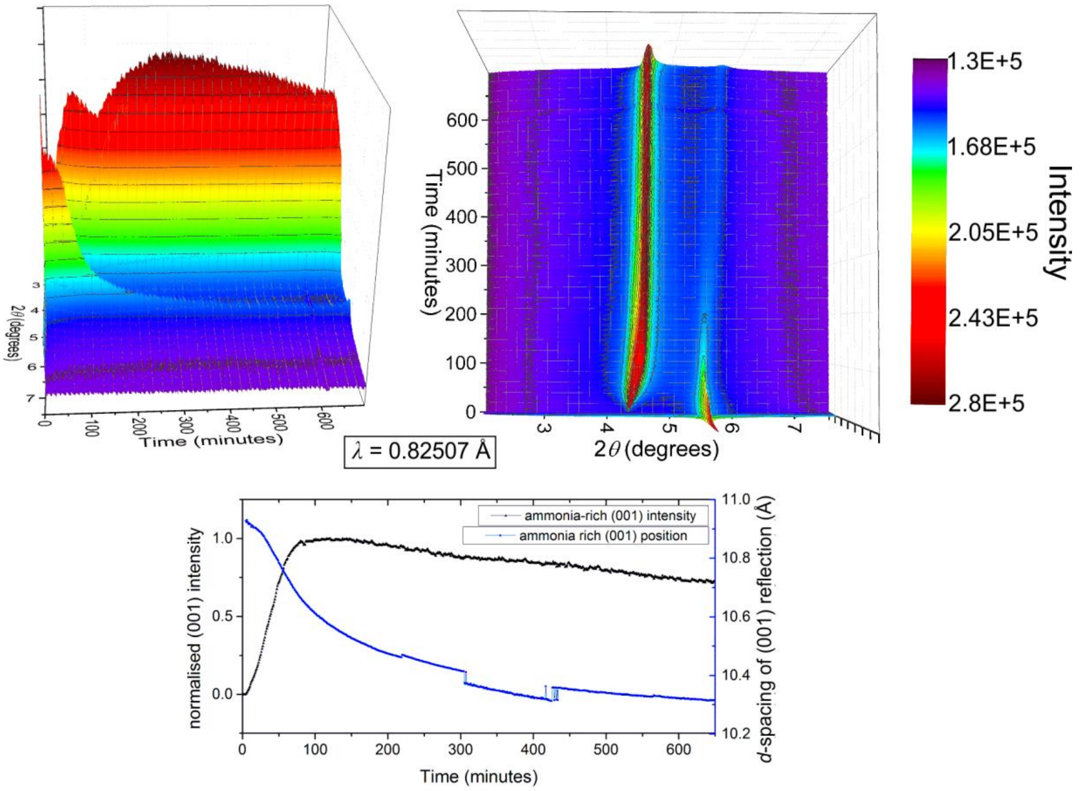

Figure 4.25 Top: colour surface plots of the absorption of ammonia into sodium ammonia intercalated iron selenide (SXC090). Bottom: integrated intensity of the product (001) peak and its *d*-spacing corresponding to spacing between Fe sites in neighbouring FeSe layers.

In the ammonia-rich product that is initially formed, the (001) peak of falls from 10.96 to 10.31 Å and the normalised intensity of this peak drops by 25 % over the course of 10 hours. One possible cause of this effect might be that the powder expanded as ammonia was absorbed and blocked any additional gas from reaching the end of the sample, then gradually the ammonia in the rich phase that did form diffused through to the rest of the unreacted ammonia-poor phase leaving an ammonia-rich phase with low occupancy of the nitrogen and hydrogen sites and a contracted unit cell:

$$Na_{0.18}(NH_{3\text{-}y})_{0.9}FeSe\ (11\ \text{Å}) + Na_{0.18}(NH_{3\text{-}y})_{0.5}FeSe\ (8.7\ \text{Å}) \rightarrow Na_{0.18}(NH_{3\text{-}y})_{\sim 0.7}FeSe\ (10.3\ \text{Å})$$

Another possible cause might be that as ammonia enters the system an internal redox process occurs between ammonia and electrons in the Fe 3d band, which has been slightly reduced by reaction with sodium. Fe would regain its +2 oxidation state by reducing ammonia and releasing hydrogen:

$$Na_{0.18}(NH_3)FeSe \rightarrow Na_{0.175}(NH_2)_{0.18}(NH_3)_{0.82}FeSe + 0.09H_2$$

The result is important in either case, as it goes to show that the ammonia-rich intercalate phase is not a line phase, even for a single given sample.

Figure 4.27 plots the intriguing behaviour of the sample synthesised during the I12 experiment described previously in section 4.2.1 in a 0.7 mm diameter capillary when first exposed to ammonia at 250 K for 200 minutes then exposed to dynamic vacuum on warming to 500 K over the course of 40 minutes, and finally annealing at that temperature for 120 minutes. Upon initial exposure of the sample to NH_3 we see the peak from the stacked phase at 7 ° rapidly disappears and the ammonia-poor phase peak at 5.5 ° diminish as the ammonia-rich phase peak at ~4.5 ° grows in. Similar behaviour to SXC090 is observed as a function of time: once the ammonia-rich phase is formed, the (001) peak of this phase shifts to higher angle and decreases in intensity. Dynamic vacuum was applied to the sample at 250 K, and the sample was heated to 500 K at 6 K min^{-1}. The ammonia-rich phase gradually converted to the ammonia-poor phase over the course of 10 minutes whilst warming between 250 K and 310 K under dynamic vacuum. As the ammonia-poor phase was heated towards 500 K, a second phase with an *I*4/*mmm* unit cell like the ammonia-poor phase appears with a reduced *c* lattice parameter, as shown by the Rietveld refinement against a pattern at 375 K in Figure 4.26. High absorption from the 0.7 mm capillary at a wavelength of 0.82699 Å and poor powder averaging from not spinning the sample prevent reliable structural parameters from being obtained. This ammonia-poor phase with the shortened *c* is also short lived as its (002) diminishes in intensity and is no longer present by ~ 475 K. Above 450 K the ammonia-poor phase begins to decompose and peaks at 7 ° and 8.5 ° corresponding the stacked phase and iron selenide, respectively begin to re-appear.

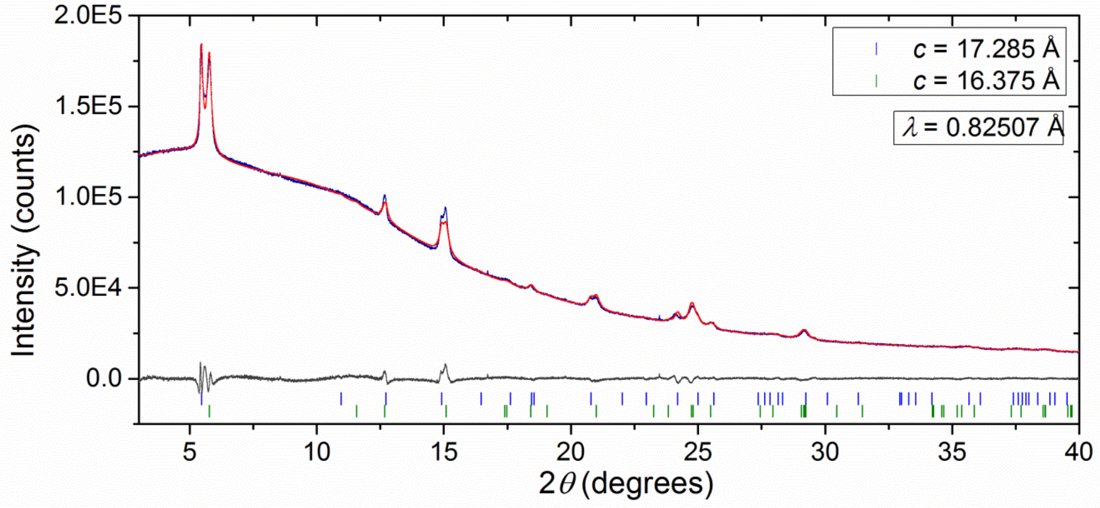

Figure 4.26 Rietveld refinement of sodium intercalated iron selenide at 375(3) K, showing two phases with *I4/mmm* unit cells, one of them the established ammonia-poor intercalate with unit cell parameters of *a* = 3.8112(4) and *c* = 17.285(5) Å, the other having a similar structure with unit cell parameters *a* = 3.8416(3) and c=16.375(4) Å.

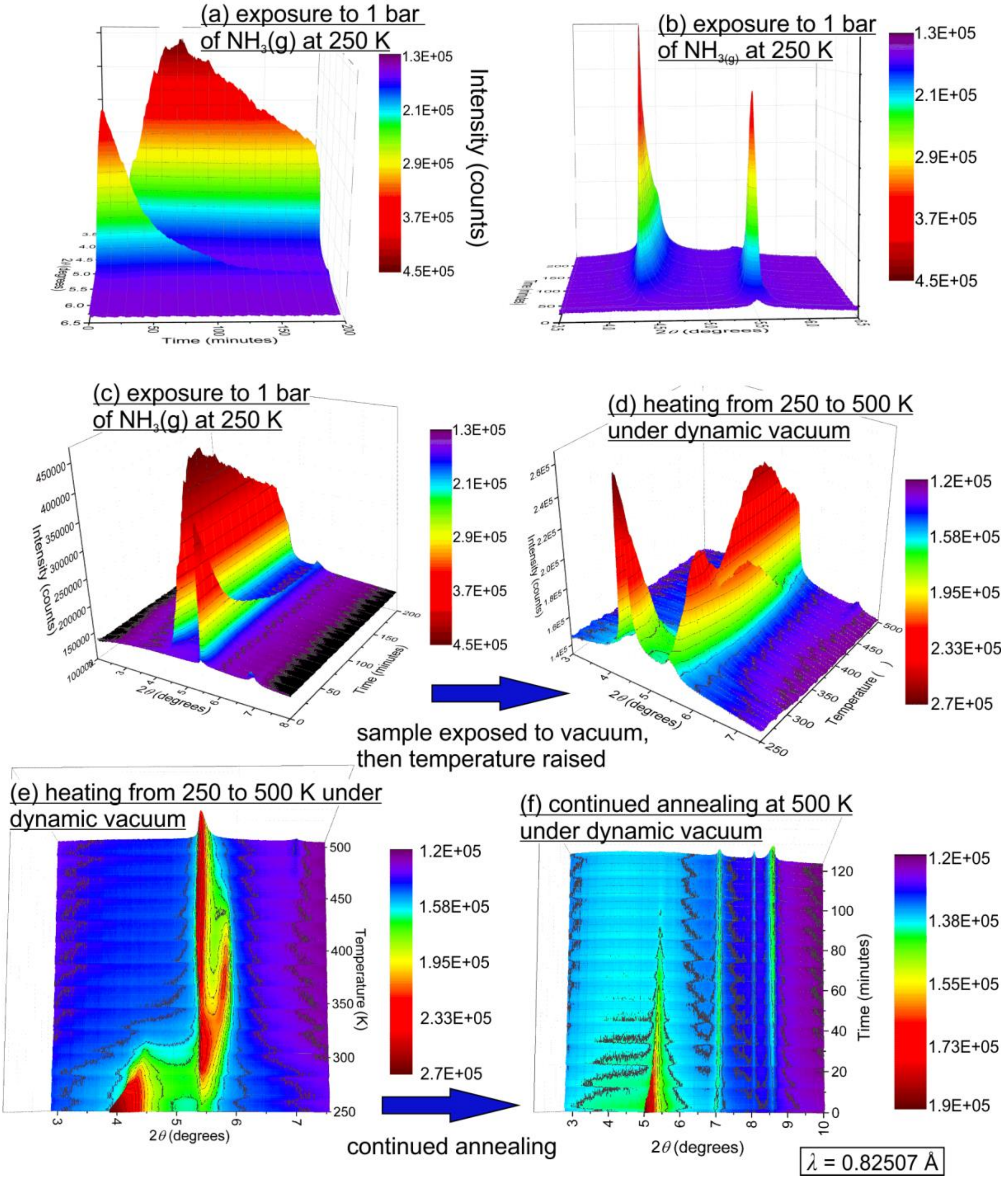

Figure 4.27 (a), (b), and (c) show the evolution of the NH_3 poor phase's (002) reflection at ~5.5 ° and the ammonia-rich phase's (001) reflection at ~ 4.3 ° under exposure to gaseous ammonia at 250 K from three perspectives. (d) and (e) show the evolution of the ammonia-rich and ammonia-poor peak upon heating the sample under dynamic vacuum to 500 K. (f) shows the evolution of the sample upon continued annealing at 500 K under dynamic vacuum.

Although it is difficult to say whether these results are being affected by blockages in the system, these observations show flexibility in the sample that has not previously been explored and underlines its complexity.

4.4 Magnetometry

The zero-field-cooled (ZFC) and field-cooled (FC) magnetic susceptibility of deuterated ammonia-poor sodium intercalated iron selenide of approximate composition $Na_{\sim0.175}(ND_3)_{\sim0.32}(ND_2)_{\sim0.18}FeSe$ (SXC090) in an applied field of 20 Oe between 2 and 60 K are shown in Figure 4.28. Two measurements of the sample are given, with the magnetisation reported as a volume susceptibility with dimensionless units as defined in chapter 2.2.8, page 60. In open circles is the measurement of the sample shortly after being synthesised in June 2012. In closed circles is the sample in January 2015 after cycling ammonia absorption/desorption in to and from the sample both in the *ex-situ* and *in-situ* experiments described previously in sections 4.2.2 and 4.3.4.1, respectively. The measurements are remarkably comparable under the circumstances; the aged sample has a slightly higher background susceptibility, due to the sensitivity of the technique this could be arising from a minute amount a magnetic impurity such as iron. The superconducting shielding fractions for the newly synthesised and aged samples as measured by the total drop in the susceptibility from above the superconducting transition to 2 K are 24 and 17 %, respectively. Both cases show a T_c as measured by the onset of superconductivity of 46 K, with a slight hump in the susceptibility curve around 32 K, which might be a second superconducting transition arising from sample inhomogeneity.

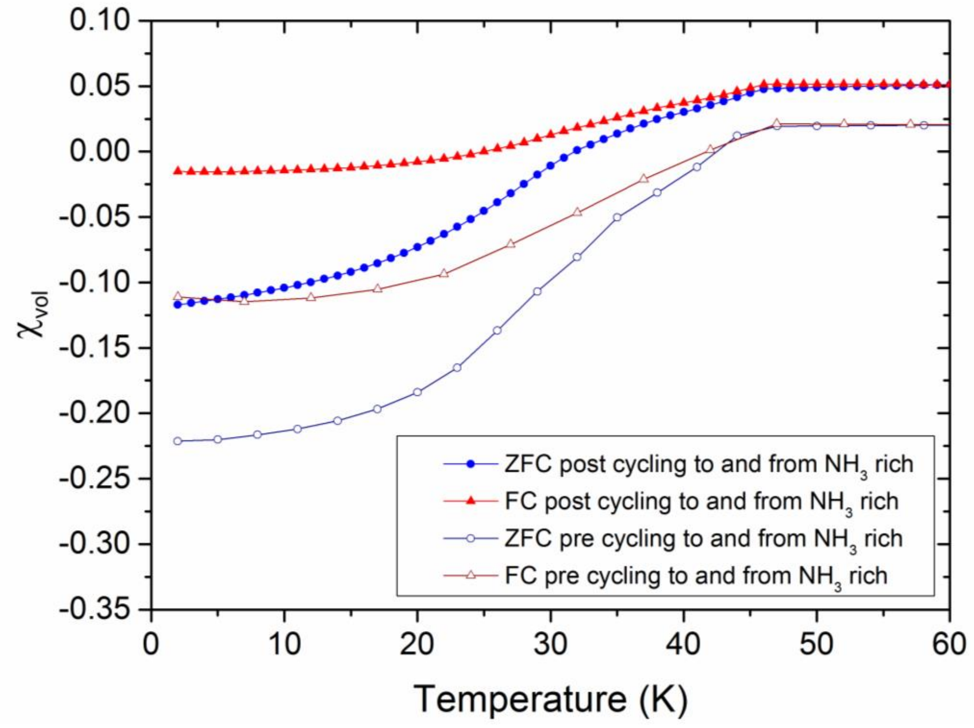

Figure 4.28 Zero-field-cooled and field-cooled magnetic susceptibility measurements

A comparison of the volume susceptibility, χ_{vol}, of several samples is given alongside their diffraction patterns in Figure 4.29. It is observed that samples SXC165 and SXC090, which have the highest proportion of the ammonia-poor intercalate phase in their diffraction patterns produce intercalate samples with the highest superconducting volume fractions, and clearest superconducting transitions at 46(1) K. A broad transition around 32 K is observed for several samples, and is most evident in sample SXC168, which was shown in the refinement corresponding to Figure 4.17 to contain ~15 % ammonia-poor sodium intercalate and ~85 % stacked phase. This lower T_c seems to be associated with the stacked phase and the samples that exhibit this transition exclusively, typically have a low superconducting volume fraction between 5 and 15 %. This transition appears to be distinct from the 37 K transition that Guo *et al*. reported for ammonia-free sodium intercalated iron selenide.[137]

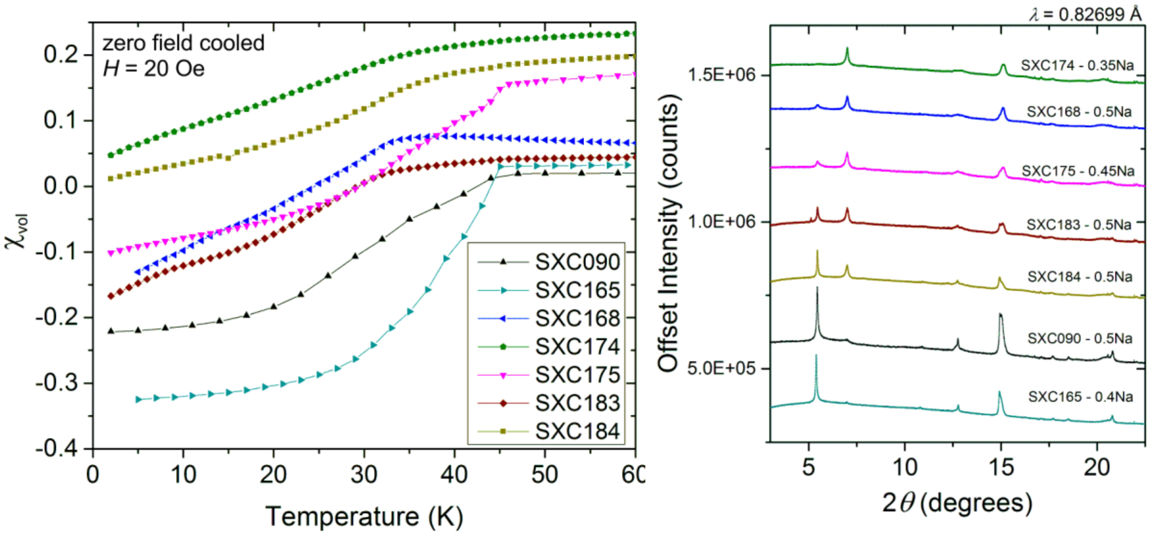

Figure 4.29 Magnetic volume susceptibility for several samples measured on warming from 2 to 60 K having been cooled in the absence of field, shown alongside the diffraction patterns for the samples.

The magnetic susceptibility of an ammonia-rich sample was measured by sealing a portion of an ammonia-poor sample under an ammonia atmosphere. This was performed by placing ~40 mg of sample (SXC175) in the bottom of a 5 mm diameter borosilicate tube in an argon-filled, dry glovebox, and closing by means of an attached Young's tap. The tube was removed from the glovebox and placed on a Schlenk line. The sample was cooled to -20 ± 5 °C and exposed to ~1 bar of ammonia pressure at that temperature for 3 hours. After that time the sample Young's tap was closed, the sample was placed in a liquid nitrogen bath, and the tube was sealed with a blowtorch, leaving an ammonia-rich sample with a partial pressure of ammonia inside the tube. The susceptibility of the ammonia-rich sample, plotted against that of the ammonia-poor parent material is shown in Figure 4.30. A T_c of 42 K is observed, reduced from 46 K in the ammonia-poor material, which is in line with the transition temperature reported by Guo *et al.*[137] A volume fraction of ~15 % is observed in the ammonia-rich sample, reduced from ~25 % in the starting material.

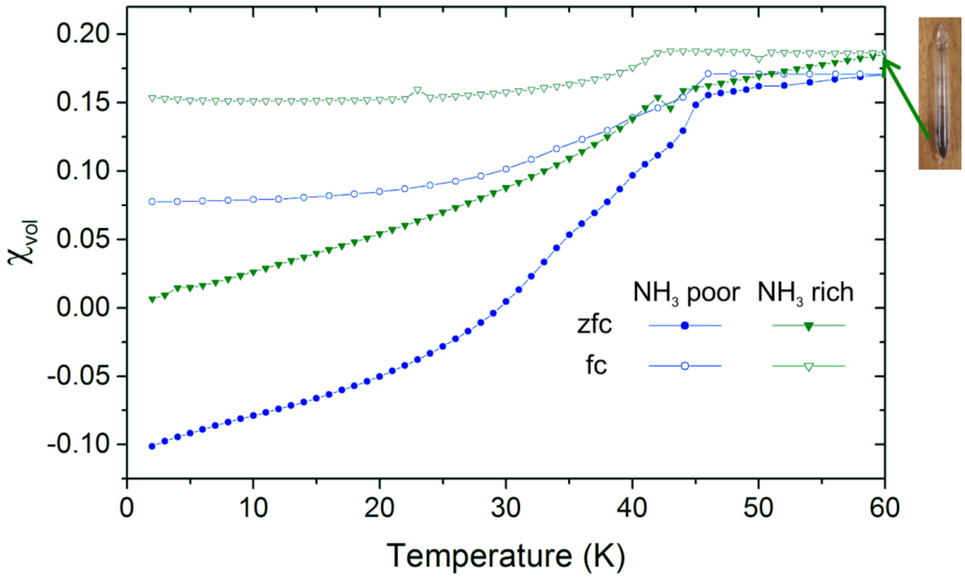

Figure 4.30 Magnetic volume susceptibility of ammonia-poor (SXC175) and ammonia-rich sodium intercalates of iron selenide. Measurements were performed in a 20 Oe field, both zero field cooled and field cooled. The ammonia-rich sample was prepared by sealing a portion of the ammonia-poor sample under an ammonia atmosphere.

4.5 Water intercalation

The observation of reversible addition of ammonia moieties in lithium- and sodium-intercalated iron selenide by exposure to the vapour raises the question of whether other polar molecules can be introduced into the interlayer.

As a test for decomposition of the sample in the air sensitive sample holders for X-ray diffraction, a 12 hour laboratory X-ray diffraction experiment was performed on a portion of sample SXC168 and the measurement was split into two 6 hour scans. The two scans shown in Figure 4.31 demonstrate the sample had converted in the sample holder over the course of about 4 hours into a highly crystalline single phase material. Rather than this phase being the ammonia-poor intercalate, the X-ray data could be accounted for using a structure similar to ammonia-rich lithium intercalate phase,[135] and ammonia-rich sodium intercalate described above, with an interlayer separation of 9.52 Å, which is between that of the ammonia-poor (~8.7 Å) and the ammonia-rich sodium intercalates (~11.0 Å).

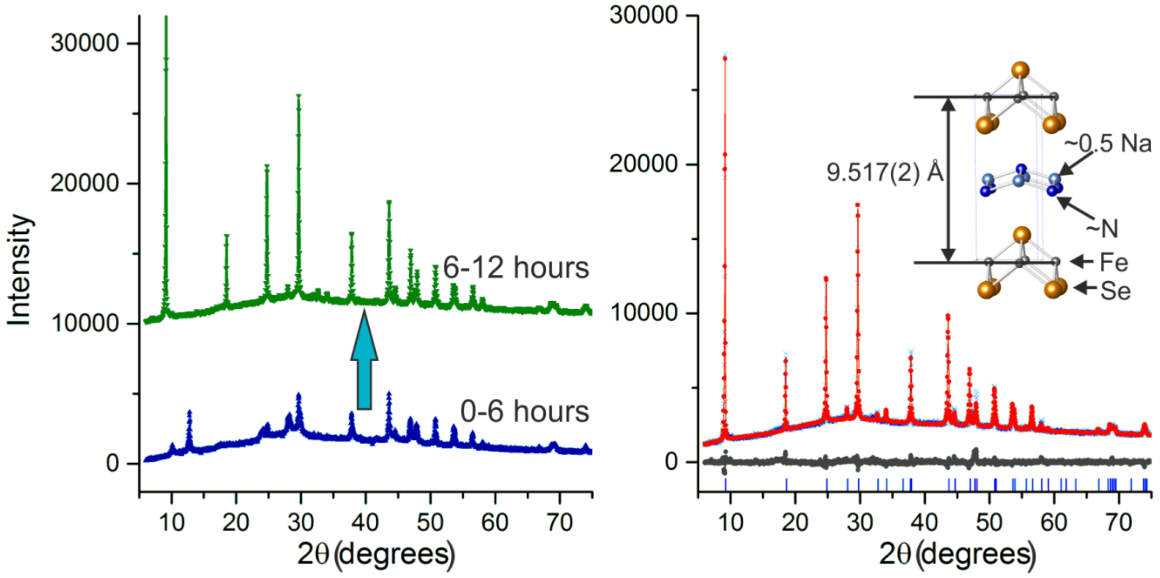

Figure 4.31 Left: two sequential 6 hour laboratory powder X-ray diffraction patterns (Cu $K_{\alpha 1}$) on a sample of nominal composition $Na_{0.5}(NH_{3-x})_{0.5-y}FeSe$ performed in a notionally air-tight sample holder showing the sample changing from a poorly crystalline multiphase sample to a highly crystalline single phase sample. Right: Rietveld refinement against the second six hour scan with the structure shown in the inset.

In a test of the same sample towards direct air exposure, rapid decomposition to a poorly crystalline FeSe phase was observed with a complete decomposition of the ~3 mg on the X-ray slide in around 30 minutes as shown in appendix V, ruling out a direct aerial oxidation process being responsible for the formation of the phase. This curious evolution was reproducible, new sample holders were designed with a different method of sealing, which showed the transformation occurring on a similar time scale. In each measurement, the sample was prepared in the an argon-filled, dry glovebox on a glass slide, sealed inside the sample holder, removed from the glovebox, and immediately measured by repeated laboratory X-ray diffraction patterns. The initial diffraction patterns for each slide were close to identical and the evolution transpired at similar rates.

The phenomenon was observed with multiple samples, SXC090, 168, 174, 183 and 184, the diffraction patterns of which were all shown previously in Figure 4.14, all showed the appearance of this phase over different time periods, and to different levels of completion before FeSe peaks began to appear in the pattern, presumably from aerial oxidation. This transformation is very similar to the absorption of ammonia into an ammonia-poor / stacked phase mix to produce a single ammonia-rich phase. It appears from the refinement that an additional source of an ammonia-like molecule, such as H_2O, is being supplied. The vapour transmission properties of the sample holder window material explain the origin of the water vapour, when comparing the transmission of water vapour and oxygen through a

0.025 mm thickness sheet of Mylar® film, approximately 2500 cc/100 in^2/24 hr of H_2O vapour are let through under the vapour pressure of the liquid at 38 °C (0.065 atm), whilst only 10 cc/100 in^2/24 hr of O_2 permeate the film at the same temperature under one atm of oxygen.[147]

In order to test the possibility that water vapour transmission was responsible for the sample evolution, the effects of sample concentration and window thickness were tested by measuring the evolution of a sodium-ammonia intercalated sample with a small sample mass and thin window, large sample mass and thin window, and large sample mass and thick window shown in Figure 4.32. For the larger sample mass, the sample was smoothed into an indented aluminium plate, this also eliminates the possibility of reaction between the sample and the vacuum grease holding it to the glass slide as the source of the transformation. It is seen that the transformation rate is dependent on both the amount of sample and the thickness of the window, strongly indicating that transmission of water vapour through the sample window is responsible.

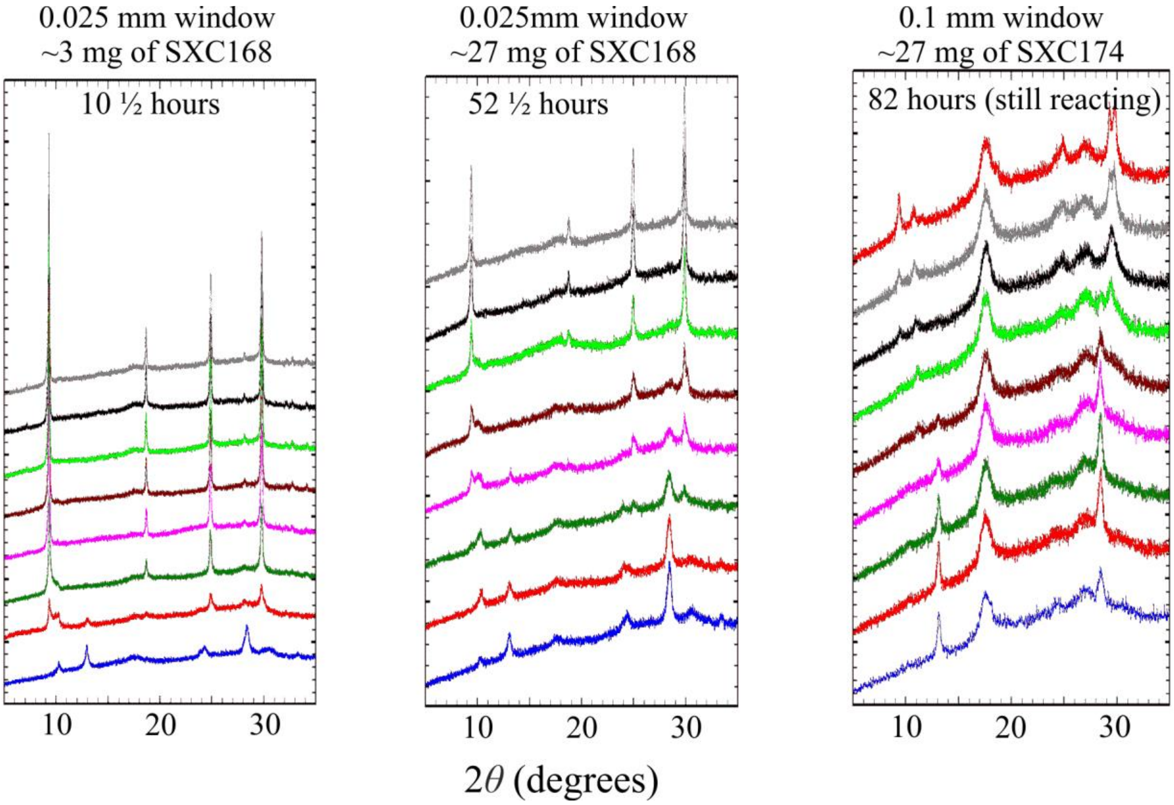

Figure 4.32 Evolution in laboratory diffraction patterns (Cu $K_{\alpha1}$) of sodium-ammonia intercalated iron selenide showing the effect of sample concentration and window thickness on the rate of water intercalation into sodium-ammonia/amide intercalated iron selenide via transmission through sample holder window. The broad feature at 17.5 ° and a smaller feature at 27 °, which are particularly strong in the third panel correspond to diffuse scattering peaks from the Mylar® window material.

It can be seen that the peak of the stacked phase at 14 ° diminishes in intensity as the (001) of the water intercalate grows in at 9 °, but between these two events the (002) of the ammonia-poor phase at 10 ° first increases then decreases in intensity. This indicates that the vacant ammonia sites in the stacked phase are first filled by H_2O giving presumably a mixed NH_3/H_2O version of the ammonia-poor phase, then there is a gradual conversion to the final water intercalate product. It is unclear as to whether water completely displaces all the ammonia in the structure or acts as a co-intercalate, neutron powder diffraction would be required to differentiate between the NH_3 and H_2O in the observed structure.

Attempts were made to replicate this behaviour in a controlled manner using a water vapour flow over the sample. To prepare a sample for powder neutron diffraction, inside a glovebox ~1 g of SXC183 non-deuterated Na-NH_3 intercalate of nominal composition $Na_{0.5}(NH_{3-x})_{0.5-y}FeSe$ showing the same behaviour in the sample holders as SXC168 was placed in an alumina boat and closed inside a silica tube using two end caps. Moist argon was allowed to flow over the sample using the setup shown in Figure 4.33. The end caps were then closed and the tube was transferred into an argon-filled glove bag in which the powder was extracted and placed in a vanadium can. Three attempts were made using this method, in the first the flow was continued for 2 hours, the second for 20 hours, and the third for 30 hours switching the flow direction over the sample half way through the time. Unfortunately none of these attempts produced the desired product, having only a minority hydrated intercalate phase with ammonia-poor and decomposition phases also present.

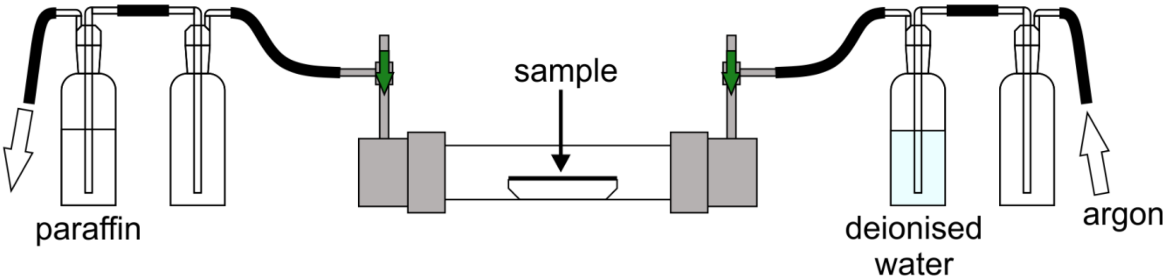

Figure 4.33 Schematic of the experimental setup used to expose ~1g of Na-NH_3 intercalated FeSe with H_2O vapour.

In an attempt to measure a hydrated sample using a synchrotron source, 0.5 mm diameter capillaries of SXC183 were loaded in the glovebox, the open ends were capped with vacuum grease and the capillaries were brought out onto the bench. A syringe was used to inject deionised water through the grease into the top of the capillary without contacting the sample where it sat in a layer above the sample with grease above it. The capillary was left in this state for overnight before sealing off the end to leave a moist argon atmosphere without any liquid water contained. Rietveld refinement against the diffraction pattern of one of the capillaries measured on I11 at Diamond Light Source shows that the sample has partially converted to the hydrated phase, with additional peaks from decomposition phases appearing as well, shown in Figure 4.34. The *a* and *c* lattice parameters for the hydrated phase from this refinement are 3.8749(3) and 9.482(2) Å, closely resembling those seen from the evolution of the ammonia-poor phase in the laboratory X-ray diffraction sample holders which are 3.8607(1) and 9.5179(6) Å, respectively.

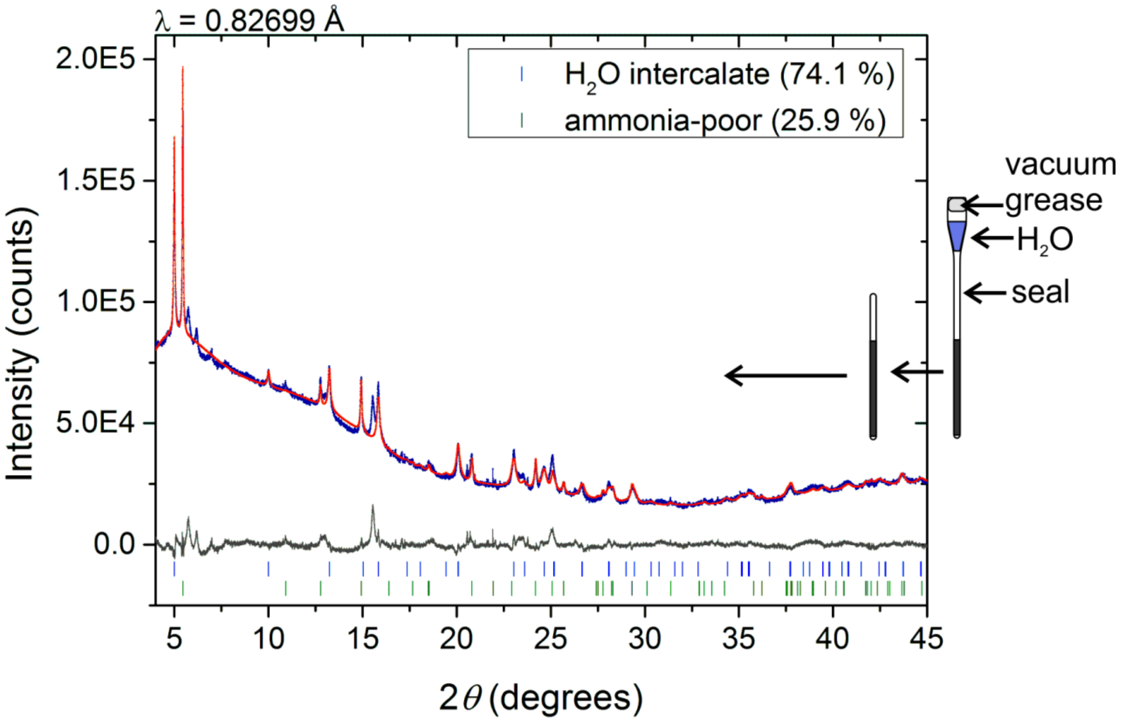

Figure 4.34 Rietveld refinement against a diffraction pattern of H_2O treated ammonia-poor sodium intercalated iron selenide taken on I11 at Diamond, UK. Sample is multiphase but does contain the same phase observed in Figure 4.31.

These results show that the absorption of water vapour by sodium and ammonia intercalated iron selenide is possible and in-fact a facile process, perhaps the early part of the decomposition in moist air. Further work is needed to develop a method of exposing the sample to a controlled atmosphere of solely moist argon, and a method of handling the sample such that it might be measured at a neutron facility in order to properly determine the structure.

4.6 Discussion, conclusions, and future work

The synthesis of sodium and ammonia intercalated iron selenide has been studied *in-situ* using powder X-ray diffraction. The products formed in ammonia solution by reaction of sodium with iron selenide are rich in intercalated ammonia, in line with the lithium system.[135] An activation energy for the reaction of 26.3 ± 1.6 $\mathrm{kJmol^{-1}}$ has been extracted by studying the intercalation at different temperatures. Future work might include a comparative study with the analogous lithium and ammonia intercalation system, and perhaps other alkali and alkaline earth metals.

Neutron powder diffraction has revealed the structure of the ammonia-rich sodium intercalate of iron selenide, which is much akin to that reported for the lithium- ammonia-system. Refinement of the nitrogen and deuterium content in the sample gives an N : D ratio of 1 : 2.8(1) which suggests partial formation of the amide, although not outside the second standard deviation of the error.

Upon removal of ammonia from the sample an ammonia-poor phase with half as much ammonia per formula unit is formed, this again shows similarity to the lithium system.[90] From Rietveld refinement against a powder X-ray diffraction pattern of a pure sample, a sodium content of 0.175(5) Na per FeSe was observed, which is consistent with the observation that using 0.15 Na is not enough to consume all the FeSe and the products using higher ratios of Na : FeSe do consume all the FeSe and produce similar products. The sodium content in the ammonia-rich sample could not be reliably extracted from the neutron refinement, refining to a value near zero but only with a small and unconvincing improvement to the agreement factor when compared to a value of 0.175.

The refined formula for the ammonia-rich phase is $\mathrm{Na_{0.175(11)}(ND_3)_{0.71(9)}(ND_2)_{0.18(9)}FeSe}$, (Na content constrained to match that obtained from the chemically sensible, refined composition of the ammonia-poor phase). The absolute formula suggests that there is no reduction of $\mathrm{Fe^{2+}}$ in the system, but within the first standard deviation of the errors $\mathrm{Fe^{2+}}$ may be reduced to $\mathrm{Fe^{1.904+}}$, and within the second to $\mathrm{Fe^{1.803+}}$. Experimental evidence and theoretical calculations[148] suggests that it is unlikely that iron is not reduced at all in the system. The refined occupancies of the lithium ammonia intercalate of iron selenide[90] show a slight reduction of iron to $\mathrm{Fe^{1.8(1)+}}$ and *ab initio* density functional theory calculations suggest that both the interlayer expansion and a slight electron doping of the Fermi level is necessary reach high T_cs in these systems.[148]

When the ammonia atmosphere around an ammonia-rich phase is removed by vacuum, it forms the ammonia-poor phase but a another phase is formed alongside in combination, which does not correspond to the ammonia-free phase observed by Guo *et al.*[137] (the ammonia-free phase is never clearly observed in this work). Characteristic features of this other phase are in the diffraction patterns of the ammonia-poor phases reported by both Ying *et al.*[89] and Guo *et al.*,[137] but they have not been modelled in their work. This second phase has been called the stacked phase in this thesis, which cannot be indexed to a high symmetry unit cell like the other phases. A reasonable fit to both X-ray and neutron powder diffraction data can be achieved by adopting a model with anti-PbO type FeSe layers with the sodium and ammonia spacer layer being present in only 6/14 layers, the remaining FeSe layers being separated only by the van der Waals gap. This model is not conclusive since a better fit to the data might be achieved with a more complex solution, such as a structure with a longer repeat-length than 14 layers, or a model with three types of layers. However, the stacked model provides vast improvement in the fit with respect to modelling the structure as a combination of non-stacked phases. Microscopy probes such as High-Angle Annular Dark Field Scanning Transmission Electron Microscopy (HAADF-STEM) might be able to validate the stacked model or otherwise provide insight into the nature of the structural distortion. This technique has been attempted on the analogous strontium system, but it was found that the samples decomposed too quickly in the electron beam.

It is found that samples with a high phase fraction of the ammonia-poor intercalate and low phase fraction of the stacked phase have a clear T_c at 46(1) K and the highest superconducting volume fractions, which goes to show that the ammonia-poor phase is indeed responsible for this transition as assigned in the reports by Ying *et al.*[89] and Guo *et al.*[137] A broad superconducting transition around 32(2) K is observed in several samples which contain the stacked phase, with superconducting volume fractions between 5 and 15 %. Its broad and varied nature is consistent with the stacking arrangement being sample dependant. The ammonia-rich sodium intercalate of iron selenide has been measured, and is found to have a T_c of 42(1) K, consistent with the transition determined by Guo *et al.* The superconducting volume fraction is found to decrease slightly when forming the ammonia-rich phase from a poorly crystalline sample containing a mixture of the ammonia-poor and stacked phases, from 24 to 17 %. Since the ammonia-rich phases have always appeared to be single phase with relatively improved crystallinity compared with the other phases, this observation suggests that the improved crystallinity is not enough to bolster the superconducting volume fraction. Further magnetometry measurements comparing the superconducting properties before and after it has been made ammonia-rich should be performed to establish whether this observation is continued in other samples.

Further synthesis in attempt to form a phase-pure ammonia-poor sample and investigate the controlling factors in the formation of the stacked phase could be attempted. One phase-pure ammonia-poor sodium intercalate sample was observed after the *in-situ* experiment when liquid ammonia gradually escaped from the reaction vessel at room temperature, a set of conditions worth replicating in a controlled way.

Cycling of the ammonia absorption from the ammonia-poor to the ammonia-rich has been shown to be a reversible process, which does not have any significant detrimental effect on the magnetic properties. Performing this cycling on HRPD at the ISIS neutron source has shown that the stacked phase is also able to reversibly absorb ammonia in order to form the phase pure ammonia-rich material, within the resolution of HRPD, and on application of vacuum returns to approximately the same stacked phase. Performing a similar cycling experiment on I11 at Diamond Light Source, the sample was shown to form a contracted version of the ammonia-rich phase with the distance between Fe in neighbouring FeSe layers reduced from 11 Å to 10.3 Å, in this phase. On warming this contracted ammonia-rich phase above 300 K under vacuum, the ammonia-poor phase is returned, but a phase separation within the ammonia-poor phase occurs and a contracted ammonia-poor phase appears, but only observed between ~350 and 475 K under vacuum. These observations are difficult to interpret with the current data and similar phases are not observed with the same sample under similar conditions in the neutron diffraction experiment but they do show further flexibility in the iron selenide layers, and that the phase diagram may be expanded even further.

Co-intercalation or exchange of water molecules with/ for ammonia is shown to be possible and a facile transformation. There have been many attempts and some successful reports of attempts to build on the intercalation of ammonia into iron selenide, by using other molecular solvents such as pyridine and ethylene-diamine as co-intercalates with the alkali metal. [149,150,151] These observations show that the intercalation of other polar protic molecules into iron selenide is possible and may be accessed through a new approach of post-synthesis exposure to solvent vapour.

Chapter 5

5. Potassium and ammonia intercalated iron selenide

5.1 Chapter introduction

The intercalation product of potassium and FeSe can be achieved in a high temperature reaction from the elements, but it seems that the majority product of this reaction is deficient in iron with a stoichiometry close to $K_{0.8}Fe_{1.6}Se_2$.[79] If the reaction 0.4 K + FeSe is attempted at elevated temperatures, rather than slightly reducing the average iron oxidation state to give $K_{0.8}Fe_2Se_2$, a disproportionation reaction occurs giving a potassium intercalate $K_{0.8}Fe_{1.6}Se_2$ with a nominal iron oxidation state of +2 plus a remainder of elemental iron.[79] Materials synthesised in this fashion do sometimes exhibit superconductivity, with T_cs of 30-40 K, however the superconducting phase is in the minority, thought to exist as a filament of composition $K_{\sim 0.3}Fe_2Se_2$ between layers the antiferromagnetic bulk phase, as was described in chapter 1.4.5, page 22.[80–87] Ying *et al*. reported that potassium intercalates into the interlayer space of FeSe in a low temperature reaction with liquid ammonia solvent, in the same fashion as Li and Na (and also Ba, Sr, Ca, Yb, and Eu) do.[89] Their report includes a diffraction pattern of a material with nominal composition $K_{0.5}FeSe_2$ that appears to contain multiple phases, and has a T_c of 40 K with a superconducting volume fraction of 11 %.

A follow up study by Ying *et al.* into the potassium-ammonia intercalate of iron selenide showed that for various samples of nominal composition of $K_x(NH_3)_yFe_2Se_2$ with x between 0.2 and 0.8, a phase gap opens between $x = 0.3$ and $x = 0.6$, where stoichiometries either side of this gap give quite different unit cell parameters and superconducting properties.[152] The compositions of their materials were determined by inductively coupled plasma atomic emission spectroscopy elemental analysis (ICP-AES), and the structures were reported from an indexing of X-ray diffraction patterns. $K_{0.3}(NH_3)_{0.47}Fe_2Se_2$ is reported to be a 44 K superconductor with an indexed *I*4/*mmm* unit cell of $a = 3.82$ Å and $c = 15.56$ Å. $K_{0.6}(NH_3)_{0.37}Fe_2Se_2$ is reported to be a 30 K superconductor, also indexed with an *I*4/*mmm* unit cell but with a shorter c cell parameter (=2 × the FeSe interlayer separation): a = 3.84 and c = 14.84 Å. Both are reported to be free of iron vacancies in the FeSe layer, and have superconducting volume fractions of around 50 %. The group described a method for extraction of ammonia from the intercalate sample whilst maintaining the topology of the lattice by slowly heating $K_{\sim0.3}(NH_3)_{0.47}Fe_2Se_2$ to 200 °C under dynamic vacuum. The product of this treatment had a reduced c lattice parameter of 14.28 Å, but with T_c unchanged at 44 K and only a small difference in the volume fraction, concluding that ammonia had been removed but had little effect on the superconductivity. By way of structural characterisation, Ying *et al.*[152] only show an indexing of the diffraction pattern in the supporting information, which shows very broad peaks and is shown to contain β-FeSe also. ICP-AES analysis on this phase is not given.

One significant point to note is that the 7.3-7.8 Å separation of the inter-FeSe-layer space in the reported $K_x(NH_3)_yFe_2Se_2$ phases is notably smaller than that of the reported $Li_x(NH_3)_yFe_2Se_2$ and $Na_x(NH_3)_yFe_2Se_2$ phases, in which there are separations of around 8.4 and 8.7 Å, respectively. This observation does not tally with the usual expectation that a larger cation leads to a larger interlayer separation, indicating that there is a considerable structural difference. In sodium- and ammonia- intercalated iron selenide, Na and NH_3 occupy different sites in the *I*4/*mmm* unit cell with sodium occupying the 2*b* Wyckoff position and the nitrogen of ammonia occupying the 2*a*. From a space filling perspective, potassium cannot stably occupy the 2*b* position in the reported unit cells and so must share the 2*a* position with ammonia; it is too large to occupy any other position between the layers. The two structures are shown side by side in Figure 5.1. This leads to the counterintuitive observation that the more potassium used in the reaction, the smaller the expansion of the iron selenide layers since a lower proportion of the larger ammonia species accompanies the potassium onto the 2*a* position.

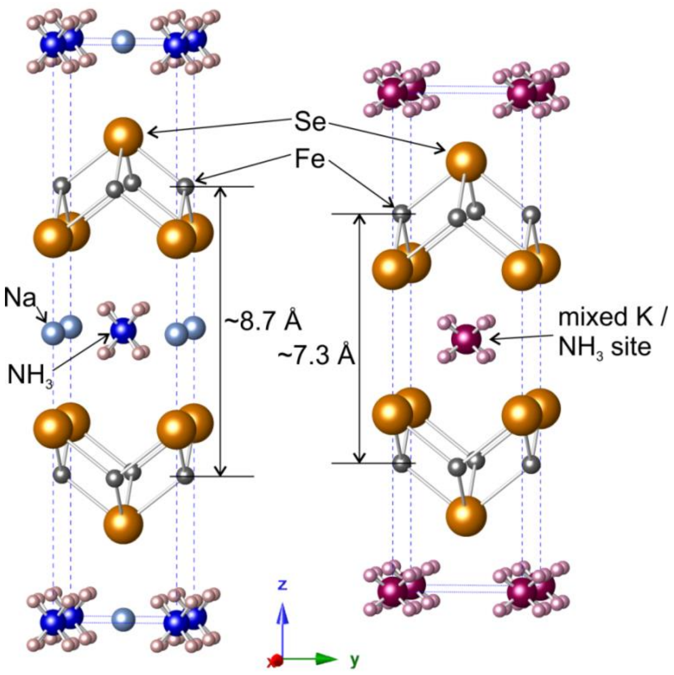

Figure 5.1 Comparison of the ammonia-poor intercalates of iron selenide for sodium and potassium.

This chapter aims to provide structural analysis, principally by X-ray and neutron powder diffraction on the reported phases of $K_x(NH_{3-y})_zFe_2Se_2$, which has been lacking in the literature so far. The synthesis of these materials has been studied *in-situ* via powder X-ray diffraction using the method described in chapter 4, showing the formation of intermediates and giving qualitative information about relative rates of formation of the phases involved. Further *in-situ* X-ray diffraction analysis has been performed, studying the process of thermal decomposition of these materials that occurs via the formation of the iron vacancy containing materials $K_{1-x}Fe_{2-y}Se_2$.

Several new phases have been identified in this K-NH_3-FeSe system. In order to help clarify which phase is being referred to in the text, the phases have been suffixed with the approximate separation between the equivalent iron sites in adjacent FeSe layers between brackets, in units of Ångströms.

5.2 Ammonia-rich potassium intercalated iron selenide

The syntheses of several potassium-ammonia intercalates of iron selenide were studied using *in-situ* powder X-ray diffraction, in unison with the experiments performed on the equivalent lithium and sodium systems on beamline I12 at Diamond Light Source. Diffraction patterns were taken continuously as the synthesis was performed, in the same fashion described in chapter 4.1 for the intercalation of sodium. As before, two dimensional diffraction patterns taken with the plate detector have been converted to one dimensional patterns by integration of the diffraction rings using the program FIT2D.[145] Graphical representation of the change in the diffraction patterns as a function of time is given by surface plots of the diffraction patterns with intensity indicated by colour. The patterns used for colour surface plotting are copies of the integrated data that have undergone a batch mode, background subtraction using Bruckner's algorithm.[146] All Rietveld refinements described in this chapter used the original, uncorrected data.

Investigations were performed on the synthesis of samples with K: FeSe ratios of 0.15 and 0.3 : 1, which Ying *et al.* had concluded in their report, correspond to two sides of a phase gap giving rise to different levels of expansion of the inter-FeSe layer space.[152]

5.2.1 Reaction of FeSe with 0.3 equivalents of K

13.1 mg of K were dissolved in ~4 ml of liquid ammonia in the bottom of a thick-walled borosilicate vessel, with 150 mg of FeSe in an isolated side arm (0.3 molar equivalents of K per FeSe). The reaction vessel was placed in a dry ice-isopropanol cooling bath contained in a bowl-shaped, glass vacuum dewar. Diffraction patterns were continually collected every 5 seconds as a mechanical rotation tipped the FeSe into the stirring solution of potassium and ammonia. The temperature of the isopropanol cooling bath at the beginning of the reaction was around -60 °C, the cooling bath was not supplied with additional dry-ice during the reaction, therefore, warmed towards room temperature over the course of about an hour.

A colour surface plot of the diffraction patterns taken during the first 30 minutes of the reaction is given in Figure 5.2. Iron selenide peaks are seen to diminish as product peaks grow in intensity. A single reflection from a crystalline intermediate peak was observed briefly at a *d*-spacing of 11.55 Å. Measurement of the reaction was continued for a total of 85 minutes, after which time the reaction vessel was set aside (not stirring). A final, single diffraction pattern of the product in the reaction vessel with ammonia was obtained after approximately 18 hours. A Rietveld refinement of this final diffraction pattern is shown in Figure 5.3 with the refined parameters reported in Table 5.1. The pattern's background was modelled with the convolution of a 3 parameter lognormal distribution and a 12th order Chebyshev polynomial.

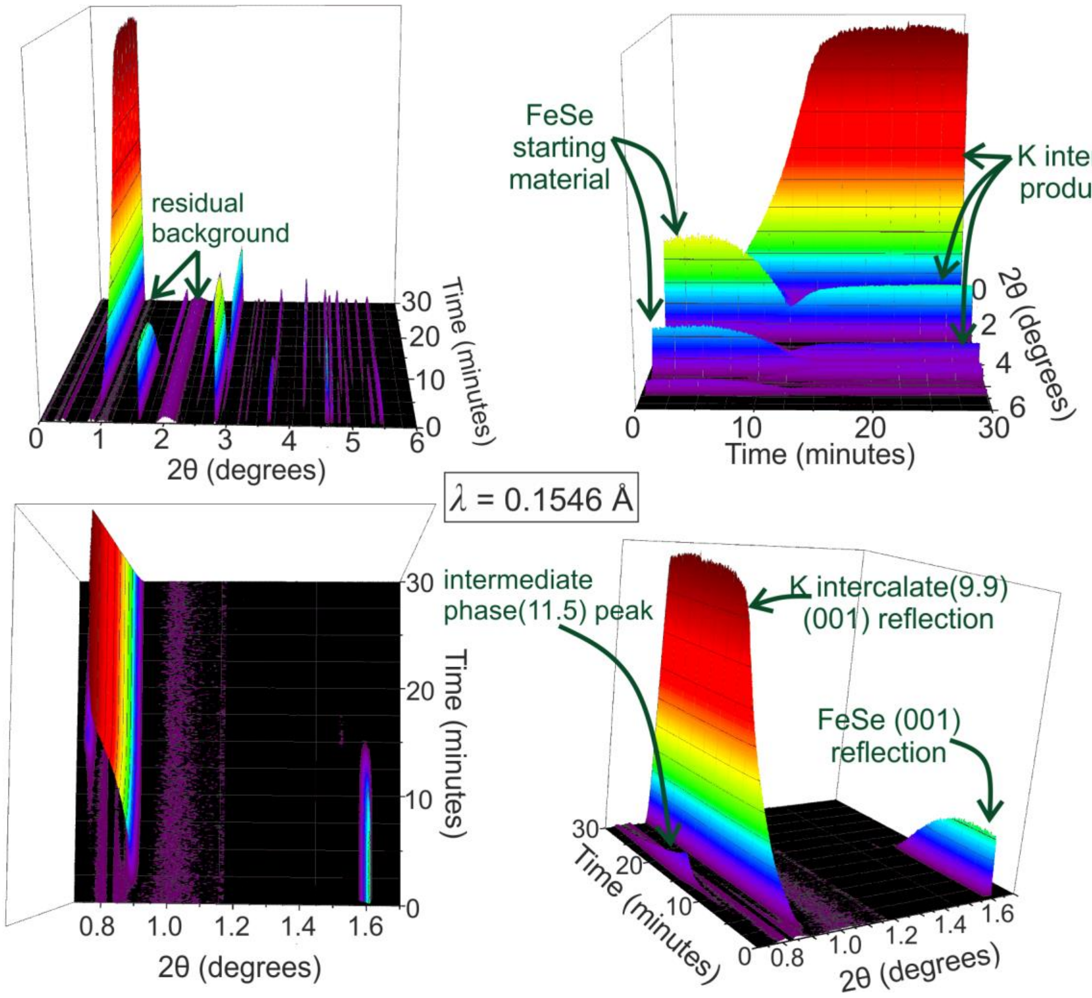

Figure 5.2 Surface plot of the X-ray diffraction patterns collected *in-situ* as 0.3 equivalents of K were reacted with 1 equivalent of FeSe in ammonia solution.

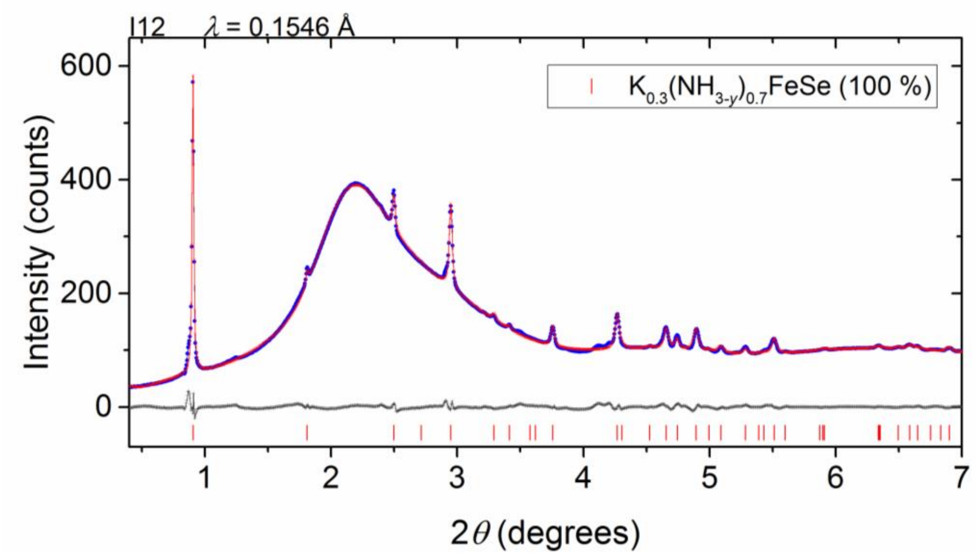

Figure 5.3 Rietveld refinement against the ammonia-rich final product(9.9) of the reaction of 0.3 equivalents of K with 1 equivalent of FeSe in ammonia solution. The pattern was taken at room temperature after the reaction was allowed to stir 'offline' for ~18 hours.

Table 5.1 Structural parameters from the Rietveld refinement shown in Figure 5.3. The N1-K2 bond distance is too short for a K-NH2/3 distance, indicating that the sites are not simultaneously occupied.

Space group	*P*4/*nmm*	**origin choice**	2
***a* / Å**	3.8409(3)	***c* / Å**	9.8800(6)
R_{wp} / %	1.61	**V / Å^3**	145.75 (3)
Fe-Se distance / Å	2.446(6)	**Temperature / °C**	22
N1-Se1 distance / Å	3.710(9)	**Se-Fe-Se α angle / °**	103.4(3)
N1-K2 distance / Å	2.119(7)	**Se-Fe-Se β angle / °**	112.57(5)

atom	**site**	**x**	**y**	**z**	**occupancy**	**U_{iso} / Å^2 × 100**
Fe1	2*a*	0.750	0.250	0	1	1.4(4)[a]
Se1	2*c*	0.250	0.250	0.152(1)	1	1.4(4)[a]
N1	2*c*	0.750	0.750	0.408(2)	0.57(5)	1.4(4)[a]
K1	2*c*	0.750	0.750	0.408(2)	0.43(5)	1.4(4)[a]
K2	2*b*	0.750	0.250	0.5	0.07(2)	1.4(4)[a]

The *in-situ* synthesis study of the intercalated materials has again revealed that the product in solution is an ammonia-rich phase, different from both compositional ranges described by Ying *et al.*[152] This obtained structure is similar to that of the ammonia-rich lithium and sodium intercalates but, remarkably, echoes the structural behaviour in the ammonia-poor intercalates in that the inter-FeSe-layer spacing of the ammonia-rich potassium intercalate (9.88 Å) is significantly smaller than that of the ammonia-rich lithium (10.5 Å) and sodium (11.0 Å) intercalates of iron selenide. The N1 site, which nitrogen solely occupies in the lithium and sodium analogues and will be referred to as site *A*, cannot be modelled as solely nitrogen in this potassium system as the nitrogen occupancy would refine to values above one, which shows that both ammonia and potassium share this position in the unit cell. The distance of site *A* from the Se1 position (3.710 Å) compares well with the distance of the Se-D distance in the deuterated-ammonia-rich lithium intercalate of FeSe (2.756 Å), plus a 1 Å N-H/D bond, supporting the conclusion that nitrogen does occupy this site and indicating that the bond angle, N-H-Se, is close to linear. The K2 site, which is equivalent to the sites that lithium and sodium occupy in their ammonia-rich intercalate structures and will be referred to as site *B*, appears to be vacant in this product(9.9): it has a refined occupancy close to zero and a distance to site *A* that is unreasonably small for a K-NH$_{2-3}$ separation when comparing to that in KNH$_2$ (~2.9 Å). The total occupancy of site *A* in the refinement in Table 5.1 is assumed to be one, as such, the occupancies of the N1 and K1 sites were constrained to sum to one. The occupancy refined for the K1 is actually higher than may reasonably be assumed from the stoichiometric ratio of the reactants, but the error on the value is still within three standard deviations the 0.3 maximum.

5.2.1.1 Batch Rietveld refinement

Rietveld refinement was carried out against each diffraction pattern in turn using a routine to systematically run the command line version of Topas academic for each pattern in turn, using the outputted parameters from one refinement as the input for the next.[113] The background of each pattern was modelled using a 3 parameter lognormal distribution and a 12th order Chebyshev polynomial, which was found to be sufficient to account for the background without modelling peak intensity. The peakshapes of all three phases (FeSe, product(9.9) and intermediate(11.5)) in the refinement were constrained to be the same to prevent an unrealistic broadening of any of the peaks to mistakenly fit the broad background. The starting material peaks are likely to broaden and the product peaks sharpen as the crystallite sizes shrink and grow, respectively, but with such a heavily featured background, this could not reasonably be refined. The intermediate phase(11.5) was given a fixed model based on the intermediate phase witnessed in the reaction of 0.15 equivalents of K with FeSe, described in the next section.

The percentage of each phase by mass as a function of reaction time is given in Figure 5.4, the reactant FeSe and product $K_{0.3}(NH_{3-y})_{0.7}FeSe$ phase(9.9) percentages cross at 50 % indicating a straight conversion. Curiously, the crystalline intermediate phase(11.5) only appears as a minor phase close to the end of the reaction. This is perhaps a consequence of the non-isothermal reaction temperature, the relative rates of formation of the intermediate(11.5) and product(9.9) may differ at different temperatures. The intermediate(11.5) may even be a stable product at certain narrow temperature range.

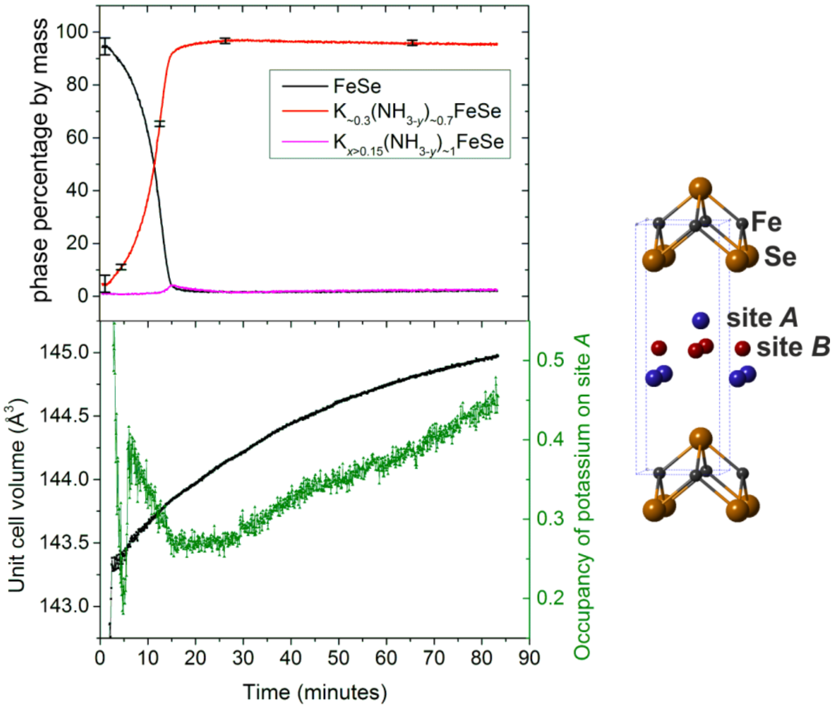

Figure 5.4 Results from a batch Rietveld refinement against all the diffraction patterns shown in Figure 5.2.

The reaction as judged by phase weight percentage appears to have completed after approximately 25 minutes, however the product(9.9) appears to continue to increase in unit cell volume after that time. The reaction was not performed isothermally, and it is not possible to confirm that this is not simply a thermal expansion, however the trend does seem to correlate to a steady increase in the scattering power (potassium occupancy) of the *A* site. If the *A* site were fully occupied after 25 minutes then it would be expected that an increase of potassium occupancy would decrease the volume of the unit cell, since it would require the replacement of the larger ammonia species. Since the volume and scattering power of the site *A* both increase over time it can be concluded that, if the increase in unit cell volume is not purely a result of thermal expansion, then the *A* site is not immediately fully occupied in this reaction scheme, but potassium and or ammonia gradually fill the site. The general trend of the occupancy of site *A* appears to be reliable after 15 minutes, once the product is of a reasonably high phase percentage. The refined values for the occupancy on the *A* site shown in Figure 5.4 are in-fact unreasonably high considering the ratio of K : FeSe. The dewar and isopropanol cooling bath introduce a particularly high background leading to the R_{wp} for a good refinement in these conditions being unreasonably low (~0.65 %). Therefore, the precise values of the refined occupancies and atomic coordinates in the unit cell carry fairly large uncertainties; however, the general trend will certainly reflect some change in the structure and does tally with the increasing volume. Further experiments are required to verify this result by determining whether the same trend is observed when the reaction is performed isothermally.

5.2.2 Reaction of FeSe with 0.15 equivalents of K

6.6 mg of K were dissolved in ~4 ml of liquid ammonia in the bottom of a thick-walled (4 mm) borosilicate vessel, with 150 mg of FeSe in an isolated side arm (0.15 molar equivalents of K per FeSe). The reaction vessel was kept at -78 °C before being installed in the beam-path, without the presence of a cooling bath or dewar. The reaction was performed at room temperature, however, the reactive solution of potassium in ammonia was not given time to equilibrate at room temperature in order to avoid complete decomposition of the solution to potassium amide. From the start of the reaction, the potassium in ammonia solution will have warmed from approximately -60 °C to room temperature over the course of approximately 15 minutes.

Diffraction patterns were initially collected for one second each, with a 0.5-second interval before the next frame. After the continual measurements were started, a mechanical rotation tipped the FeSe into the stirring reactive solution. 50 minutes in to the reaction, it was judged to be proceeding slowly enough to increase the data acquisition time to 4 seconds, with a 1 second interval between frames, this provided a better signal-to-noise ratio at the compromise of time resolution.

A colour surface plot of the diffraction patterns taken in just over two hours is given in Figure 5.5; a much more complicated story emerges in this reaction than the reaction with 0.3 equivalents of K. Throughout the reaction there are two well defined peaks present at low angle corresponding to two crystalline phases with different c lattice parameters. The peak at 0.77 ° (a d-spacing of 11.55 Å) appears rapidly at the start of the reaction then decreases in intensity. This peak can be assigned to what will be referred to as a crystalline intermediate phase(11.5). The second well-defined peak that begins at a 2θ angle of 0.90 ° (a d-spacing of 9.88 Å), in the early stages, corresponds to a phase with very similar lattice parameters to those observed in the final product(9.9) of the reaction of FeSe with 0.3 equivalents of K. As the reaction continues, the intensity of this peak diminishes, and then increases again, eventually forming the single remaining product. The decrease in intensity of the peak at 0.90 ° is linked with an increase in the inter-FeSe-layer separation in this phase as evidenced by a shift of its position towards lower angles. When the peak begins to increase in intensity again its position is roughly constant at 0.87 ° (a *d*-spacing of 10.10 Å). Between these two well-defined peaks exists a broad region of intensity, which is above the background level and not present at the start of the reaction. Broadening of this kind between the two phases indicates that conversion from one to the other occurs through some intermediary transition state with a highly metastable structure that is partway between the two structures. Modelling of this broad region might be achieved in a number of ways, in this work it has been treated as a poorly crystalline intermediate with a broad Gaussian peakshape as shown in the peak fit to the right of Figure 5.5. This phase is modelled across the whole pattern but, as a consequence of its broad peakshape, has little impact on the intensity outside of this low angle region other than a broad and small contribution to the background. The lattice parameters and unit cell contents have been constrained to be close to halfway between those in the crystalline intermediate and the product.

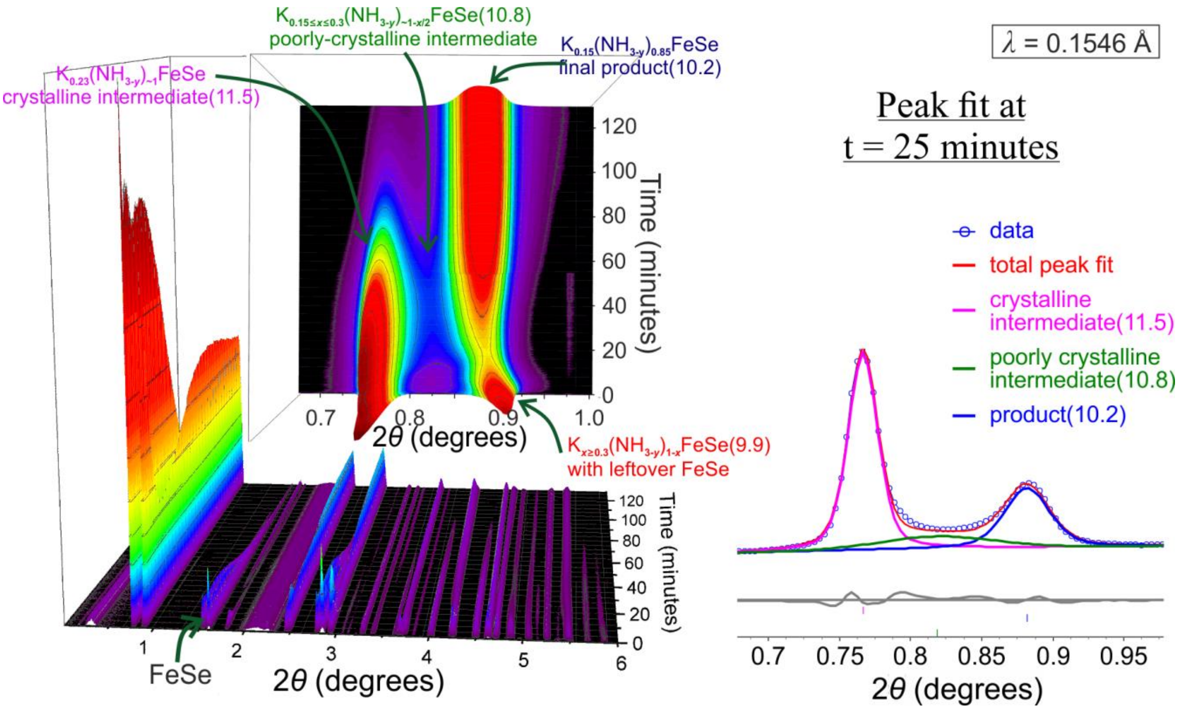

Figure 5.5 Left: surface plot of the X-ray diffraction patterns collected *in-situ* as 0.15 equivalents of K were reacted with 1 equivalent of FeSe in ammonia solution. Right: a peak fitting of the diffraction pattern at 25 minutes of the region of the diffraction pattern, which for these structures, relates to the separation of the iron selenide layers.

Individual Rietveld refinements against patterns at several points in time, including one against the material after 18 hours of continued stirring 'offline' are shown in Figure 5.6, with some of the refined structural parameters for each phase reported in the Tables following and full details of the refined parameters in appendix VIII. The final product is again a new ammonia-rich phase(10.2) with an inter-FeSe-layer spacing of 10.19 Å: significantly larger than the final product of the reaction with 0.3 equivalents of FeSe (9.88 Å), but far below that of the crystalline intermediate (11.55 Å). The occupancy of potassium on the proposed site *B* in the product is again consistently close to zero, which shows that again, potassium shares site *A* with the nitrogen of ammonia, contrary to the behaviour of the ammonia-rich lithium and sodium intercalates of iron selenide.

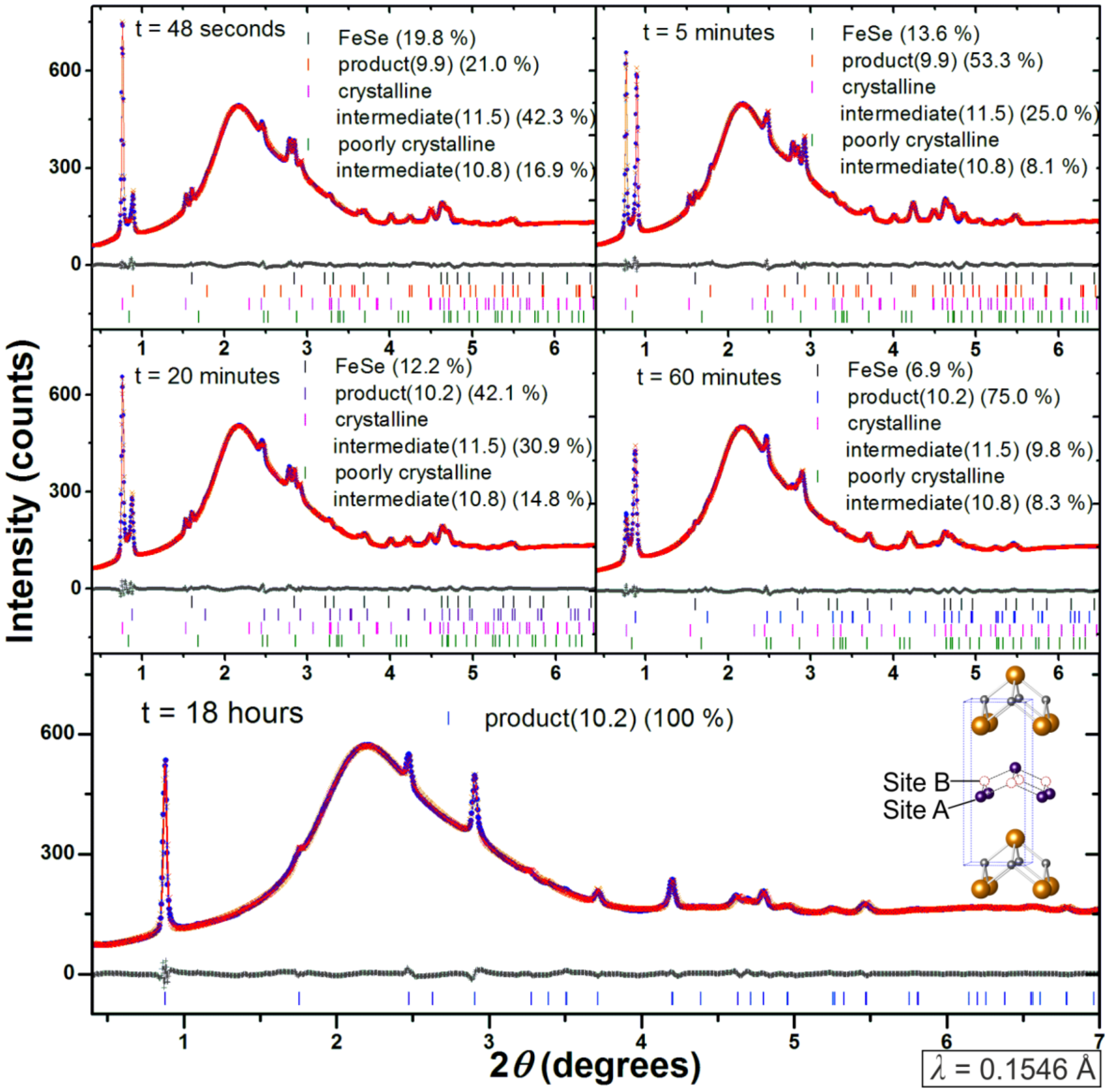

Figure 5.6 Rietveld refinements against diffraction patterns at several time intervals in the reaction of 0.15 equivalents of K with one FeSe in ammonia solution.

Table 5.2 Parameters from the Rietveld refinement shown in Figure 5.6 (top left pattern).

Reaction time	48 seconds		R_{wp}	1.18 %	
phase and weight percentage	**Unit cell parameters**		**site *A* occupancy of N**	**site *A* occupancy of K**	**site *B* occupancy of K**
	***a* (Å)**	***c* (Å)**			
crys. int. (11.5) 42.3%	3.8037(6)	11.5375(6)	0.83(3)	0.17(3)	0.18(3)
product (9.9) 21.0%	3.814(1)	9.898(2)	0.61(6)	0.39(6)	0.00(2)
poorly crys.int. (10.8) 16.9%	3.803	10.491	0.9	0.1	0.1

Table 5.3 Parameters from the Rietveld refinement shown in Figure 5.6 (top right pattern).

Reaction time	5 minutes		R_{wp}	1.24 %	
phase and weight percentage	**Unit cell parameters**		**site *A* occupancy of N**	**site *A* occupancy of K**	**site *B* occupancy of K**
	***a* (Å)**	***c* (Å)**			
crys. int. (11.5) 25.0%	3.8053(6)	11.5589(6)	0.83(4)	0.17(4)	0.19(4)
product (9.9) 53.3%	3.8229(4)	9.8951(6)	0.61(4)	0.39(4)	0.00(2)
poorly crys.int. (10.8) 8.1%	3.803	10.491	0.9	0.1	0.1

Table 5.4 Parameters from the Rietveld refinement shown in Figure 5.6 (middle left pattern).

Reaction time	20 minutes		R_{wp}	1.31 %	
phase and weight percentage	**Unit cell parameters**		**site *A* occupancy of N**	**site *A* occupancy of K**	**site *B* occupancy of K**
	***a* (Å)**	***c* (Å)**			
crys. int. (11.5) 30.9%	3.8140(8)	11.5515(9)	0.84(5)	0.16(5)	0.16(3)
product (10.2) 42.1%	3.8229(4)	10.0186(6)	0.74(4)	0.26(4)	0.00(4)
poorly crys.int. (10.8) 14.8%	3.818(8)	10.82(4)	0.8	0.2	0.1

Table 5.5 Parameters from the Rietveld refinement shown in Figure 5.6 (middle right pattern).

Reaction time	60 minutes		R_{wp}		1.00 %
phase and weight percentage	Unit cell parameters		site *A* occupancy of N	site *A* occupancy of K	site *B* occupancy of K
	a (Å)	*c* (Å)			
crys. int. (11.5) 9.8%	3.826(2)	11.496(3)	0.82(9)	0.18(9)	0.14(5)
product (10.2) 75.0%	3.8331(5)	10.103(2)	0.72(4)	0.28(4)	0.00(1)
poorly crys.int. (10.8) 8.3%	3.813(9)	10.75(5)	0.9	0.1	0.1

Table 5.6 Parameters from the Rietveld refinement shown in Figure 5.6 (bottom pattern).

Reaction time	18 hours		R_{wp}		0.98 %
phase and weight percentage	Unit cell parameters		site A occupancy of N	site A occupancy of K	site B occupancy of K
	a (Å)	*c* (Å)			
product (10.2) 100%	3.8601(4)	10.1899(9)	0.62(4)	0.38(4)	0.00(1)

Table 5.7 Full structural parameters for the final product of the K0.15 + FeSe reaction in liquid ammonia solution. The N1-K2 bond distance is too short for a K-NH2/3 distance, which supports the refinement of zero occupancy on the K2 site.

Space group	*P*4/*nmm*	origin choice	2
a / Å	3.8601(4)	*c* / Å	10.1899(9)
R_{wp} / %	1.61	Volume / Å^3	151.83(3)
Fe-Se distance / Å	2.464(6)	Temperature / °C	22
N1-Se1 distance / Å	3.84(2)	Se-Fe-Se *α* angle / °	103.2(3)
N1-K2 distance / Å	2.113(9)	Se-Fe-Se *β* angle / °	112.7(2)

atom	site	x	y	z	occupancy	U_{iso} / Å^2 × 100
Fe1	2*a*	0.750	0.250	0	1	1.6(3)[a]
Se1	2*c*	0.250	0.250	0.150(1)	1	1.6(3)[a]
N1	2*c*	0.750	0.750	0.415(2)	0.62(4)	1.6(3)[a]
K1	2*c*	0.750	0.750	0.415(2)	0.38(4)	1.6(3)[a]
K2	2*b*	0.750	0.250	0.5	0.00(1)	1.6(3)[a]

[a] thermal displacement parameters have all been constrained to a refine to single value

The crystalline intermediate(11.5) has an inter-FeSe-layer spacing that is consistent with the structure of the lithium and sodium intercalate systems, fitting nicely into a trend; Li - 10.59 Å,[135] Na - 11.00 Å, K – 11.55 Å. The site *B* occupancy of potassium in the crystalline intermediate(11.5) consistently refines to a positive, non-zero value and the site *A* occupancy of potassium is significantly lower than that refined in the final ammonia-rich product(10.2). Both of these facts support the conclusion that the observed intermediate(11.5) is analogous to the ammonia-rich lithium and sodium intercalates of iron selenide. Site *A* for the crystalline intermediate(11.5) is refined to have a partial occupancy of potassium indicating it may be shared between ammonia and a small fraction of potassium. However, from the quality of these data and without a pure sample it is not possible to conclude with any certainty that some potassium still shares site *A* in the intermediate(11.5). A comparison of the structures of the product and intermediate is given below in Figure 5.7.

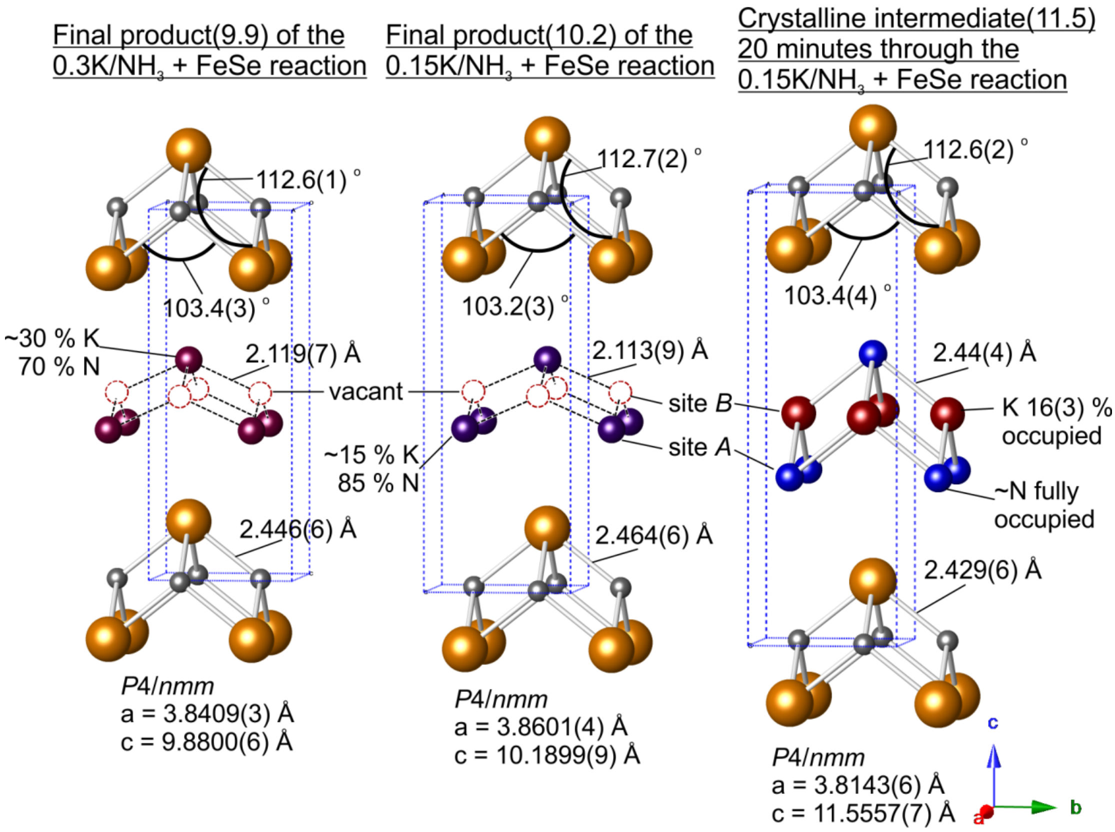

Final product(9.9) of the $0.3K/NH_3$ + FeSe reaction

Final product(10.2) of the $0.15K/NH_3$ + FeSe reaction

Crystalline intermediate(11.5) 20 minutes through the $0.15K/NH_3$ + FeSe reaction

Figure 5.7 Comparison of the structures of ammonia-rich potassium intercalated iron selenides

5.2.2.1 Batch Rietveld refinement

The systematic Rietveld refinement against all ~3000 diffraction patterns was performed in the same manner as described in for the case of the reaction with 0.3 potassium equivalents. A total of four Rietveld phase models were included in the refinement: the starting material (FeSe), the crystalline intermediate(11.5), the poorly crystalline intermediate(10.8), and a single model for the initially formed product(9.9), which shifts in position to become the final product(10.2). The peakshapes of the crystalline intermediate(11.5), the product(9.9-10.2), and FeSe were found to vary from one another considerably, and as such could not be refined using only one function. The peakshapes of these three phases were each refined individually using a two Gaussian and Lorentzian parameters, and given limits such that the peakshapes could not become broad enough to incorrectly model the background. The peakshape of the poorly crystalline intermediate(10.8) was given a fixed Lorentzian component and allowed to refine with a single Gaussian term that was constrained to appropriate width limits. Its lattice parameters were given limits to prevent them from moving more than ~0.1 Å from the halfway point between those of the crystalline intermediate and product. The unit cell contents were fixed at an appropriate-midway value. The percentage of each phase by weight as a function of reaction time is given in Figure 5.8.

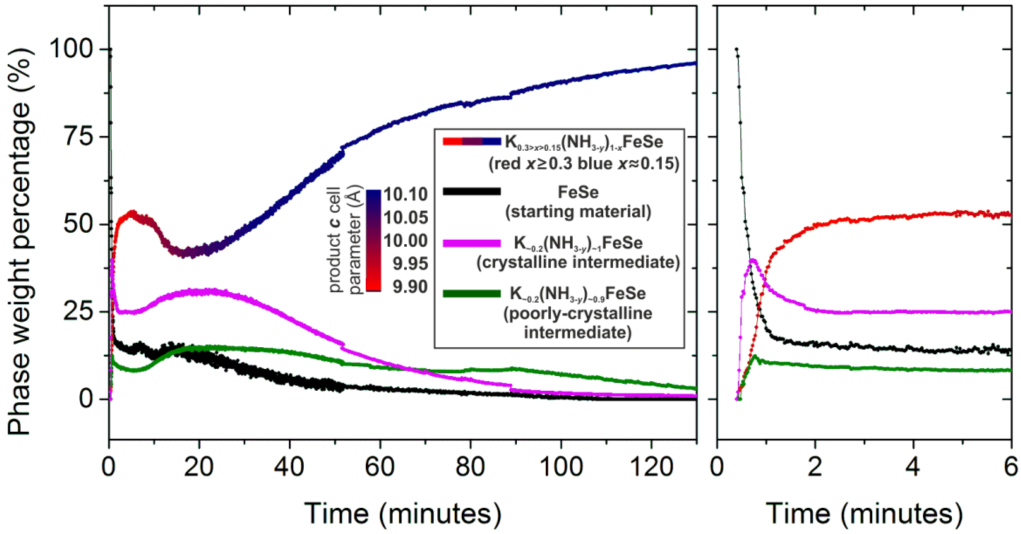

Figure 5.8 Phase percentages by mass of starting materials, products and intermediates in the reaction of 0.15 equivalents of potassium with iron selenide as a function of time, as determined by Rietveld refinements of the diffraction patterns at 1.5 second intervals up to 47 minutes then 5 second intervals thereafter.

In the first minute of the reaction, the crystalline intermediate(11.5) (pink line) forms faster than the initial ammonia-rich product(9.9) (red line), but then begins to decrease in phase percentage as it converts to the final ammonia-rich product(10.2) (blue line) via the poorly crystalline intermediate(10.8) (green line). The product that initially forms does not consume all the FeSe, as evidenced by the sharp drop in FeSe phase percentage from 100 to 18 % followed by a much slower decrease. This indicates that the initially formed product(9.9) is richer in potassium, and its lattice parameters (a= 3.814(1), c = 9.898(2) Å) are consistent with the product of the reaction of FeSe with 0.3 equivalents. After two minutes of the reaction, a more gradual shift towards the final ammonia-rich product(10.2) (red line becomes blue), with which all the FeSe is consumed is observed. To accomplish this, potassium from the already-formed $K_{0.3}(NH_{3-y})_{0.7}FeSe$ phase(9.9) must be replaced by ammonia, before re-intercalating with ammonia into the unreacted FeSe to form $K_{0.15}(NH_{3-y})_{\sim 0.85}FeSe$(10.2). Between 5 and 25 minutes, as $K_{0.3}(NH_{3-y})_{\sim 0.7}FeSe$(9.9) transforms to $K_{0.15}(NH_{3-y})_{\sim 0.85}FeSe$(10.2), the phase percentage of this transforming product(9.9-10.2) decreases, while the phase percentage of the crystalline intermediate(11.5) $K_{\sim 0.2}(NH_{3-y})_{\sim 1}FeSe$ (pink line) increases. The phase percentage of the poorly crystalline state(10.8) (green line), which bridges between $K_{0.15\leq x\leq 0.3}(NH_{3-y})_{1-x}FeSe$ (red/blue) and $K_{\sim 0.2}(NH_{3-y})_{\sim 1}FeSe$ (pink) also increases in this 5 to 25 minute window. This ‘yo-yoing’ of the phase percentages of the intermediates shows that the phases are all interconverting, and implies the intermediates(11.5 and 10.8) may mediate the transformation of $K_{0.3}(NH_{3-y})_{\sim 0.7}FeSe$(9.9) to $K_{0.15}(NH_{3-y})_{\sim 0.85}FeSe$(10.2). After 25 minutes, when $K_{0.15}(NH_{3-y})_{\sim 0.85}FeSe$ is established as the product phase, the phase percentages of the intermediates decrease as the percentage of the final product increases. An overview of this reaction scheme is given in Figure 5.9.

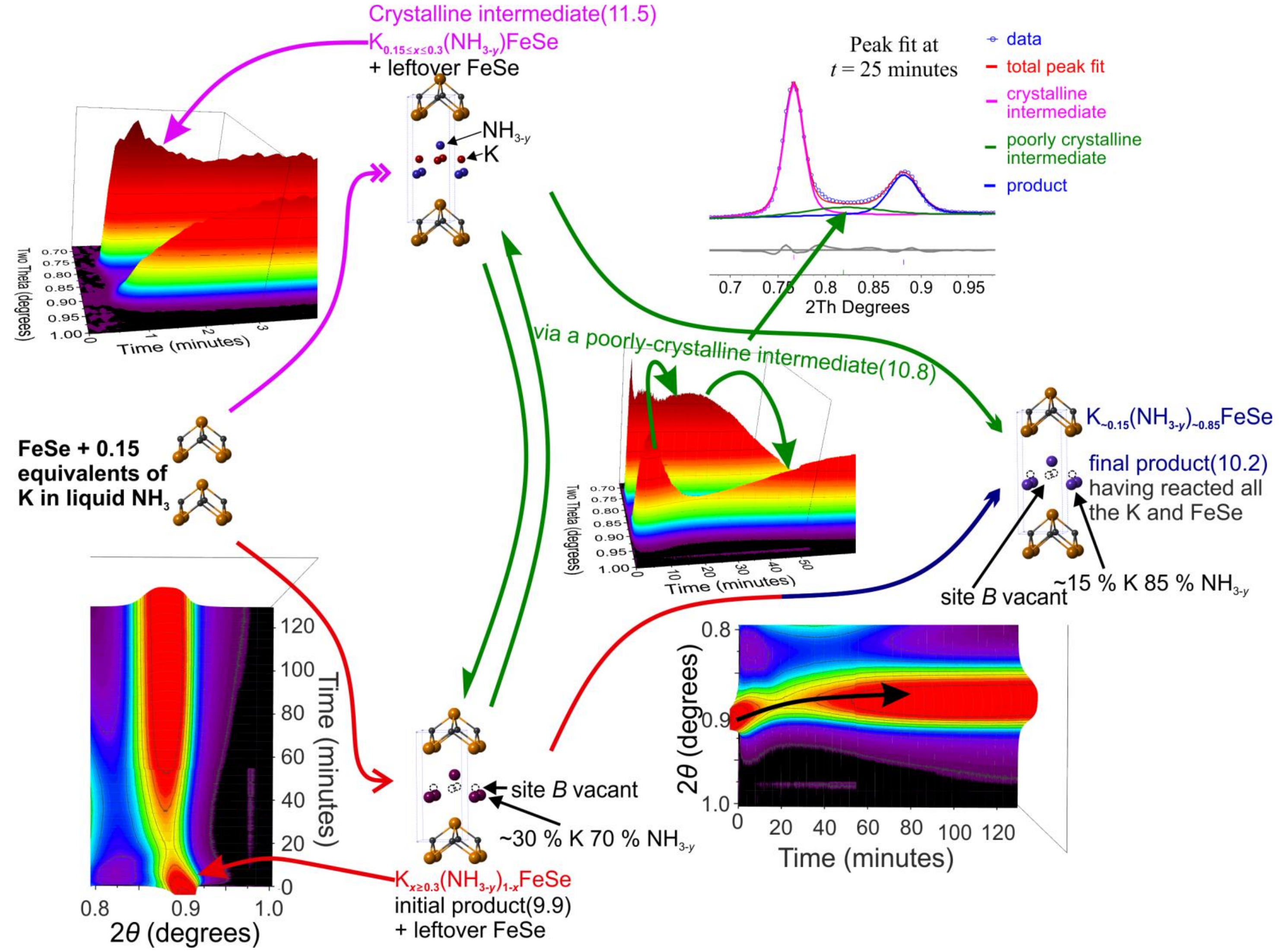

Figure 5.9 Reaction scheme for the reaction of 0.15 equivalents of potassium with 1 equivalent of FeSe in liquid ammonia solution.

Figure 5.10 looks at the volume of the ammonia-rich product phase(9.9-10.2) as a function of time, which shows a sharp increase until ~40 minutes, which tallies with the internal reaction:

$K_{0.3}(NH_{3\text{-}y})_{0.7\text{-}x}FeSe + FeSe + (1+x\text{-}x') NH_3 \rightarrow 2 K_{0.15}(NH_{3\text{-}y})_{0.85\text{-}x'}FeSe$ **Equation 5.1**

Then a more gradual increase in volume after 40 minutes occurs, similar to that observed in the reaction with 0.3 equivalents of potassium, which might be caused by a the gradual filling of vacancies on the site *A* in the structure.

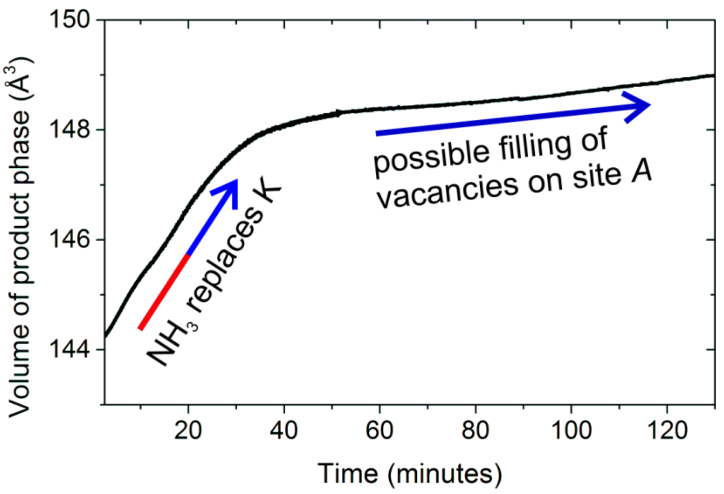

Figure 5.10 Plot of volume of the ammonia-rich product phase against time from the Rietveld refinement against all the diffraction patterns shown in Figure 5.5.

5.2.3 Summary of the ammonia-rich phases

The chemistry of the ammonia-rich potassium intercalates of iron selenide is dominated by potassium’s reluctance to occupy the same site in the crystal structure that lithium or sodium would (site *B*). The products formed in solution have potassium and ammonia sharing a single site (site *A*), in a similar way to the ammonia-poor products obtained after evacuation, which have been reported previously[152] and will be discussed in detail in section 5.3.

Very different behaviours are observed when FeSe is reacted with 0.15 equivalents of FeSe and 0.3 equivalents of FeSe. This may be partially influenced by the non-isothermal reaction conditions that were used but also reflects the rates that K and NH_3 are able to enter the structure. In both the reaction with 0.15 potassium equivalents and the reaction with 0.3, there is a continued gradual increase in the unit cell volume of the product even after the reaction appears complete. This increase in volume warrants further investigation: it may be just a thermal expansion but it may also be a sign of a continued absorption of ammonia – filling vacancies on the shared potassium / ammonia site (site *A*). From the reaction with 0.15 equivalents it is clear that all the potassium is consumed in a reaction with FeSe almost immediately, as evidenced by a discontinuous fall in the rate of FeSe consumption. A slower series of interconversions redistribute the potassium with the remaining unreacted FeSe, whilst ammonia continues to slowly enter the system. A second phase forms during the reaction that has been called the crystalline intermediate(11.5), which appears only in a minor and momentary fashion in the 0.3 equivalents reaction and in a major and more long-lived fashion with 0.15 equivalents, which is modelled with K and NH_3 occupying distinct sites in the structure. It is unclear at this time whether this phase might be stabilised at any particular stoichiometry, solution concentration, or temperature, which warrants further investigation. This crystalline intermediate phase(11.5) has the longest *c* lattice parameter of the K/NH_3 intercalates and most closely resembles the analogous ammonia-rich Li and Na intercalates of iron selenide.

Unfortunately the ammonia-poor potassium iron selenide intercalates are not susceptible towards re-ammoniation with exposure to the gas in the same manner as the lithium and sodium are. Attempts were made to re-expose deuterated samples to one bar of ammonia pressure at -20 °C in a vanadium can for neutron diffraction, in the same way as was performed for the lithium and sodium systems, however, no conversion back to the ammonia-rich phases was observed. This presumable indicates slow reaction kinetics.

5.3 The ammonia-poor potassium intercalates of iron selenide

Neutron and X-ray powder diffraction experiments were carried out in order to determine the structures of the ammonia-poor potassium intercalates, which are the products obtained after evaporation of the ammonia solvent and exposure of the ammonia-rich phases to vacuum. Two samples were synthesised with K : FeSe ratios of 0.15 : 1 and 0.3 : 1 using deuterated ammonia as the solvent. The same synthesis procedure as was used for the deuterated ammonia-poor sodium intercalate of iron selenide, described in section 4.2.2 (page 95), was used for both of these deuterated samples, using freshly cut pieces of K (Sigma Aldrich, 99.5%) in place of Na. The reaction using 0.3 equivalents of potassium per FeSe was allowed to stir for 2 hours after the ND_3 was condensed, the reaction using 0.15 equivalents was performed in a thick-walled Schlenk tube capable of withstanding 180 psi, which allowed the reaction solution to be warmed to 0 °C under ammonia pressure, and was stirred at this temperature overnight. Before recondensing the ND_3 that had been stirring at 0 °C, the reaction vessel was cooled to below -38 °C. After the ND_3 had been recaptured, the samples were each evacuated under dynamic vacuum for 3 minutes before returning them to the glovebox.

Neutron powder diffraction was performed on the ammonia-poor products using the GEM instrument at ISIS neutron source. The samples were loaded into vanadium cans inside an argon-filled, dry glovebox and sealed with a pressed indium gasket. Synchrotron powder X-ray diffraction was also performed, on beamline I11 at Diamond Light Source, with the same samples that were used for the neutron experiment prepared in sealed 0.5 mm diameter borosilicate capillaries under an argon atmosphere.

5.3.1 $K_{0.3}(ND_{2.6(4)})_{0.14(2)}FeSe$

5.3.1.1 Neutron Diffraction

For the ammonia-poor product of the reaction between 0.3 equivalents of K with FeSe in ND_3, data were collected at both room temperature and 5 K in a cryostat. Unfortunately, the 5 K data were complicated by the addition of a solid N_2 phase arising from a leak in the Cryostat, for this reason the room temperature data have been used for structural determination. Rietveld refinement was carried out in Topas version 5,[113] fitting simultaneously against time-of-flight diffraction patterns from all six of GEM's detector banks using one structural model. A broad peak, likely to originate from magnetic ordering, is observed in bank 1 (2θ = 9.4 °) and bank 2 (2θ = 18.0 °) at a *d*-spacing of around 10.8 Å, but not in any of the other banks. A model for the magnetic scattering has been included in banks 1 and 2 only. The sample's peakshape in each bank showed unusual broadening, which could be matched, to a reasonable degree, by inclusion of a Stephens type anisotropic peak broadening in the model,[153] but may be a sign of sample inhomogeneity. Due to the low occupancy of the deuterium site (between two and three eighths of the nitrogen site occupancy), a restraint to the distance between the nitrogen and deuterium has been included, stipulating that the distance should be 1.00 ± 0.05 Å.

Rietveld refinement of the nuclear unit cell against banks 4 and 6 are shown in Figure 5.11, alongside a diagram of the refined structure. The refined structural parameters are given in Table 5.8, fits to all 6 banks are given in appendix IX

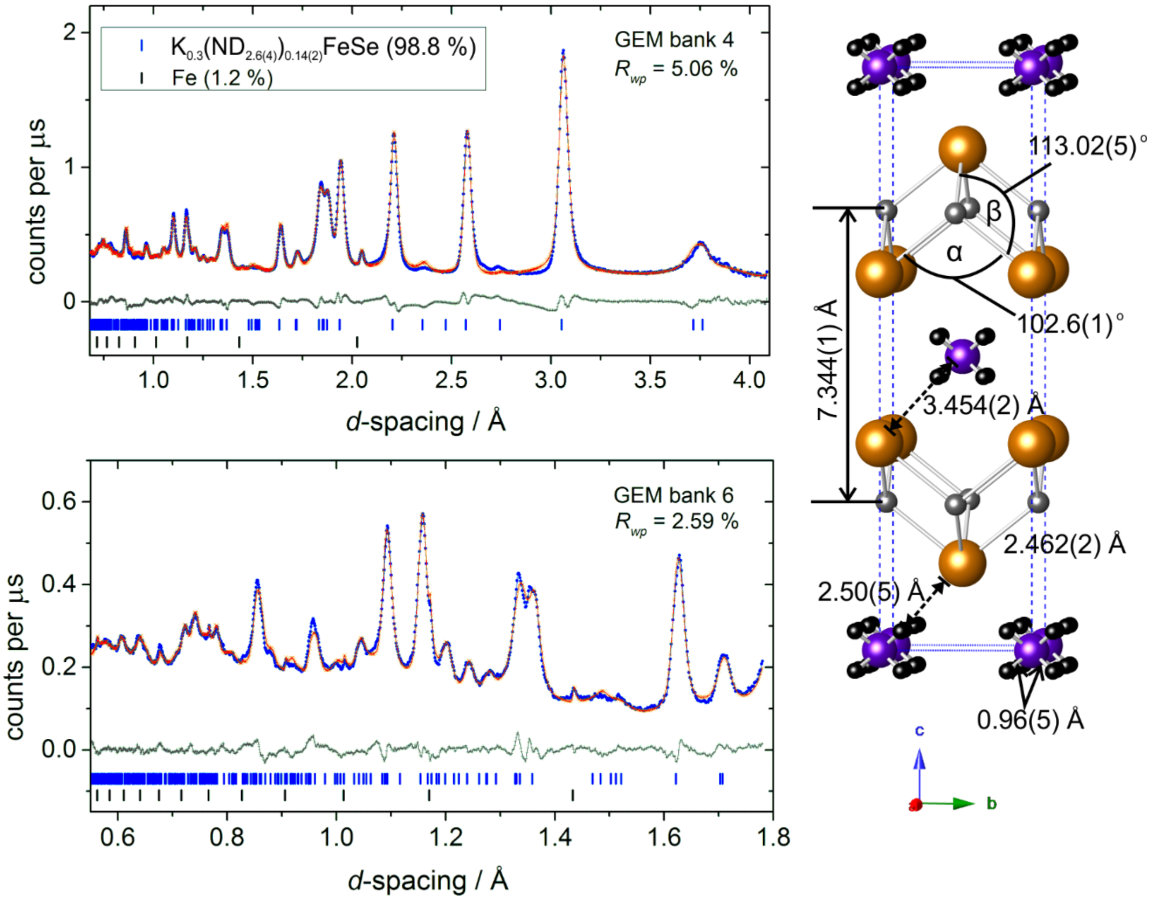

Figure 5.11 Rietveld refinement against time of flight neutron diffraction data from the GEM instrument at ISIS, showing two banks. The main phase(7.4) from the refinement is shown alongside the figure.

The structural trait of potassium and ammonia sharing a site that was seen in the ammonia-rich intercalate structures is continued in the ammonia-poor phases. It should be noted that neither ammonia or potassium have their ideal bond distances fully satisfied by sharing the site; the Se-D distance of 2.50(5) Å is shorter than usual for a Se-H bond in other intercalates (~2.75 Å), and the K-Se distance of 3.454(2) Å is longer than that in K_2Se (3.330 Å).[154] This dissatisfaction will, in part, give rise to the relatively poor crystallinity of the samples, as the local environment about ND_3 and K will distort to closer meet the ideal distances, which explains the highly anisotropic shape of selenium's thermal displacement ellipsoid, which is elongated along the *c* axis.

Table 5.8 Parameters obtained from the Rietveld refinement of $K_{0.3}(ND_{2.6(3)})_{0.14(2)}FeSe$, corresponding to the fit shown in Figure 5.11.

Temperature / K	295	***a* / Å**	3.8429(4)
Space group	*I*4/*mmm*	***c* / Å**	14.689(2)
R_{wp} / %	4.95	***V* / Å^3**	216.93(6)
N-D distance / Å	0.96(5)	**K-Se distance / Å**	3.454(2)
Fe-Se distance / Å	2.462(2)	**Se-Fe-Se (*α*) angle / °**	102.6(1)
D-Se distance / Å	2.50(5)	**Se-Fe-Se (*β*) angle / °**	113.02(5)

atom	**site**	**x**	**y**	**z**	**Occupancy**	**U_{11} / Å^2 × 100**	**U_{33} / Å^2 × 100**
Fe	4*d*	0	0.5	0.25	1.000(7)	1.09(4)	2.9(3)
Se	4*e*	0	0	0.3556(2)	1	0.10(7)	6.4(4)
N	2*a*	0	0	0	0.27(3)	6.9(8)	5.5(2)
K	2*a*	0	0	0	0.6	6.9(8)	5.5(2)
D	16*m*	0.151(9)	0.151(9)	0.034(3)	0.089(4)	6.9(8)	5.5(2)

Interestingly, this sample, which exhibits high T_c superconductivity as will be shown in section 5.4, shows signs of scattering from magnetic order, with a broad reflection at a *d*-spacing value around 10.8 Å that is not present in X-ray diffraction patterns of the same sample. Since only one reflection is clearly observed, the information that can extracted is limited and the degree of uncertainty in any modelling is high. That being said, an appropriate model will be put forth, which gives a good fit to the data and provides an idea of the magnitude of the magnetic moment that is associated with the intensity of the reflection.

The broad, high *d*-spacing reflection can be indexed to a √8 expansion of the nuclear unit cell along the *a* and *b* cell parameters. Knowing this, a √8×√8×1 supercell in *P*1 symmetry was built with the aid of ISODISTORT.[155] Rather than refining the magnitude of each iron moment in *x*, *y*, and *z* (96 variables), the ISODISTORT software represents these variables in a different format: as 96 symmetry adapted linear combinations (modes). Each mode produces an effect on several of the magnitudes of the iron moment in *x*, *y*, and *z*, and any given combination of the 32 iron moments in *x*, *y*, and *z*, can also be achieved by a combination of one or more of the 96 modes (the number depending on the degree of symmetry between the 32 iron moments). This gives a quick and convenient manner of modelling the symmetry relationships on the iron moments using the minimal number of variables, without having to impose the relations between the iron moments manually each time a new model is attempted.

The magnetic cell was refined separately from the nuclear cell, but modelling only the magnetic contributions to the scattering, and constraining atom positions and unit cell parameters to be equivalent to that of an expanded nuclear cell. Each single mode was trialled in turn and it was found that a double striped antiferromagnetic ordering, with the moments directed along *c* gave the best fit to the data (mode given label mDT2(a,b,c,d) [Fe:d:mag]A2 in ISODISTORT). The *a* and *b* axis are inequivalent in the magnetically ordered model, with ferromagnetic ordering along *c*, ferromagnetic ordering along *a*, and antiferromagnetic ordering of every other iron moment along *b*. This gives the magnetic ordering shown in Figure 5.12, with double stripes of ferromagnetically aligned spins, that are of antiferromagnetically aligned with each other. This ordering of spins can be described in magnetic space group P_Cbam (number 55.363 in Topas/ ISODISTORT, which use Belov-Neronova-Smirnova notation[156]), structural parameters are given in Table 5.9.

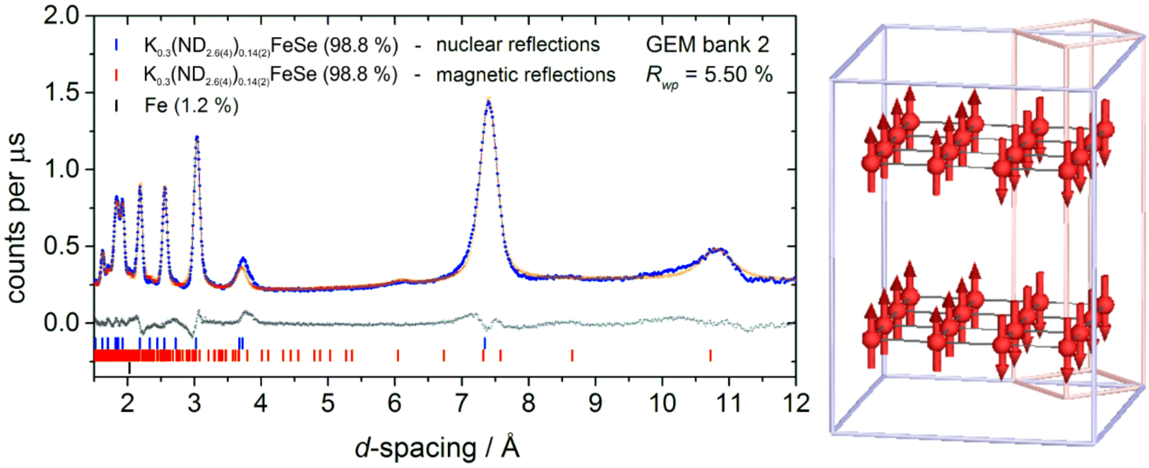

Figure 5.12 Rietveld refinement of the $K_{0.3}(ND_{2.6(3)})_{0.14(2)}FeSe$ phase(7.4) against time of flight neutron diffraction data from GEM's bank 2 (2*θ* = 18 °). Included in the model is the magnetically ordered structure of the Fe^{2+} moments shown to the right.

Table 5.9 Parameters for the magnetic component to the structure of $K_{0.3}(ND_{2.6(3)})_{0.14(3)}FeSe$, corresponding to the ordering shown in Figure 5.12.

space group	P_Cbam	***a***	10.869(8)
b	10.869(8)	***c***	14.689(2)

site	***x***	***Mx* / *µ***	***y***	***My* / *µ***	***z***	***Mz* / *µ***
Fe1	0.875	0	0.125	0	0.25	1.12(5)
Fe2	0.875	0	0.375	0	0.75	1.12(5)

It is worth comparing the magnetic ordering observed here to both the magnetic order in LaOFeAs and the order observed in $K_{0.8}Fe_{1.6}Se_2$. The ordered moment in LaOFeAs that is associated with the antiferromagnetically ordered state, closely bordering the superconducting state, has magnitude of around 0.1 μ_B, and has its onset around 150 K.[56] In $K_{0.8}Fe_{1.6}Se_2$ the antiferromagnetic state is a bulk ordering, seemingly not correlated to the superconducting state with an ordered moment of around 3.5 μ_B at room temperature.[78] In $K_{1-x}Fe_{2-y}Se_2$ samples, the magnetic order sometimes appears to coexist with superconductivity, but that is because there is an intrinsic phase separation into a magnetic portion of the sample that is separate from small regions that are compositionally different and exhibit the superconducting state.[80–84,87]

The magnetically ordered state in the $K_{0.3}(ND_{2.6(4)})_{0.14(2)}FeSe(7.4)$ more closely resembles that of $K_{0.8}Fe_{1.6}Se_2$, the ordered moment is larger than is typical of an iron based superconductor, and most convincingly; the sample still superconducts at ~30 K even with an ordered moment at room temperature. It is also observed that the moments in $K_{0.3}(ND_{2.6(4)})_{0.14(2)}FeSe(7.4)$ align along the *c* axis as they do in $K_{0.8}Fe_{1.6}Se_2$ rather than in the *ab* plane as they do in LaOFeAs (albeit with a degree of uncertainty since the magnetic model for the intercalated material is from only one peak). A comparison of the magnetic structures is given in Figure 5.13. An ordered magnetic moment of 1.12 μ_B is consistent with the superconducting volume fraction in this sample being only ~15 % if there is some degree of phase separation into magnetically ordered and superconducting phases that is not detectable in the neutron powder diffraction.

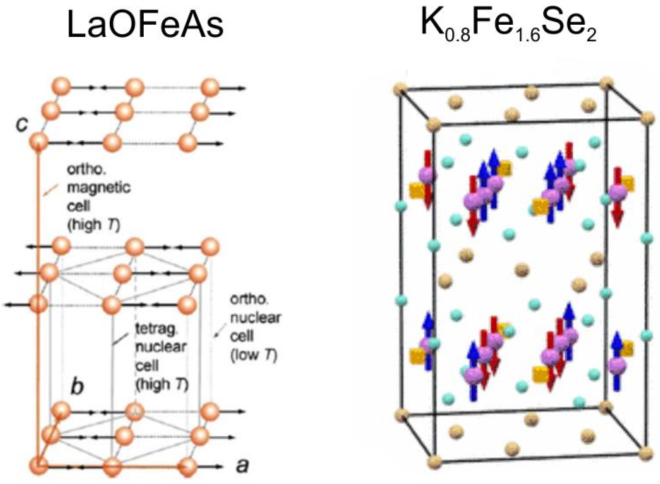
LaOFeAs

$K_{0.8}Fe_{1.6}Se_2$

Figure 5.13 Literature magnetic structures for LaOFeAs, taken from reference 56 **and $K_{0.8}Fe_{1.6}Se_2$ taken from reference** 78**.**

5.3.1.2 Synchrotron X-ray diffraction

Higher resolution is currently attainable at synchrotrons with X-rays than at neutron sources, and so to assess the possibility of any phase separation: the same sample from the neutron diffraction experiment was measured on beamline I11 at Diamond Light Source.

Rietveld refinement against the diffraction pattern and the fit is shown in Figure 5.14. The peakshapes of the sample are broad again, a Stephens type anisotropic broadening[153] is required to model the peaks effectively. The poor crystallinity of these samples hinders the amount of information that can be extracted from the fit. A relatively low number of peaks are resolvable since there is an intensity drop off as a function of 2θ in X-ray diffraction, and the poor crystallinity broadens peaks, flattening them at high angles. The structure of the potassium intercalates is complex, and to fit the X-ray diffraction data to a high standard requires a more complicated model than the data can reliably be used to extract: the fit shown in Figure 5.14, which is clearly not perfect, has an R_{wp} of 0.93 %.

There are signs in the X-ray diffraction pattern, marked by black arrows in the inset of Figure 5.14, that the sample contains approximately four molar percent of the vacancy ordered form of $K_{0.8}Fe_{1.6}Se_2$. This may be inherent to the sample, but could also have arisen when the capillary was sealed, since when heated above ~200 °C, the samples decompose to the $K_{0.8}Fe_{1.6}Se_2$ structure (as will be shown in section 5.4).

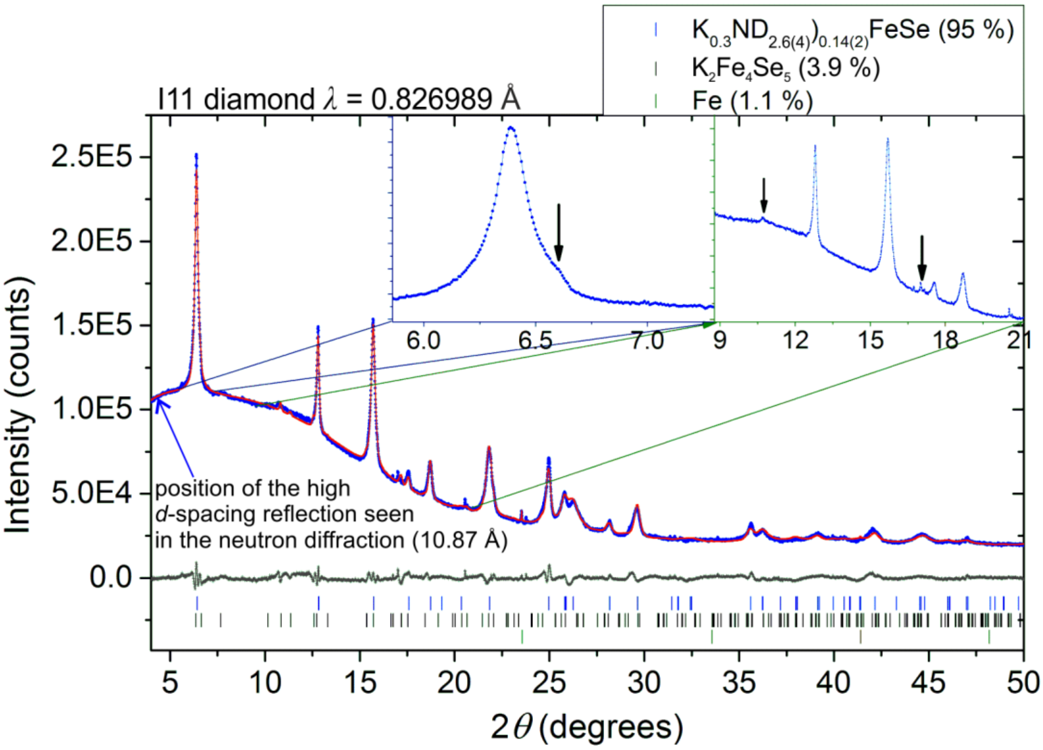

Figure 5.14 Rietveld refinement against the X-ray diffraction pattern of $K_{0.3}(ND_{2.6(4)})_{0.14(2)}FeSe(7.4)$ using the neutron model, with a small $K_2Fe_4Se_5$ impurity present.

5.3.2 $K_{0.15}(ND_{2.9(3)})_{0.35(3)}FeSe$

5.3.2.1 Neutron Diffraction

For the ammonia-poor product of the reaction between 0.15 equivalents of K with FeSe in ND_3, data were collected using the GEM instrument at ISIS at both room temperature and 5 K in a cryostat. As before, the room temperature data were used for the structural determination instead of the 5 K data due to a solid N_2 phase arising in the cryostat at low temperature. Rietveld refinement was carried out in Topas version 5,[113] fitting simultaneously against time-of-flight diffraction patterns from all six of GEM's detector banks using one structural model. No magnetic scattering was observed in either the room temperature or 5 K diffraction patterns. A Stephens type anisotropic peak broadening has again been included in the model,[153] but sample peakshapes again suggest there may be some inhomogeneity. The reaction was found to leave some unreacted FeSe starting material, consistent with the work of Ying *et al.*[152].

Rietveld refinement of the nuclear unit cell against banks 4 and 6 are shown in Figure 5.15, alongside a diagram of the refined structure. The refined structural parameters are given in Table 5.10, fits to all 6 banks are given in appendix IX.

The unit cell of this ammonia-poor phase(7.9) has a larger *c* parameter than the ammonia-poor phase(7.4) of section 5.3.1, a difference that arises from the differing levels of potassium and ammonia in the structure. A site displaced from nitrogen by around 0.6 Å in the *c* axis was identified, which consistently refined with non-zero scattering length. This distance is too short to be a deuterium but is 3.32(2) Å from selenium, which is the right distance from selenium to correspond to a K-Se bond (*cf.* 3.330 Å in K_2Se). Given that the K-Se distance is ~0.12 Å shorter than ideal in the ammonia-poor $K_{0.3}$ system(7.4), which has the smaller interlayer expansion out of the ammonia-poor $K_{0.15}$ and $K_{0.3}$ intercalates, it makes sense that the K site would be displaced from the (000) position in the unit cell in this case(7.9), because the distance between the (000) position and selenium is now 0.39 Å longer than the ideal K-Se distance.

The close approach of the potassium and nitrogen sites forbids them from being occupied at the same time in the local structure. Likewise, the *4e* site of potassium could only be a maximum of half occupied since two potassium positions 1.26 Å from each other cannot be mutually occupied. Large correlations exist between the occupancy of the potassium site and its thermal displacement parameters, as well as the occupancy and thermal displacement of the nitrogen site. The occupancy of the potassium site consistently refined to values higher than could reasonably be expected from the stoichiometries of the reactant materials, and so had to be fixed at 0.15 per FeSe. The occupancy of the nitrogen site was given a maximum limit in the refinement of 0.7, to which it readily refined. The deuterium occupancy refines to a sensible ratio of the 70 % occupied N site (2.9 × 2/16), which with the given nitrogen site occupancy corresponds to a slight amount of amide formation, and suggests a slight reduction in the iron oxidation state as well; in line with all other superconducting intercalates of iron selenide. However, the constraints imposed on the refinement lead to an additional degree of uncertainty regarding the exact composition of the material.

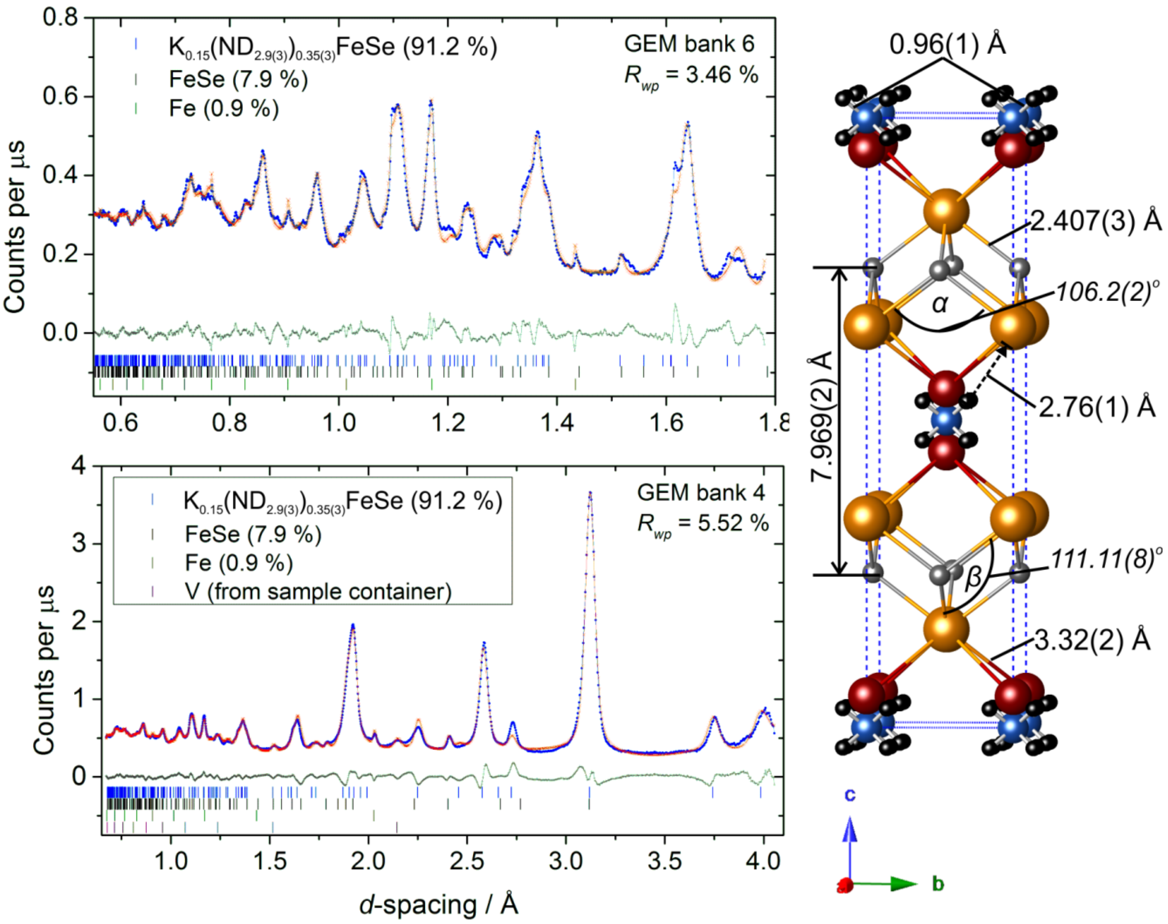

Figure 5.15 Rietveld refinement of the ammonia-poor potassium intercalate K$_{0.15}$(ND$_{2.9(3)}$)$_{0.35(3)}$FeSe phase(7.9) against time of flight neutron diffraction data from the GEM instrument at ISIS, showing two banks. The main phase from the refinement is shown alongside the figure, in which potassium is displaced from the origin along *c* to achieve a better bonding distance to selenium. The occupancies of the nitrogen and potassium site are such that only one species occupies the position between the layers at any one instance.

Table 5.10 Parameters obtained from Rietveld refinement of the $K_{0.15}(ND_{2.9(3)})_{0.35(3)}FeSe$ phase(7.9), corresponding to the fit shown in Figure 5.11.

Temperature / K	295	***a* / Å**	3.8503(3)
Space group	*I*4/*mmm*	***c* / Å**	15.938(3)
***R*$_{wp}$ / %**	4.76	***V* / Å^3**	236.27(6)
N-D distance / Å	0.96(1)	**K-Se distance / Å**	3.32(2)
Fe-Se distance / Å	2.407(3)	**Se-Fe-Se (*α*) angle / °**	106.2(2)
D-Se distance / Å	2.76(1)	**Se-Fe-Se (*β*) angle / °**	111.11(8)
N-Se distance / Å	3.721(3)		

atom	**site**	**x**	**y**	**z**	**Occupancy**	**U_{11} / Å^2 × 100**	**U_{33} / Å^2 × 100**
Fe	4*d*	0	0.5	0.25	0.98(2)	0.77(8)	5.2(5)
Se	4*e*	0	0	0.3406(3)	1	1.4(1)	4.9(5)
N	2*a*	0	0	0	0.70(5)	3.8(6)	0.0(9)
K	4*e*	0	0	0.040(6)	0.15	3.8(6)	0.0(9)
D	16*m*	0.133(2)	0.133(2)	0.0396(7)	0.254(9)	0.7(3)	0.5(1)

Unlike the $K_{0.3}$ ammonia-poor intercalate of iron selenide(7.4), the $K_{0.15}$ ammonia-poor intercalate(7.9) shows no sign of long-range magnetic order in the low angle banks of the GEM instrument. Figure 5.16 shows a Rietveld refinement including only the nuclear phase of the product and impurities against a diffraction pattern from Bank 2 (18 °) of the GEM instrument, with no magnetic structure.

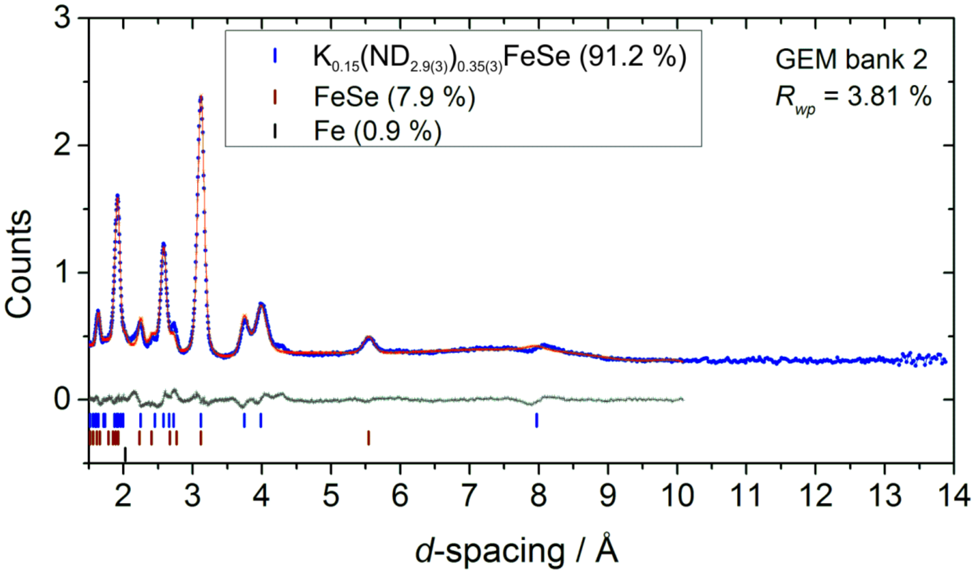

Figure 5.16 Rietveld refinement of the $K_{0.15}(ND_{2.9(3)})_{0.35(3)}FeSe$ model against time of flight neutron diffraction data from GEM's bank 2 (2*θ* = 18 °). No reflections from a magnetic ordering are observed.

5.3.2.2 Synchrotron X-ray diffraction

As with $K_{0.3}(ND_{2.6(4)})_{0.14(2)}FeSe$(7.4), the same sample(7.9) from the neutron diffraction experiment was measured on beamline I11 at Diamond Light Source in order to corroborate the neutron diffraction results and see if a higher resolution diffraction experiment could give any further insight as to the phase homogeneity. The diffraction pattern, shown in Figure 5.17, shows a large degree of asymmetric broadening towards higher angles, particularly in reflections with a large l component such as the (002) and the (013). The broadening of these peaks appears to be smooth, rather than a shoulder, which implies that it is not a separation into two phases, but a continual phase width. A broadening in this direction, on these reflections, shows that the c cell parameter, and hence the interlayer spacing, does not take a single value, but has a continuum, which spreads unevenly towards lower interlayer separations. One way to model such an asymmetry is with two or more phases with slightly different unit cell parameters and different peakshapes, and constraining the unit cell contents to be the same, as has been done in the bottom half of Figure 5.17. In this refinement one phase has a = 3.8541(2), c = 15.920(3) Å and the other a = 3.8218(9), c = 15.715(7) Å. Equivalent sites in both phases have the same occupancies, thermal displacement parameters, positions in the xy plane, and the same position along z relative to the c cell parameter. The occupancies used were those from the neutron refinement with deuterium sites omitted from the fit. Included also in the fit is a Stephens type anisotropic peak broadening function[153] for the phase with the larger unit cell, and a March-Dollase type preferred orientation term[157] in the (001) plane, which is also necessary to model the peaks to a high standard.

Even with a high resolution instrument, many of the observable reflections are coalesced and most peaks with d-spacings below 1.5 Å are flattened by thermal displacements and structural disorder such that they are hard to discern from the background. The information that can be reliably extracted from X-ray diffraction of these materials is limited, as shown the small value of R_{wp} (0.88 %) of the fit shown in Figure 5.17. It appears that the X-ray data are compatible with the model obtained from neutron diffraction, but show that the sample is inhomogeneous outside the resolution of the neutron diffraction experiment. These X-ray diffraction data are insufficient for accurate Rietveld refinement to characterise the inhomogeneity any further.

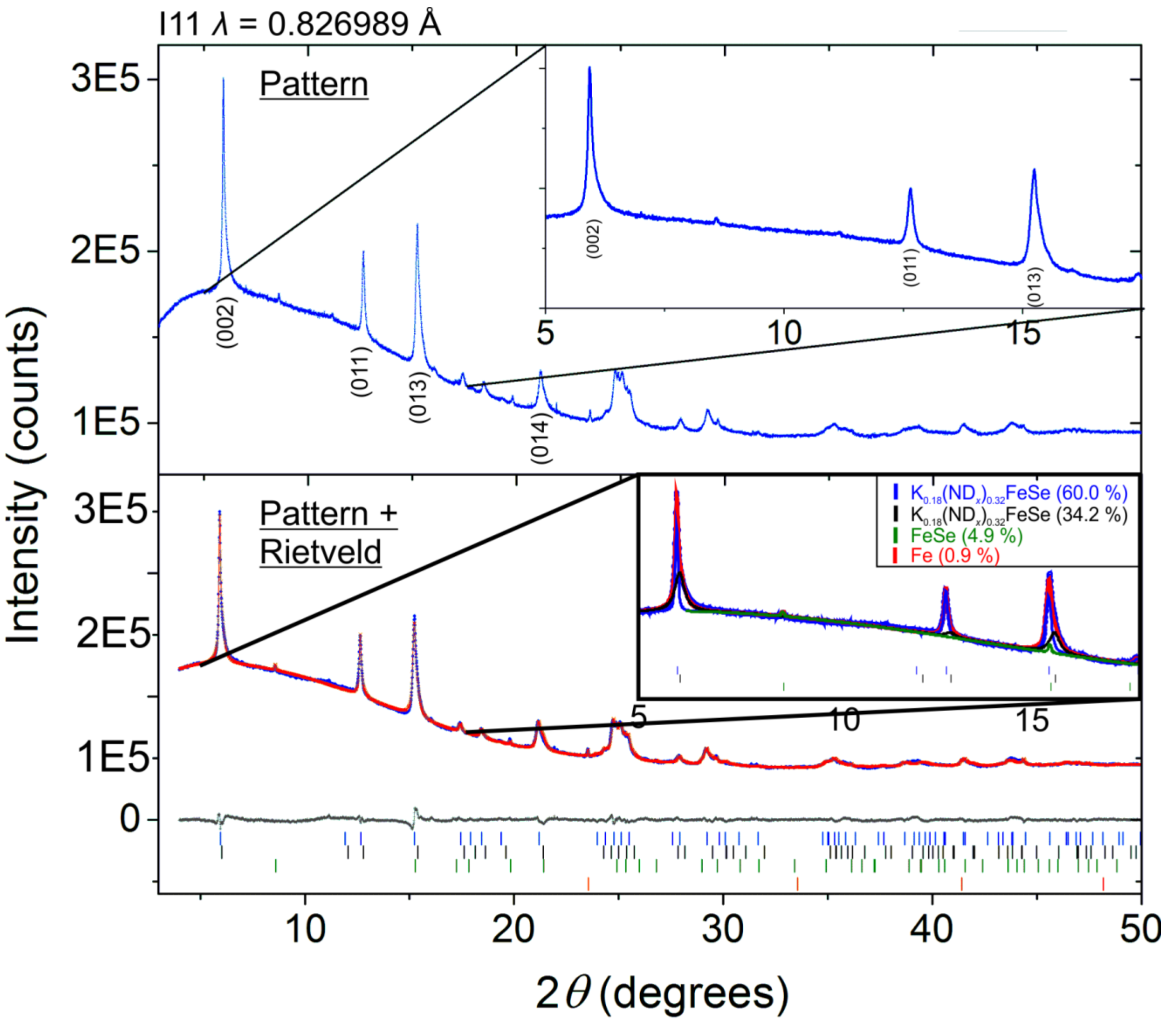

Figure 5.17 Rietveld refinement against the X-ray diffraction pattern of $K_{0.15}(ND_{2.9(3)})_{0.35(3)}FeSe$ using the neutron model. An asymmetric broadening of the peaks towards higher is observed, which has been modelled as two separate phases in the Rietveld refinement.

5.4 Magnetometry

Measurements on the magnetic properties of the ammonia-poor potassium intercalated iron selenides(7.4 and 7.9) were carried out using a Quantum Design SQUID magnetometer. To carry out the measurements, approximately 40 mg of the sample were loaded into a gelatine capsule, before placing it inside the magnetometer. The sample was cooled in the absence of a field to 2 K then a 20 Oe field was applied and the magnetisation (*M*) was measured as a function of temperature (*T*) in 1 K steps up to 60 K. The samples were then cooled back to 2 K with the field still applied the *M* versus *T* measurements repeated up to 60 K.

Figure 5.18 shows the magnetic susceptibility as a function of temperature for the two samples used for neutron diffraction. The susceptibility is given as volume susceptibility in dimensionless units, as defined in equation 2.33 (chapter 2.2.8, page 60).

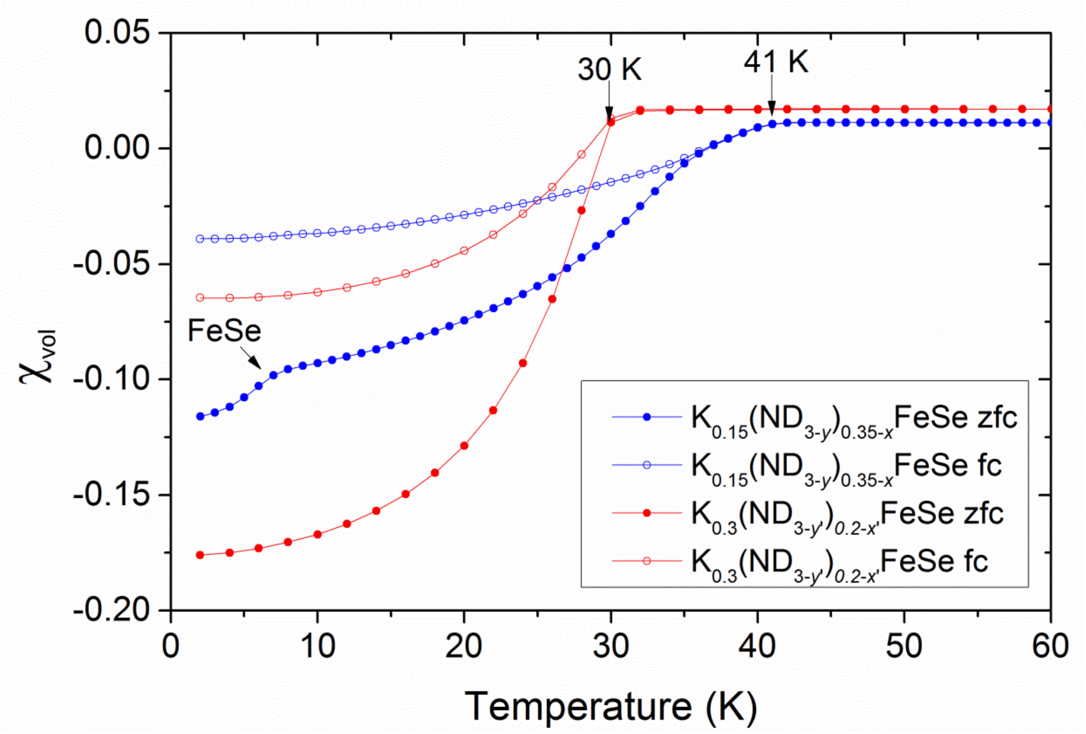

Figure 5.18 Plot of the zero field cooled (zfc) and field cooled (fc) volume susceptibility against temperature from SQUID magnetometry carried out on the samples from the neutron diffraction experiments that were described in section 5.3.

The $K_{0.3}$ product(7.4) is a 30 K superconductor, consistent with the $K_{0.3}(NH_3)_{0.185}FeSe$ phase reported by Ying *et al.* (labelled as $K_{0.6}Fe_2Se_2(NH_3)_{0.37}$ in their report).[152] A volume fraction of 18 % is observed in the deuterated sample, but the paper by Ying *et al.* reported a superconducting volume fraction of 52 %. A volume fraction of significantly less than 100 % is consistent with some degree of magnetic phase separation within the sample: separate domains exist, one of which is magnetically ordered and one is superconducting, but they are structurally indistinguishable within the resolution of most diffraction techniques, given the inherently poor crystallinity of the samples. Figure 5.16 shows the superconducting volume fractions of several, non-deuterated, samples, one of which shows a volume fraction of 35 %, so there clearly is some sample-dependant variation in the volume fraction, which is likely an indicator of the degree of phase separation. There is further scope for neutron diffraction experiments to establish if the intensity of the magnetic scattering peak inversely correlates with the superconducting volume fraction. The T_c of samples SXC170 and SXC152 show a suppression relative to SXC127 and

SXC129, meaning that the superconducting component in the sample is not a line phase, and it is likely that SXC152 and SX170 have a different level of electronic doping, arising from different amounts of amide formation during the reaction.

The $K_{0.15}$ product(7.9) has a T_c onset of 41 K, which is within a margin of error of the 44 K assignment report by Ying *et al.*,[152] given that the onset transition is broad. The superconducting volume fraction is about 13 %. A second drop in the susceptibility at 8 K is indicative of a small amount of leftover FeSe from the reaction, consistent with the diffraction experiments. Superconducting volume fractions between 3 and 15 % have been observed for all samples synthesised in the 0.15 K per FeSe compositional ratio, which shows the superconductivity is not bulk. The most probable cause of the low volume fractions is inhomogeneity suggested by the poor crystallinity of the samples as shown by the asymmetric broadening in the *00l* peaks, although the samples of this composition reported by Ying *et al*. also show the same asymmetric broadening in their diffraction patterns, but have volume fractions of up to 44 %.

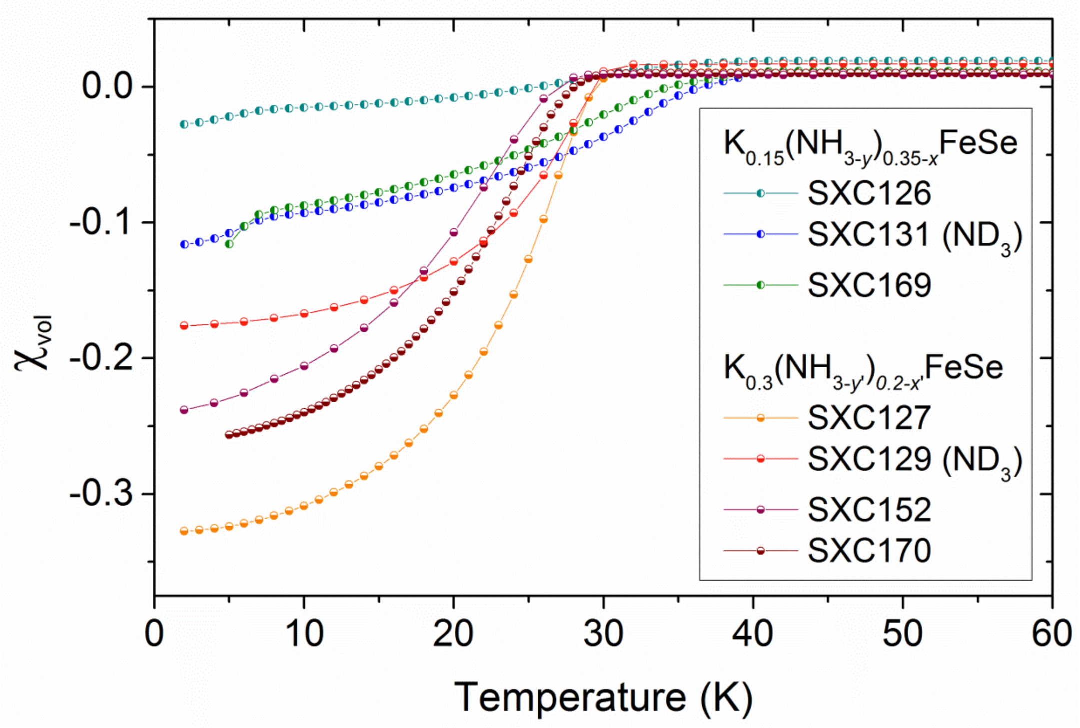

Figure 5.19 Plot of the zero field cooled volume susceptibility against temperature from SQUID magnetometry performed on several potassium and ammonia(-poor) intercalated iron selenide samples in a 20 Oe field.

5.5 Products of annealing

5.5.1 Thermogravimetric analysis (TGA)

TGA under an argon atmosphere was carried out on the two samples used in the neutron diffraction experiment. It was necessary to expose each of the samples to air for ~ 10 seconds while transferring from an air-tight transport vessel to a pre-weighed alumina crucible on the instrument. The samples were then placed under an argon flow for the duration of the experiment. The samples were each heated from room temperature to 600 °C at a rate of 5 °C min^{-1}. The plot of mass against temperature is shown in Figure 5.20, a rise in the mass at the start of the measurement arises from a buoyancy effect, which remains constant after about 50 °C. A main mass loss feature occurs between 200 and 300 °C in both samples. The more potassium rich intercalate(7.4) undergoes the smaller drop in its mass; consistent with the observation that the more potassium intercalated into the FeSe layers, the fewer sites remain for ammonia. An approximation of the size of the mass loss event shows both potassium intercalates of iron selenide lose an amount which is consistent with the mass of ammonia in each structure as modelled in refinement against the neutron data (1.56 % for the $K_{0.3}$ product(7.4) and 4.04 % for the $K_{0.15}$ product(7.9)).

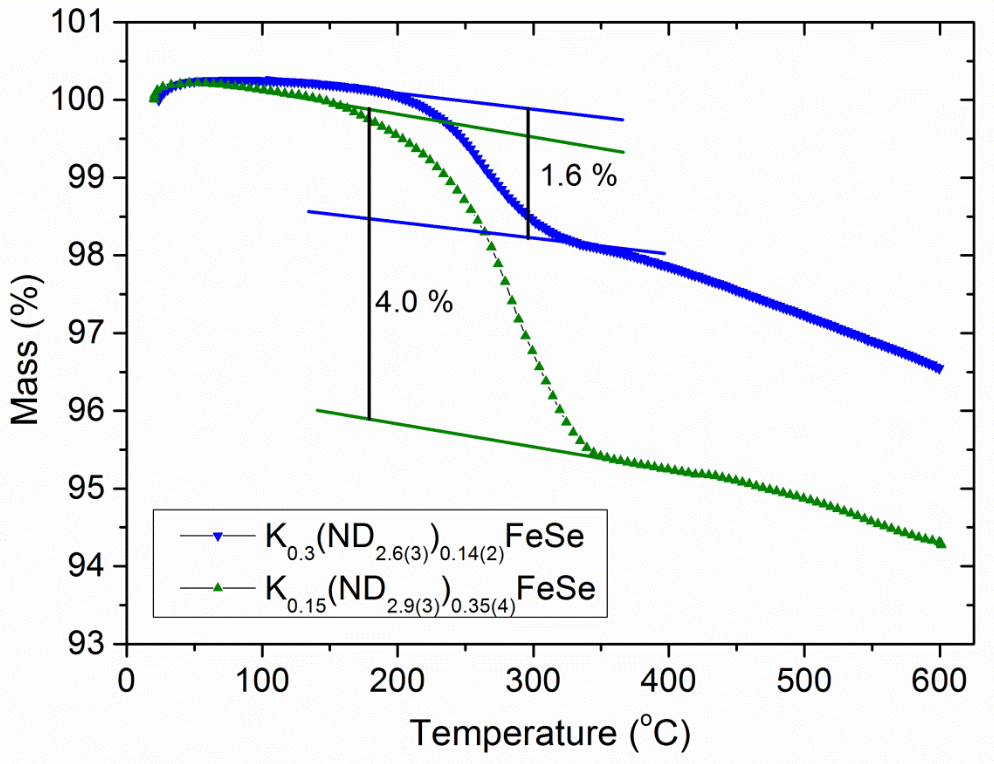

Figure 5.20 Thermogravimetric analysis of the deuterated ammonia and potassium intercalated iron selenide samples that were studied with neutron diffraction in section 5.3.

5.5.2 *In-situ* powder X-ray diffraction analysis of decomposition products

The products from the TGA analysis after annealing at 600 °C appeared mainly to be comprised of Fe, FeSe, and K_2Se from their X-ray diffraction patterns. Taking into account that the main mass-loss event occurs by 300 °C, it was found that by annealing the potassium intercalates at 300 °C for only one minute then quenching the sample in ice water the product was very similar to the $K_xFe_{2-y}Se_2$ phase, which are synthesised at ~1000 °C from a reaction of the elements.[79]

The decomposition processes for samples synthesised with a K : FeSe ratio of 0.15, 0.3 and 0.5 have been measured *in-situ* by powder X-ray diffraction on beamline I11 at Diamond Light Source. The sample synthesised with a K : FeSe ratio of 0.5 appears very similar in structure to the product(7.4) of the reaction with 0.3 equivalents, near identical X-ray diffraction patterns as shown in Figure 5.21, however their decomposition products are quite different.

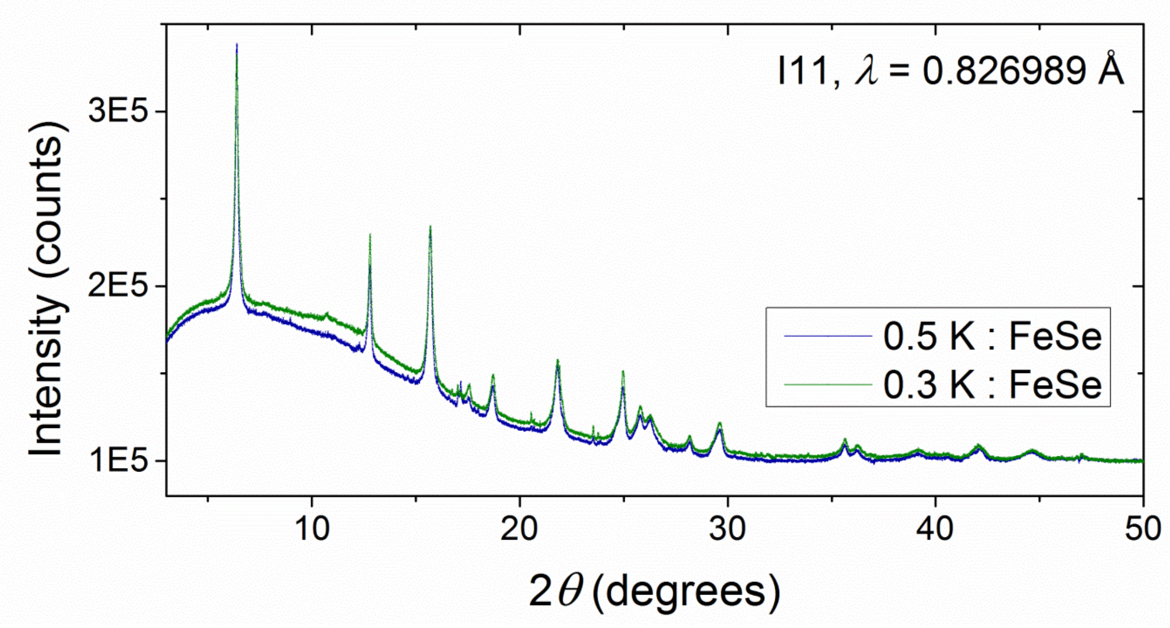

Figure 5.21 Overlay of the diffraction patterns of two potassium and ammonia intercalated iron selenide samples before they were annealed at 400 °C. The two samples have nearly identical diffraction patterns, despite one being synthesised with 0.2 more equivalents of potassium than the other.

The samples were loaded into 0.5 mm diameter borosilicate capillaries inside an argon-filled, dry glovebox, then sealed with an argon atmosphere still inside. The capillaries were positioned on the diffractometer with a hot-air blower directed at them, the temperature of which could be controlled remotely. The sample was warmed at a rate of 6 °C min^{-1}, whilst 10 (2 × 5) second diffraction patterns were continuously being collected, with around 8 seconds of delay between collections. The progression of the diffraction pattern as a function of temperature can be seen in the plots Figure 5.22, in which the diffraction patterns are shown in a surface plot with colour indicating intensity. In each case, between 25 and 180 °C the (002) reflection of the intercalate moves to a lower angle as thermal expansion occurs, but at around 180 °C the peak begins to decrease in intensity along with a broadening and shift towards higher angles. The shift to higher angles in the (002) reflection ends by around 300 °C, after which temperature the broadened peak becomes sharp again at a higher 2θ position than it had at 180 °C, which shows that the c lattice parameter has contracted sharply then stabilised; consistent with the loss of ammonia/ decomposition and loss of amide. Accompanying this shift in the (002) reflection of the ammonia-poor intercalate, is the appearance of elemental iron in the sample, observable in Figure 5.22 by the growth of the (110) reflection. The elemental iron phase arises as iron is ejected from the iron selenide layer to give the iron vacancy containing $K_xFe_{2-y}Se_2$ phase.

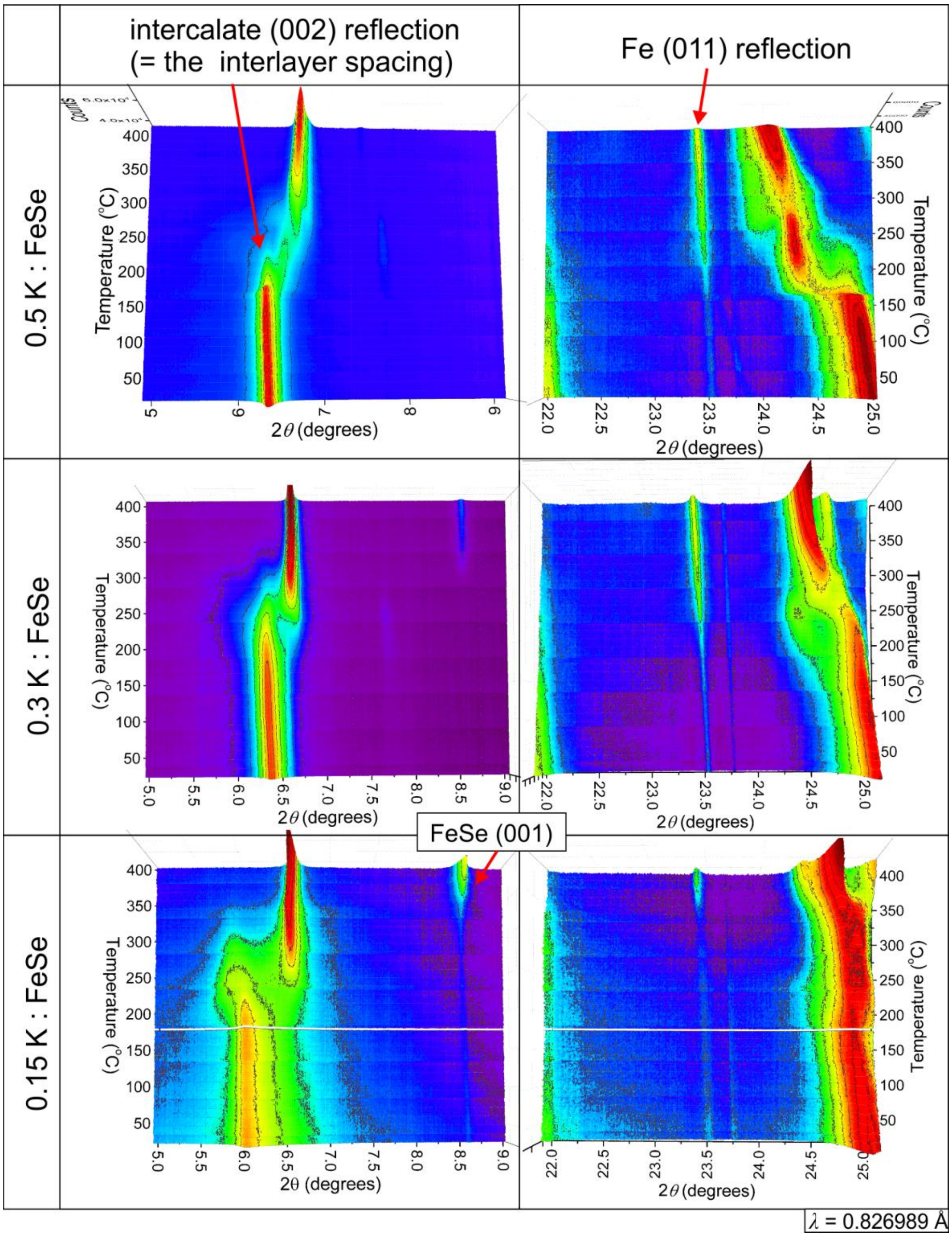

Figure 5.22 Surface plots of the diffraction patterns taken *in-situ* as the ammonia-poor potassium intercalated iron selenides were heated from 25 to 400 °C at a rate of 6 °C min^{-1}. The plots on the left show the region where reflections corresponding to the separation between iron selenide layers occur. The plots on the right show the region where the 110 reflection of elemental iron occurs.

When 0.5 or 0.3 equivalents of potassium per FeSe are used, the appearance of the (110) reflection of iron perfectly coincides with the shift in the (002) reflection of the ammonia-poor intercalate(7.4) that corresponds to the loss of ammonia/ loss and decomposition of amide, meaning that the iron vacancies are introduced simultaneously as the ammonia is expelled. Rietveld refinement against the diffraction patterns for the 0.5 K equivalent case was carried out in a batch mode refinement. Figure 5.23 shows the lattice parameter of the intercalate phase clearly begins to reduce at the same temperature as the phase percentage of iron begins to grow (~175 °C).

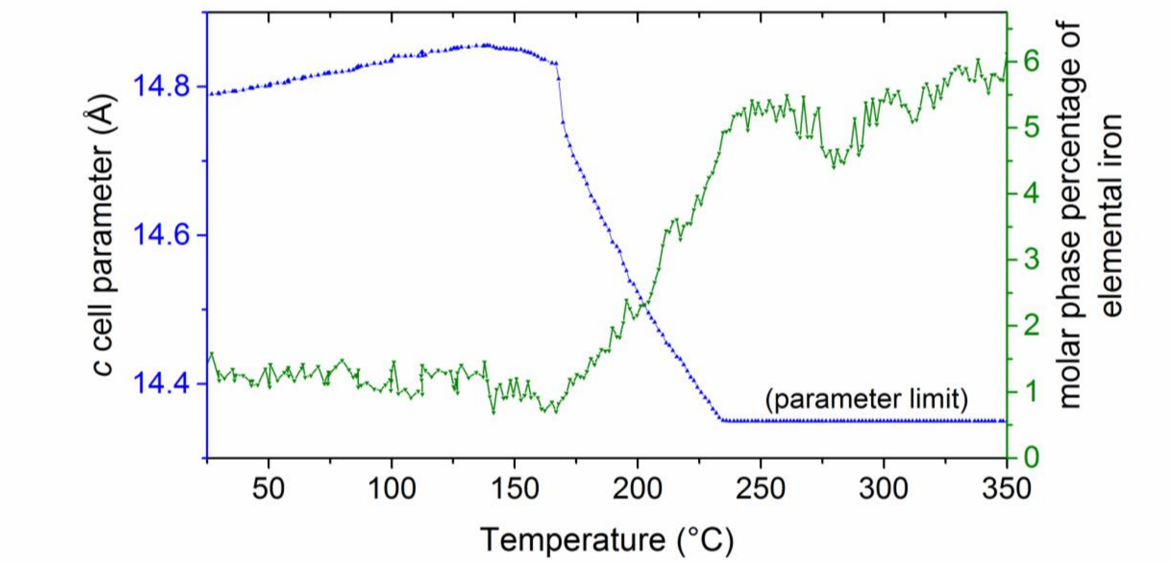

Figure 5.23 Parameters from the Rietveld refinement against diffraction patterns taken when the ammonia-poor starting phase(7.4) was made with a reaction ratio 0.5 K : 1 FeSe. The temperature at which the separation between iron selenide layers begins to decrease (= 0.5 * the *c* cell parameter) is found to coincide with the temperature at which the phase percentage of elemental iron begins to rise.

When 0.3 and 0.15 equivalents of potassium per FeSe had been used to synthesis the ammonia-poor starting material, a tetragonal iron selenide phase is also observed at higher temperatures. This phase corresponds to the expulsion of both ammonia and potassium from the interlayer and is necessary to balance the reaction equation:

$$K_x(NH_{3\text{-}a})_b Fe_2Se_2 \;\rightarrow\; \frac{x}{x'}\,K_{x'}Fe_{2\text{-}y}Se_2 \;+\; 2\left(1\text{-}\frac{x}{x'}\right)\,FeSe \;+\; y\frac{x}{x'}\,Fe \qquad \textbf{Equation 5.2}$$

$K_{x'}Fe_{2\text{-}y}Se_2$ phases have been reported in the phase region $0.5 \leq x' \leq 1$ $0.5 \leq y < 0$[75,79,84,88,158] and so it is expected that low concentrations of intercalated potassium will not be able to satisfy $x = x'$ in a thermodynamically stable manner. This leads to FeSe being formed as a portion of the decomposition product. Interestingly, the formation of the FeSe phase does not appear to begin until a higher temperature than what is required to expel ammonia and elemental iron from the system is reached. This indicates that it might be possible to trap metastable $K_xFe_{2\text{-}y}Se_2$ phases with $x < 0.5$ by annealing at ~280 °C, but it may be that the FeSe phase is present but amorphous below ~350 °C.

When only 0.15 equivalents of potassium per FeSe had been used to synthesis the ammonia-poor starting material(7.9), elemental iron does not appear to form until much higher temperatures in the annealing, along with the iron selenide (bottom right panel of

Figure 5.22). This curious observation may indicate that metastable $K_{\sim0.3}Fe_2Se_2$ phases may be isolated. However, this phase is never alone in the diffraction patterns and there is too much complexity to accurately refine an iron occupancy of the phase whilst there is some of the starting material remaining. It cannot be said with any certainty that a $K_{\sim0.3}Fe_2Se_2$ phase can be formed by this annealing method.

Following the *in-situ* experiments, the samples were removed them from the hot-air stream, cooling them rapidly to room temperature. The samples were then re-measured at room temperature using the Mythen detector with a longer collection time. Rietveld refinement against the diffraction patterns of the products of annealing at room temperature are shown in Figure 5.25, with a comparison of the refined parameters given in Table 5.12. Full refinement parameters for these phases are given in appendix X.

The $K_xFe_{2-y}Se_2$ phases sometimes show an ordering of the vacancies, which is particularly prevalent when x~0.8 and y~0.4, for which the vacancy ordered superstructure is as shown in Figure 5.24. This structure is related to the parent structure by √5 expansion along *a* with the symmetry reduced from *I*4/*mmm* to *I*4/*m*. The superstructure has been used in the refinements of the annealed products to assess the degree of iron vacancy ordering, if any.

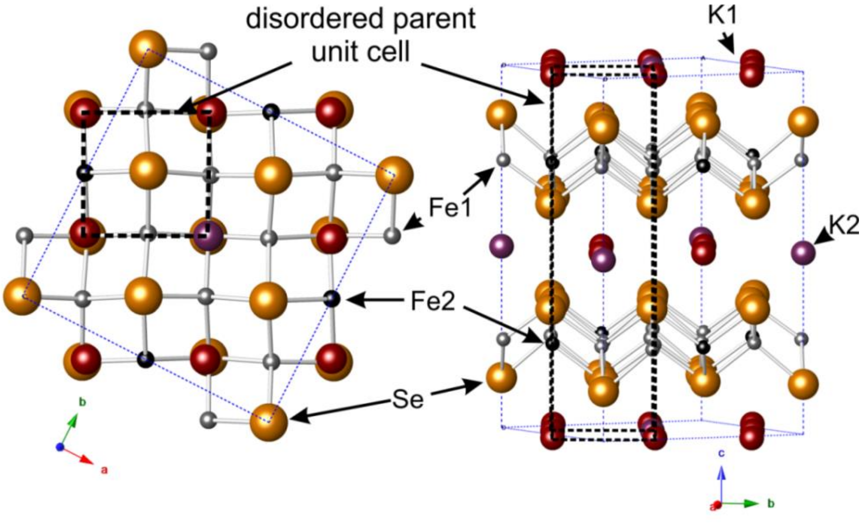

Figure 5.24 Structure of iron vacancy ordered $K_{0.8}Fe_{1.6}Se_2$ which corresponds to a √5 expansion along *a* of the parent $ThCr_2Si_2$ type structure shown in the black dotted line. In a sample with fully vacancy ordering and a stoichiometry $K_2Fe_4Se_5$, the Fe2 sites are fully vacant and the Fe1 sites fully occupied.

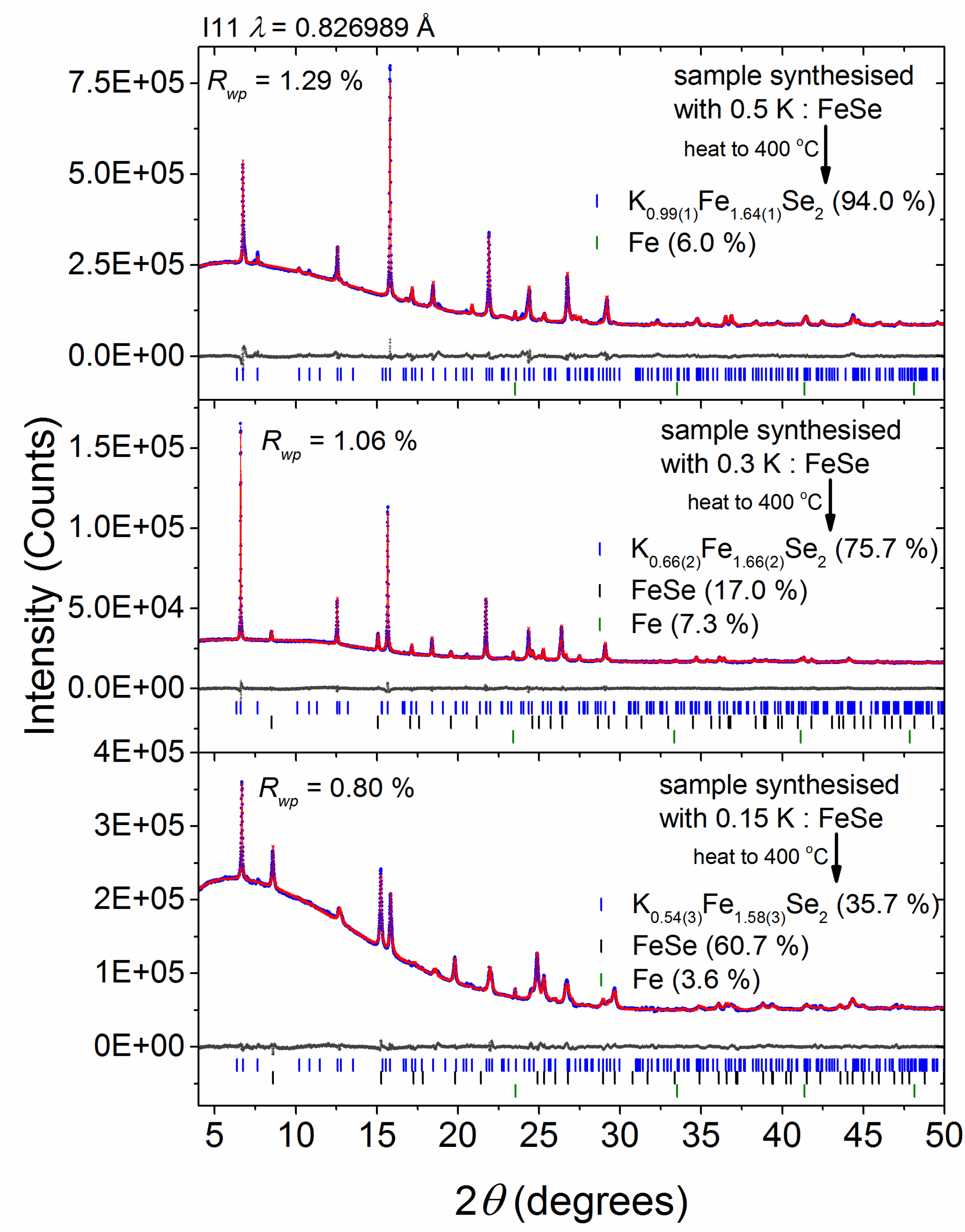

Figure 5.25 Rietveld refinement against the diffraction patterns of the final products of the annealing experiments shown in Figure 5.22. The top and bottom patterns were collected at room temperature after the sample had been annealed then quenched, the middle pattern was taken at 400 °C, since the sample capillary broke before a room temperature pattern could be taken.

Table 5.11 General structure of the vacancy ordered $K_xFe_{2-y}Se_2$ obtained in the high temperature synthesis from the elements,[79] and from annealing the potassium and ammonia intercalated iron selenide phases.

General structure in space group *I4/m*					
a	**= $\sqrt{5}$ × parent *a* cell parameter**		***c***	**= parent *c* cell parameter**	
atom	**site**	**x**	**y**	**z**	**Occupancy**
K1	8*h*	xK1	yK1	0.5	occK1
K2	2*b*	0	0	0.25	occK2
Fe1	16*i*	xFe1	yFe1	zFe1	occFe1
Fe2	4*d*	0	0	0.25	occFe2
Se2	16*i*	xSe1	ySe1	ZSe1	1
Se1	4*e*	0	0	zSe2	1

Table 5.12 Refined structural parameters from the fits in Figure 5.25. Fe oxidation states assume that Se is a divalent anion.

K:FeSe ratio	***a* / Å**	***c* / Å**	**occK1**	**occK2**	***x***	**occFe1**	**occFe2**	***2-y***	***Fe ox. state***
0.5: 1	8.7602(2)	14.048(1)	0.98(4)	0.99(2)	0.99(1)	0.886(7)	0.56(2)	1.64(1)	1.84(1)
0.3:1	*	*	0.65(1)	0.71(5)	0.66(2)	0.838(8)	0.79(3)	1.66(2)	2.01(3)
0.15:1	8.6712(3)	14.173(1)	0.61(4)	0.23(8)	0.54(3)	0.81(2)	0.72(4)	1.58(3)	2.19(5)

*** The capillary of the annealed sample with 0.3 equivalents of potassium broke before a final collection at room temperature could be taken. Reported occupancy values are from a refinement at 400 °C, which is the refinement shown in Figure 5.25. The unit cell parameters of the 0.3 potassium equivalent material at 400 °C, are *a* = 8.7686(1) and *c* = *14.3633(3) Å, cf.* the 0.15 potassium equivalent material at 400 °C, which has *a* =8.7530(3), *c* = 14.389(1) Å.**

In each of the three cases, the molar phase fraction of FeSe relative to $K_xFe_{2-y}Se_2$ is approximately as would be expected from equation 5.2 given the initial K : FeSe ratios and the refined value of x in product. The molar phase fraction of elemental iron in each case is far lower than would be expected given the refined value y, which could be a result of not all the expelled iron crystallising.

It is found that an approximately 20 % iron vacancies are introduced into the structures of the potassium intercalates of iron selenide annealed to 400 °C, with little correlation to the amount of potassium in the system. There appears to be marginal ordering of the vacancies, with small differences in the occupancy of the Fe1 and Fe2 sites, particularly when the synthesis ratio of K : FeSe is 0.5, but in the $K_{0.15}$ and $K_{0.3}$ cases the vacancies remain largely disordered.

With 0.5 K per FeSe as the synthesis composition used, it appears that all the potassium that was used in the synthesis is retained in the vacancy ordered structure. In contrast, when the synthesis composition is 0.15 or 0.3 K per FeSe, less potassium is present in the system than is needed to give a stable single phase ternary compound, and so a disproportionation occurs to give some FeSe with no K in the interlayer and bring the amount of potassium in the remaining superstructure up towards a minimum value. This observation tallies with the observation that $K_xFe_{2-y}Se_2$ materials synthesised at high temperature are most often found with a range of x between 0.7 and 1.[79]

The synthesis with 0.15 equivalents of K per FeSe has an unusually high disparity between the occupancy of the K1 and K2 sites, but with an R_{wp} of 0.8 %, this carries a large degree of uncertainty. This low R_{wp} arises from the sample being largely comprised of a rather poorly crystalline iron selenide phase, with many of the peaks overlapping with those of the $K_xFe_{2-y}Se_2$ phase.

The $K_{0.5}$ product has a larger a cell parameter, a shorter c cell parameter, and overall a higher volume than the other two products. This arises as a consequence of the higher fraction of potassium in the system: the a cell parameter is a $\sqrt{10}$ expansion of the Fe-Fe bond distance in the superstructure and this bond distance is expected to expand if iron is reduced. Since the bond angles in the FeSe layer are relatively flexible, these adapt to the change in a in such a way that lowers the c cell parameter.

5.6 Discussion and conclusions

The chemistry of the potassium intercalates are governed by the necessity that potassium must share a site with NH_3/NH_2 in the inter-FeSe-layer space as compared with the smaller alkali metals, lithium or sodium, which take different sites surrounding NH_3/NH_2.

The ammonia-poor iron selenide intercalate structure, which is based on the $ThCr_2Si_2$ structure, can accommodate 0.5-z K per FeSe where z is the amount of NH_3/NH_2 that accompanies potassium into the structure. Ying *et al*. showed that the more potassium used in the synthesis, the shorter interlayer separation, with a broad phase gap opening between 0.15 and 0.3 equivalents of potassium per FeSe.[152] These two compositions, $K_{0.15}$ and $K_{0.3}$, have been studied by neutron diffraction in this report.

In $K_{0.3}(ND_{2.6(4)})_{0.14(2)}FeSe(7.4)$ potassium and ammonia share a site, which gives average bond distances that are a weighted average between ideal distances of potassium and ammonia, but are ideal for neither. In $K_{0.15}(ND_{2.9(3)})_{0.35(3)}FeSe(7.9)$, this average is weighted so far in favour of the coordination environment of ND_3/ND_2 that the K is displaced off the site along the *c* axis in order to achieve a better bond distance to Se. The composition of these intercalates suggests that part of the electron doping introduced by potassium is absorbed by ammonia to form amide, but there is still a slight reduction of the average iron oxidation state. The average iron oxidation state in $K_{0.3}(ND_{2.6(4)})_{0.14(2)}FeSe$ is $Fe^{1.76(6)+}$ and in $K_{0.15}(ND_{2.9(3)})_{0.35(3)}FeSe$ is $Fe^{1.89(11)+}$, but these values and errors rely on the assumption that all the potassium supplied in the reaction has intercalated between the FeSe layers, which introduces an additional undefined error.

$K_{0.3}(ND_{2.6(4)})_{0.14(2)}FeSe(7.4)$ has a T_c of 30 K, and $K_{0.15}(ND_{2.9(3)})_{0.35(3)}FeSe(7.9)$ a T_c of 41 K. The superconducting volume fractions of the potassium intercalates of iron selenide that have been synthesised for this work fall into the range 2-35 %, with conclusively bulk superconductivity never observed. Magnetic order is observed in the $K_{0.3}(ND_{2.6(4)})_{0.14(2)}FeSe(7.4)$ phase, with an ordered moment of 1.1 μ_B at room temperature, indicative of a phase separation, but the structures of the superconducting and magnetically ordered phases are too similar to distinguish by diffraction methods, given the low crystallinity of the samples. Further work is necessary to see if the superconducting volume fraction in this system is inversely correlated to the phase fraction of the magnetically ordered phase. The $K_{0.15}(ND_{2.9(3)})_{0.35(3)}FeSe(7.9)$ phase does not show magnetic ordering but also has a low superconducting volume fraction, which may also be a result of a phase separation that is unresolvable at this time (although an asymmetric broadening of *hkl* reflections with large *l* components is seen in the synchrotron X-ray diffraction).

The ammonia-rich phases of the potassium intercalates have been identified for the first time. A metastable intermediate phase with an 11.5 Å separation between the FeSe layers was observed, which has the same structure as the Li (10.5 Å) and Na (11.0 Å) ammonia-rich intercalates. However, the final ammonia-rich products of the potassium intercalations into iron selenide, like the ammonia-poor systems, have potassium and ammonia sharing a site. This site sharing yields structures with less expanded interlayer separations than the ammonia-rich phases with smaller alkali metals (Li and Na), and leads to the product(9.9) of a reaction with more equivalents of potassium (0.3 per FeSe) having a more expanded interlayer space than the product(10.2) with less potassium (0.15 per FeSe).

The reaction to form $K_{0.3}(NH_{3\text{-}y})_{0.7\text{-}x}FeSe(9.9)$ occurs much faster than the reaction to form $K_{0.15}(NH_{3\text{-}y})_{0.85\text{-}x}FeSe(10.2)$, with $K_{0.3}(NH_{3\text{-}y})_{0.7\text{-}x}FeSe$ being an intermediate along the way to forming $K_{0.15}(NH_{3\text{-}y})_{0.85\text{-}x}FeSe$ when a stoichiometry of 0.15 K : FeSe is used. The *in-situ* study of these reactions has shown that a series of interconversions occur between the ammonia-rich phases, and has given a basic idea of their relative rates of formation. The volume of the final ammonia-rich products of the reactions is observed to increase as a function of time even after all the FeSe is consumed and the reaction is seemingly complete. This expansion may just be thermal expansion, since the reactions were not performed isothermally; however there is evidence to suggest that this expansion is from the ammonia site being filled gradually. The conclusion that vacancies on the ammonia site are gradually filled would explain why in the ammonia-poor $K_{0.15}(ND_{2.9(3)})_{0.35(3)}FeSe$ sample, which was synthesised with a reaction time of ~14 hours, the nitrogen site has its maximum occupancy, while the $K_{0.3}(ND_{2.6(4)})_{0.14(2)}FeSe$ sample, which had a reaction time of ~2 hours, appears to be less than fully occupied. Further *in-situ* investigations in isothermal conditions with differing ratios of K : FeSe are required in order to see: if the extended intermediate phase can be stabilised, if the volume expansion in the final product is just from thermal expansion, and if ammonia-rich products with higher ratios of potassium than 0.5 K: FeSe can be formed. This last point is of interest since the general formula $K_x(NH_{3-y})_{1-x}FeSe$ for the ammonia-rich materials would seem to allow up to $x = 1$, but such high levels of potassium are incompatible with the ammonia-poor structural formula $K_x(NH_{3-y'})_{0.5-x}FeSe$.

The potassium and ammonia intercalates of iron selenide are found to eject ammonia/amide but retain the topology of the anti-PbO type FeSe layers when annealed up to 400 °C and quenched. The product that is formed includes iron vacancies as iron is ejected from the system to form $K_xFe_{2-y}Se_2$ phases, akin to those in the literature formed at high temperatures (~1000 °C).[75] The expulsion of iron from the FeSe layer appears to be coincident in temperature with the expulsion of ammonia from the interlayer space in $K_{0.3}(NH_{3-y})_{0.2-x}FeSe$, which shows that no $K_{0.6}Fe_2Se_2$ phase (without iron vacancies) is formed. In $K_{0.15}(NH_{3-y})_{0.35-x}FeSe$ the expulsion of iron appears to occur after the expulsion of ammonia which suggests it might be possible to stabilise a $K_{0.3}FeSe$ phase, but this phase is never single at the applied ramp rate of 6 °C min^{-1}, and the diffraction pattern is too complex to conclusively say that this is the majority phase formed.

The addition of 0.5 equivalents of potassium per FeSe does not appear to contract the unit cell of the ammonia-poor phase beyond that of $K_{0.3}(NH_{3-y})_{\sim 0.2}FeSe$, indicating that the same amount of potassium is intercalated in both cases. The remaining potassium that is not intercalated when 0.5 equivalents are used, probably forms a potassium amide phase that remains in the powder but is not observable in the diffraction pattern. Annealing of the

0.3 K and 0.5 K powder samples yields a $K_xFe_{2-y}Se_2$ phase in both cases, but x is higher (close to 1) when 0.5 equivalents were used in the initial synthesis. This implies the transformation from ammonia-poor intercalate to $K_xFe_{2-y}Se_2$ does not have to be an intramolecular process, but can occur in a reaction with the impurity source of potassium.

The annealing of the ammonia-poor potassium intercalates of iron selenide provides a new route to the $K_xFe_{2-y}Se_2$ phases that may be able to expand on the range of values that x and y are known to be able to take. Further study of the annealing process may yield further insight into the parameters which control the rates product formation and expand this phase diagram.

Chapter 6

6. Synthesis and characterisation of CaFeSeO

6.1 Chapter introduction

In general terms, chalcogenide materials are more likely to adopt structures with asymmetric coordinations about the anion than oxide materials. Take the example of TiO_2 versus TiS_2; the oxide in TiO_2 has a local symmetry of D_{3h} from its first nearest neighbours, while the sulfide of TiS_2 has a local symmetry of C_{3v}. Both structures have titanium octahedrally coordinated by the anion, but TiS_2 forms a layered structure with more edge-sharing of the octahedra, which can be tolerated because the asymmetrically coordinated sulfide can be polarised to shield the Ti-Ti repulsion. When a material contains both an oxide and chalcogenide anion, it will often adopt one of a range of layered structures with oxophilic and chalcophilic cations separated into different layers. Such oxychalcogenide materials are a relatively under-explored with respect to either pure oxide or pure chalcogenides. The oxypnictide iron based superconductor, $LnO_{1-x}F_xFeAs$, which adopt the ZrCuSiAs structure type is a fine example of this structural theme; containing PbO type $[Ln_2O_2]^{2+}$ layers acting as charge reservoirs which can be doped to induce superconductivity in the anti-PbO type $[Fe_2As_2]^{2-}$ layers.[41] It was in an attempt to make a selenide equivalent to LaFeOAs that CaFeSeO was synthesised, trying to form a structure with a charge neutral CaO layer occupying the interlayer space of FeSe. While unsuccessful in reaching the target crystal structure, the product has a new and complex structure and exhibits interesting magnetic properties. The following examples give some background to this new structure by showing just a few of the intricate structures that oxychalcogenides are known to adopted, and demonstrating how small changes in composition can give very varied structures. A diagram showing the structures from the literature is given in Figure 6.1.

CaZnOS has a non-centrosymmetric structure consisting of puckered hexagonal CaO and ZnS layers arranged so that Zn is coordinated by three S atoms, which form part of a ZnS puckered layer, and an O atom in a neighbouring CaO layer.[159] The ZnS_3O tetrahedra are aligned with their Zn-O bonds parallel to the *c* axis resulting in a polar structure. Ferroelectricity is not observed in the structure as switching of the polarisation would require the ZnS_3O tetrahedra to flip direction under an applied electric field, which has a high energy barrier in the crystal structure. Pyroelectricity is possible for the crystal structure; however the pyroelectric coefficient, p, which gives a measure of the change in polarisation as a function of temperature was shown to be negligible between room temperature and 100 °C.[160]

BaZnOS adopts a centrosymmetric layered structure with an unusual Zn coordination environment for the solid state.[161] Zn atoms are tetrahedrally coordinated by two oxygen atoms and two sulphur atoms. The ZnO_2S_2 tetrahedra share all of their vertices, forming two sets of parallel chains along the a and c axes. The puckered zinc oxysulfide layers formed by joining these chains are separated by barium cations.

$Na_2Fe_2OSe_2$ adopts a variant of the K_2MgF_4 structure, in which layers of $[Fe_2OSe_2]^{2-}$ are separated by double layers of Na^+. Iron occupies a distorted octahedral environment with two oxide and four selenide vertices sharing 2 edges and 4 faces. The material is a narrow band gap semiconductor that shows antiferromagnetism with $T_N = 73$ K.[162]

$CeMn_{0.5}OSe$ adopts a variant of the ZrCuSiAs structure in which the Mn atoms half occupy the crystal site in a long range disordered manner.[163] A series of $A_2O_2MOSe_2$ compounds with A = La - Pr and M = Mn - Co are known to adopt a related structure layered with the $[A_2O_2]^{2+}$ fluorite type layers separated by $[MOSe_2]^{2-}$ layers in which the transition metal is in a distorted octahedral environment with two axial oxide ions and four equatorial selenide ions.[164] The compositionally similar materials β-$La_2O_2MSe_2$ (M = Mn, Fe) adopt an unusual structure in which the transition metal sits on two distinct sites: one in a distorted MSe_4O_2 octahedra and the other in disordered MSe_4 tetrahedra.[165]

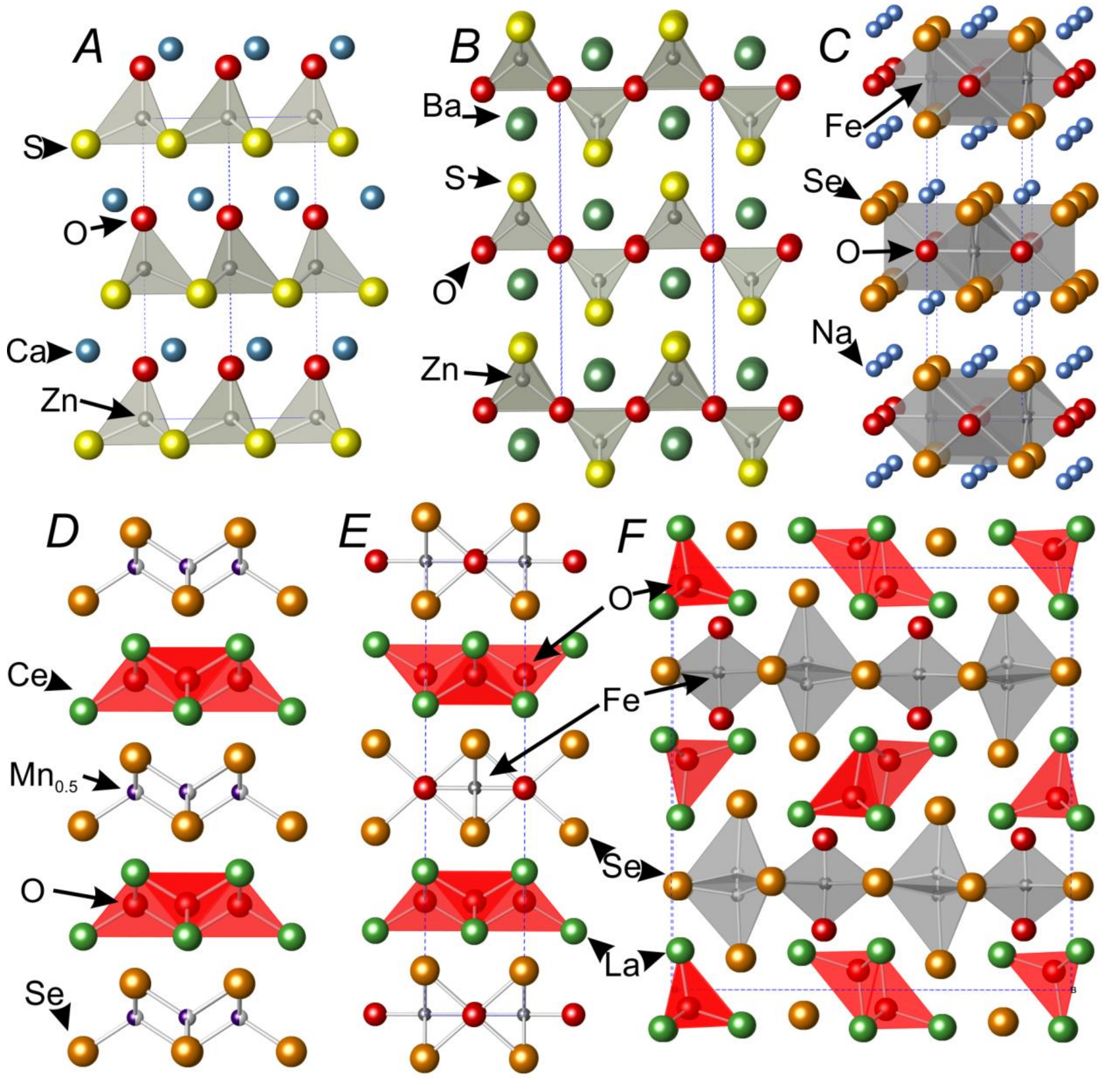

Figure 6.1 Crystal structures of various oxychalcogenides. *A*: CaZnOS, *B*: BaZnOS, C: $Na_2Fe_2OSe_2$, *D*: $CeMn_{0.5}OSe$, *E*: $La_2O_2FeOSe_2$, and *F*: $La_2O_2FeSe_2$.

6.2 Synthesis and initial characterisation

CaFeSeO was synthesised by reaction of CaO (Sigma Aldrich ≥ 99.99 %) and FeSe (synthesis described in section 2.1.4) in a 1:1 stoichiometry. Direct reaction of CaO with iron (Alfa Aesar 99.998 %) and selenium (Alfa Aesar 99.999 %) powders, without the pre-synthesis of iron selenide was found to produce the same product with a higher level of impurities. The reactants were ground together inside an argon-filled, dry glovebox with an agate mortar and pestle for approximately 20 minutes, until evenly dispersed. The ground powder was transferred to a 13 mm pellet die, which was tied inside a polythene bag to protect the atmosphere around the sample before transferring to a pellet press outside the glovebox. The pellet was pressed under a ~2 tonne force before quickly returning it to the glovebox, where it was extracted from the die and polythene bag. The pellet was placed inside an alumina crucible, which was in turn placed inside a flame-dried silica tube. The silica tube was closed by means of a Young's tap and taken outside the glovebox to be sealed under dynamic vacuum using an oxygen/butane blowtorch. The sealed reaction vessel was heated in a furnace at a rate of 5 °C min^{-1} to 750 °C, at which temperature the sample was annealed for 60 hours. The furnace was then switched off, and the sample allowed to cool before extracting the sample in the glovebox, and regrinding to form a powder, which was an orange-brown colour. Repeated annealing was not found to have any effect on sample purity.

Parts of the analysis have been performed on two samples (SXC195 and SXC223), both synthesised with same composition. They have the same lattice parameters (within laboratory X-ray experimental error), and show near identical diffraction patterns. Both contain a 1.5 molar percent CaSe impurity, but no other impurities have been identified. An overlay of the diffraction patterns of the two samples is given in appendix XI.

CaFeSeO was found to be stable under air as judged by comparing X-ray diffraction patterns performed under air and in an air-sensitive sample holder. Samples were stored in an argon-filled, dry glovebox to prevent long term degradation and the reported measurements have been performed under air-sensitive conditions unless otherwise stated.

6.2.1 Indexing and Pawley refinement

After observing no changes to the diffraction pattern with and without exposure to air on the Philips diffractometer, a good signal to noise, high resolution X-ray diffraction pattern of sample SXC195 was taken (in air) using the PANalytical Empyrean diffractometer. Data were collected over the 2θ range 5 - 115 °, in steps of 0.0262 °. The pattern could be indexed to an orthorhombic unit cell with dimensions of 3.89 × 13.20 × 5.92 Å. Performing the indexing using TOPAS academic[113] suggested either $C222$ or $C222_1$ symmetry. Pawley (structure-independent) refinement using either of the predicted symmetries successfully fitted the data to an excellent standard with only one small peak at 38 ° unidentified, a Pawley refinement to this effect in $C222_1$ symmetry is given in Figure 6.2. Modelling of the pattern in $P222$ or $C222$ symmetry did not produce any improvement to the fit over $C222_1$ symmetry, indicating that the *C*-centring and 2_1 symmetry element are both present in the structure.

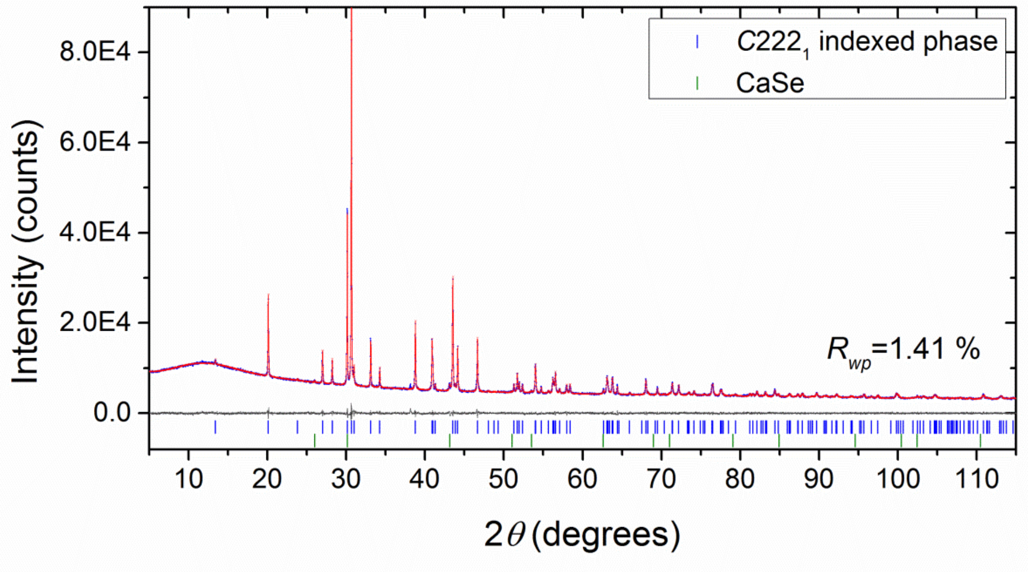

Figure 6.2 Pawley Refinement of a $C222_1$ unit cell with lattice parameters $a = 3.89$, $b = 13.20$, and $c = 5.92$ Å against a laboratory X-ray powder diffraction pattern ($\lambda = 1.54056$ Å) of CaFeSeO.

6.3 Charge-flipping structural solution of CaFeSeO

An initial check of the Inorganic Crystal Structure Database (ICSD) for materials with similar compositions, unit cell parameters, and/or symmetries could not match the indexed phase to any known structure type. Furthermore, a literature search did not identify any recent materials that might have the same structure, and so the arrangement of atoms within the unit cell was investigated by charge-flipping.

Charge-flipping is an *ab initio* structure solution technique, which can be implemented to solve a structure from X-ray powder diffraction data without any prior knowledge of the unit cell contents or symmetry. This technique, developed by Oszlányi and Sütő,[98] attempts to produce meaningful electron density maps from the observed data. First a randomly selected phase set for the structure factors is generated. Electron density maps are produced from the inverse Fourier transform of the combination of structure factor amplitudes and phase set. All points in the resulting electron density map that show electron density above a threshold, δ, are accepted, and those below the threshold are multiplied by a factor of -1 (hence "charge-flipping"); note that the value of δ is a small proportion of a peak that would be observed for a light atom. The newly generated electron density map then undergoes a Fourier transform to give a set of temporary structure factors and phases. This phase set is then combined with observed structure factors and inverse Fourier transformed to give a new electron density map. This process is then repeated many times and the progression of the algorithm is monitored by an R-factor, which is minimised in the process. The results given from charge-flipping tell us about areas of electron density in real space, and if information on the unit cell contents is given, then atoms can be assigned to areas of electron density based on matching the atomic number to the relative sizes of the electron density pockets in the charge-flipping results.

Charge-flipping was implemented using TOPAS academic.[113] Prior knowledge of the symmetry is not required for charge-flipping algorithm however, if it has been determined then it may be used as a constraint set by the user to improve the reliability and speed of the solution. Similarly, information on the unit cell contents can be included so that atoms can be assigned automatically to the electron density present, which constrains the relative electron densities of picked positions in the unit cell. The powder diffraction data shown previously in Figure 6.2 were used for the structural solution, using peaks up to a maximum *d*-spacing of 0.97 Å (105 ° in 2θ). $C222_1$ symmetry was imposed on the solution, and the unit cell was constrained to contain Ca, Fe, Se, and O.

Results from the repeated charge-flipping runs consistently identified a potential site for selenium. A second position was identified as iron, but was ~2.99 Å from selenium, which is a typical Ca-Se interionic distance, and so this site was identified as Ca. The structural solution placed calcium and oxygen on the same site, which was ~2.52 Å from the selenium, typical of an Fe-Se interionic distance, and so this site was identified as iron. The position of oxygen in the unit cell could not be determined by charge-flipping, but this could be determined intuitively by placement at a bonding distance from both Ca and Fe, whilst avoiding close O-Se contacts. The solution proposed directly by charge-flipping and the solution arrived at by reasonable interpretation of the charge-flipping result are displayed in Figure 6.3.

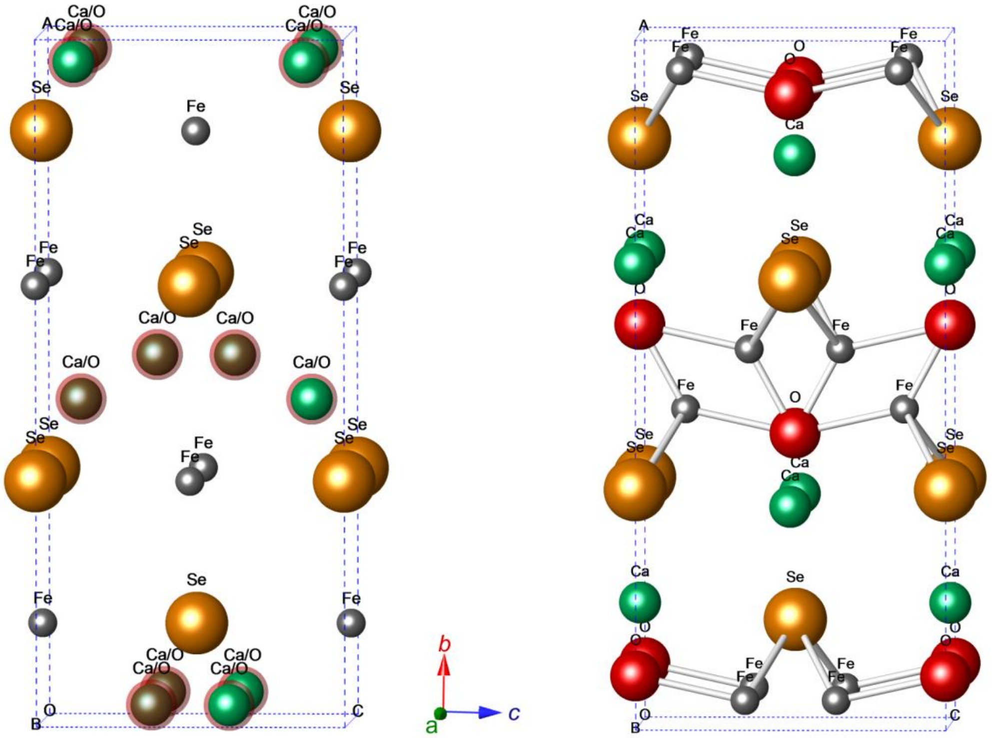

a) proposed solution from charge flipping

b) adapted from charge flipping

Figure 6.3 Diagram showing the structure of CaFeSeO that was arrived at by charge-flipping and subsequent chemically sensible arrangement of the cation sites.

The CaFeSeO structural model shown in the figure above, which was arrived at by charge-flipping with the $C222_1$ (number 20) space group symmetries in place, has additional symmetry elements and can be classed in the higher order space group *Cmcm* (number 63).

6.3.1 Rietveld refinement starting from the charge-flipped solution

A synchrotron powder X-ray diffraction pattern of CaFeSeO (sample SXC195) was obtained using I11 instrument at Diamond Light Source, with the high resolution MAC detector. In order to evaluate the validity of the model obtained through charge-flipping, Rietveld refinement of the structural model was carried out against these data. Refinement of the lattice parameters, atomic positions, occupancies, and anisotropic thermal displacements leads to a fairly good fit to the data as shown in Figure 6.4, but leaves several small peaks with under-predicted intensity as marked by ***** in the inset of the figure. One peak of low but significant intensity at 20.2 ° could not be accounted for by the model nor by any known impurity phase. This peak at 20.2 ° is coincident with the symmetry forbidden (102) reflection, which indicates that the symmetry assignment may be incorrect.

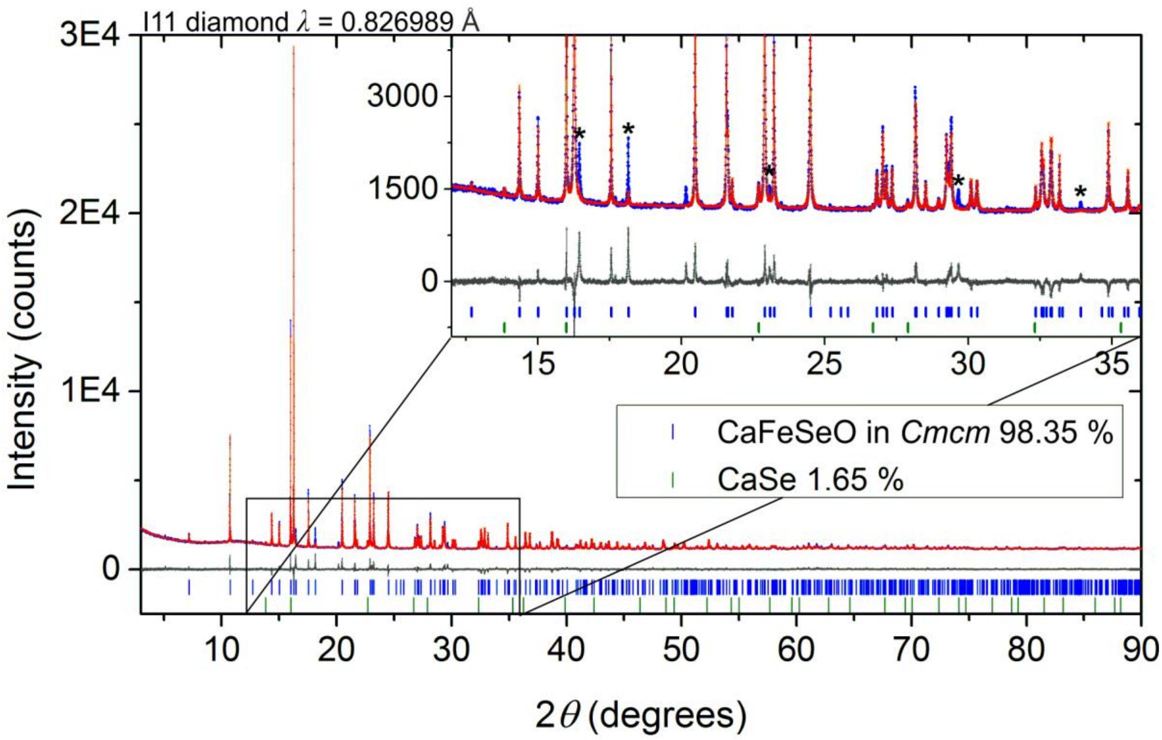

Figure 6.4 Rietveld refinement of the CaFeSeO model in *Cmcm* symmetry against synchrotron powder X-ray diffraction, with an R_{wp} of 9.73 %. A close-up of the low intensity peaks between 12 and 36 ° is given in the inset. Peaks that are predicted but given too low an intensity are marked *.

In the *Cmcm* model arrived at through charge-flipping; Ca, Se, and O are located on sites with multiplicities of 4, while the iron site has a multiplicity of 8. Iron is located in distorted tetrahedra with 2 oxygen and 2 selenium vertices, which appear to be linked by edges and faces however, the Fe-Fe distances between these linkages are very close (1.72 and 1.71 Å) and iron site refines to have an occupancy of 0.486(2). This implies that, on a local scale, alternating sites are vacant such that the tetrahedra are linked only through the vertices, as represented in Figure 6.5.

Given that the vacancies on the iron site are ordered in the local structure, a sensible next step for the structural determination was to see if an long-range ordering of the iron vacancies could give an improved intensity match to the weak peaks in the X-ray diffraction pattern.

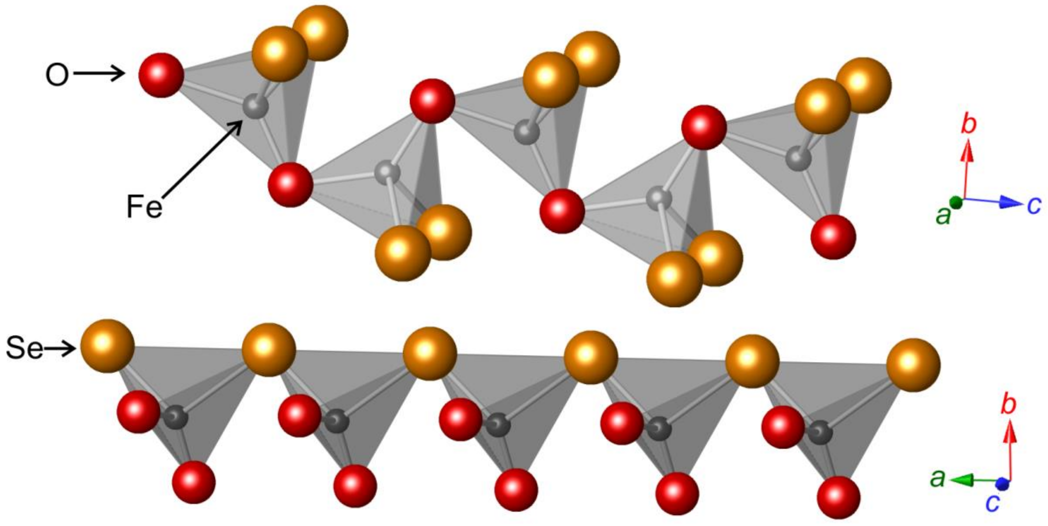

Figure 6.5 Deduced local coordination environment of iron in CaFeSeO from Rietveld refinement in *Cmcm* symmetry. The iron tetrahedra are joined in a 2D network, with oxide vertex linkages along the *c* axis and selenide linkages along the *b*. An interwoven CaSe layer separates the 2D FeSeO layers, which are stacked along *a*.

Starting from the model obtained from the refinement in Figure 6.4, a supercell that is expanded 2-fold along *a* (*a* = 7.78, *b* = 13.22, c = 5.93 Å) in *P*1 symmetry was built such that the possible ordering schemes represented in Figure 6.6 could be trialled. Unit cell parameters, atomic coordinates, other site occupancies, and thermal displacement parameters were fixed to give an equivalent structure to that obtained from the refinement in space group *Cmcm*, such that the only difference in the between the model used in Figure 6.4 and the models used in Figure 6.6 is the ordering of the iron vacancies. In each refinement shown in Figure 6.6, 8 of the 16 total iron sites were constrained to be fully occupied and 8 were constrained to be fully vacant to give the displayed arrangements of vertex sharing tetrahedra. It is observed that ordering scheme **A** introduces intensity exclusively to peaks that were given lower than observed intensity in the parent disordered model (marked by *****). Scheme **A** is the only ordering that improves the R_{wp} of the fit, even without additional refinement of the atomic coordinates, site occupancies, and thermal displacements. Ordering scheme **C** does not introduce any improvement to the intensity match and predicts scattering intensity at many angles where it is not observed. Ordering schemes **B** and **D** both introduce intensity to match some, but not all, of the * marked reflections and predict unobserved intensity elsewhere in the pattern. However, schemes **B** and **D** do predict intensity at the peak marked ◆ which matches the position of the (102) of the 3.89 × 13.22 × 5.93 Å unit cell, and is not given intensity by ordering scheme **A**.

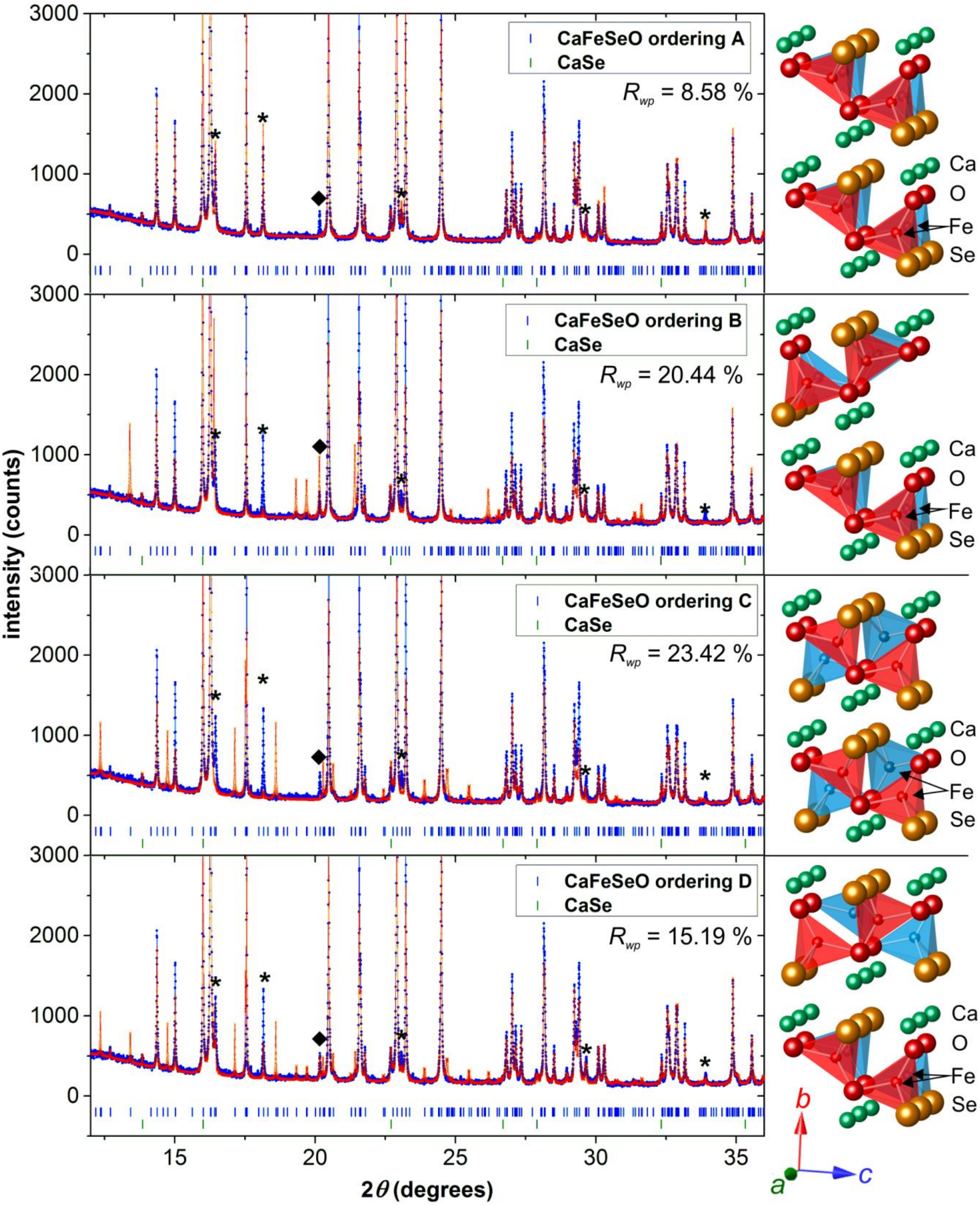

Figure 6.6 Rietveld refinement of the iron vacancy ordered structures shown beside each diffraction pattern: red and blue tetrahedra are used here only to distinguish $FeSe_2O_2$ tetrahedra linked by selenide vertices. Peaks marked * are predicted but given zero intensity by the *Cmcm* model, in which iron vacancies are disordered, and which has an R_{wp} of 10.90 %. The peak marked ◆ at 20.2 ° matches the position of the (102) of the 3.89 × 13.22 × 5.93 Å unit cell, and is symmetry forbidden in *Cmcm*.

To complement the powder X-ray diffraction analysis, electron diffraction was performed on the material in an attempt to accurately determine the symmetry of the system, and identify which, if any of the proposed orderings can explain the observed *hkl* reflections of a single crystallite.

6.4 Electron diffraction

Unlike X-rays and neutrons, electrons carry a negative charge and interact with both the electrons and nuclei in a material via Coulombic forces. Electrons are scattered much more strongly than X-rays, owing to a direct interaction with the local electric field (the electrons in the atom do not act as a secondary point source as is the case with X-rays). Structural solution and refinement from electron diffraction data is not often attempted due to problems in performing structure factor calculations, as well as difficulties in obtaining accurate scattering intensities, although this is being developed.[166] That being said, the strong scattering interaction between electrons and crystalline materials makes electron diffraction an excellent technique for obtaining the correct systematic absences to index the crystallographic unit cell and identifying any additional long range ordering features of the material, such as weak superstructure reflections or diffuse scattering.

Electron diffraction measurements and analysis were carried out on CaFeSeO (sample SXC223) by Professor Joke Hadermann at the University of Antwerp in order to complement the X-ray diffraction analysis by an independent determination of the dimensions and symmetry of the structure. The sample was ground (in air) and dispersed in ethanol on a holey carbon grid.

Several electron diffraction patterns from different *hkl* projections are shown in Figure 6.7. The basic reflections could be indexed using an orthorhombic unit cell with approximately a = 13.24 Å, b = 3.88 Å, c = 5.84 Å in extinction symbol *Cc*--, which gives the reflection conditions; hkl: $h+k=2n$, $h0l$: $h=2n$, $hk0$: $h+k=2n$, and $0kl$: $k,l=2n$. This extinction symbol means that the indexed cell of the material may fall into the space group *Ccmm* (63), *Cc*2*m* (40) or $Ccm2_1$ (36). *Ccmm* matches the model arrived at through charge-flipping (different setting of the same space group). Of the ordering schemes for the iron vacancies displayed previously in Figure 6.6, only **A,** which provided the best fit to the X-ray data, matches these results; it can be described with the unit cell measured by electron diffraction in $Ccm2_1$ symmetry. **C** and **D** require a unit cell with doubling of the 3.88 Å cell parameter, and **B** does not have *C* centring.

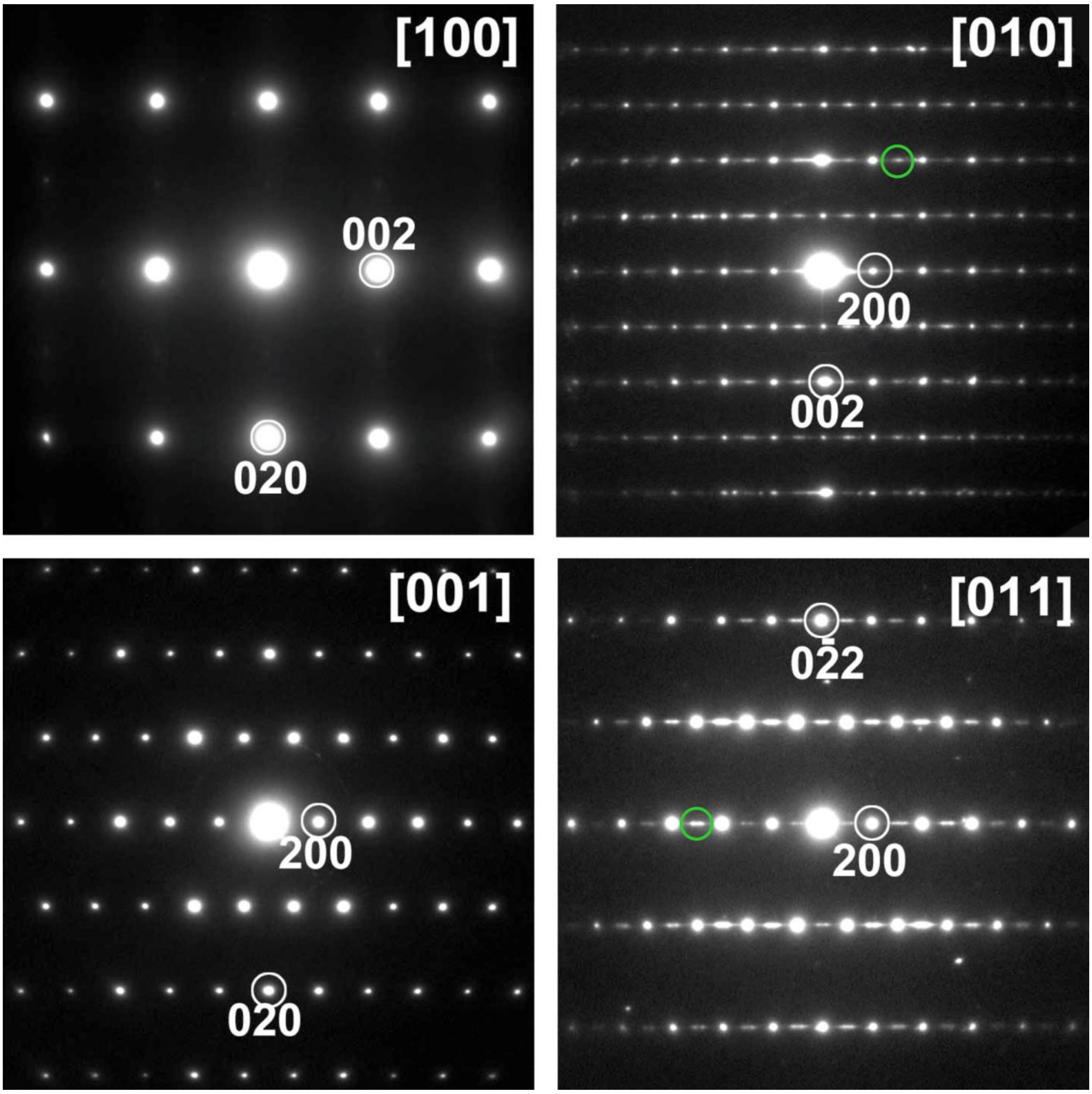

Figure 6.7 Electron diffraction patterns from CaFeSeO crystallites taken along the several planes, from which an orthorhombic unit cell with *a* = 13.24 Å, *b* = 3.88 Å, c = 5.84 Å is indexed. Additional reflections circled in green in the [010] and [011] zones are not from the indexed cell (see text).

While the basic reflections may be indexed simply, there appears to be additional complexity in the electron diffraction patterns of the [010] and [011] zones, which show several rows (circled in green in Figure 6.7) of almost continuous extra reflections along the *a**-axis (*a* = 13.24 Å). An enlargement of these rows is given in Figure 6.8, in which it can be seen that these rows are individual, low intensity reflections that are very closely spaced, not just streaks. This observation is indicative of additional longer range ordering, on a scale larger than the indexed unit cell. With close inspection of [100] pattern it can be seen that there may be very weak reflections at the positions k = odd. If these k = odd reflections in the [100] pattern were part of the basic reflections then the condition for $0kl$ reflections would be $l=2n$, however, they may be linked to the weak lines of reflections seen in the [010] and [011] patterns, and as such may be part of some superstructure and not the parent symmetry of the system, the interpretation is ambiguous at this stage.

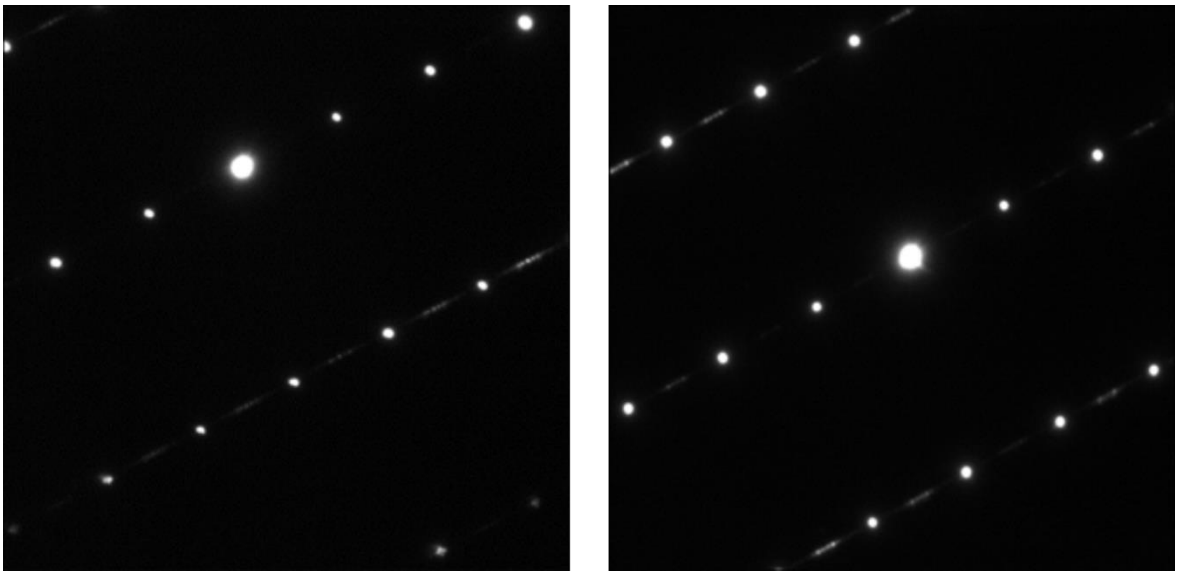

Figure 6.8 Close up of the electron diffraction in the [010] (left) and [011] (right) planes, showing rows of finely spaced diffraction spots.

6.4.1 Space group settings

The space groups of the indexed cell for the electron diffraction results, have been defined with *a* as the longest unit cell parameter rather than *b*. It is usual to set the axes of an orthorhombic crystal with the longest cell parameter along *b*, which is done as the default convention in the international tables for crystallography.[167] Elsewhere in this report the *a* and *b* unit cell parameter are switched relative to how they were reported by electron diffraction, such that $a = 3.88$, $b = 13.24$, and $c = 5.94$ Å. In this axis setting the *Cc*-- extinction symbol becomes *C*-*c*-, and the three space groups defined at the start of section 6.4 transform accordingly: $Ccm2_1$ becomes $Cmc2_1$, *Ccmm* becomes *Cmcm,* and *Cc*2*m* becomes *C*2*cm*.

6.5 Midway summary

CaFeSeO appears to have an orthorhombic unit cell with dimensions of approximately 3.88 × 13.24 × 5.94 Å. Initial structural solution, performed with powder X-ray diffraction data using charge-flipping gave a sensible structural model with a good fit to the data in space group *Cmcm* (number 63). In this structural model, iron is coordinated by 2 oxide and 2 selenide ions in a distorted tetrahedron. Fe^{2+} occupies a site with an 8-fold multiplicity while Ca^{2+}, Se^{2-}, and O^{2-} occupy 4-fold sites, *i.e.* there are twice as many positions that satisfy the 2 oxide, 2 selenide coordination than there are Fe^{2+} ions in the unit cell. In the *Cmcm* model the Fe^{2+} is fully disordered, half occupying the 8-fold position, however, Rietveld refinement shows that a certain ordering of these sites yields an improvement to the fit. This ordering has $Cmc2_1$ symmetry (space group 36) with unit cell axes of $a = 3.88$ Å, $b = 13.24$ Å, and $c = 5.94$ Å. The vacancy ordered structure is shown alongside the disordered structure in Figure 6.9.

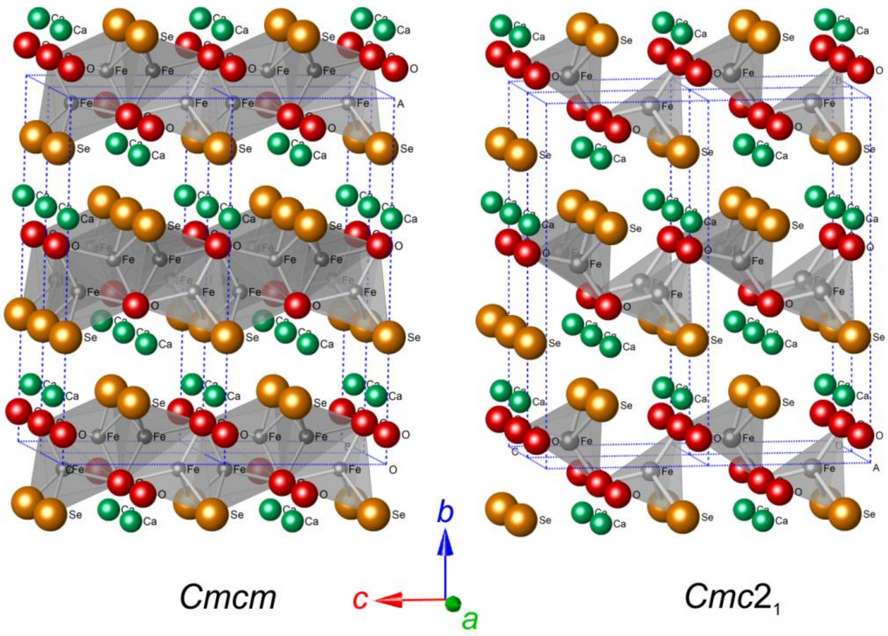

Figure 6.9 Comparison of the *Cmcm* model obtained via charge-flipping in which the Fe sites are fully disordered, and the $Cmc2_1$ model arrived at through Rietveld refinement, in which the iron vacancies have a specific ordering.

Electron diffraction concurs that the basic reflections of the material may be indexed with the space group $Cmc2_1$, however there are further weak diffraction peaks that are indicative of additional long range order in the material with a longer repeat length, which may be incommensurate with the unit cell. Similar evidence that the $Cmc2_1$ vacancy ordered model does not fully describe the system is evident in a powder X-ray diffraction pattern with a very high signal-to-noise ratio that was that was collected (on sample SXC223) using the mythen detector on I11. Several low intensity reflections are observed that do not fit the *hkl* selection rules for a *C*-*c*- extinction coefficient, but do index to the same orthorhombic cell. Particularly visible is the (102) reflection with an integrated intensity of 3.8 % that of the strongest peak in the pattern (as evaluated by Pawley refinement), but the (031), (012), (050), (032), (051), (122), and (161) are also observed, each with around 0.4 % of the strongest peak's intensity. There are also four unidentified peaks in the pattern, the largest of which has an intensity of approximately 0.1 % that of the strongest peak. These do not index to the same unit cell or any simple expansion of it, but also cannot be identified as an impurity given the known phases of combinations of the constituent elements. It is probable that the order/disorder of the iron site in the structure holds the answer to the unpredicted *hkl* reflections, and possibly the unidentified reflections also.

There are two sets of four positions in CaFeSeO's unit cell for four Fe^{2+} ions, which cannot be occupied simultaneously. Each set consists of vertex sharing planes of $FeSe_2O_2$ distorted tetrahedra. Given this situation; systematic switches in the linkages, which would switch from one set of positions to the other, might easily give rise to a modulated order in the crystal structure. Illustrative representations of these switches are displayed in Figure 6.10. These linkages occur in the *ac* plane, it is also unclear how order is maintained along the stacking direction *b*, which might further give rise to additional long-range order features.

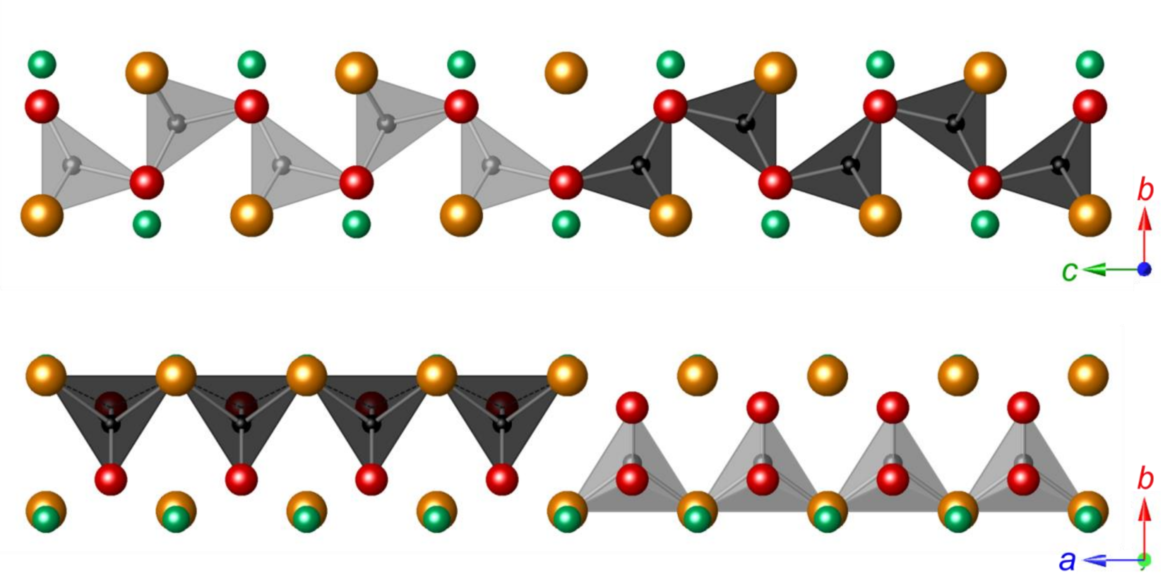

Figure 6.10 Representation of the possible defects in the iron vacancy ordering that might give rise to a switch from iron in one site to the other. Grey and black tetrahedra represent two possible orderings of the iron sites/vacancies in an *ac* plane.

The $Cmc2_1$ model does not require full ordering of the 8 iron positions in the unit cell (*i.e.* does not require only grey or only black tetrahedra, using Figure 6.10 for reference), but instead groups them into two crystallographic sites, each with a multiplicity of 4 (the grey and black) and requires the occupancy of all positions corresponding to the same site to be the same (all grey positions must have the same occupancy, as must all black). Refinements in $Cmc2_1$ symmetry to such effect typically show around 90 % occupancy on one site and 10 % occupancy on the other. To some extent the reflections that are not predicted in $Cmc2_1$ symmetry can be modelled by allowing the iron occupancy of each of the 8 iron positions in the unit cell to refine independently between 0 and 1, Figure 6.11 shows the effect of this. The model used for the lower fit in the figure has had its overall symmetry reduced to *P*1, but constraints were implemented such that the structure retains the symmetry relations between all atomic positions and thermal displacements, *i.e.* only the iron occupancies have no symmetry relationships. In fact, some order of the occupancies is still observed with the *P*1 model; the 8 sites refined with occupancies 1.00(17), 1.00(17), 0.74(18), 0.63(18), 0.31(23), 0.22(23), 0.00(21), and 0.00(21), in such a way that there are alternating layers along the stacking direction, *b*, that are fully ordered (all grey no black) and around 70 % ordered (70 % grey 30 % black). The fit to the additional peaks is improved by modelling in this way, which indicates that a certain ordering of the iron site occupancies is responsible for them.

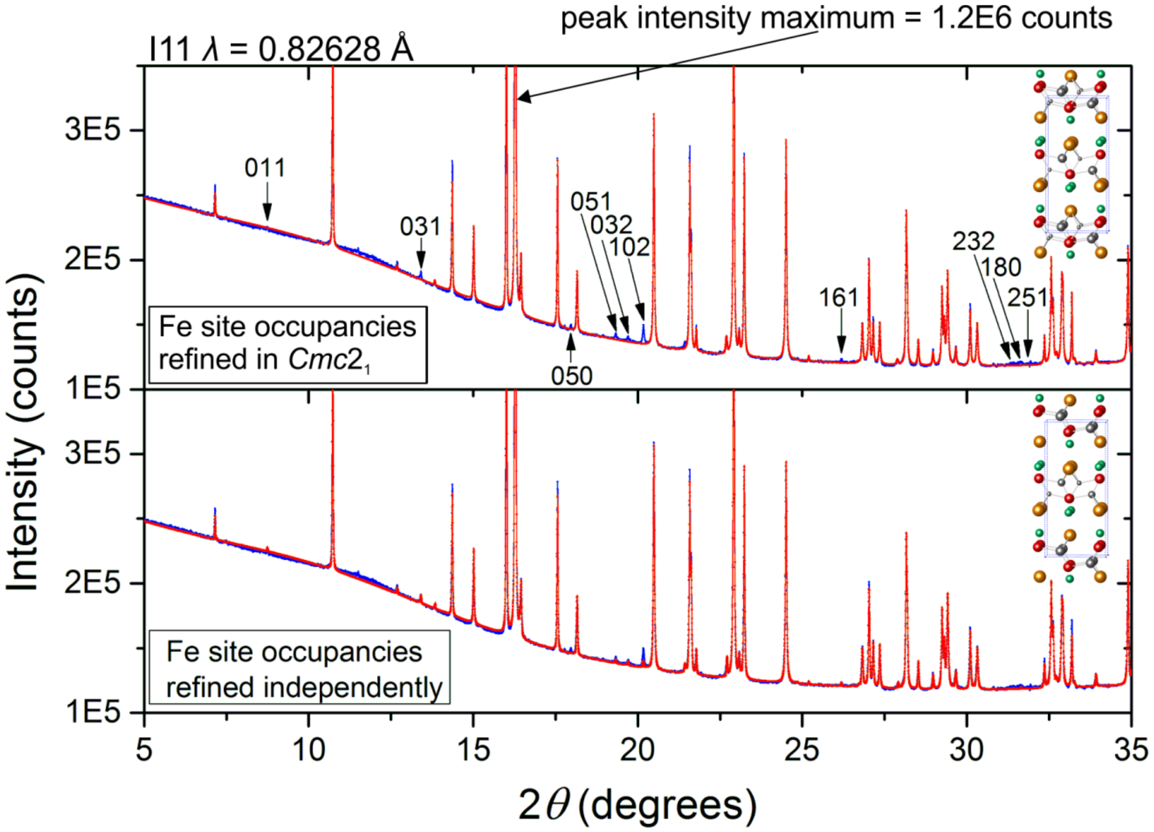

Figure 6.11 Rietveld refinement against a high signal-to-noise diffraction pattern of CaFeSeO (SXC223), showing just the low intensity region. The top pattern highlights the indexed reflections cannot have intensity in *Cmc*2_1 symmetry. The bottom refinement shows some intensity match to these peaks that has been gained by allowing the iron occupancies of all sites in the unit cell to refine independently. The structures at the inset display the iron site in grey as larger for a higher occupancy.

To summarise: the ordering of the iron positions in the structure of CaFeSeO is not yet fully understood. Of the eight iron positions in the 3.89 × 13.22 × 5.93 Å unit cell, dividing them (in a specific manner) into two groups; one 90 % occupied and one 10 % occupied, gives a marked improvement over having all eight positions 50 % occupied. Slight further improvement to the fit can be achieved by further dividing the eight positions into four groups; one 100 %, one 70 %, one 30 %, and one 0 % occupied, but no ordering of the 8 sites in the given unit cell can fully match the intensity of all the observed peaks in the X-ray pattern, and there are some very weak peaks that do not index. A model using a larger unit cell or possibly a modulation of the iron vacancy ordering would be required to fully model the low intensity peaks, and further experiments are required to accurately build such a model and fully characterise these finer structural details, which will be addressed at the end of this chapter. Moving forward in this report, the 90:10 ordered model in $Cmc2_1$ symmetry will be used for the characterisation, since the 100:70:30:0 model adds further structural complexity without a providing a full answer to the additional low intensity peaks. A further fit to neutron diffraction data using the 100:70:30:0 model is provided in appendix XII, which agrees with the X-ray data, showing that the additional indexed reflections can be partially but not completely matched in intensity by this model.

6.6 Structural determination

6.6.1 Neutron powder diffraction

Neutron powder diffraction data were collected by Dr Ron Smith, through the GEM Xpress service at ISIS neutron source. The sample (SXC195) was initially measured at room temperature on the Polaris instrument. Unfortunately, a sample misalignment as described in appendix XIII caused a splitting of the peaks the lower angle banks 1, 2, and 3. The sample was re-measured on the GEM instrument, but with a shorter collection time than would be ideal. In order to make full use of the available data, Rietveld refinement was carried out against GEM banks 2-6 and Polaris banks 4 and 5, simultaneously using one structural model. GEM bank 1 was of too low a signal-to-noise ratio to be usefully included in the refinement; this pattern is also given in appendix XIII.

Figure 6.12 shows the result of the Rietveld refinement against the neutron diffraction data. As with the X-ray diffraction pattern, there are a few, low intensity reflections observed, which index to the orthorhombic unit cell but are not predicted by the current structural model (iron vacancy ordering). These reflections, where clearly observable, are labelled appropriately in the figure.

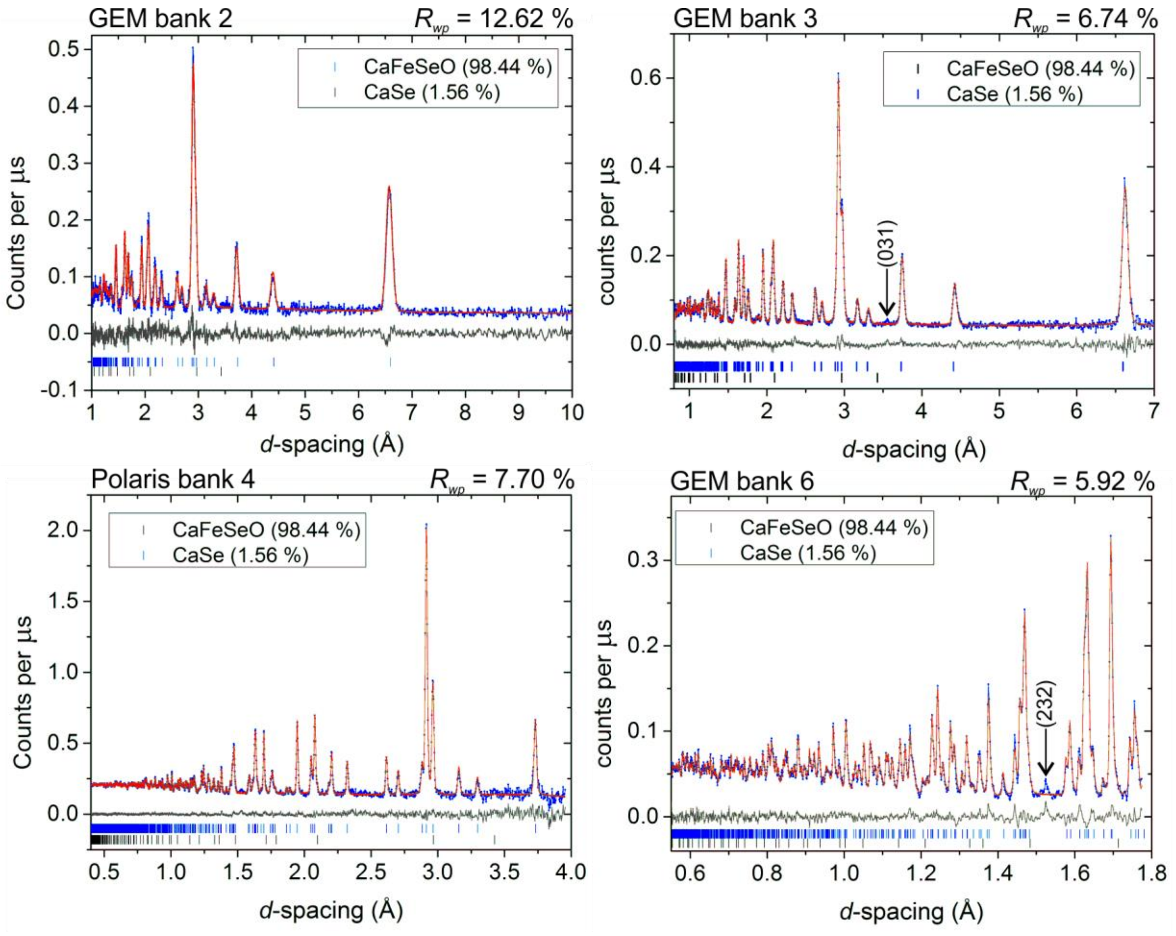

Figure 6.12 Rietveld refinement against time-of-flight powder neutron diffraction patterns of CaFeSeO (SXC195) from several detector banks.

The scattering caused by oxygen in X-ray diffraction is somewhat dwarfed by the scatterings of Se, Fe, and Ca. In neutron diffraction however, the scattering lengths of all species are of a more comparable magnitude, thus the atomic positions, occupancies and thermal displacements can be determined more reliably. It is found that with only one oxygen site, the distance to both Fe1 and Fe2 is larger than expected for an Fe-O bond. Improvement to the fit can be achieve by splitting the oxygen site in two, refining the position of the second site along *c* (the direction of the oxide linkages) but fixing the position along *a* and *b* to be the same as the first site (directions of the selenide linkages and the stacking, respectively). The occupancies of both iron sites and both oxygen sites were allowed to refine without constraint. Sites Fe1 and O1 have relative positions corresponding to an Fe-O bond, as do sites Fe2 and O2 together, but pairing sites Fe1 and O2 or Fe2 and O1 results in unsuitable bond distances. It may be concluded that in the local structure: either Fe1 and O1 or Fe2 and O2 are present at the same time. This conclusion is supported by the refined occupancies: without restraint Fe1 and O1 have the same occupancy within error, as do Fe2 and O2, and the combined occupancy of Fe1 and

Fe2, or O1 and O2 is close to one. A similar splitting of the Se site did not yield significant improvement to the fit, and its thermal displacement ellipsoid does not show signs of large displacement along any one direction, and so selenium was refined on a single site. The thermal displacement ellipsoids of Ca, Se, Fe1, and O1 were refined anisotropically, while those of Fe2 and O2 were refined as isotropic to avoid over-parameterising these low occupancy sites. The refined structure is given in Table 6.1-6.3 and shown in Figure 6.13 with the displayed atoms size and shapes determined by their relative thermal ellipsoids.

Table 6.1 Refined atomic structural parameter and bond distances from Rietveld refinement against powder neutron diffraction data for CaFeSeO. The bond distances in red are incongruous, showing that the Fe1 and O2 sites, or Fe2 and O1 sites are not simultaneously occupied in the local structure.

Instrument	GEM, Polaris	**Temperature /K**	295
Sample	CaFeSeO (SXC195)	**Space group**	$Cmc2_1$
R_{wp} / %	7.80	***a* / Å**	3.8916(1)
***b* / Å**	13.1952(5)	***c* / Å**	5.9266(2)
V / Å^3	304.33(2)	**Fe1-Se distance / Å**	2.575(2)
Fe2-Se distance / Å	2.50(1)	**Fe1-O1 distance / Å**	1.902(4) 1.943(6)
Fe2-O2 distance / Å	1.95(10) 1.98(6)	**Ca-Se distance / Å**	2.944(4) 3.041(2)
Ca-O1 distance / Å	2.316(2)	**Ca-O2 distance / Å**	2.31(1)
Fe1-O2 distance / Å	1.70(3) 2.4(1)	**Fe2-O1 distance / Å**	1.79(2) 2.38(2)

Table 6.2 Refined atomic coordinates and occupancies for CaFeSeO, from GEM/ Polaris.

atom	**site**	**x**	**Y**	**z**	**Occupancy**
Se	4*a*	0	0.65359(9)	0.60255	1
Ca	4*a*	0.5	0.6693(2)	0.1071(6)	1
Fe1	4*a*	0.5	0.4566(1)	0.2463(4)	0.885(4)
Fe2	4*a*	0	0.552(1)	0.464(3)	0.094(3)
O1	4*a*	0.5	0.5759(1)	0.066(1)	0.86(3)
O2	4*a*	0.5	0.5759(1)	0.14(2)	0.09(3)

Table 6.3 Refined thermal displacement parameters for CaFeSeO, from GEM, Polaris. Atoms Fe2 and O2 were refined isotropically.

atom	**U_{11} / Å^2 × 100**	**U_{22} / Å^2 × 100**	**U_{33} / Å^2 × 100**	**U_{23} / Å^2 × 100**
Se	0.87(9)	0.74(6)	0.63(8)	0.14(8)
Ca	0.6(1)	1.3(1)	0.1(1)	0.1(1)
Fe1	0.59(9)	1.18(8)	0.18(6)	0.41(6)
Fe2	1.2(5)	1.2(5)	1.2(5)	0
O1	1.0(2)	0.2(2)	0.3(2)	0.0(1)
O2	3.9(18)	3.9(18)	3.9(18)	0

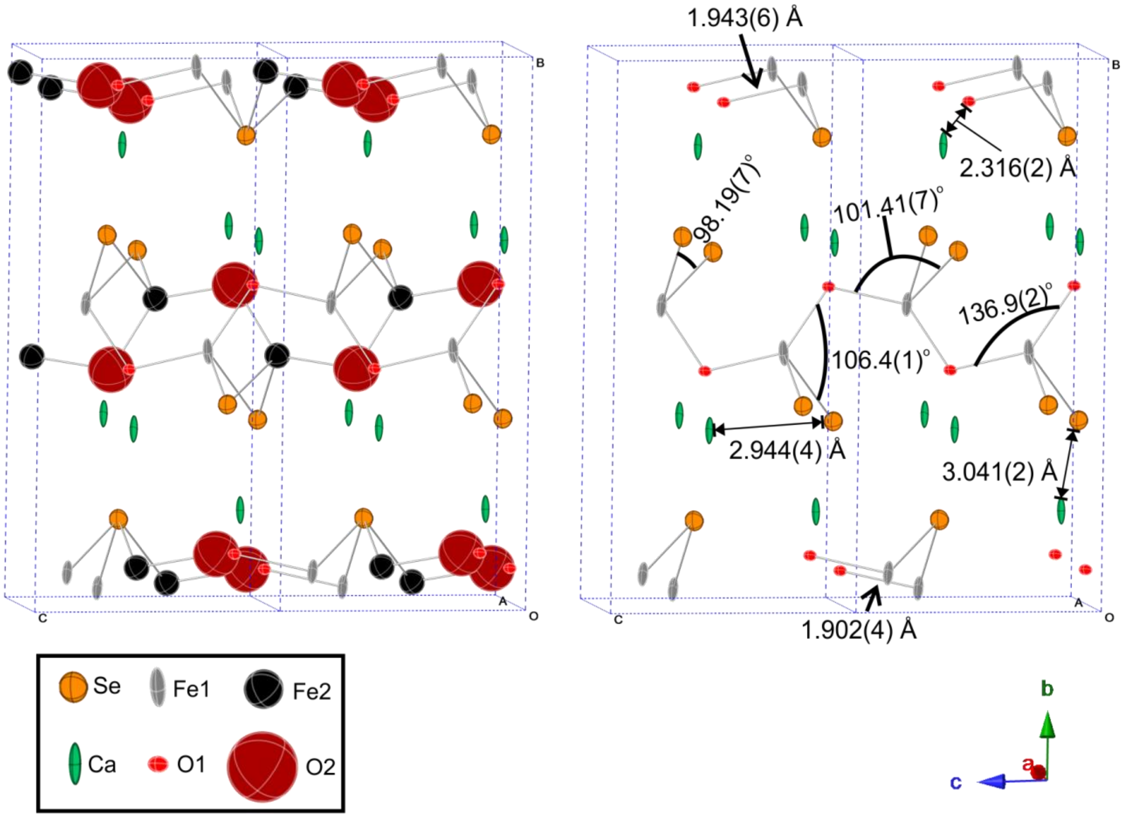

Figure 6.13 (Left) diagrammatic representation structure of CaFeSeO from Rietveld refinement against powder diffraction data. Sites are displaced with their relative sizes and shapes determined by the refined thermal ellipsoid. (Right) the same structure is shown without Fe2 and O2 sites which arise from vacancy disorder.

The structure is a distorted form of the BaZnOS structure, which was introduced at the start of this chapter. A visual comparison of the two structures is given in Figure 6.14. For clarity, the Fe2 and O2 sites in the CaFeSeO model have not been included in the diagram, but the tetrahedral sites that Fe2 would occupy have been shown with a black outline. The BaZnOS structure is well ordered, but in the CaFeSeO structure; the larger anion (Se *vs.* S) and smaller cation (Ca *vs.* Ba) cause the oxide positions move out of a single *ac* plane, and the Fe positions to move in towards that *ac* plane, which gives rise to the possibility of a second iron position.

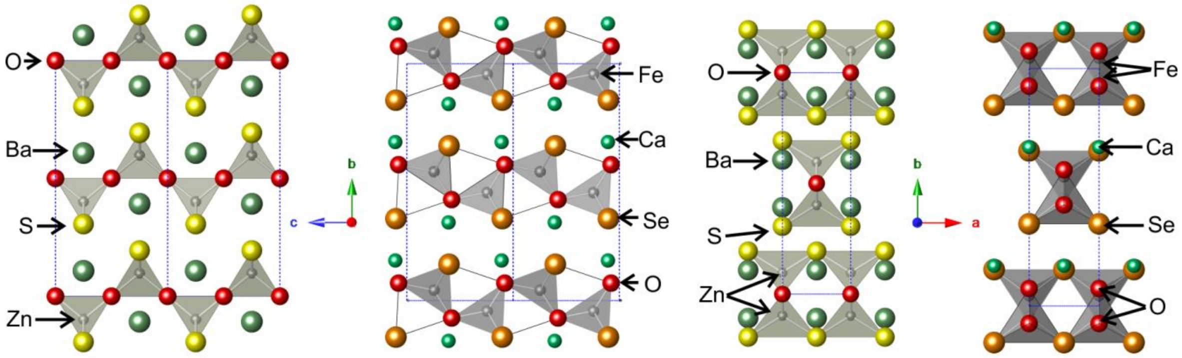

Figure 6.14 Comparison of the BaZnOS and CaFeSeO structures.

6.6.2 Synchrotron powder X-ray diffraction

The model refined by neutron powder diffraction is in excellent agreement with that from Rietveld refinement against the powder X-ray diffraction data obtained on I11 using the high resolution MAC detector (same sample SXC195). A comparison of the refined parameters is given in appendix XIV.

6.7 Magnetometry

Measurements on the magnetic properties of CaFeSeO were carried out using a Quantum Design SQUID magnetometer. Approximately 40 mg of CaFeSeO (SXC195) were loaded into a gelatine capsule, before placing inside the magnetometer. The sample was cooled in the absence of a field to 5 K then a 1000 Oe field was applied and the magnetisation (M) was measured as a function of temperature (T) in 10 K steps up to 295 K. After reaching 295 K, the sample was cooled back to 5 K, this time in the presence of the 1000 Oe field, and the measurement on warming was repeated. A plot of magnetic susceptibility in units of emu per mole against temperature is given in Figure 6.15. A transition in the susceptibility occurs around 155 K, which appears to be ferromagnetic in character. Following this observation, the magnetic hysteresis was measured above the magnetic transition at 200 K and 162 K, on the transition at 150 K, and below the transition at 120 K, 80 K, 40 K, and 2 K. These measurements were performed by cooling the sample to each temperature in a 5 T field then measuring M as a function of the applied field, H, between 5 T and -5 T then back from -5 T to 5 T. In order to remove the hysteresis in the sample between measurements, it was warmed to above the transition temperature (200 K) in a 5 T field before cooling back down to the next temperature. Plots of these hysteresis loops are given in Figure 6.16 with the magnetisation plotted in units of Bohr magnetons per formula unit.

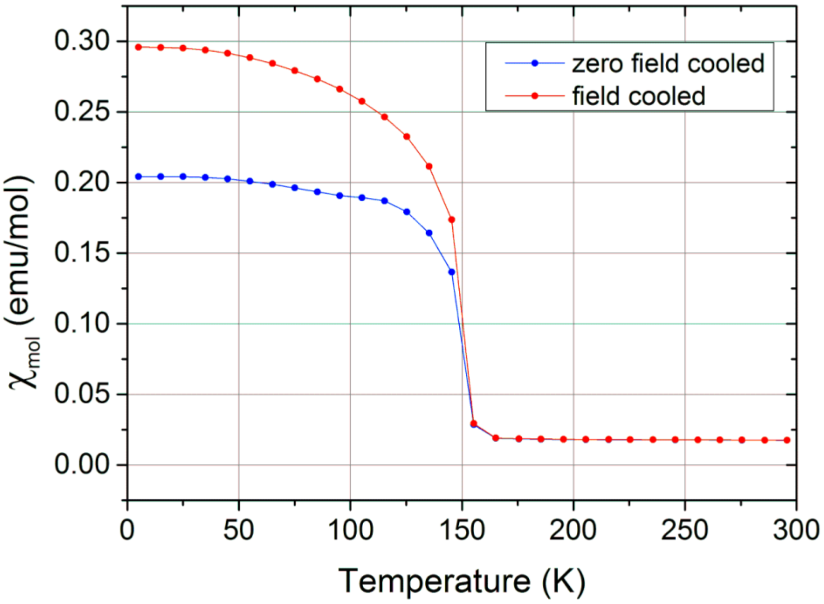

Figure 6.15 Magnetic susceptibility versus temperature plot for CaFeSeO (SXC195) measured on warming in a 1000 Oe applied field, both having cooled in the absence and with the field applied.

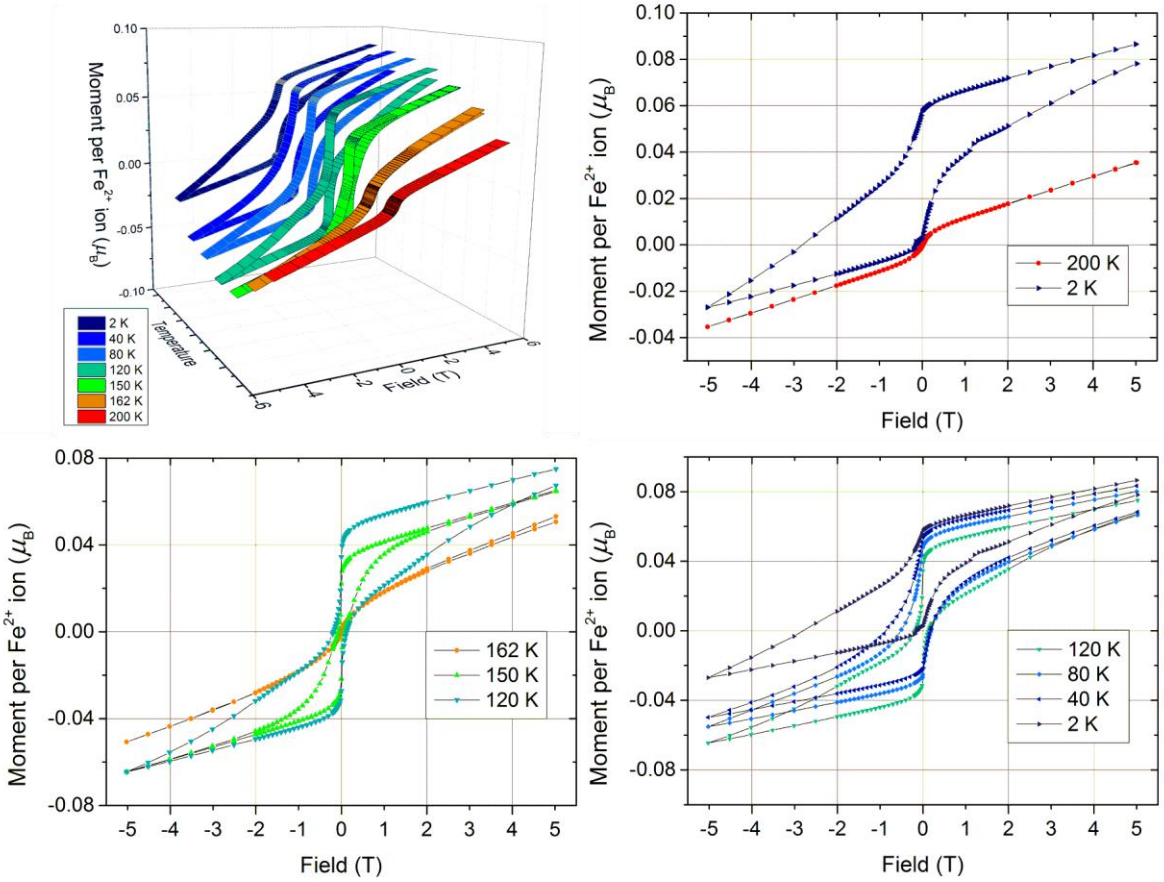

Figure 6.16 Magnetic hysteresis plots of CaFeSeO (SXC195), showing the variation in the magnetisation as a function of the cycled field at several temperatures.

There is a magnetic hysteresis at lower temperatures, the onset of which is between 162 and 150 K; the same temperature that the transition in the M versus T plot occurs. The hysteresis shows a vertical displacement, shifting the centre of the hysteresis loop at 0 T above 0 μ_B, a characteristic property of a spin glass. This displacement is strikingly potent in this sample, to such affect that at 2 K the magnetisation on reducing the field from -5 T to 0 T, the magnetic response of the sample is still positive in magnitude.

The saturation magnetic moment per Fe^{2+} at 2 K and 5 K is 0.087 μ_B. Given the glassy behaviour observed and that the spin only formula would expect the much larger magnetic moment per Fe^{2+} (4 μ_B) were all the spin domains aligned with the field, it is likely that there is an antiferromagnetic spin coupling. The ferromagnetic signature in the *M vs. T* and the non-zero moment of the sample at low temperature is indicative of a weak canting of the antiferromagnetically aligned spins.

Further work is necessary to characterise the glassy nature of the material, chiefly AC SQUID magnetometry measurements, in which the dynamics of a spin glass' freezing process can be studied by measuring the AC susceptibility as a function of field. Other techniques that can study this process include μSR and neutron spin echo spectroscopies.[168]

6.8 Variable temperature diffraction

6.8.1 *In-situ* X-ray powder diffraction between 295 and 110 K

In order to investigate whether any structural transition occurs at the magnetic transition temperature, X-ray diffraction patterns of a sample of CaFeSeO (SXC223) were collected on the synchrotron powder diffraction beamline I11 at Diamond Light Source, as the sample was cooled between the temperatures of 295 and 110 K using a Cryostream. The sample was cooled at a rate of approximately 6 K min^{-1}, collecting a diffraction pattern for 14 seconds (2 × 7 s) using the mythen detector, with an interval of approximately 10 seconds between collections. In order to spot any subtle changes in the structure, high signal-to-noise ratio patterns were collected at room temperature and 110 K (stable temperature) using the mythen detector with an 80-second (4×20 s) collection time. These two patterns are shown in overlay in Figure 6.17, there are no additional peaks or noticeable differences in the peak intensity between these two patterns.

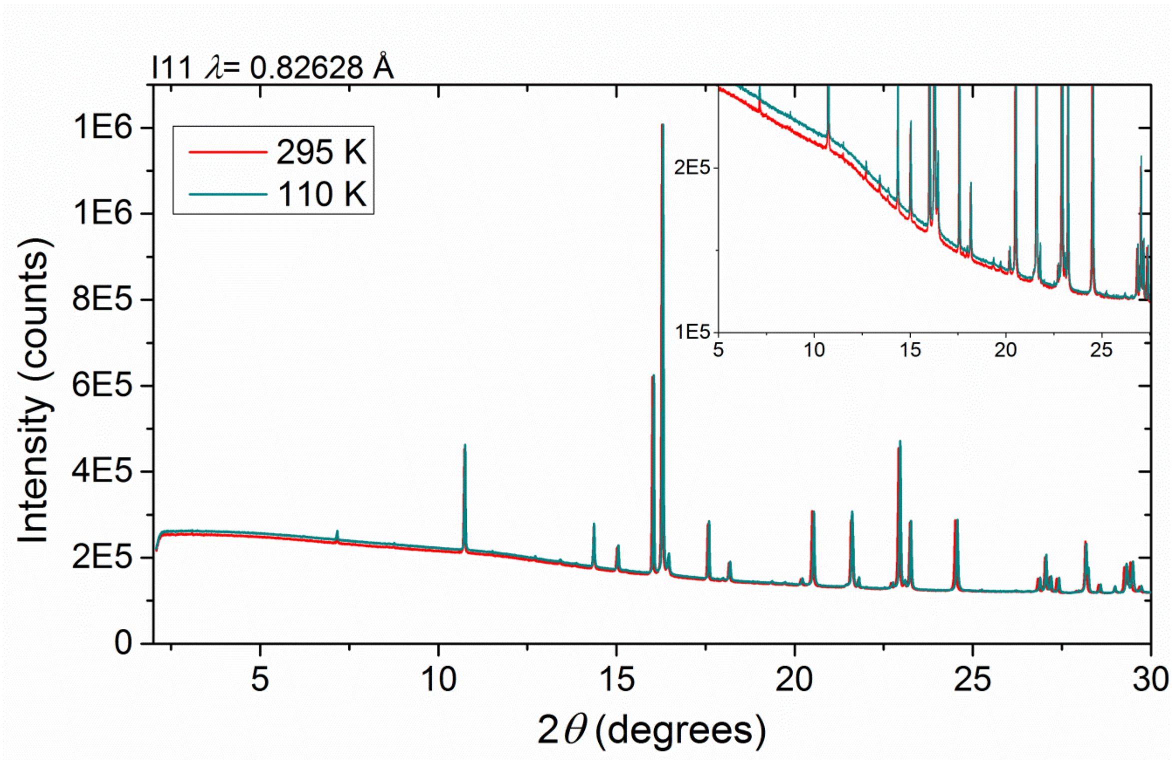

Figure 6.17 Overlay of the powder X-ray diffraction patterns of CaFeSeO (SXC223) measured on beamline I11 at Diamond Light Source at 110 K and 295 K.

Rietveld refinement was carried out against each diffraction pattern in turn using the same batch refinement procedure, which uses the outputted parameters from one refinement as the input for the least squares refinement of the next model for the next pattern. No evident correlations between the temperature and any structural phase parameters such as the occupancies of the iron sites are observed, but there is an interesting variation in the *a* and *b* lattice parameters around the magnetic transition temperature.

Figure 6.18 shows the temperature dependence of the lattice parameters *a*, *b*, and *c* normalised to their values at room temperature. The *a* and *c* unit cell parameters contract at approximately the same rate, which are the directions along which the iron tetrahedra are linked by selenide vertices and oxide vertices, respectively. Also plotted is the normalised *d*-spacing of the (102) reflection, which is the most intense reflection that indexes to the unit cell but is not predicted by the iron vacancy ordering scheme used. The identical contraction of the (102) peak and the *a* and *c* cell parameters is further evidence of the peak belonging to the structure and not arising from an impurity. The *b* cell parameter, along which the layers are stacked, contracts far more slowly as a function of temperature than *a* or *c*. The thermal contraction of cell parameters appears to contain a discontinuity at around 155 K, coincident with the magnetic ordering temperature. This discontinuity is particularly evident in the *b* cell parameter, in which the rate of contraction increases rapidly as shown in the bottom half of Figure 6.18.

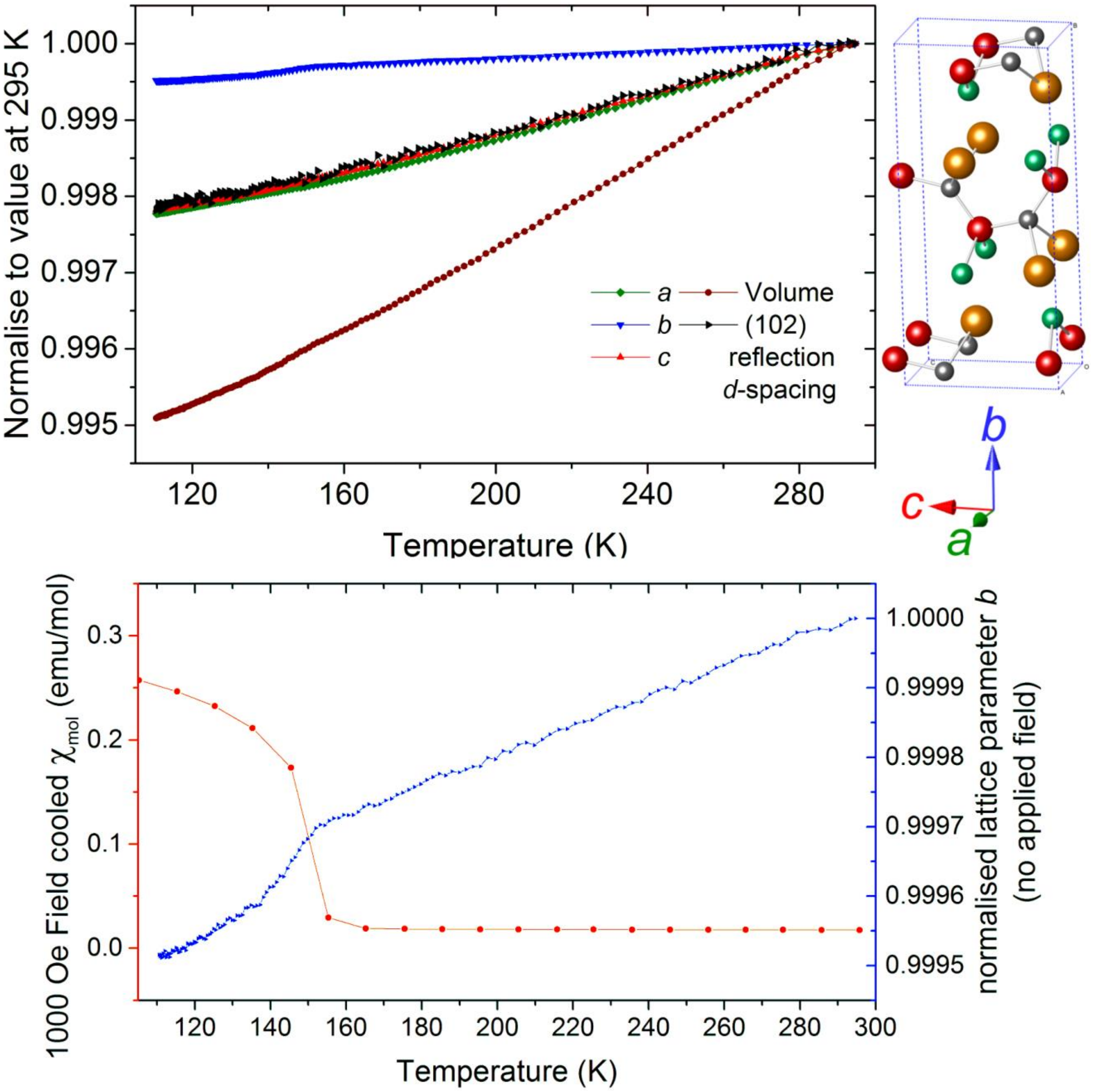

Figure 6.18 Top: variation in the lattice parameters of CaFeSeO as a function of temperature, normalised to their values at 295 K. Bottom: plot showing the overlap in the onset of the magnetic transition and a slight structural change causes a discontinuous shrinkage along *b*.

The discontinuous variation in the thermal contraction of the lattice parameters around the magnetic transition temperature is indicative of this being a magnetostriction effect. Magnetostriction is a common property of ferromagnets, and can be either a positive (*e.g.* iron) or negative (*e.g.* nickel) expansion of the material along the direction of the ferromagnetic ordering. Magnetostriction is usually volume conserving, as it appears to be in Figure 6.18, the contraction in *b* is matched by expansions in *a* and *c*. The extent of the magnetostriction effect can be defined by the coefficient, λ, as the fractional change in the length as the magnetisation of the material increases from zero to the saturation value.

Since the system is orthorhombic the magnetostriction coefficients, λ_a, λ_b, and λ_c, can be defined as:

$$\boldsymbol{\lambda_a = \frac{\Delta a}{a}\ ,\ \lambda_b = \frac{\Delta b}{b}\ ,\ \lambda_c = \frac{\Delta c}{c}} \qquad \textbf{Equation 6.1}$$

where Δa is the difference between the measured value of a and the expected value of a based on the thermal contraction of the material above the transition temperature. An Einstein model has been used to extract the pre-transition thermal contraction of each unit cell parameter:

$$\boldsymbol{x = x_0 + \frac{C_{\mathrm{E}}}{\exp(\frac{\theta_{\mathrm{E}}}{T} - 1)}} \qquad \textbf{Equation 6.2}$$

where x is the lattice parameter a, b or c, x_0 is expected lattice parameter at 0 K, C_{E} is the Einstein constant, θ_{E} is the Einstein temperature, and T is the temperature. The thermal contractions of the three lattice parameters have been fitted using a least squares refinement of equation 6.2 to the observed values of a, b, and c, over the region 295-160 K. The thermal contraction of the material is approximately linear over this region, and so values for the Einstein constant and Einstein temperature carry large errors. An Einstein model has been used instead of a linear model because the slowing of the rate of thermal contraction in the a and c unit cell parameters around the magnetic transition temperature will have a contribution from both the magnetostriction and the normal drop in the rate of contraction that is expected from the thermal motion of the atoms. Hence, using an Einstein model provides a slightly better estimation of the expected values for the lattice parameters below the magnetic ordering temperature, and a more accurate reading of λ. The thermal contraction models for the three lattice parameters are shown in Figure 6.19, with the extracted values for λ_a, λ_b, and λ_c given in Table 6.4.

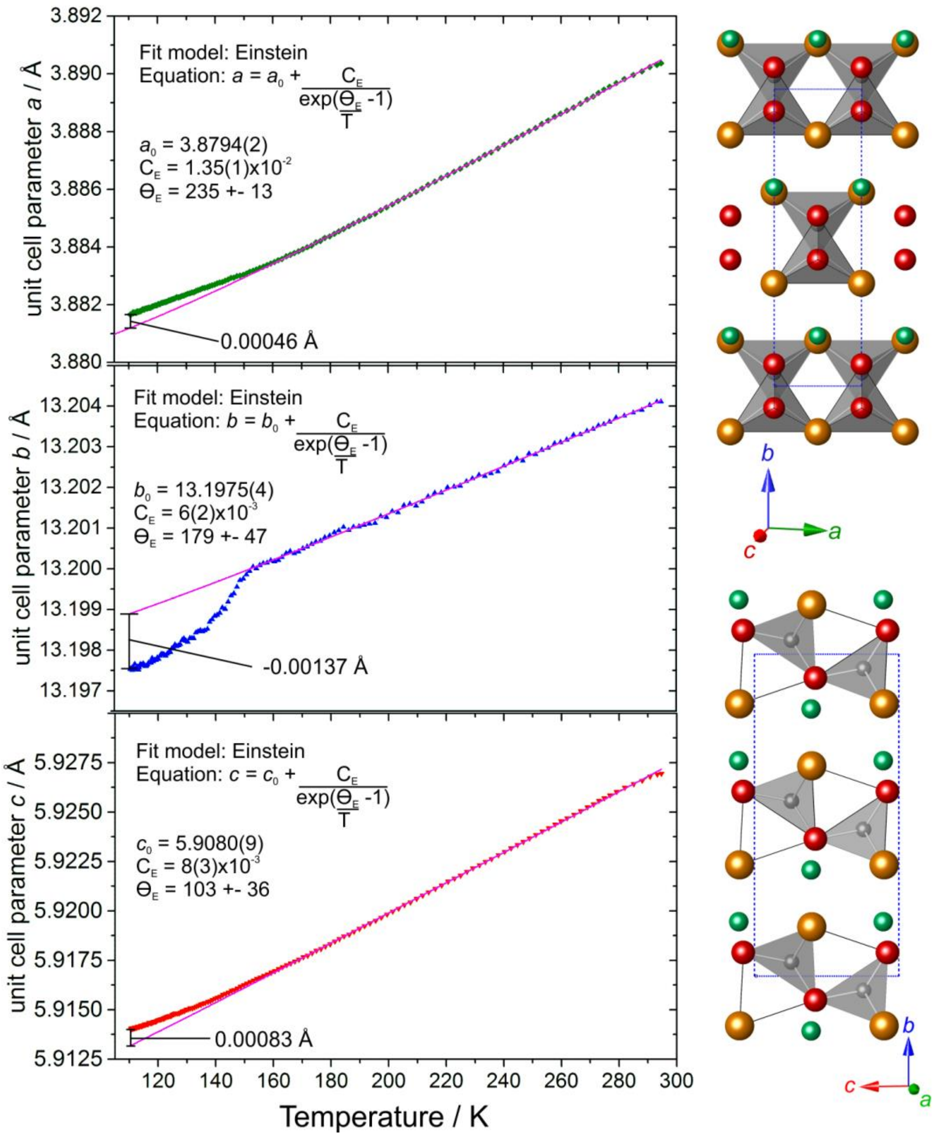

Figure 6.19 Thermal contraction of the *a*, *b*, and *c* unit cell parameters of orthorhombic CaFeSeO, modelled with equation 6.2.

Table 6.4 Parameters from a least squares fitting of equation 6.2 to the lattice parameters shown in Figure 6.19 over the region 295-160 K and the magnetostriction coefficients based on equation 6.1.

unit cell parameter	parameter zero value	C_E / × 10^{-3}	θ_E / K	λ / × 10^{-6}
a	3.8794(2)	13.5(1)	235(13)	+141(5)
b	13.1975(4)	6(2)	179(47)	-100(5)
c	5.9080(9)	8(3)	103(36)	+119(4)

6.8.2 Probing the magnetic structure with neutron powder diffraction

In the SQUID magnetometry, below ~155 K CaFeSeO shows some degree of canted antiferromagnetic coupling between Fe^{2+} moments, but also spin glass behaviour. In the introduction to this thesis, it was said that a spin glass exhibits no long range magnetic order. To recap: they are magnetically frustrated systems, in which defects relax the frustration in finite sized clusters. These clusters are randomly linked by the frustrated surroundings and can be frozen into one of many possible ground states by cooling below T_f. Long range order is not expected because the clusters orient randomly relative to one another, however, signs of spin glass behaviour do not fully exclude magnetic order because the antiferromagnetic clusters can be large enough to give rise to magnetic scattering.

Powder neutron diffraction has been carried out at low temperatures, in order to investigate whether any magnetic order can be observed at below the magnetic transition temperature. Neutron diffraction data for a sample of CaFeSeO (SXC223) were collected using the WISH diffractometer at ISIS, UK. The excellent resolution of WISH at high *d*-spacings makes it well suited for investigations of magnetic structures. The sample was loaded into a vanadium can and sealed with a pressed indium gasket inside a helium-filled, dry glovebox. The sample can was mounted inside a Cryostat, at 180 K and a measurement of the sample was performed at this temperature after allowing appropriate time for thermal equilibration. After measurement at 180 K, the sample was cooled to 5 K and measured again. Changes to the peak intensities of the structural reflections are clearly observable in Figure 6.20, which shows the diffraction patterns of detector banks 2 and 5 (along with Rietveld refinements) at 180 K and 5 K plotted on the same scale. Rietveld refinement of the nuclear cell was carried out, starting from the $Cmc2_1$ model refined against the GEM/Polaris data. As before, a few low intensity reflections that fit to the unit cell but not the symmetry of the model are observed, which likely originate from a higher degree of long-range iron vacancy ordering than is currently modelled.

Refinement of a magnetic structure model was performed using Topas academic version 5.[113] No expansion of the nuclear unit cell was required to index the magnetic scattering reflections. Refinement of the magnetic contribution to the reflections was carried out by modelling them as separate phase in $P1$ symmetry and considering only them magnetic contributions from the iron sites. The unit cell parameters and positions of the iron atoms were constrained to be the same as those in the parent cell of $Cmc2_1$ symmetry. The model for the $P1$ symmetry magnetic cell was developed with the aid of ISODISTORT[155] and the arrangement of magnetic moments shown in Figure 6.21 was arrived at by trialling the different symmetry modes. A magnetic moment on the Fe1 sites of approximately 3.6 μ_B was first identified, with antiferromagnetic ordering along *c* (the oxide linkages) and ferromagnetic ordering along *a* (the selenide linkages) and *b* (the stacking direction). This magnetic structure was found to model most of the magnetic peaks with a moderate fit (this ordering is given the label mGM4[Fe1:a:mag]A″ _2(a) in ISODISTORT). Further to this, a ferromagnetic canting of the spins with a moment of ~1.2 μ_B along *b* is observed, which roughly directs the moments along one of the Fe-O bonds in the tetrahedra (the mode that describes this is labelled mGM4[Fe1:a:mag]A″ _1(a)). Given that only these two modes are required to describe the scattering from the magnetic structure, the Shubnikov space group can be assigned as $Cm'c2_1'$ (labelled in Topas/ ISODISTORT as space group number 36.174).

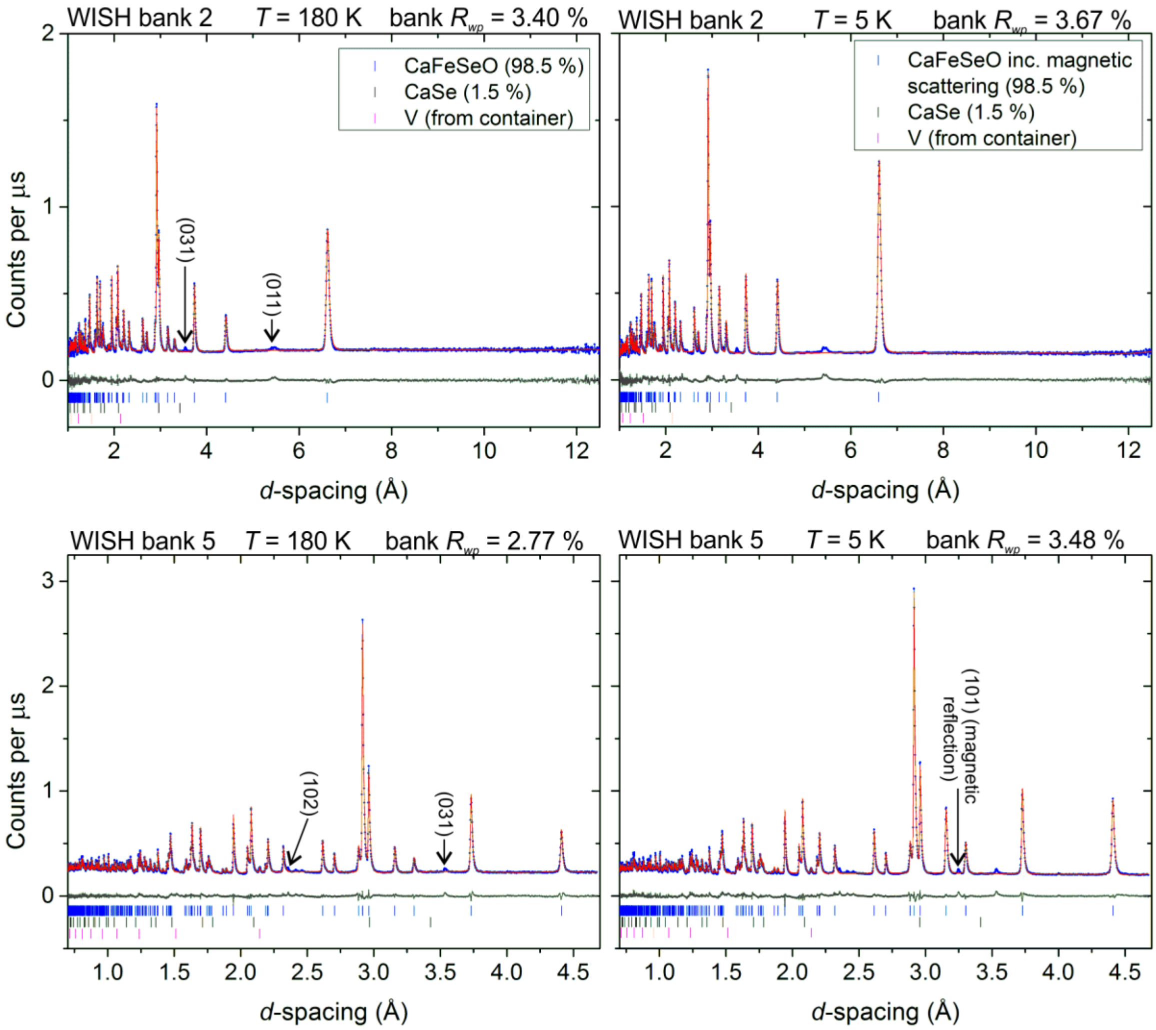

Figure 6.20 Rietveld refinement against Time-of-flight powder neutron diffraction patterns in the 58 ° (bank 2) and 153 ° (bank 5) banks of the WISH instrument at ISIS, UK. The plots on the left show the diffraction patterns at 180 K, and on the right show the patterns of the same sample, on the same scale, at 5 K. A magnetic contribution of the main phase is refined at 5 K.

Table 6.5 Comparison of Rietveld refinement parameters from neutron diffraction data for CaFeSeO collected on the WISH instrument at temperatures above the magnetic transition and close to base.

Temperature	180 K	5 K
R_{wp} / %	3.53	3.65
nuclear symmetry	$Cmc2_1$	$Cmc2_1$
magnetic symmetry	-	$Cm'c2_1'$
a / Å	3.89046(9)	3.88760(6)
b / Å	13.2145(3)	13.2145(3)
c / Å	5.9258(1)	5.9227(1)
Fe1 occupancy	0.872(3)	0.873(3)
Fe2 occupancy	0.108(2)	0.104(2)
Fe^{2+} moment (μ_B) ($\sqrt{(M_y^2 + M_z^2)}$)	-	3.83(3)

Table 6.6 Structural parameters from Rietveld refinement against CaFeSeO neutron powder diffraction data from the WISH instrument, collected at 5 K.

atom	**site**	**x / M_x(μ_B)**	**y / M_y(μ_B)**	**z / M_z(μ_B)**	**Occupancy**
Se	4*a*	0	0.65430(8)	0.60255	1
Ca	4*a*	0.5	0.6688(1)	0.1084(6)	1
Fe1	4*a*	0.5	0.4555(1)	0.2440(4)	0.873(3)
Fe1 moment(μ_B)		*0*	*1.27(8)*	*3.61(2)*	
Fe2	4*a*	0	0.537(1)	0.462(2)	0.104(2)
Fe2 moment(μ_B)		*0*	*-1.27(8)*	*-3.61(2)*	
O1	4*a*	0.5	0.5733(1)	0.0629(8)	0.90(2)
O2	4*a*	0.5	0.5733(1)	0.164(8)	0.09(1)

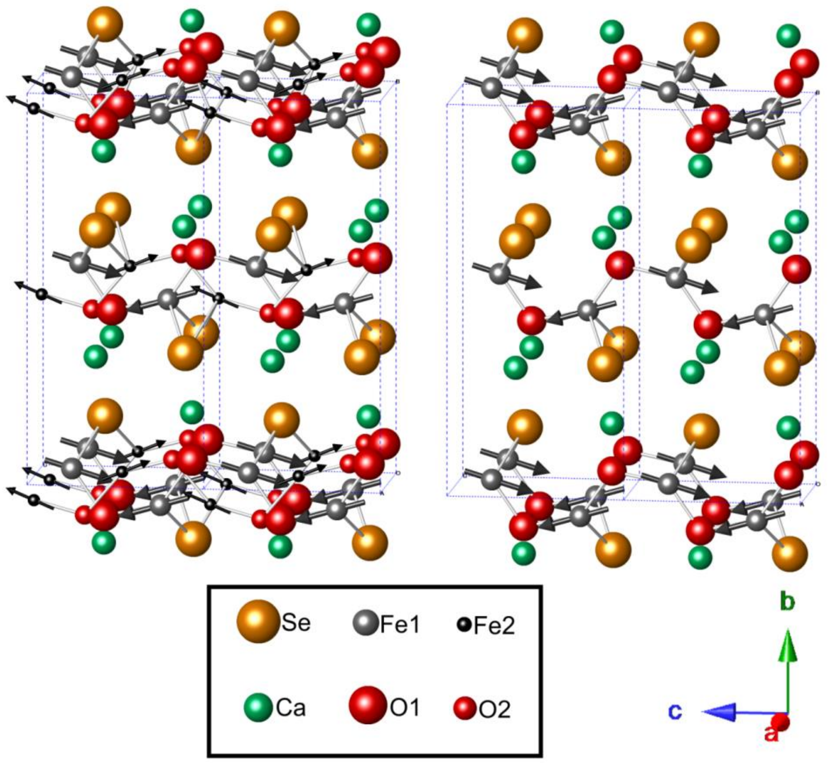

Figure 6.21 Diagram of the nuclear and magnetic structure as refined from neutron powder diffraction at 5 K, with arrows showing the direction of the Fe^{2+} magnetic moments. The diagram on the left shows the full average structure, and on the right shows the local structure.

The moments of the low occupancy Fe2 sites were constrained to have the same magnitude as those in the Fe1 sites. Whether the canting direction is matching or opposite to that of the Fe1 site has a minimal effect on the agreement factor of the fit, but does affect the magnitude of the moment along *b*; a matching canting giving 1.09 μ_B and an opposing canting giving 1.27 μ_B. By inspection of the structure shown in Figure 6.21 it is expected that the canting of the Fe2 spins is opposed and value is 1.26 μ_B: if an iron on site Fe1 moves to site Fe2 through the face of a tetrahedra, then in order to maintain both the phase of the main magnetic component along *c* and the direction of the moment along the Fe-O bond, the direction of the canting must flip.

If the magnetic ordering in the system were throughout the whole sample and saturated, then the expected magnetic moment would equal *gJ*. Since the degeneracy of the Fe^{2+} 3d orbitals is completely broken in the $Cmc2_1$ space group, $L \approx 0$ and $J \approx S$, so with 4 unpaired electrons an Fe^{2+} moment of 4 μ_B is expected. The observation of a slightly lower (3.83(3)) ordered moment is congruous with the system exhibiting some frustration. Covalency between iron and the anions might also serve to decrease the moment.

One additional peak at high *d*-spacing, shown in Figure 6.22, is observable the lowest angle bank of WISH that cannot be indexed to the orthorhombic unit cell, or any linear or quadratic expansion of the cell parameters. At this time, the peak cannot be identified, but it is unlikely that an unknown impurity could give rise to a single peak at such a high *d*-spacing, which suggests that the peak arises from some modulation of the structure that is incommensurate with the parent crystal structure. This peak is only clearly observed in this diffraction pattern, which is to be expected given the uniquely high resolution of the WISH instrument at long *d*-spacings. Further insight into the origin of this may come from further analysis using electron diffraction and microscopy.

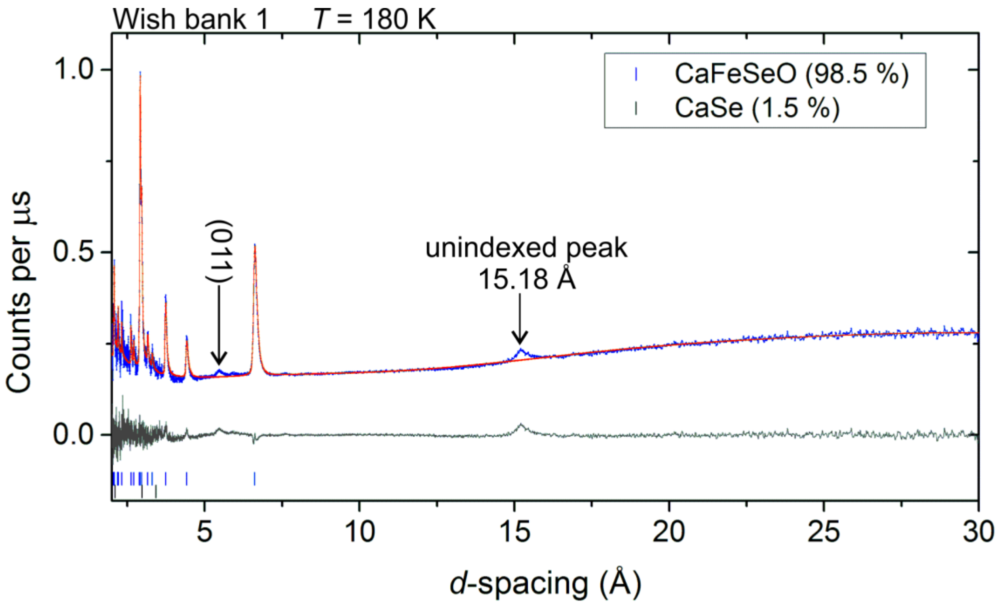

Figure 6.22 Rietveld refinement against a powder neutron diffraction pattern of CaFeSeO taken at 180 K on the WISH instrument at ISIS. A reflection at 5.4 Å is indexed by the unit cell but not modelled but the current iron vacancy ordered model. An unindexed peak at 15.18 Å likely arises from some incommensurate modulation in the structure.

6.9 Discussion, conclusions, and future work

A new material, CaFeSeO, has been synthesised, and large headway has been made in to the characterisation of its structure and properties, but some further work is necessary. CaFeSeO adopts a new crystal structure, the basic form of which has been solved by charge-flipping from powder X-ray diffraction data.[98] the structural model has been refined using X-ray diffraction performed on beamline I11 at Diamond Light Source and neutron diffraction on GEM and Polaris at ISIS neutron source.

The structure consists of staggered layers of vertex sharing [FeO_2Se_2] distorted tetrahedra, with calcium between the layers: coordinating 2 oxide and 2 selenide species in one layer, and another 2 selenides in the next. This structure is a distorted form of the BaZnOS structure. In the BaZnOS structure, there are four Zn^{2+} ions in the unit cell, which fully occupy a 4-fold symmetry site. In the distorted form, CaFeSeO, there are four Fe^{2+} ions in the unit cell but the site becomes effectively 8-fold, leaving four vacancies. Only four of the eight positions can be filled simultaneously due to interatomic distance restraints, but more than one option exists as to which four are chosen. Curiously rather than the vacancies being fully ordered or fully disordered among the two sets of four iron positions, they are have a distribution which on average places 90 % on one set and 10 % on the other. This 90:10 ordering captures the average occupancies of these sites quite well but further complexity exists in the system, as evidenced by features in the electron diffraction patterns and additional peaks in the X-ray and neutron diffraction patterns, which likely arise from additional long range ordering of the iron sites. High-Angle Annular Dark Field Scanning Transmission Electron Microscopy (HAADF-STEM) images might provide insight into the nature of the modulation present. The technique has been used to show modulation in the crystal structure of the $Sr_2MnO_2Cu_{2-x}S_2$ system, which is caused by an incommensurate ordering of the copper vacancies when x ~ 0.7.[169]

CaFeSeO shows a peculiar mixture of magnetic behaviours, including signatures of a spin glass, ordered antiferromagnet, and an ordered ferromagnet, but all of these can be rationalised by the refined nuclear and magnetic structure of the material. Long-range magnetic order exists in the system below the magnetic transition temperature of 155 K, which is a canted antiferromagnet with a total iron moment of ~3.8 $\mu_{B.}$ The slightly lower than expected moment (a moment of 4 μ_B expected for Fe^{2+} in a highly asymmetric coordination environment) is consistent with large domains of long-range ordered moments, separated by spin glass domains. The spin glass behaviour likely arises from the disorder of the iron positions in the system, which could easily create a domain structure. The canting of the iron moments along the stacking direction in the structure, *b*, is consistent with the ferromagnetic signature in the magnetometry that saturates at a low magnetisation value.

A magnetostriction effect is seen in the lattice parameters around the magnetic ordering temperature, which causes a contraction of the unit cell along the direction of the ferromagnetic canting, *b*, and an expansion of the *a* and *c* unit cell parameters with a conservation of volume. The magnetostriction coefficients at 110 K in the absence of field for the three directions have been determined, but a further study of the material in an applied magnetic field and ranging to lower temperatures is required in order to determine the saturation values for this effect.

Chapter 7

7. Summary, conclusions, and future work

This thesis reports the structure, properties, and chemistry of a series of iron chalcogenide and pnictide systems, with an emphasis on materials that exhibit high temperature superconductivity.

Chapter 3 examined the oxidative deintercalation of sodium and iron from superconducting NaFeAs using iodine dissolved in THF at room temperature. This reaction produces a product that appears to adopt the $ThCr_2Si_2$ structure, but there is an inherent loss of crystallinity in the product relative to the starting material. The product was originally reported to have a stoichiometry of $NaFe_2As_2$,[92] but a later report suggested that iron is also deintercalated in the reaction, producing vacancies on the iron site.[94] The latter report by Friederichs *et al.* used powder X-ray diffraction data and EDX to assign stoichiometries of $Na_{0.99(4)}Fe_{1.67(2)}As_2$ and $Na_{0.9(0.2)}Fe_{1.7(2)}As_2$, respectively. The work in chapter 3 uses EXAFS, a local probe, to study the deintercalated product, which confirms that iron is deintercalated along with sodium and giving further insight into the structure.

A dramatic loss of local order occurs between NaFeAs and $NaFe_{2-y}As_2$ as probed by EXAFS, along with the loss of long-range order that is seen in the diffraction patterns. This loss of local structure in the EXAFS is characteristic of iron vacancies in the anti-PbO type FeAs layers, which introduce a structural disorder component to the Debye-Waller factors of the various scattering paths that flattens the features in the EXAFS.[128,130] Modelling of the iron and arsenic edge EXAFS of $NaFe_{2-y}As_2$ shows that a non-defective $ThCr_2Si_2$ type structure does not model the data and the vacancies must be taken into consideration. The effect of vacancies on the local structure of $NaFe_{2-y}As_2$ is to create some disparity in the Fe-As bond length, which depends on whether the arsenic environment has 4 or 3 iron nearest neighbours. Modelling the proportional weight of the Fe-As scattering paths with 3 and 4 neighbouring gives the refined formula $NaFe_{1.7(4)}As_2$, consistent with the work done by Friederichs *et al.*[94]

Superconductivity in the iron pnictides and chalcogenides is observed in many systems that contain in anti-PbO type Fe*Pn*/*Ch* layers, with iron in or near a +2 oxidation state. Superconductivity in these systems is commonly brought about by partial reduction or oxidation of Fe^{2+}, which changes the position of the Fermi level. Substitution of Ba for K in $Ba_{1-x}K_xFe_2As_2$ prompts superconductivity in the system, with T_c being maximised at 38 K for $x = 0.4$,[49] corresponding to an Fe average oxidation state of +2.2. T_c decreases when $x > 0.4$, and T_c is reduced in KFe_2As_2 ($Fe^{2.5+}$) to 3.7 K.[170] $NaFe_{1.7}As_2$ would appear to be a 10 K superconductor with an iron oxidation state of +3, but the origin of the superconductivity is likely to be from an intrinsic phase separation as occurs in the better-investigated $K_{1-x}Fe_{2-y}Se_2$ series ($x \approx 0.2$; $y \approx 0.4$).[80,84,131–134] X-ray absorption spectroscopy and X-ray diffraction both primarily characterise the most numerous environments in the sample, hence it cannot be ruled out that superconductivity only occurs in small domains that have not been resolved by these measurements. Characterisation of such domains may be complicated because of the sample’s lack thermal robustness and crystallinity, which have been key in identifying the phase separation in the $K_{1-x}Fe_{2-y}Se_2$ series.

There may be further scope for investigation into reports that superconducting transition temperatures as high as 25 K appear exist in NaFeAs samples that have undergone deintercalation.[92] This transition has been assigned to a $Na_{1-x}FeAs$ phase,[93] which has not undergone a structural transition to $NaFe_{1.7}As_2$.[94] Synthesis of several $Na_{1-x}FeAs$ samples might be attempted in order to probe whether iron vacancies in the iron arsenide layer are present or not in the $Na_{1-x}FeAs$ samples using EXAFS, and assignment of oxidation states could be carried out from the XANES. *In-situ* investigations into the synthesis of $NaFe_{2-y}As_2$ from NaFeAs could potentially be performed to characterise the order of events in the transformation, and determine if $Na_{1-x}FeAs$ is an intermediate.

Chapter 4 examined the synthesis, structure, properties and various chemistries of the products of a reaction between sodium in liquid ammonia solution and superconducting β-FeSe. The reaction intercalates both sodium and ammonia into the FeSe interlayer space in a similar manner to that observed in the more investigated lithium and ammonia system.[135] It is reported for the reaction of lithium with β-FeSe in liquid ammonia that a co-intercalation of both lithium and ammonia occurs into the FeSe interlayer.[89,90] In liquid ammonia solution this produces a product with a stoichiometry refined from neutron diffraction data of “$Li_{0.3(1)}(ND_{2.7(1)})_{0.85(5)}FeSe$”, known as the ammonia-rich phase and adopts a structure akin to ZrCuSiAs.[135] When exposed to a vacuum, as is done in the normal course of removal of the ammonia solvent to produce dry solid products, there is a partial loss of ammonia which gives an ammonia-poor product with a structure akin to $ThCr_2Si_2$ and a refined stoichiometry of “$Li_{0.6(1)}(ND_2)_{0.2(1)}(ND_3)_{0.8(1)}Fe_2Se_2$”.[90]

The reaction of sodium with iron selenide in liquid ammonia produces an ammonia-rich sodium intercalate with the same structure type as the ammonia-rich lithium intercalate, with the refined formula $Na_{0.175(11)}(ND_3)_{0.71(9)}(ND_2)_{0.18(9)}FeSe$. The absolute values for the refined stoichiometry suggests that the iron oxidation state is not reduced at all in the ammonia-rich intercalate product, however, the error is large relative to these values, with the first, second, and third standard deviations allowing average oxidation states of +1.9, +1.8, and +1.7, respectively.

Rates for the formation of the ammonia-rich sodium intercalate of iron selenide have been extracted by following the process of intercalation with *in-situ* powder X-ray diffraction at various temperatures. Rate constants at four temperatures have been acquired by fitting the data with an Avarmi-Erofe'ev model of the reaction rate, which fit to the Arrhenius equation, giving an activation energy of 26.3 ± 1.6 kJ mol^{-1}. Future work performing a similar variable temperature *in-situ* study into the structurally analogous lithium system would make for a good comparison.

Upon removal of liquid ammonia from the sample an ammonia-poor phase with half as much ammonia per formula unit is formed. This again shows similarity to the lithium system.[90] However, a structurally complex second phase arises alongside the ammonia-poor phase when the ammonia vapour is removed from the sample by vacuum or argon flow. Characteristic features of this other phase, which has been called the "stacked phase", are also present in the diffraction patterns of the ammonia-poor phases reported by both Ying *et al.*[89] and Guo *et al.*[137], but they have not been modelled in their work. The stacked phase cannot be indexed to a high symmetry unit cell like the ammonia-rich or ammonia-poor phases, but can be modelled with a supercell comprised of 14 FeSe layers, with varying species separating the layers. This work underlines the complexity in the behaviour of this system that has been glossed over in the literature. HAADF-STEM measurements on samples containing the ammonia-poor and stacked phases might provide insight into whether the stacked phase is truly of the nature described in the Rietveld refinement model, which might not be the only interpretation of the data. These measurements might also reveal whether the stacked and ammonia-poor phases are truly separate crystallites, or whether the stacked phase encapsulates the ammonia-poor phase. However, these measurements are likely to be hampered by thermal instability in the beam leading to decomposition.

The relative phase fractions of the ammonia-poor and stacked sodium intercalate phases are observably connected to the magnetic behaviour of the sample as a whole. The ammonia-poor phase is responsible for as superconducting transition at 46(1) K and high superconducting volume fractions, in line with the assignment in the reports by Ying *et al.*[89] and Guo *et al.*[137] A broad superconducting transition around 32(2) K is observed in several samples containing the stacked phase, with superconducting volume fractions between 5 and 15 %. The magnetometry of an ammonia-rich sodium intercalate of iron selenide has been measured, and is found to have a T_c of 42(1) K, consistent with the transition determined by Guo *et al.* Further magnetometry measurements on ammonia-rich samples could be performed by re-exposing samples that show a different ratio of ammonia-poor : stacked phases to an ammonia atmosphere so that a correlation between the properties of the parent sample and daughter ammonia-rich sample after re-ammoniation might be established.

Cycling of the ammonia absorption from the ammonia-poor phase to the ammonia-rich phase has been shown to be a reversible process, which does not have any significant detrimental effect on the magnetic properties. The stacked phase is also found to transform into the ammonia-rich phase when exposed to ammonia vapour, with no resolvable phase separation in any of the ammonia-rich products. *In-situ* investigation of the ammonia cycling performed on beamline I11 at Diamond Light Source showed that the ammonia-rich and ammonia-poor phases can adopt a range of lattice parameters and as such are not just line phases. The origin of this phase-width is likely to be a variation in the specific amount of ammonia that is intercalated or the amount of amide that is formed, but further investigation of this is required.

Intercalation of water molecules into the interlayer space of FeSe has been shown to be possible, starting from ammonia-poor/ stacked sodium intercalated iron selenide, forming a structure that is analogous to the ammonia-rich phase. It is unclear at this time as to whether H_2O is exchanging with NH_3 or co-intercalating with it, and further synthetic and analytic work might be attempted to find an effective synthesis and storage procedure for this material on a > 100 mg scale. This method of intercalation into the interlayer space of FeSe might also be attempted using other the vapours of other polar molecules and other synthetic methods for intercalation of molecules might be attempted also. Difficulties have been encountered by this research group in the past when trying to intercalate other amines between iron selenide layers using the alkali metals in the amine solution, but a recent report from Hosono's group suggests that diamines can be intercalated if liquid ammonia is used as a solvent and it is proposed to investigate these intercalates *in-situ*.[171]

Chapter 5 examined the synthesis, structure, properties and various chemistries of the products of a reaction between potassium and superconducting β-FeSe in a liquid ammonia solution. A study by Ying *et al.* [152] into the ammonia-poor structures of this system showed that for various samples of nominal composition of $K_x(NH_3)_yFeSe$ with x between 0.1 and 0.4, a phase gap opens between $x = 0.15$ and $x = 0.3$, where stoichiometries either side of this gap give quite different unit cell parameters and superconducting properties. They go on to report that annealing $K_{0.15}(NH_3)_{0.35}FeSe$ under dynamic vacuum at 200 °C yields $K_{0.15}FeSe$, with all the ammonia removed from the structure. The work in this thesis reports the ammonia-rich structures for these compositions, discovers an intermediate in the synthesis process, refines the structures and compositions of the ammonia-poor intercalates using powder neutron diffraction, and studies the annealing of the phases, which causes them to lose ammonia and elemental iron to form $K_xFe_{2-y}Se_2$ phases.

The ammonia-rich phases of the potassium intercalates have been identified for the first time, by studying the reaction between potassium and FeSe in liquid ammonia with *in-situ* powder X-ray diffraction. The ammonia-rich potassium phases cannot be reformed from the ammonia-poor phases by exposure to ammonia vapour as the lithium and sodium phases can, and so analysing the products of the reaction as they form in liquid ammonia solution has been the only way study them. Further investigation is necessary to assess the kinetic barrier to reforming the ammonia-rich potassium phases once they have formed the ammonia-poor phases by loss of ammonia.

The chemistry of the potassium intercalates are governed by the necessity that potassium must share a site with NH_3/NH_2^- in the FeSe interlayer space as compared with the smaller alkali metals, lithium or sodium, which take different sites surrounding NH_3/NH_2^-. This is true in both the ammonia-rich phases and the ammonia-poor phases, leading to the counterintuitive observations that potassium-ammonia intercalates of FeSe are less expanded perpendicular to the FeSe layers than their lithium and sodium analogues, and that intercalating more potassium in the interlayer region yields a product with a shorter interlayer expansion, because less of the larger ammonia species accompanies it into the interlayer. Reaction with more potassium also causes more amide to be intercalated into the structure as opposed to ammonia, which will also add to the contraction due to ionic bonding contributions.

The *in-situ* study of these reactions has shown that a series of interconversions occur between the ammonia-rich phases, and has provided a preliminary investigation of their relative rates of formation. Two ammonia-rich products of these reactions have been identified, which are distinguished from each other by differing interlayer separations and differing ratios of the potassium and ammonia sharing a site between the FeSe interlayer, which are 9.89 Å with 30 % K : 70 % $NH_{3/2}$ and 10.19 Å with 15 % K : 85 % $NH_{3/2}$. A further metastable intermediate phase with an 11.55 Å separation between the FeSe layers was observed, in which potassium is able to take a different site to ammonia in the interlayer, and the structure of this phase is similar to that of the Li (10.59 Å)[135] and Na (11.00 Å) ammonia-rich intercalates. Further investigations could be performed into whether the intermediate phase can be stabilised as a function of K : FeSe ratio and temperatures. Further *in-situ* study of the synthesis of the ammonia-rich potassium intercalates could also reveal whether samples with $x > 0.3$ in the formula $K_x(NH_{3-y})_{1-x}FeSe$ be formed and clarify whether the unit cell expansion that was seen in the products is actually a compositional and structural change, or just thermal expansion.

The structures of the ammonia-poor intercalates, obtained after loss of ammonia from the products formed in solution, have been refined using powder neutron diffraction on samples synthesised with deuterated ammonia. When 0.3 equivalents of potassium were used, a product with the refined formula $K_{0.3}(ND_{2.6(4)})_{0.14(2)}FeSe$ was obtained, in which potassium and ammonia share a site. When 0.15 equivalents of potassium are used, a product with the refined formula $K_{0.15}(ND_{2.9(3)})_{0.35(3)}FeSe$ is obtained. The key differences between the two structures originate from a size mismatch between K^+ and NH_3/NH_2^-, and K^+ can either share the NH_3/NH_2^- site as it does in $K_{0.3}(ND_{2.6(4)})_{0.14(2)}FeSe$, or be displaced off it as it is in $K_{0.15}(ND_{2.9(3)})_{0.35(3)}FeSe$. This difference may be the origin of the phase gap that opens up between these two compositions. The refined compositions of these two intercalates carry fairly large intrinsic uncertainties, but suggest a slight reduction of the average iron oxidation state, with some amide formation also. The average iron oxidation state in $K_{0.3}(ND_{2.6(4)})_{0.14(2)}FeSe$ is $Fe^{1.76(6)+}$ and in $K_{0.15}(ND_{2.9(3)})_{0.35(3)}FeSe$ is $Fe^{1.89(11)+}$, not significantly different given the uncertainties.

In line with literature reports,[152] $K_{0.3}(ND_{2.6(4)})_{0.14(2)}FeSe$ is found to have a T_c of 30 K and $K_{0.15}(ND_{2.9(3)})_{0.35(3)}FeSe$ a T_c of 41 K, but both have relatively low superconducting volume fractions that are likely caused by inhomogeneity in the samples. Magnetic order is observed in the $K_{0.3}(ND_{2.6(4)})_{0.14(2)}FeSe$ intercalate, with an ordered moment of around

1.1 μ_B at room temperature. The coexistence of magnetism and superconductivity is well established in the iron arsenide superconductors, such as $NaFe_{1-x}Co_xAs$,[52] but the ordered moment in $K_{0.3}(ND_{2.6(4)})_{0.14(2)}FeSe$ appears to be higher than is typical. This is suggestive of an electronic phase separation into superconducting and magnetic phases, but the structures of the superconducting and magnetically ordered phases are too similar to distinguish by diffraction methods, given the low crystallinity of the samples. Further investigation could be performed to establish whether there is an inverse correlation between the magnitude of the magnetic scattering intensity and the superconducting volume fraction, as would be expected if these two effects arise from competing electronic phases. The $K_{0.15}(ND_{2.9(3)})_{0.35(3)}FeSe$ phase does not show magnetic ordering but also has a low superconducting volume fraction, which may also be a result of a inhomogeneity that is unresolvable.

Annealing of the ammonia-poor potassium intercalates of iron selenide up to 400 °C is found to eject ammonia/amide and elemental iron but retain the topology of the anti-PbO type FeSe layers. The product that is formed includes iron vacancies as iron is ejected from the system to form $K_xFe_{2-y}Se_2$ phases, akin to those in the literature formed at high temperatures.[75] The expulsion of iron from the FeSe layer appears to be coincident in temperature with the expulsion of ammonia from the interlayer space in $K_{0.3}(NH_{3-y})_{0.2-x}FeSe$, which shows that a $K_{0.6}Fe_2Se_2$ phase is not formed. In $K_{0.15}(NH_{3-y})_{0.35-x}FeSe$ the expulsion of iron appears to occur after the expulsion of ammonia and so it might be possible to stabilise a $K_{0.15}FeSe$ phase as claimed by Ying *et al.*,[152] but this phase is never single at the applied ramp rate of 6 °C min^{-1}, and the diffraction pattern is too complex to conclusively say that this ammonia-free phase is formed without any iron vacancies in the FeSe layer. Further investigation into the crossover region between $K_x(NH_{3-z})_{\sim 0.5-x}FeSe$ and $K_{x'}Fe_{2-y}Se_2$ where $K_{0.3}Fe_2Se_2$ might be formed, which occurs between 175 and 300 °C could be carried out. This region has a very complicated diffraction profile and requires further analysis.

The annealing of the ammonia-poor potassium intercalates of iron selenide provides a new route to the $K_xFe_{2-y}Se_2$ phases that may be able to expand on the range of values that x and y are known to be able to take. Further study of the annealing process may yield further insight into the parameters which control the rates product formation and expand this phase diagram. Kinetic information about rate of formation and rate at which elemental iron is lost in $K_xFe_{2-y}Se_2$ samples might be gained by rapidly exposing samples to a hot air stream above the structural transition temperature at 300, 340, 380, 420, and 460 °C, and measuring the conversion rate.

The K-NH_3-FeSe phase system has been shown to be vast and complicated, with three-ammonia-rich structures, two ammonia-poor structures, and several $K_xFe_{2-y}Se_2$ structures available. A similarly complicated picture has emerged in the Ba-NH_3-FeSe system that has been recently reported by Yusenko *et al.*[172], who performed the synthesis of the barium- ammonia- intercalate inside of a capillary and studied the process using *in-situ* X-ray diffraction at the ESRF. The method for performing this chemistry was significantly different from the method described here and by Sedlmaier *et al.*[135] They were able to identify six different phases, and isolate three of them. A schematic of the phase system from their paper is given below in Figure 7.1. These observations highlight that the surface may only have been scratched so far on the extensive number of phases that can be formed from β-FeSe as a starting material, and the importance of *in-situ* characterisation techniques in the analysis of these materials.

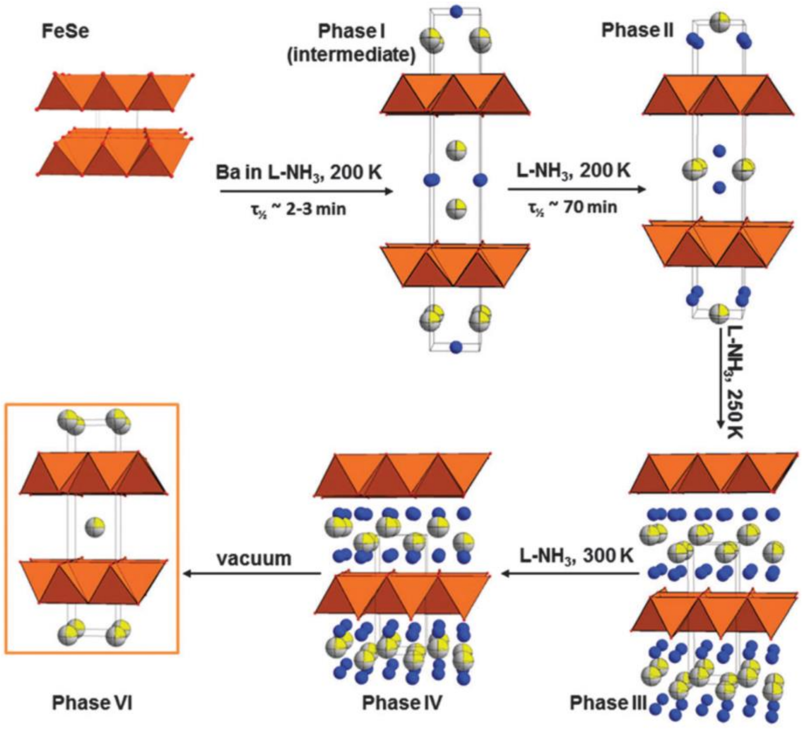

Figure 7.1 Schematic representation from reference 172 **of the reaction of Ba and β-FeSe in liquid ammonia medium at different temperature (Ba is shown as grey-yellow spheres, nitrogen in blue).**

The increase in T_c from 8 K in β-FeSe to 30-46 K in the various ammonia intercalates of iron selenide is remarkable, and what controls the extent of this increase is an intriguing question. The increase in T_c might be attributed to various factors, the two that are most likely to have a large influence are the increase in the FeSe interlayer separation and the electron doping of the Fermi surface. Guterding *et al.* performed *ab initio* density functional theory calculations of the band structure for the ammonia-poor and ammonia-rich lithium intercalates of iron selenide based on the structural models in the papers by Burrard-Lucas *et al.*[90] and Sedlmaier *et al.*[135] to elucidate the origin of the differing T_cs (43 and 39 K, respectively).[148] Their work concluded that increasing separation of the iron selenide layers should increase T_c by increasing the two-dimensionality of the Fermi surface, but electron doping should also increase the T_c.

The emerging picture for the correlation between T_c and the interlayer separation is that separating the FeSe layers will increase the T_c of the material up to a point, which is probably reached at a separation around 8.7 Å, but any further increase to the separation has minimal influence on optimising the Fermi surface and increasing T_c. Additional factors, primarily the degree to which the electrons provided by the intercalated electropositive metal changes the position of the Fermi level by electron doping, are responsible for further modifying the T_c. A plot of interlayer separation against T_c is given in Figure 7.2, which can be said to match the above description, but does not show a clear correlation between the two axes plotted.

For the time being, it must be concluded that this is a very complicated phase system and there may be many factors that contribute to the control of the superconducting properties. Further in-depth characterisation of many other ammonia and alkali / alkaline-earth intercalated iron selenide phases will be required in order to establish meaningful correlations between the structures and superconducting properties.

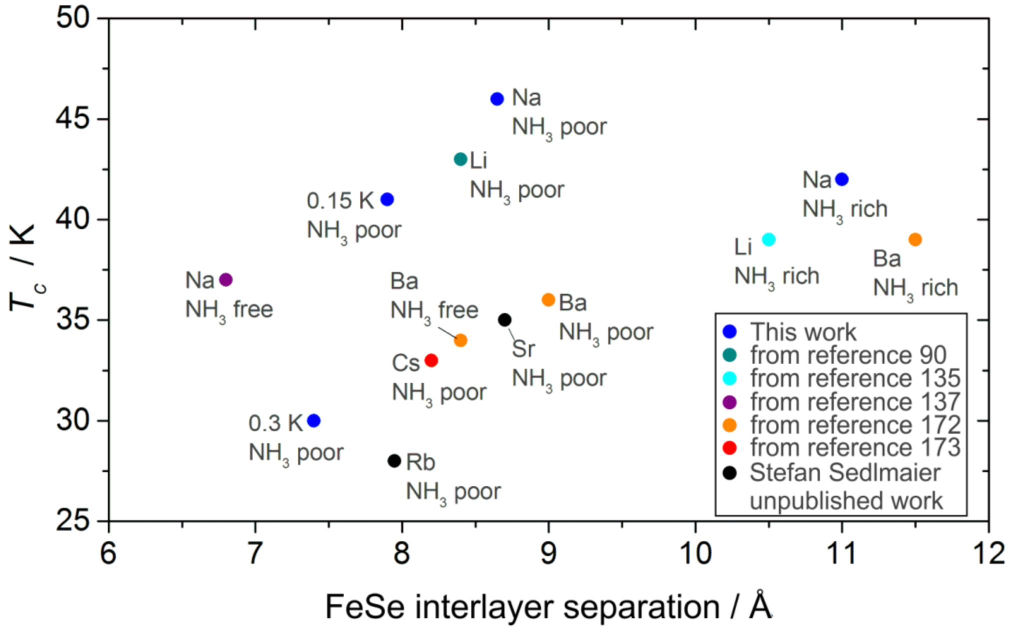

Figure 7.2 Plot of interlayer separation for the reported alkali and alkaline earth intercalates of iron selenide with reported T_cs that can be attributed to a specific phase[90,135,137,172,173] with the given interlayer separation.

Chapter 6 examined the synthesis, structure and properties of CaFeSeO, a newly discovered material. The material adopts a new crystal structure that can be thought of as a distorted form of the BaZnSO structure, with vertex linked 2D layers of [$FeSe_2O_2$] tetrahedra, bridged by calcium ions. The structure was solved from laboratory X-ray powder diffraction data by charge-flipping, and refined using the Rietveld method against neutron and synchrotron X-ray, powder diffraction data.

The key consequence of the distortion from the BaZnSO structure to the CaFeSeO structure is an increase in the multiplicity of the iron site in the unit cell, which leads to half of the positions that can possibly accommodate iron remaining vacant in CaFeSeO. The ordering of the vacancies is neither complete nor random, but approximately 90 % on one set of sites and 10 % on another. This ordering model provides a good fit to the data, and is a close description of the average structure, but there are indications from electron diffraction and unindexed weak reflections in the X-ray and neutron diffraction patterns that a complex modulation exists in the structure that has not been accounted for using the current model. There is more that can be learnt about the structure of CaFeSeO, and further work is required to extract this information. HAADF-STEM should be the next technique used in the attempt to determine the nature of the structural complexity.

The ordered magnetic structure of CaFeSeO has been determined by variable temperature neutron diffraction. Long-range magnetic order exists in the system below the magnetic transition temperature of 155 K, which is a canted antiferromagnet with a total iron moment of ~3.8 μ_B. The canting of the iron moments along the stacking direction in the structure, *b*, is consistent with the ferromagnetic signature in the magnetometry that saturates at a low magnetisation value. Strong magnetic hysteresis is observed below the 155 K transition temperature that is characteristic of spin glass type behaviour. This is likely to arise from the structural disorder of the iron positions in the material. AC SQUID magnetometry should be performed to characterise the spin glass behaviour and measure the dynamics of the spin glass freezing process. Further technique such as muon-spin spectroscopy might also provide insight into this complex magnetic material.

A magnetostriction effect is seen in the lattice parameters of the orthorhombic crystal structure around the magnetic ordering temperature, which causes a contraction of the unit cell along the direction of the ferromagnetic canting, *b*, and an expansion of the *a* and *c* unit cell parameters with a conservation of volume. The magnetostriction coefficients at 110 K in the absence of field for the three directions have been found to be +141(5), -100(5) and +119(4) ppm, for λ_a, λ_b, and λ_c, respectively. To study the effect of applied field on the magnetostriction and extract the true magnitudes of the magnetostriction coefficients at the saturation point, a second experiment should be performed to study the lattice parameters as a function of applied field and temperature. The WISH instrument at ISIS neutron source would be a good instrument for this, given that it has a dedicated 13.6 T magnet and cryostat available. The magnetic structure as a function of temperature could be studied simultaneously.

Bibliography

[1] K. Mizushima, P.C. Jones, P.J. Wiseman, and J.B. Goodenough, Mater. Res. Bull. **15**, 783 (1980).

[2] P.A. Madden and M. Wilson, Chem. Soc. Rev. **25**, 339 (1996).

[3] G. Just and P. Paufler, J. Alloys Compd. **232**, 1 (1996).

[4] W. Nieuwenkamp and J.M. Bijvoet, Zeitschrift Fuer Krist. Krist. Krist. Und Krist. **81**, 469 (1932).

[5] D.A. Winn, J.M. Shemilt, and B.C.H. Steele, Mater. Res. Bull. **11**, 559 (1976).

[6] F.R. Gamble, J.H. Osiecki, M. Cais, R. Pisharody, F.J. Disalvo, and T.H. Geballe, Science **174**, 493 (1971).

[7] G.V. Subba Rao and M.V. Shafer, *Intercalated Layered Materials Chapter 3* (Springer Science & Business Media, 1979).

[8] R. Schöllhorn and A. Weiss, Zeitschrift Für Naturforsch. B **27B**, 1277 (1972).

[9] M.S. Whittingham, J. Chem. Soc. Chem. Commun. 328 (1974).

[10] K. Takada, H. Sakurai, E. Takayama-Muromachi, F. Izumi, R.A. Dilanian, and T. Sasaki, Nature **422**, 53 (2003).

[11] J.D. Jorgensen, M. Avdeev, D.G. Hinks, J.C. Burley, and S. Short, Phys. Rev. B **68**, 214517 (2003).

[12] K. Takada, H. Sakurai, E. Takayama-Muromachi, F. Izumi, R.A. Dilanian, and T. Sasaki, J. Solid State Chem. **177**, 372 (2004).

[13] S. Yamanaka, H. Kawaji, K. Hotehama, and M. Ohashi, Adv. Mater. **8**, 771 (1996).

[14] X. Chen, L. Zou, X. Zhang, J. Qin, M. Inokuchi, and M. Kinoshita, J. Incl. Phenom. Macrocycl. Chem. **46**, 105 (2003).

[15] J. Zheng, H. Zhang, S. Dong, Y. Liu, C.T. Nai, H.S. Shin, H.Y. Jeong, B. Liu, and K.P. Loh, Nat. Commun. **5**, 2995 (2014).

[16] H. Kamerlingh Onnes, Commun. from Phys. Lab. Univ. Leiden **12**, 120 (1911).

[17] V.K. Steiner and P. Grassmann, Phys. Zeitschrift **36**, 527 (1935).

[18] H. Kamerlingh Onnes, Commun. from Phys. Lab. Univ. Leiden Suppl. Mater. **29**, (1911).

[19] W. Meissner and R. Ochsenfeld, Naturwissenschaften **21**, 787 (1933).

[20] F. London and H. London, Proc. R. Soc. A Math. Phys. Eng. Sci. **149**, 71 (1935).

[21] V.L. Ginzburg and L.D. Landau, Zhurnal Eksp. I Teor. Fiz. **20**, 1064 (1950).

[22] E. Maxwell, Phys. Rev. **78**, 477 (1950).

[23] C. Reynolds, B. Serin, W. Wright, and L. Nesbitt, Phys. Rev. **78**, 487 (1950).

[24] J. Bardeen, L.N. Cooper, and J.R. Schrieffer, Phys. Rev. **108**, 1175 (1957).

[25] Y. Wang and Y. Ma, J. Chem. Phys. **140**, 040901 (2014).

[26] D. Duan, Y. Liu, F. Tian, D. Li, X. Huang, Z. Zhao, H. Yu, B. Liu, W. Tian, and T. Cui, Sci. Rep. **4**, 6968 (2014).

[27] A.P. Drozdov, M.I. Eremets, and I.A. Troyan, arXiv.org 1412.0460 (2014).

[28] B. Matthias, T. Geballe, S. Geller, and E. Corenzwit, Phys. Rev. **95**, 1435 (1954).

[29] T. Berlincourt and R. Hake, Phys. Rev. Lett. **9**, 293 (1962).

[30] J. Nagamatsu, N. Nakagawa, T. Muranaka, Y. Zenitani, and J. Akimitsu, Nature **410**, 63 (2001).

[31] J.G. Bednorz and K.A. Müller, Zeitschrift Für Phys. B Condens. Matter **64**, 189 (1986).

[32] R. Cava, R. van Dover, B. Batlogg, and E. Rietman, Phys. Rev. Lett. **58**, 408 (1987).

[33] M. Wu, J. Ashburn, C. Torng, P. Hor, R. Meng, L. Gao, Z. Huang, Y. Wang, and C. Chu, Phys. Rev. Lett. **58**, 908 (1987).

[34] R. Hazen, C. Prewitt, R. Angel, N. Ross, L. Finger, C. Hadidiacos, D. Veblen, P. Heaney, P. Hor, R. Meng, Y. Sun, Y. Wang, Y. Xue, Z. Huang, L. Gao, J. Bechtold, and C. Chu, Phys. Rev. Lett. **60**, 1174 (1988).

[35] J.L. Tallon, R.G. Buckley, P.W. Gilberd, M.R. Presland, I.W.M. Brown, M.E. Bowden, L.A. Christian, and R. Goguel, Nature **333**, 153 (1988).

[36] R. Hazen, L. Finger, R. Angel, C. Prewitt, N. Ross, C. Hadidiacos, P. Heaney, D. Veblen, Z. Sheng, A. El Ali, and A. Hermann, Phys. Rev. Lett. **60**, 1657 (1988).

[37] A. Damascelli, Z. Hussain, and Z.-X. Shen, Rev. Mod. Phys. **75**, 473 (2003).

[38] P.A. Lee, N. Nagaosa, and X.-G. Wen, Rev. Mod. Phys. **78**, 17 (2006).

[39] Y. Kamihara, H. Hiramatsu, M. Hirano, R. Kawamura, H. Yanagi, T. Kamiya, and H. Hosono, J. Am. Chem. Soc. **128**, 10012 (2006).

[40] M. Tegel, I. Schellenberg, R. Pöttgen, and D. Johrendt, Zeitschrift Für Naturforsch. B **63**, 1057 (2008).

[41] Y. Kamihara, T. Watanabe, M. Hirano, and H. Hosono, J. Am. Chem. Soc. **130**, 3296 (2008).

[42] R. Zhi-An, L. Wei, Y. Jie, Y. Wei, S. Xiao-Li, C. Guang-Can, D. Xiao-Li, S. Li-Ling, Z. Fang, and Z. Zhong-Xian, Chinese Phys. Lett. **25**, 2215 (2008).

[43] Z.A. Ren, J. Yang, W. Lu, W. Yi, G.C. Che, X.L. Dong, L.L. Sun, and Z.X. Zhao, Mater. Res. Innov. **12**, 105 (2008).

[44] P. Cheng, L. Fang, H. Yang, X. Zhu, G. Mu, H. Luo, Z. Wang, and H. Wen, Sci. China Ser. G Physics, Mech. Astron. **51**, 719 (2008).

[45] T. McQueen, M. Regulacio, A. Williams, Q. Huang, J. Lynn, Y. Hor, D. West, M. Green, and R. Cava, Phys. Rev. B **78**, 024521 (2008).

[46] C. Wang, Y.K. Li, Z.W. Zhu, S. Jiang, X. Lin, Y.K. Luo, S. Chi, L.J. Li, Z. Ren, M. He, H. Chen, Y.T. Wang, Q. Tao, G.H. Cao, and Z.A. Xu, Phys. Rev. B **79**, 054521 (2009).

[47] M. Xu, F. Chen, C. He, H.-W. Ou, J.-F. Zhao, and D.-L. Feng, Chem. Mater. **20**, 7201 (2008).

[48] H. Takahashi, H. Soeda, M. Nukii, C. Kawashima, T. Nakanishi, S. Iimura, Y. Muraba, S. Matsuishi, and H. Hosono, Sci. Rep. **5**, 7829 (2015).

[49] M. Rotter, M. Tegel, and D. Johrendt, Phys. Rev. Lett. **101**, (2008).

[50] M.J. Pitcher, D.R. Parker, P. Adamson, S.J.C. Herkelrath, A.T. Boothroyd, R.M. Ibberson, M. Brunelli, and S.J. Clarke, Chem. Commun. 5918 (2008).

[51] J.H. Tapp, Z. Tang, B. Lv, K. Sasmal, B. Lorenz, P.C.W. Chu, and A.M. Guloy, Phys. Rev. B **78**, 060505 (2008).

[52] D.R. Parker, M.J. Pitcher, P.J. Baker, I. Franke, T. Lancaster, S.J. Blundell, and S.J. Clarke, Chem. Commun. (Camb). 2189 (2009).

[53] D.R. Parker, M.J.P. Smith, T. Lancaster, A.J. Steele, I. Franke, P.J. Baker, F.L. Pratt, M.J. Pitcher, S.J. Blundell, and S.J. Clarke, Phys. Rev. Lett. **104**, 057007 (2010).

[54] N. Ni, J.M. Allred, B.C. Chan, and R.J. Cava, Proc. Natl. Acad. Sci. U. S. A. **108**, E1019 (2011).

[55] X. Zhu, F. Han, G. Mu, P. Cheng, B. Shen, B. Zeng, and H.-H. Wen, Phys. Rev. B **79**, 220512 (2009).

[56] J.W. Lynn and P. Dai, Phys. C Supercond. **469**, 469 (2009).

[57] Q. Huang, J. Zhao, J.W. Lynn, G.F. Chen, J.L. Luo, N.L. Wang, and P. Dai, Phys. Rev. B **78**, 54529 (2008).

[58] M.J. Pitcher, T. Lancaster, J.D. Wright, I. Franke, A.J. Steele, P.J. Baker, F.L. Pratt, W.T. Thomas, D.R. Parker, S.J. Blundell, and S.J. Clarke, J. Am. Chem. Soc. **132**, 10467 (2010).

[59] D. Johrendt, H. Hosono, R.-D. Hoffmann, and R. Pöttgen, Zeitschrift Für Krist. **226**, 435 (2011).

[60] J.-H. Chu, J. Analytis, C. Kucharczyk, and I. Fisher, Phys. Rev. B **79**, 014506 (2009).

[61] A.J. Drew, C. Niedermayer, P.J. Baker, F.L. Pratt, S.J. Blundell, T. Lancaster, R.H. Liu, G. Wu, X.H. Chen, I. Watanabe, V.K. Malik, A. Dubroka, M. Rössle, K.W. Kim, C. Baines, and C. Bernhard, Nat. Mater. **8**, 310 (2009).

[62] J.D. Wright, T. Lancaster, I. Franke, A.J. Steele, J.S. Möller, M.J. Pitcher, A.J. Corkett, D.R. Parker, D.G. Free, F.L. Pratt, P.J. Baker, S.J. Clarke, and S.J. Blundell, Phys. Rev. B **85**, 054503 (2012).

[63] S. Jiang, H. Xing, G. Xuan, C. Wang, Z. Ren, C. Feng, J. Dai, Z. Xu, and G. Cao, J. Phys. Condens. Matter **21**, 382203 (2009).

[64] L. E. Klintberg, S. K. Goh, S. Kasahara, Y. Nakai, K. Ishida, M. Sutherland, T. Shibauchi, Y. Matsuda, and T. Terashima, J. Phys. Soc. Japan **79**, 123706 (2010).

[65] Z.R. Ye, Y. Zhang, F. Chen, M. Xu, Q.Q. Ge, J. Jiang, B.P. Xie, and D.L. Feng, Phys. Rev. B **86**, 035136 (2012).

[66] C.-H. Lee, A. Iyo, H. Eisaki, H. Kito, M. Teresa Fernandez-Diaz, T. Ito, K. Kihou, H. Matsuhata, M. Braden, and K. Yamada, J. Phys. Soc. Japan **77**, 083704 (2008).

[67] F.-C. Hsu, J.-Y. Luo, K.-W. Yeh, T.-K. Chen, T.-W. Huang, P.M. Wu, Y.-C. Lee, Y.-L. Huang, Y.-Y. Chu, D.-C. Yan, and M.-K. Wu, Proc. Natl. Acad. Sci. U. S. A. **105**, 14262 (2008).

[68] Y. Mizuguchi, F. Tomioka, S. Tsuda, T. Yamaguchi, and Y. Takano, Appl. Phys. Lett. **93**, 152505 (2008).

[69] S. Medvedev, T.M. McQueen, I.A. Troyan, T. Palasyuk, M.I. Eremets, R.J. Cava, S. Naghavi, F. Casper, V. Ksenofontov, G. Wortmann, and C. Felser, Nat. Mater. **8**, 630 (2009).

[70] K.-W. Yeh, T.-W. Huang, Y. Huang, T.-K. Chen, F.-C. Hsu, P. M. Wu, Y.-C. Lee, Y.-Y. Chu, C.-L. Chen, J.-Y. Luo, D.-C. Yan, and M.-K. Wu, EPL (Europhysics Lett. **84**, 37002 (2008).

[71] Y. Mizuguchi, F. Tomioka, S. Tsuda, T. Yamaguchi, and Y. Takano, J. Phys. Soc. Japan **78**, 074712 (2009).

[72] E.L. Thomas, W. Wong-Ng, D. Phelan, and J.N. Millican, J. Appl. Phys. **105**, 073906 (2009).

[73] A. Kumar, R.P. Tandon, and V.P.S. Awana, IEEE Trans. Magn. **48**, 4239 (2012).

[74] T.M. McQueen, Q. Huang, V. Ksenofontov, C. Felser, Q. Xu, H. Zandbergen, Y.S. Hor, J. Allred, A.J. Williams, D. Qu, J. Checkelsky, N.P. Ong, and R.J. Cava, Phys. Rev. B **79**, 014522 (2009).

[75] J. Guo, S. Jin, G. Wang, S. Wang, K. Zhu, T. Zhou, M. He, and X. Chen, Phys. Rev. B **82**, 180520 (2010).

[76] A.F. Wang, J.J. Ying, Y.J. Yan, R.H. Liu, X.G. Luo, Z.Y. Li, X.F. Wang, M. Zhang, G.J. Ye, P. Cheng, Z.J. Xiang, and X.H. Chen, Phys. Rev. B **83**, 060512 (2011).

[77] P. Zavalij, W. Bao, X.Q.F. Wang, J.J. Ying, X.H. Chen, D.M. Wang, J.B. He, X.Q.F. Wang, G.F. Chen, P.-Y.Y. Hsieh, Q. Huang, and M.A. Green, Phys. Rev. B **83**, 132509 (2011).

[78] W. Bao, Q.-Z. Huang, G.-F. Chen, D.-M. Wang, J.-B. He, and Y.-M. Qiu, Chinese Phys. Lett. **28**, 086104 (2011).

[79] J. Bacsa, A.Y. Ganin, Y. Takabayashi, K.E. Christensen, K. Prassides, M.J. Rosseinsky, and J.B. Claridge, Chem. Sci. **2**, 1054 (2011).

[80] Y. Texier, J. Deisenhofer, V. Tsurkan, A. Loidl, D.S. Inosov, G. Friemel, and J. Bobroff, Phys. Rev. Lett. **108**, 237002 (2012).

[81] V. Ksenofontov, G. Wortmann, S.A. Medvedev, V. Tsurkan, J. Deisenhofer, A. Loidl, and C. Felser, Phys. Rev. B **84**, 180508 (2011).

[82] A. Charnukha, A. Cvitkovic, T. Prokscha, D. Pröpper, N. Ocelic, A. Suter, Z. Salman, E. Morenzoni, J. Deisenhofer, V. Tsurkan, A. Loidl, B. Keimer, and A. V. Boris, Phys. Rev. Lett. **109**, 017003 (2012).

[83] F. Chen, M. Xu, Q.Q. Ge, Y. Zhang, Z.R. Ye, L.X. Yang, J. Jiang, B.P. Xie, R.C. Che, M. Zhang, A.F. Wang, X.H. Chen, D.W. Shen, J.P. Hu, and D.L. Feng, Phys. Rev. X **1**, 021020 (2011).

[84] D.P. Shoemaker, D.Y. Chung, H. Claus, M.C. Francisco, S. Avci, A. Llobet, and M.G. Kanatzidis, Phys. Rev. B **86**, 184511 (2012).

[85] Z. Wang, Y. Cai, Z.W. Wang, C. Ma, Z. Chen, H.X. Yang, H.F. Tian, and J.Q. Li, Phys. Rev. B **91**, 064513 (2015).

[86] Y. Liu, Q. Xing, W.E. Straszheim, J. Marshman, P. Pedersen, and T.A. Lograsso, (2015).

[87] M. Tanaka, Y. Yanagisawa, M. Fujioka, S.J. Denholme, S. Funahashi, Y. Matsushita, N. Ishizawa, T. Yamaguchi, H. Takeya, and Y. Takano, 14 (2015).

[88] Z. Shermadini, H. Luetkens, R. Khasanov, A. Krzton-Maziopa, K. Conder, E. Pomjakushina, H.-H. Klauss, and A. Amato, Phys. Rev. B **85**, 100501 (2012).

[89] T.P. Ying, X.L. Chen, G. Wang, S.F. Jin, T.T. Zhou, X.F. Lai, H. Zhang, and W.Y. Wang, Sci. Rep. **2**, 426 (2012).

[90] M. Burrard-Lucas, D.G. Free, S.J. Sedlmaier, J.D. Wright, S.J. Cassidy, Y. Hara, A.J. Corkett, T. Lancaster, P.J. Baker, S.J. Blundell, and S.J. Clarke, Nat. Mater. **12**, 15 (2013).

[91] E.-W. Scheidt, V.R. Hathwar, D. Schmitz, A. Dunbar, W. Scherer, F. Mayr, V. Tsurkan, J. Deisenhofer, and A. Loidl, Eur. Phys. J. B **85**, 279 (2012).

[92] M. Gooch, B. Lv, K. Sasmal, J.H. Tapp, Z.J. Tang, A.M. Guloy, B. Lorenz, and C.W. Chu, Phys. C Supercond. **470**, S276 (2010).

[93] I. Todorov, D.Y. Chung, H. Claus, C.D. Malliakas, A.P. Douvalis, T. Bakas, J. He, V.P. Dravid, and M.G. Kanatzidis, Chem. Mater. **22**, 3916 (2010).

[94] G.M. Friederichs, I. Schellenberg, R. Pottgen, V. Duppel, L. Kienle, J.S.A. der Gueinne, and D. Johrendt, Inorg. Chem. **51**, 8161 (2012).

[95] W. Schuster, H. Mikler, and K.L. Komarek, Monatshefte Fur Chemie **110**, 1153 (1979).

[96] A. Patterson, Phys. Rev. **46**, 372 (1934).

[97] A. Altomare, G. Cascarano, C. Giacovazzo, A. Guagliardi, M.C. Burla, G. Polidori, and M. Camalli, J. Appl. Crystallogr. **27**, 435 (1994).

[98] G. Oszlányi and A. Süto, Acta Crystallogr. A. **60**, 134 (2004).

[99] B. Ravel and M. Newville, J. Synchrotron Radiat. **12**, 537 (2005).

[100] M. Newville, J. Synchrotron Radiat. **8**, 322 (2001).

[101] E. Stern, Phys. Rev. B **48**, 9825 (1993).

[102] S.P. Thompson, J.E. Parker, J. Potter, T.P. Hill, A. Birt, T.M. Cobb, F. Yuan, and C.C. Tang, Rev. Sci. Instrum. **80**, 075107 (2009).

[103] N. Tartoni, S.P. Thompson, C.C. Tang, B.L. Willis, G.E. Derbyshire, A.G. Wright, S.C. Jaye, J.M. Homer, J.D. Pizzey, and A.M.T. Bell, J. Synchrotron Radiat. **15**, 43 (2008).

[104] A.J. Dent, G. Cibin, S. Ramos, A.D. Smith, S.M. Scott, L. Varandas, M.R. Pearson, N.A. Krumpa, C.P. Jones, and P.E. Robbins, J. Phys. Conf. Ser. **190**, 012039 (2009).

[105] E. Prince, editor , *International Tables for Crystallorgraphy Volume C*, 3rd ed. (Kluwer Academic Publishers, 2004).

[106] G. Caglioti, A. Paoletti, and F.P. Ricci, Nucl. Instruments **3**, 223 (1958).

[107] R.A. Young, *The Rietveld Method* (Oxford University Press, 1993).

[108] S. Hull, R.I. Smith, W.I.F. David, A.C. Hannon, J. Mayers, and R. Cywinski, Phys. B Condens. Matter **180-181**, 1000 (1992).

[109] P. Day, J. Enderby, W. Williams, L. Chapon, A. Hannon, P. Radaelli, and A. Soper, Neutron News **15**, 19 (2004).

[110] W. Williams, R. Ibberson, P. Day, and J. Enderby, Phys. B Condens. Matter **241-243**, 234 (1997).

[111] H.M. Rietveld, Acta Crystallogtaphica **22**, 151 (1967).

[112] H.M. Rietveld, J. Appl. Crystallogr. **2**, 65 (1969).

[113] A.A. Coelho, *TOPAS Academic: General Profile and Structure Analysis Software For Powder Diffraction Data* (Bruker AXS; Karlsurhe, Germany, 2012).

[114] G.S. Pawley, J. Appl. Crystallogr. **14**, 357 (1981).

[115] W.E. Garner, *Chemistry of the Solid State* (1955).

[116] D.A. Young, *Decomposition of Solids* (Pergamon Press, 1966).

[117] M.E. Brown, D. Dollimore, and A.K. Galwey, *Reactions in the Solid State. Chapter 3 in Comprehensive Chemical Kinteics* (1980).

[118] A. Khawam and D.R. Flanagan, J. Phys. Chem. B **110**, 17315 (2006).

[119] S.L. Johnson, R.A. de Souza, U. Staub, P. Beaud, E. Möhr-Vorobeva, G. Ingold, A. Caviezel, V. Scagnoli, W.F. Schlotter, J.J. Turner, O. Krupin, W.-S. Lee, Y.-D. Chuang, L. Patthey, R.G. Moore, D. Lu, M. Yi, P.S. Kirchmann, M. Trigo, P. Denes, D. Doering, Z. Hussain, Z.-X. Shen, D. Prabhakaran, and A.T. Boothroyd, Phys. Rev. Lett. **108**, 037203 (2012).

[120] T. Kubacka, J.A. Johnson, M.C. Hoffmann, C. Vicario, S. de Jong, P. Beaud, S. Grübel, S.-W. Huang, L. Huber, L. Patthey, Y.-D. Chuang, J.J. Turner, G.L. Dakovski, W.-S. Lee, M.P. Minitti, W. Schlotter, R.G. Moore, C.P. Hauri, S.M. Koohpayeh, V. Scagnoli, G. Ingold, S.L. Johnson, and U. Staub, Science **343**, 1333 (2014).

[121] R. Cortes-Gil, D.R. Parker, M.J. Pitcher, J. Hadermann, and S.J. Clarke, Chem. Mater. **22**, 4304 (2010).

[122] S. Avci, J.M. Allred, O. Chmaissem, D.Y. Chung, S. Rosenkranz, J.A. Schlueter, H. Claus, A. Daoud-Aladine, D.D. Khalyavin, P. Manuel, A. Llobet, M.R. Suchomel, M.G. Kanatzidis, and R. Osborn, Phys. Rev. B **88**, 094510 (2013).

[123] C.W. Chu, F. Chen, M. Gooch, A.M. Guloy, B. Lorenz, B. Lv, K. Sasmal, Z.J. Tang, J.H. Tapp, and Y.Y. Xue, Phys. C Supercond. **469**, 326 (2009).

[124] A.F. Wang, X.G. Luo, Y.J. Yan, J.J. Ying, Z.J. Xiang, G.J. Ye, P. Cheng, Z.Y. Li, W.J. Hu, and X.H. Chen, Phys. Rev. B **85**, 224521 (2012).

[125] S. Li, C. de la Cruz, Q. Huang, G. Chen, T.-L. Xia, J. Luo, N. Wang, and P. Dai, Phys. Rev. B **80**, 020504 (2009).

[126] R.A. Jishi and H.M. Alyahyaei, Adv. Condens. Matter Phys. **2010**, 1 (2010).

[127] D. Evtushinsky, V. Zabolotnyy, L. Harnagea, A. Yaresko, S. Thirupathaiah, A. Kordyuk, J. Maletz, S. Aswartham, S. Wurmehl, E. Rienks, R. Follath, B. Büchner, and S. Borisenko, Phys. Rev. B **87**, 094501 (2013).

[128] A. Iadecola, B. Joseph, L. Simonelli, A. Puri, Y. Mizuguchi, H. Takeya, Y. Takano, and N.L. Saini, J. Phys. Condens. Matter **24**, 115701 (2012).

[129] T.A. Tyson, T. Yu, S.J. Han, M. Croft, G.D. Gu, I.K. Dimitrov, and Q. Li, Phys. Rev. B **85**, 024504 (2012).

[130] H. Sun, D.N. Woodruff, S.J. Cassidy, G.M. Allcroft, S.J. Sedlmaier, A.L. Thompson, P.A. Bingham, S.D. Forder, S. Cartenet, N. Mary, S. Ramos, F.R. Foronda, B.H. Williams, X. Li, S.J. Blundell, and S.J. Clarke, Inorg. Chem. **54**, 1958 (2015).

[131] S. V. Carr, D. Louca, J. Siewenie, Q. Huang, A. Wang, X. Chen, and P. Dai, Phys. Rev. B **89**, 134509 (2014).

[132] S.C. Speller, T.B. Britton, G.M. Hughes, A. Krzton-Maziopa, E. Pomjakushina, K. Conder, A.T. Boothroyd, and C.R.M. Grovenor, Supercond. Sci. Technol. **25**, 084023 (2012).

[133] V. Yu Pomjakushin, A. Krzton-Maziopa, E. V Pomjakushina, K. Conder, D. Chernyshov, V. Svitlyk, and A. Bosak, J. Phys. Condens. Matter **24**, 435701 (2012).

[134] S.C. Speller, P. Dudin, S. Fitzgerald, G.M. Hughes, K. Kruska, T.B. Britton, A. Krzton-Maziopa, E. Pomjakushina, K. Conder, A. Barinov, and C.R.M. Grovenor, Phys. Rev. B **90**, 024520 (2014).

[135] S.J. Sedlmaier, S.J. Cassidy, R.G. Morris, M. Drakopoulos, C. Reinhard, S.J. Moorhouse, D. O’Hare, P. Manuel, D. Khalyavin, and S.J. Clarke, J. Am. Chem. Soc. **136**, 630 (2014).

[136] G.R. Williams and D. O’Hare, Chem. Mater. **17**, 2632 (2005).

[137] J. Guo, H. Lei, F. Hayashi, and H. Hosono, Nat. Commun. **5**, 4756 (2014).

[138] J.D. Hancock and J.H. Sharp, J. Am. Ceram. Soc. **55**, 74 (1972).

[139] J. Graetz and J.J. Reilly, J. Phys. Chem. B **109**, 22181 (2005).

[140] A.K. Sheridan and J. Anwar, Chem. Mater. **8**, 1042 (1996).

[141] J.R. Houston, R.S. Maxwell, and S.A. Carroll, Geochem. Trans. **10**, 1 (2009).

[142] A.P. Wilkinson, J.S. Speck, A.K. Cheetham, S. Natarajan, and J.M. Thomas, Chem. Mater. **6**, 750 (1994).

[143] S.J. Price, J.S.O. Evans, R.J. Francis, and D. O’Hare, Adv. Mater. **8**, 582 (1996).

[144] S.F. Hulbert, J. Br. Ceram. Soc. **6**, 11 (1969).

[145] A.P. Hammersley, *FIT2D: An Introduction and Overview* (ESRF internal report, 1997).

[146] S. Brückner, J. Appl. Crystallogr. **33**, 977 (2000).

[147] DuPont, *http://usa.dupontteijinfilms.com/informationcenter/downloads/Chemical_Properties.pdf* (2003).

[148] D. Guterding, H.O. Jeschke, P.J. Hirschfeld, and R. Valenti’, Phys. Rev. B **91**, 41112 (2015).

[149] P.K. Biswas, A. Krzton-Maziopa, R. Khasanov, H. Luetkens, E. Pomjakushina, K. Conder, and A. Amato, Phys. Rev. Lett. **110**, 137003 (2013).

[150] HatakedaTakehiro, NojiTakashi, KawamataTakayuki, KatoMasatsune, and KoikeYoji, J. Phys. Soc. Japan **82**, 3 (2013).

[151] A. Krzton-Maziopa, E. V Pomjakushina, V.Y. Pomjakushin, F. von Rohr, A. Schilling, and K. Conder, J. Phys. Condens. Matter **24**, 382202 (2012).

[152] T. Ying, X. Chen, G. Wang, S. Jin, X. Lai, T. Zhou, H. Zhang, S. Shen, and W. Wang, J. Am. Chem. Soc. **135**, 2951 (2013).

[153] P.W. Stephens, J. Appl. Crystallogr. **32**, 281 (1999).

[154] E. Zintl, A. Harder, and B. Dauth, Zeitschrift Fuer Elektrochemie **40**, 588 (1934).

[155] B.J. Campbell, H.T. Stokes, D.E. Tanner, and D.M. Hatch, J. Appl. Crystallogr. **39**, 607 (2006).

[156] H. Grimmer, Acta Crystallogr. Sect. A **65**, 145 (2009).

[157] W.A. Dollase, J. Appl. Crystallogr. **19**, 267 (1986).

[158] Y. Mizuguchi, H. Takeya, Y. Kawasaki, T. Ozaki, S. Tsuda, T. Yamaguchi, and Y. Takano, Appl. Phys. Lett. **98**, 042511 (2011).

[159] S.A. Petrova, V.P. Mar’evich, R.G. Zakharov, E.N. Selivanov, V.M. Chumarev, and L.Y. Udoeva, Dokl. Chem. **393**, 255 (2003).

[160] T. Sambrook, C.F. Smura, S.J. Clarke, K.M. Ok, and P.S. Halasyamani, Inorg. Chem. **46**, 2571 (2007).

[161] S. Broadley, Z.A. Gál, F. Corà, C.F. Smura, and S.J. Clarke, Inorg. Chem. **44**, 9092 (2005).

[162] J.B. He, D.M. Wang, H.L. Shi, H.X. Yang, J.Q. Li, and G.F. Chen, Phys. Rev. B **84**, 205212 (2011).

[163] I. Ijjaali, K. Mitchell, C.L. Haynes, A.D. McFarland, R.P. Van Duyne, and J.A. Ibers, J. Solid State Chem. **176**, 170 (2003).

[164] D.G. Free, N.D. Withers, P.J. Hickey, and J.S.O. Evans, Chem. Mater. **23**, 1625 (2011).

[165] E.E. McCabe, D.G. Free, B.G. Mendis, J.S. Higgins, and J.S.O. Evans, Chem. Mater. **22**, 6171 (2010).

[166] E. Mugnaioli, T. Gorelik, and U. Kolb, Ultramicroscopy **109**, 758 (2009).

[167] T. Hahn, U. Shmueli, A.J.C. Wilson, and E. Prince, editors , *International Tables for Crystallography* (D. Reidel Publishing Company, 2005).

[168] S. Blundell, *Magnetism in Condensed Matter (Oxford Master Series in Physics)* (Oxford University Press, 2001).

[169] J.N. Blandy, A.M. Abakumov, K.E. Christensen, J. Hadermann, P. Adamson, S.J. Cassidy, S. Ramos, D.G. Free, H. Cohen, D.N. Woodruff, A.L. Thompson, and S.J. Clarke, APL Mater. **3**, 041520 (2015).

[170] J.S. Kim, E.G. Kim, G.R. Stewart, X.H. Chen, and X.F. Wang, Phys. Rev. B **83**, 172502 (2011).

[171] F. Hayashi, H. Lei, J. Guo, and H. Hosono, Inorg. Chem. **54**, 3346 (2015).

[172] K. V Yusenko, J. Sottmann, H. Emerich, W.A. Crichton, L. Malavasi, and S. Margadonna, Chem. Commun. (Camb). **51**, 7112 (2015).

[173] L. Zheng, M. Izumi, Y. Sakai, R. Eguchi, H. Goto, Y. Takabayashi, T. Kambe, T. Onji, S. Araki, T.C. Kobayashi, J. Kim, A. Fujiwara, and Y. Kubozono, Phys. Rev. B **88**, 094521 (2013).

[174]*The ILL Yellow Book* (2008).

Appendices

I. Details of additional diffractometers used

Laboratory diffractometer - Philips PW1710

This low-resolution, somewhat aged instrument is used primarily to assess the purity of starting materials. It utilises a Bragg-Brentano geometry (reflection) with a fixed Cu X-ray source and a detector on the 2θ axis.

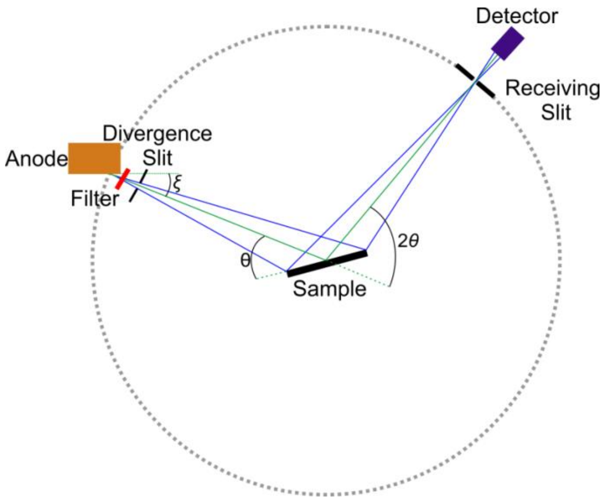

Figure I.i Bragg-Brentano diffraction geometry: X-rays are reflected from the sample.

The sample is mounted on a flat plate, which rotates at half the angular velocity of the detector so as to remain at a tangent to the focusing circle with the detector-sample distance remaining constant ("butterfly" mode). The instrument is equipped with a secondary monochromator, and as such has both $K_{\alpha1}$ and $K_{\alpha2}$ radiation with a low fluorescence background.

Laboratory diffractometer - PANalytical X'pert

Two PANalytical X'pert diffractometers have been used in this work, which will be referred to as ICL and CRL. The ICL X'pert is a high resolution instrument operating in the Bragg-Brentano geometry, used to collect high quality data suitable for Rietveld refinement. A Ge (111) monochromator on the incident beam selects $K_{\alpha1}$ radiation exclusively, 0.04 mm soller slits are used to collimate the beam with the option of using 0.02 mm slits (at the cost of intensity). The CRL X'pert is similar but does not feature a primary monochromator, making it a higher intensity, lower resolution instrument. A secondary monochromator was installed in 2012, which gives the instrument a lower intensity, (but still higher than the ICL machine) with a reduced background. Air-stable samples may be mounted on a rotation stage that spins the sample in the beam allowing for greater exposure of the crystallite surfaces, giving better powder averaging.

Laboratory diffractometer - PANalytical Empyrean

The PANalytical Empyrean was installed in 2014 as a high resolution instrument, with higher intensity than the X'pert machines. Similar to the ICL X'pert, the empyrean is equipped with A Ge (111) monochromator on the incident beam path and soller slits. The Machine is designed such that it can be operated in Bragg-Brentano or Debye-Scherrer geometry interchangeably; a stage which can spin a capillary mounted on a goniometer in the beam is available such that samples in sealed borosilicate or glass capillaries can be measured on this diffractometer. Cu radiation is of quite a long wavelength for transmission experiments, typical transition metal compounds require high levels of dilution and narrow diameter capillaries if high levels of absorption are to be avoided. Reflection from the surface of the capillary may be present in the diffraction pattern if this is not sufficiently done.

Synchrotron diffractometer - ID31 - high resolution powder diffraction at the ESRF

In 2014 the ID31 diffractometer was transferred to ID22, and ID31 is now a micro-focus beamline. This section refers to ID31 in its previous set-up. ID31 was an undulator sourced beamline at the ESRF in Grenoble, optimised for high resolution powder diffraction. The beamline operates in the 5-60 keV energy range and diffraction patterns are typically measured using X-ray radiation in the range 0.3 - 0.9 Å, with 0.4 Å being the standard choice. Monochromation of the beam is performed by a cryogenically cooled Si (111) double-crystal. The instrument operates in a Debye-Scherrer geometry and the detector bank is comprised of nine scintillation detectors which are preceded by Si (111) analyser crystals, they are arranged 2 ° apart and measure diffracted intensity as function of 2θ. The principal difference between ID31 and I11 is that the incident beam on ID31 contains a high flux of shorter wavelength X-rays, which has the advantage of enabling more accurate determination of atomic coordinates *i.e.* measurements out to high values of $\sin\theta/\lambda$. The higher flux of shorter wavelength photons on ID31 also allows sample absorption to be reduced in most cases compared with I11.

Similar specification sample environments to all those available on I11 at Diamond Light Source are also available on ID31 at the ESRF.

Neutron diffractometer - D2B - high resolution powder diffraction at the ILL

D2B is a high resolution constant wavelength diffractometer at the Institut Laue-Langevin (ILL) reactor neutron source in Grenoble, France. D2B was built for high resolution studies, but also has the option of sacrificing resolution for intensity. A schematic of the instrument is given in Figure I.ii. The white beam from the H11 moderator is first collimated before monochromation. The monochromator is made up of 28 germanium (115) crystals with a large mosaic spread to compensate for intensity loss from the very high take-off angle (135 °) which optimises resolution. Rotation of the monochromator can be performed to illuminate different $h\ k\ l$ planes to provide several discrete wavelength options for the neutrons. The optimum available wavelength is 1.594 Å, which maximises intensity since the wavelength is close to the peak in the thermal beam. A wavelength of 2.398 Å is also commonly used for structures with high *d*-spacing reflections, particularly those with large, antiferromagnetically ordered magnetic unit cells.

The detector is composed of by 128 ^{3}He counting tubes, set at 1.25 º intervals that are able to measure an angular range of $5\ º \leq 2\theta \leq 165\ º$ and cover a *d*-range of 0.8 – 18 Å, using 1.59 Å neutrons. The intervals between detectors are filled by moving the detector, typically by 25 steps of 0.05 °. The height of the detector is 200 mm, however the curvature of the Debye Scherrer cones leads to peak broadening and asymmetry at the edges of the detector, so typically only the middle third of the collected data is used. The maximum dimensions of the beam at the sample position measure 2 × 5 cm, which allows large volume samples to be measured.

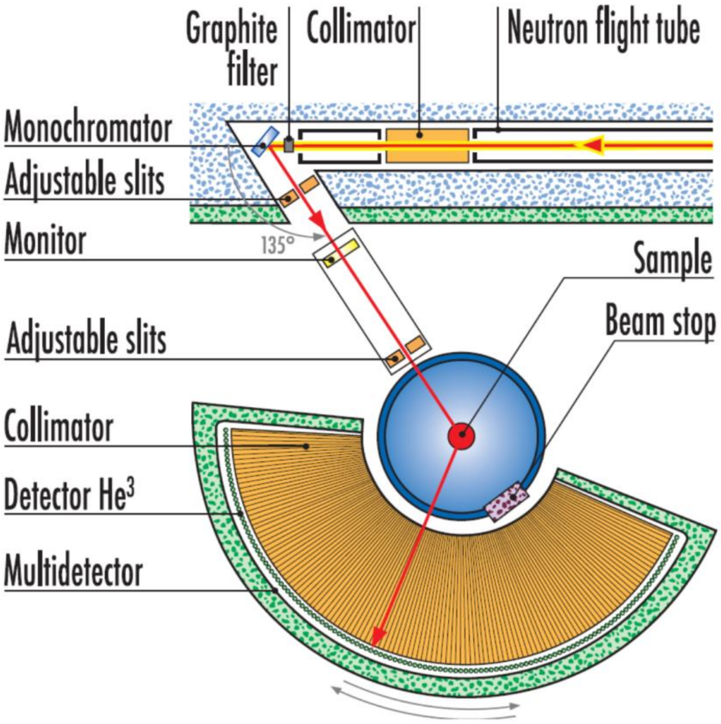

Figure I.ii D2B instrument setup (taken from the ILL yellow book).[174]

II. Supporting measurement for NaFe$_{2-y}$As$_2$

Two data sets were obtained for Na$_{1-x}$Fe$_{2-y}$As$_2$. For one measurement the sample was treated as air-stable and was supported in a cellulose pellet. In a second measurement on the Fe edge the sample was supported in a BN pellet and handled as if air-sensitive. To avoid exposure to air the sample was prepared in an argon filled dry-box. The pellet was sealed between two pieces of Kapton® tape, and transported to the beamline in heat-sealed aluminised polythene bags.

Data were processed and analysed using Athena and Artemis, part of the Demeter software package.[99] The XANES plot below shows the edge position of Na$_{1-x}$Fe$_{2-y}$As$_2$ to be identical when handled with and without exposure to air, this confirms that the oxidation process to produce a compound with Fe in the +3 oxidation state proceeds in the reaction with iodine and not an any subsequent aerial oxidation step.

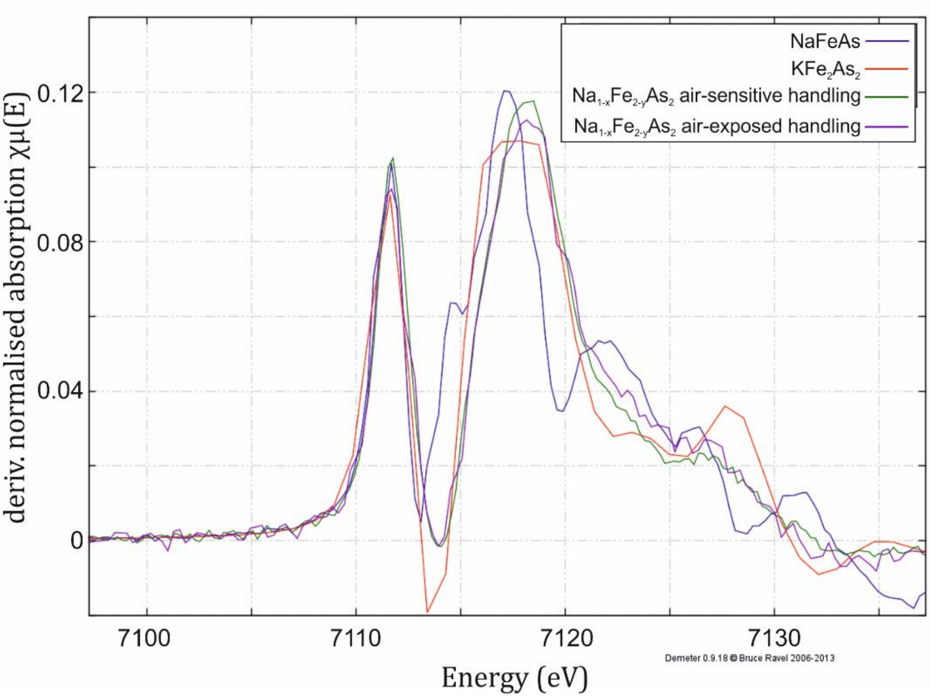

Figure II.i First derivative of the normalised Fe *K*-edge XANES for iron arsenide samples.

EXAFS fits to a model with and without vacancies are shown below. Inclusion of a second Fe-As scattering path to model the vacancy influenced environment is still necessary to describe the $Na_{1-x}Fe_{2-y}As_2$ system. A comparison of the refined parameters for the air exposed sample in a cellulose pellet and the non-air-exposed sample in a BN pellet is given in the following table. The two refinements do not exhibit significant differences confirming that there is no significant change to the local structure of $Na_{1-x}Fe_{2-y}As_2$ on the length scale the can be probed by EXAFS.

Modelled as $NaFe_2As_2$:

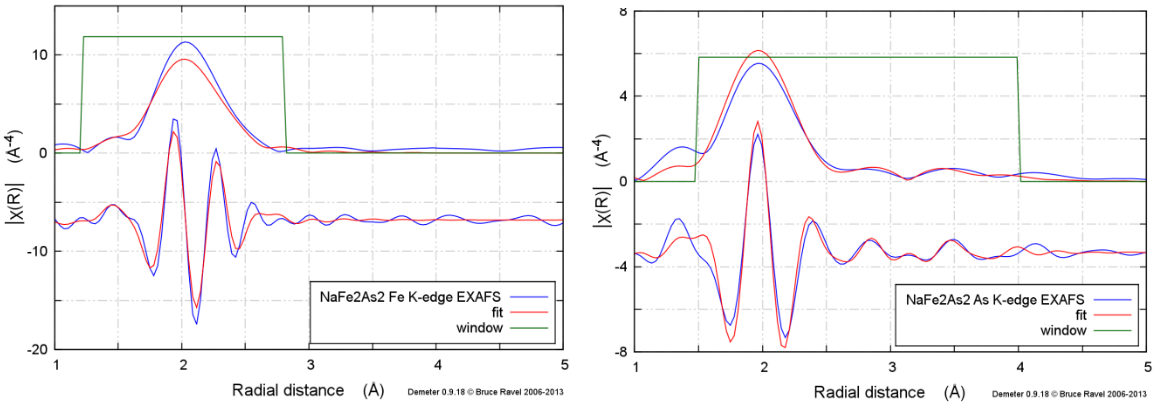

Modelled as $NaFe_{2-y}As_2$:

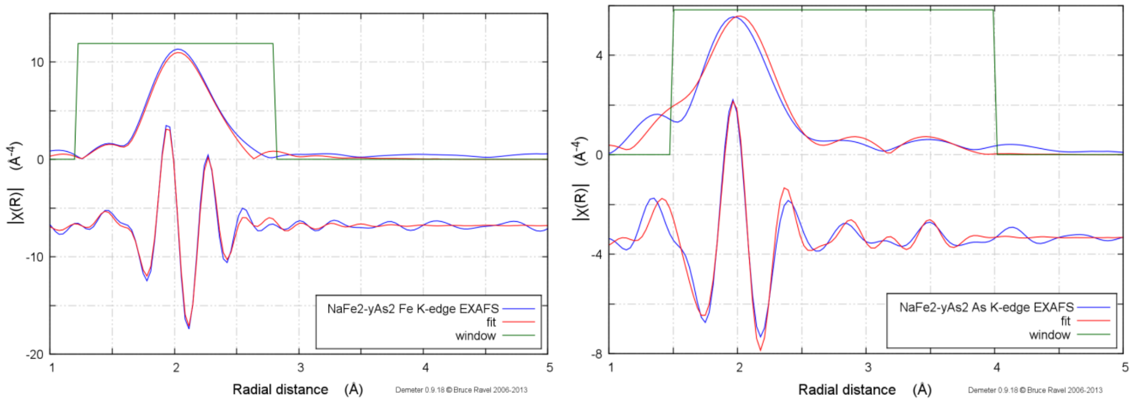

Figure II.ii Fits to the iron (left) and arsenic (right) EXAFS for $Na_{1-x}Fe_{2-y}As_2$ handled in an air sensitive manner. using models without vacancies (top) and with vacancies (bottom) with agreement R-factors of 0.0520 and 0.0143, using 14 and 17 of 24 independent points, respectively.

Table II.i Comparison of Refined parameters from EXAFS data for $Na_{1-x}Fe_{2-y}As_2$ handled in air and handled as air sensitive.

Parameter	Handled in air in a cellulose pellet	Handled under inert conditions in a BN pellet
RFe-As (N=4) (Å)	2.378(10)	2.372(13)
σ^2Fe-As (N=4)	0.006(1)	0.006(2)
RFe-As (N=3) (Å)	2.24(2)	2.20(3)
σ^2Fe-As (N=3)	0.010(2)	0.003(6)
Weighting parameter *w*	0.59(14)	0.7(2)
R As-As1 (Å)	3.17(4)	3.16(4)
σ^2As-As1	0.011(4)	0.009(5)
R As-As2 (Å)	3.7(2)	3.7(4)
σ^2As-As2	0.04(6)	0.05(11)
R As-As3 (Å)	3.80(7)	3.80(9)
σ^2As-As3	0.021(8)	0.020(10)
R Fe-Fe1 (Å)	2.70(3)	2.70(4)
σ^2Fe-Fe1	0.016(4)	0.030(8)
S_0^2As	1.00000(2)	0.8(2)
S_0^2Fe	0.68(7)	0.9(3)

III. Quantitative fitting of $Li_{1-x}Fe_x(OH)Fe_{1-y}Se$ EXAFS

It is observed in the EXAFS that vacancies in the [$Fe_{1-y}Se$] layer lead to a loss of local ordering outside of the first coordination shell. For samples with high vacancy concentrations there is no appreciable EXAFS signal beyond the first coordination shell ($R>3$). For samples with low vacancy concentrations a good fit to the full EXAFS can be achieved out to a radial distance of 5.5 Å from the absorber by modelling single and multiple scattering paths originating entirely from the FeSe layer, with the addition of the Fe–O path from the Li/Fe(OH) layer which contributes towards the first coordination shell.

Below are fits to the Fe *K*-edge EXAFS for (a) an iron-poor, non-superconducting sample $Li_{0.80}Fe_{0.20}(OH)Fe_{0.88}Se$ with a high proportion of iron vacancies in the FeSe layer. (b) The lithiated superconducting product $Li_{0.93}Fe_{0.07}(OH)Fe_{1.00}Se$, in which the vacancies in the FeSe layer have been filled by a reaction of (a) with lithium metal in ammonia solution. (c) The fit to the Fe *K*-edge EXAFS for an iron-rich superconducting hydrothermally-synthesised compound, $Li_{0.81}Fe_{0.19}(OH)Fe_{0.96}Se$, which was made with relatively few vacancies in the iron selenide layer without the lithium in ammonia treatment.

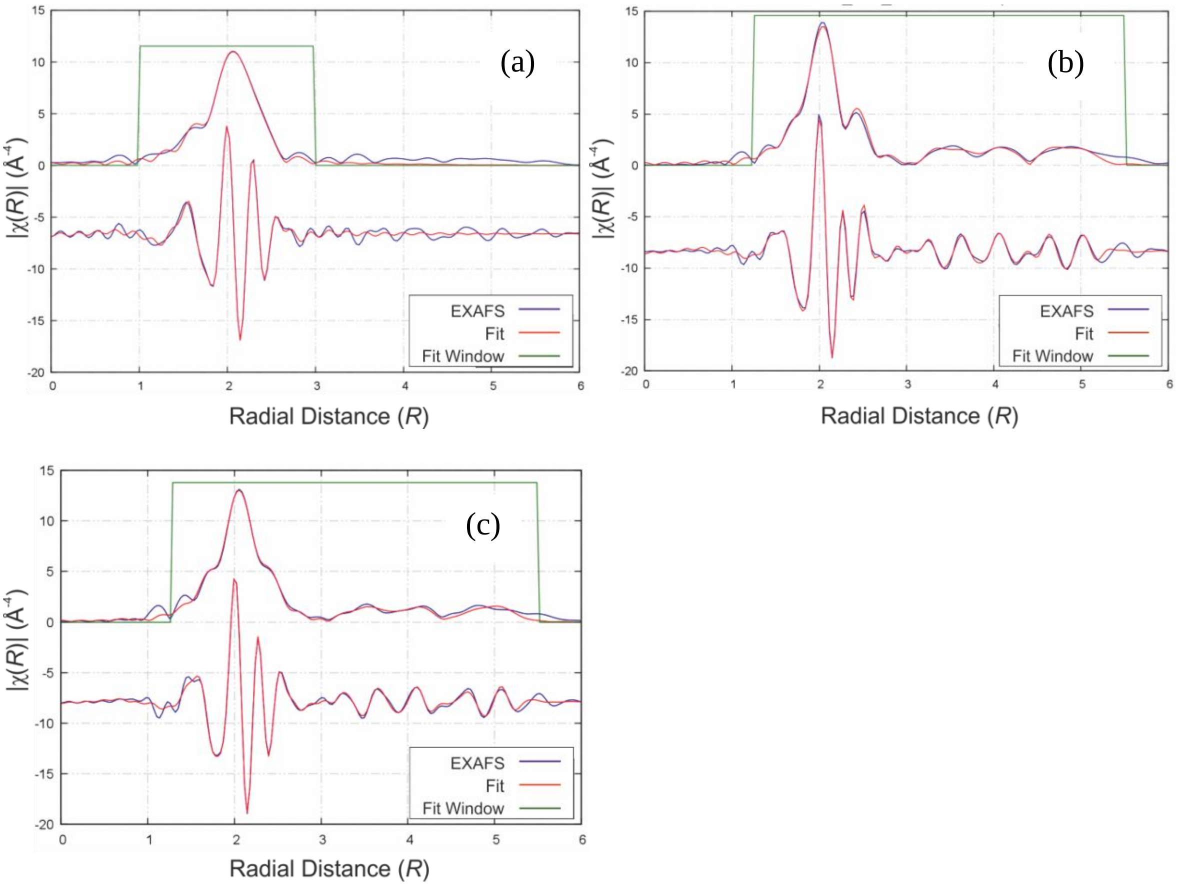

Figure III.i fits against the fourier transform of the Fe *K*-edge EXAFS for (a) $Li_{0.80}Fe_{0.20}(OH)Fe_{0.88}Se$, (b) $Li_{0.93}Fe_{0.07}(OH)Fe_{1.00}Se$, and (c) $Li_{0.81}Fe_{0.19}(OH)Fe_{0.96}Se$.

Table III.i Refinements summarised in the table show strong agreement between the average structure as probed by diffraction techniques and the local structure of $Li_{1-x}Fe_x(OH)Fe_{1-y}Se$ with low values of y. The diffraction measurements carried out on these samples are detailed in reference 130.

Scattering path	$Li_{0.80}Fe_{0.20}(OH)Fe_{0.88}Se$ difference between EXAFS and diffraction calculated path length (Å)	$Li_{0.81}Fe_{0.19}(OH)Fe_{0.96}Se$ difference between EXAFS and diffraction calculated path length (Å)	$Li_{0.93}Fe_{0.07}(OH)Fe_{1.00}Se$ difference between EXAFS and diffraction calculated path length (Å)
Fe1-Se 1st neighbour, single scattering	0.003(4)	0.003(3)	0.007(4)
Debye-Waller	0.0052(4)	0.0058(3)	0.0058(5)
Fe-Fe 1st neighbour, single scattering	0.027(9)	-0.003(4)	-0.017(6)
Debye-Waller	0.0120(8)	0.0088(3)	0.0075(6)
Fe2-O 1st neighbour, single scattering	0.00(3)	-0.02(2)	0.05(6)
Debye-Waller	0.005(2)	0.001(2)	0.01(2)
Fe1-Se-Fe 1st neighbours, acute triangle	Not modelled	0.04(6)	-0.03(4)
Debye-Waller		0.008(8)	0.007(6)
Fe1-Fe 2nd neighbour, single scattering	Not modelled	0.01(6)	-0.01(3)
Debye-Waller		0.014(4)	0.015(4)
Fe1-Se-Fe 1st and 2nd neighbours, double scattering	Not modelled	0.0(1)	0.02(7)
Debye-Waller		0.007(5)	0.006(8)
Fe1-Se 2nd neighbour, single scattering	Not modelled	0.03(6)	-0.02(3)
Debye-Waller		0.021(8)	0.014(2)
Fe-Fe 3rd neighbour, single scattering and forward scattering paths through 1st neighbouring Fe	Not modelled	0.03(2)	-0.09(3)
Debye-Waller		0.017(6)	0.02(1)

IV. Fits to sodium- ammonia- intercalate of iron selenide after synthesis, under argon

Table IV.i Rietveld refinement parameters from the fit shown in Figure 4.12

	Ammonia-poor	**Ammonia-rich**
Instrument	I12	
Temperature / K	298	
Space group	*I*4/*mmm*	*P*4/*nmm*
***a* / Å**	3.809(5)	3.83(1)
***c* / Å**	17.356(7)	10.917(9)
Volume / Å^3	251.8(1)	
Molar phase percentage	86.4	13.6

Table IV.ii Atomic positions, site occupancies and thermal displacements from the Rietveld refinement of the ammonia-poor phase shown in Figure 4.12.

atom	**site**	**x**	**y**	**z**	**Occupancy**	**Beq**
Fe	4d	0	0.5	0.25	1[a]	1[a]
Se	4e	0	0	0.3411(6)	1[a]	1[a]
N	2a	0	0	0	1[a]	1[a]
Na	2b	0	0	0.5	0.55(6)	1[a]

[a] not refined

Table IV.iii Atomic positions, site occupancies and thermal displacements from the Rietveld refinement of the ammonia-rich phase shown in Figure 4.12

site	**atom**	**x**	**y**	**z**	**Occupancy**	**B_{eq} / Å^2**
Fe	2*a*	0.75	0.25	0	1[a]	1[a]
Se	2*c*	0.25	0.25	0.133(9)	1[a]	1[a]
N	2*c*	0.75	0.75	0.86(5)	1[a]	1[a]
Na	2*b*	0.75	0.25	0.5	1.0(2)	1[a]

[a] not refined

V. Air sensitivity of sodium and ammonia intercalated iron selenide

Figure V.i shows the decomposition of sodium ammonia intercalated iron selenide (mixed ammonia-poor and stacked phases) into iron selenide. (a) a 15 minute diffraction pattern of the material taken on the empyrean diffractometer in a sealed argon atmosphere (b) a 60 minutes diffraction pattern of the same material, immediately after it had been exposed to air and (c) a 60 minute diffraction pattern of the material following on immediately after (b). The material in (c) indexes entirely to FeSe. This decomposition appears to have been completed ~30 minutes through pattern (b)

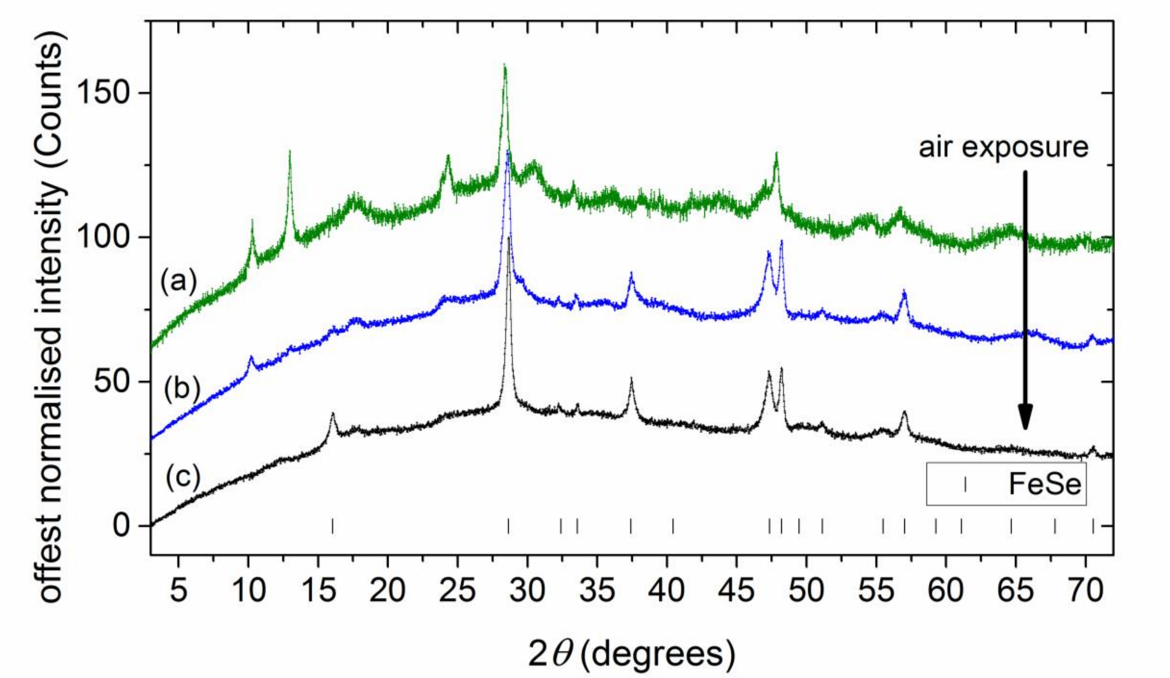

Figure V.i Evolution of the X-ray diffraction pattern (λ = 1.54046 Å) of sodium and ammonia intercalated iron selenide on air exposure (see text above).

VI. Exposure of the ammonia-poor phase to vacuum

Side peaks on the diffraction pattern of ammonia-poor sodium intercalated iron selenide after it is exposed to a vacuum are observable in Figure VI.i, showing that the ammonia-poor phase is unstable with respect to vacuum.

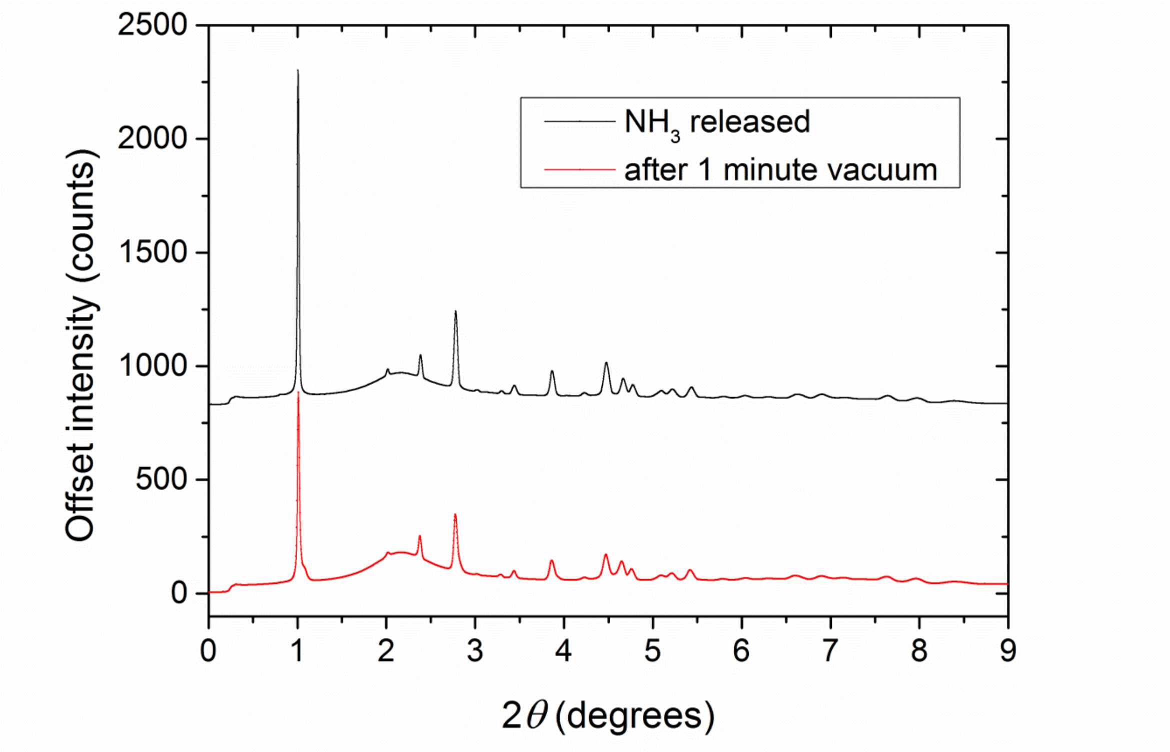

Figure VI.i Change in the X-ray diffraction pattern (λ = 0.1546 Å) of a pure ammonia-poor sodium intercalated iron selenide sample after it has been exposed to vacuum.

Figure VI.ii shows the development of the diffraction pattern of a sodium intercalated iron selenide phase upon exposure to vacuum. Following the *in-situ* measurements on of the intercalation of sodium and ammonia into iron selenide on beamline I12, the reaction vessel (Schlenk tube) was moved to a fume hood and the ammonia solution was allowed to evaporate under a flow of argon gas. Once no more liquid ammonia was present the product was placed under dynamic vacuum for between one minute and ninety minutes. The following diffraction patterns were taken of the product while it was under an argon atmosphere then after it was exposed to vacuum for the 5 minutes. Exposure of the same sample was continued and diffraction patterns were taken during several time intervals. The sample does not seem to continue to develop with continued exposure to vacuum.

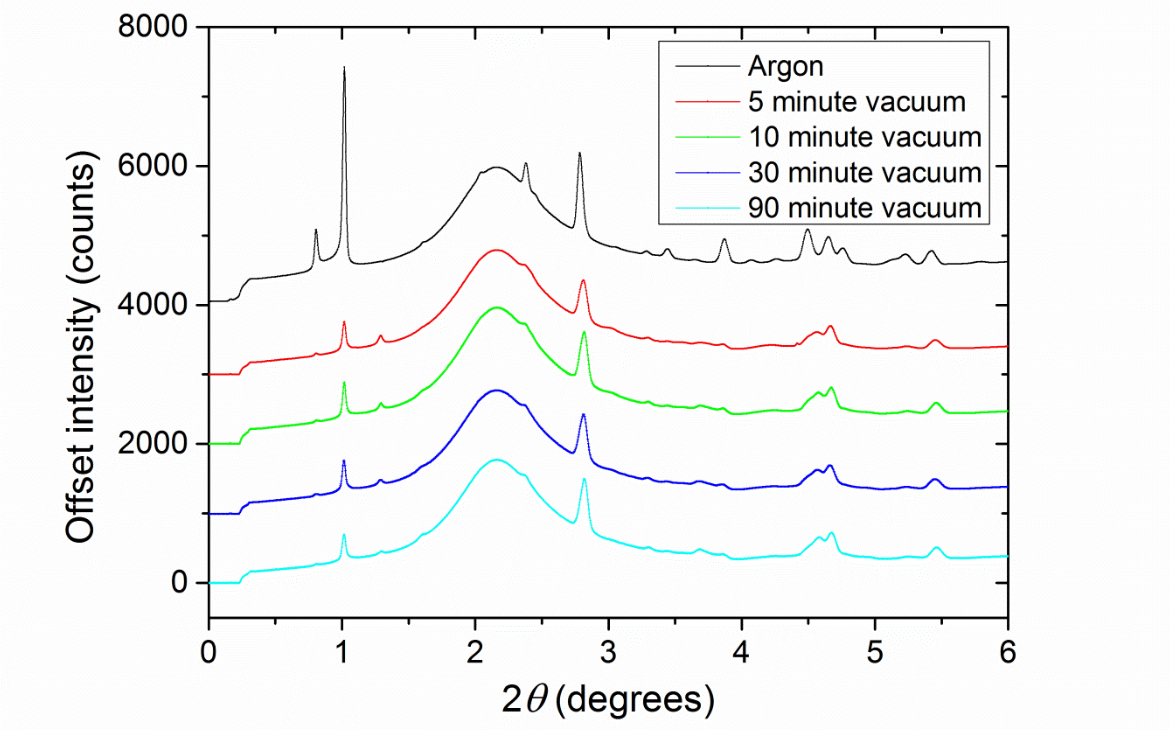

Figure VI.ii Evolution of the powder X-ray diffraction pattern (λ = 0.1546 Å) of a sodium- and ammonia-intercalated iron selenide sample on exposure to vacuum.

VII. Rietveld refinement against Polaris data for SXC090

Rietveld refinement against the Polaris data for the sodium and ammonia intercalated sample SXC090. The fits shown below against diffraction patterns from Polaris' five detector banks give a poor quality fit when using only the ammonia-poor sodium intercalate model. These fits correspond to the left hand side of Figure 4.18 in the main document, and are for comparison with a model that includes a stacked phase.

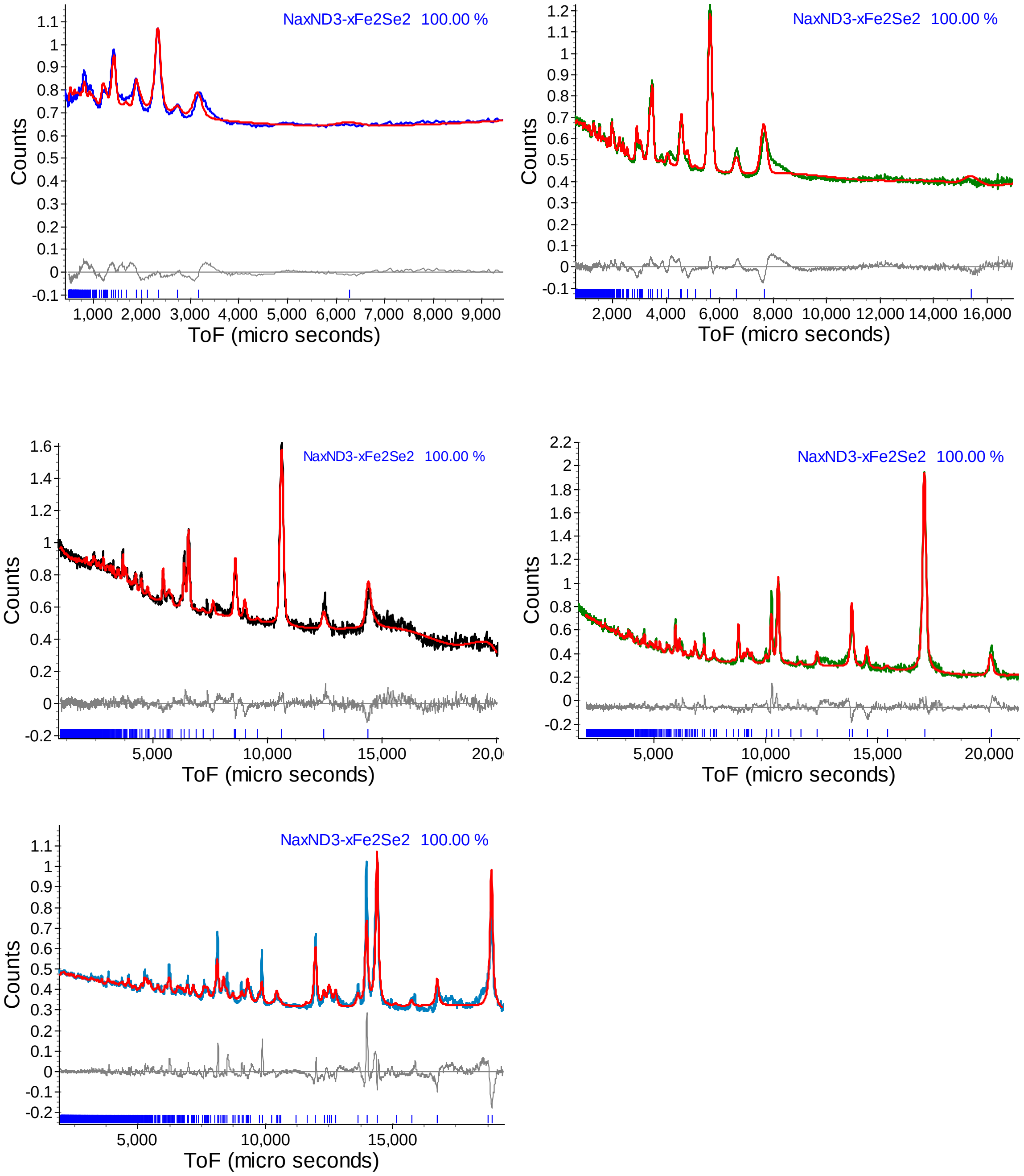

Figure VII.i Rietveld refinement against ToF powder neutron diffraction patterns of ammonia-poor sodium intercalated iron selenide (SXC090) using a single unit cell of I4/mmm symmetry.

Table VII.i Refined Rietveld parameters for the fit to the Polaris data using an ammonia-poor intercalate model, without the inclusion of the stacked phase, corresponding to the fits shown on the previous page and to the left hand side of Figure 4.18 in the main document.

Instrument	POLARIS	**Temperature / K**	5
Space group	*I*4/*mmm*	**Volume / Å^3**	253.20(4)
***a* / Å**	3.7741(8)	**R_{wp} / %**	1.68
***c* / Å**	17.001(5)		
Fe-Se distance / Å	2.385(2)	**N-D1 distance / Å**	0.92(8)
Na-Se distance / Å	2.792(4)	**N-D2 distance / Å**	0.93(4)

atom	**Site**	**x**	**y**	**z**	**occupancy**	**U_{11} / Å^2 × 100**	**U_{33} / Å^2 × 100**
Fe	2*a*	0	0.5	0.25	0.80(1)	0.01(6)	
Se	2*c*	0	0	0.3358(2)	1	0.00(8)	0.9(2)
N	2*c*	0	0	0	0.93(4)	1.8(3)	
Na	8*j*	0	0	0.5	0.35^a	6.2(9)^b	
D1	8*j*	0.112(8)	0.112(8)	0.042(2)	0.17(7)	6.2(9)^b	
D2	2*b*	0	0	0.054(5)	0.17(2)	6.2(9)^b	

Table VII.ii Refined Rietveld parameters for the fit to the Polaris data using both an ammonia-poor intercalate of iron selenide model and a stacked phase model. These parameters correspond to the fits on the right hand side of Figure 4.18, and the fits in Figure 4.19 in the main document.

	Ammonia-poor $Na_{0.35}(NH_{2.45(13)})Fe_{1.97(2)}Se_2$	**Stacked phase**
Instrument	POLARIS	
Temperature / K	5	
Space group	*I*4/*mmm*	*P*1
a / Å	3.7841(3)	3.7826(3)
c / Å	17.099(2)	95.82(4)
V / Å^3	244.85(5)	1370.3(7)
mass phase percentage	49.9	50.1

Table VII.iii Refined Rietveld parameters for the ammonia poor intercalate phase that accompanies the stacked phase in Figure 4.19 in the main document. Parameters for the stacked phase are given in the main document in Table 4.5.

atom	**Site**	**x**	**y**	**z**	**Occupancy**	**U_{eq} / Å^2 × 100**
Fe	2*a*	0	0.5	0.25	0.986(8)	0.03(6)
Se	2*c*	0	0	0.3411(6)	1	0.25(8)
N	2*c*	0	0	0	1.00(7)[a]	4.6(7)
Na	8*j*	0	0	0.5	0.55(6)	6.3(6)[b]
D1	8*j*	0.134(5)	0.134(5)	0.037(2)	0.24(2)	6.3(6)[b]
D2	2*b*	0	0	0.077(3)	0.27(3)	6.3(6)[b]

[a] parameter was refined to a maximum imposed limit of 1

[b] parameters were refined together as a single value and refined to a maximum imposed limit

VIII. Refinement parameters for fits to diffraction patterns at set time intervals in the 0.15 $K_{(NH3)}$ + FeSe reaction.

Tables VIII.i-iii Full Rietveld refinement parameters for Table 5.2 in the main document.

Crystalline intermediate at *t* = 48 seconds			
Space group	*P*4/*nmm*	**origin choice**	2
***a* / Å**	3.8037(6)	***c* / Å**	11.5375(7)
R_{wp} / %	1.19	**Volume / Å^3**	166.93(5)

atom	site	x	y	z	occupancy	Beq / Å^2
Fe1	2*a*	0.75	0.25	0	1	1^a
Se1	2*c*	0.25	0.25	0.1343(8)	1	1^a
N1	2*c*	0.75	0.75	0.386(5)	0.83(3)	3^a
K1	2*c*	0.75	0.75	0.386(5)	0.17(3)	3^a
K2	2*b*	0.75	0.25	0.5	0.18(3)	3^a

Product phase at *t* = 48 seconds			
Space group	*P*4/*nmm*	**origin choice**	2
***a* / Å**	3.814(1)	***c* / Å**	9.897(2)
R_{wp} / %	1.19	**Volume / Å^3**	143.98(9)

atom	site	x	y	z	occupancy	Beq / Å^2
Fe1	2*a*	0.75	0.25	0	1	1^a
Se1	2*c*	0.25	0.25	0.162(2)	1	1^a
N1	2*c*	0.75	0.75	0.434(4)	0.61(3)	3^a
K1	2*c*	0.75	0.75	0.434(4)	0.39(3)	3^a
K2	2*b*	0.75	0.25	0.5	0.00(2)	3^a

poorly-crystalline intermediate at *t* = 48 seconds			
Space group	*P*4/*nmm*	**origin choice**	2
***a* / Å**	3.803	***c* / Å**	10.491
R_{wp} / %	1.19	**Volume / Å^3**	151.49

atom	site	x	y	z	occupancy	Beq / Å^2
Fe1	2*a*	0.75	0.25	0	1	5^a
Se1	2*c*	0.25	0.25	0.15	1	5^a
N1	2*c*	0.75	0.75	0.405	0.9	5^a
K1	2*c*	0.75	0.75	0.405	0.1	5^a
K2	2*b*	0.75	0.25	0.5	0.1	5^a

Tables VIII.iv-vi Full Rietveld refinement parameters for Table 5.3 in the main document.

<table>
<tr><th colspan="7">Crystalline intermediate at t = 5 minutes</th></tr>
<tr><td colspan="2">Space group</td><td colspan="2">$P4/nmm$</td><td colspan="2">origin choice</td><td>2</td></tr>
<tr><td colspan="2">a / Å</td><td colspan="2">3.8053(6)</td><td colspan="2">c / Å</td><td>11.5589(6)</td></tr>
<tr><td colspan="2">R_{wp} / %</td><td colspan="2">1.24</td><td colspan="2">Volume / Å^3</td><td>166.93(5)</td></tr>
<tr><td>atom</td><td>site</td><td>x</td><td>y</td><td>z</td><td>occupancy</td><td>Beq / Å^2</td></tr>
<tr><td>Fe1</td><td>$2a$</td><td>0.75</td><td>0.25</td><td>0</td><td>1</td><td>1[a]</td></tr>
<tr><td>Se1</td><td>$2c$</td><td>0.25</td><td>0.25</td><td>0.1361(9)</td><td>1</td><td>1[a]</td></tr>
<tr><td>N1</td><td>$2c$</td><td>0.75</td><td>0.75</td><td>0.377(6)</td><td>0.83(4)</td><td>3[a]</td></tr>
<tr><td>K1</td><td>$2c$</td><td>0.75</td><td>0.75</td><td>0.377(6)</td><td>0.17(4)</td><td>3[a]</td></tr>
<tr><td>K2</td><td>$2b$</td><td>0.75</td><td>0.25</td><td>0.5</td><td>0.19(4)</td><td>3[a]</td></tr>
</table>

<table>
<tr><th colspan="7">Product phase at t = 5 minutes</th></tr>
<tr><td colspan="2">Space group</td><td colspan="2">$P4/nmm$</td><td colspan="2">origin choice</td><td>2</td></tr>
<tr><td colspan="2">a / Å</td><td colspan="2">3.8229(4)</td><td colspan="2">c / Å</td><td>9.8959(6)</td></tr>
<tr><td colspan="2">R_{wp} / %</td><td colspan="2">1.24</td><td colspan="2">Volume / Å^3</td><td>143.98(9)</td></tr>
<tr><td>atom</td><td>site</td><td>x</td><td>y</td><td>z</td><td>occupancy</td><td>Beq / Å^2</td></tr>
<tr><td>Fe1</td><td>$2a$</td><td>0.75</td><td>0.25</td><td>0</td><td>1</td><td>1[a]</td></tr>
<tr><td>Se1</td><td>$2c$</td><td>0.25</td><td>0.25</td><td>0.1596(7)</td><td>1</td><td>1[a]</td></tr>
<tr><td>N1</td><td>$2c$</td><td>0.75</td><td>0.75</td><td>0.416(2)</td><td>0.61(3)</td><td>3[a]</td></tr>
<tr><td>K1</td><td>$2c$</td><td>0.75</td><td>0.75</td><td>0.416(2)</td><td>0.39(3)</td><td>3[a]</td></tr>
<tr><td>K2</td><td>$2b$</td><td>0.75</td><td>0.25</td><td>0.5</td><td>0.00(2)</td><td>3[a]</td></tr>
</table>

<table>
<tr><th colspan="7">poorly-crystalline intermediate at t = 5 minutes</th></tr>
<tr><td colspan="2">Space group</td><td colspan="2">$P4/nmm$</td><td colspan="2">origin choice</td><td>2</td></tr>
<tr><td colspan="2">a / Å</td><td colspan="2">3.803</td><td colspan="2">c / Å</td><td>10.491</td></tr>
<tr><td colspan="2">R_{wp} / %</td><td colspan="2">1.24</td><td colspan="2">Volume / Å^3</td><td>151.49</td></tr>
<tr><td>atom</td><td>site</td><td>x</td><td>y</td><td>z</td><td>occupancy</td><td>Beq / Å^2</td></tr>
<tr><td>Fe1</td><td>$2a$</td><td>0.75</td><td>0.25</td><td>0</td><td>1</td><td>5[a]</td></tr>
<tr><td>Se1</td><td>$2c$</td><td>0.25</td><td>0.25</td><td>0.15</td><td>1</td><td>5[a]</td></tr>
<tr><td>N1</td><td>$2c$</td><td>0.75</td><td>0.75</td><td>0.405</td><td>0.9</td><td>5[a]</td></tr>
<tr><td>K1</td><td>$2c$</td><td>0.75</td><td>0.75</td><td>0.405</td><td>0.1</td><td>5[a]</td></tr>
<tr><td>K2</td><td>$2b$</td><td>0.75</td><td>0.25</td><td>0.5</td><td>0.1</td><td>5[a]</td></tr>
</table>

Tables VIII.vi-viii Full Rietveld refinement parameters for Table 5.4 in the main document.

Crystalline intermediate at *t* = 20 minutes

Space group	*P*4/*nmm*	origin choice	2
a / Å	3.8141(8)	*c* / Å	11.5557(8)
R_{wp} / %	1.31	Volume / $Å^3$	168.11(6)

atom	site	x	y	z	occupancy	Beq / $Å^2$
Fe1	2*a*	0.75	0.25	0	1	1^a
Se1	2*c*	0.25	0.25	0.1302(8)	1	1^a
N1	2*c*	0.75	0.75	0.367(5)	0.84(4)	3^a
K1	2*c*	0.75	0.75	0.367(5)	0.16(4)	3^a
K2	2*b*	0.75	0.25	0.5	0.16(3)	3^a

Product phase at *t* = 20 minutes

Space group	*P*4/*nmm*	origin choice	2
a / Å	3.8229(4)	*c* / Å	10.0186(6)
R_{wp} / %	1.31	Volume / $Å^3$	146.65(9)

atom	site	x	y	z	occupancy	Beq / $Å^2$
Fe1	2*a*	0.75	0.25	0	1	1^a
Se1	2*c*	0.25	0.25	0.171(1)	1	1^a
N1	2*c*	0.75	0.75	0.420(3)	0.74(4)	3^a
K1	2*c*	0.75	0.75	0.420(3)	0.26(4)	3^a
K2	2*b*	0.75	0.25	0.5	0.00(2)	3^a

poorly-crystalline intermediate at *t* = 20 minutes

Space group	*P*4/*nmm*	origin choice	2
a / Å	3.818(8)	*c* / Å	10.82(4)
R_{wp} / %	1.31	Volume / $Å^3$	157.7(9)

atom	site	x	y	z	occupancy	Beq / $Å^2$
Fe1	2*a*	0.75	0.25	0	1	5^a
Se1	2*c*	0.25	0.25	0.15	1	5^a
N1	2*c*	0.75	0.75	0.405	0.9	5^a
K1	2*c*	0.75	0.75	0.405	0.1	5^a
K2	2*b*	0.75	0.25	0.5	0.1	5^a

Tables VIII.ix-xi Full Rietveld refinement parameters for Table 5.5 in the main document.

<table>
<tr><th colspan="7">Crystalline intermediate at t = 60 minutes</th></tr>
<tr><td colspan="2">Space group</td><td colspan="2">$P4/nmm$</td><td colspan="2">origin choice</td><td>2</td></tr>
<tr><td colspan="2">a / Å</td><td colspan="2">3.826(2)</td><td colspan="2">c / Å</td><td>11.496(3)</td></tr>
<tr><td colspan="2">R_{wp} / %</td><td colspan="2">1.00</td><td colspan="2">Volume / Å^3</td><td>168.3(2)</td></tr>
<tr><td>atom</td><td>site</td><td>x</td><td>y</td><td>z</td><td>occupancy</td><td>Beq / Å^2</td></tr>
<tr><td>Fe1</td><td>2a</td><td>0.75</td><td>0.25</td><td>0</td><td>1</td><td>1^a</td></tr>
<tr><td>Se1</td><td>2c</td><td>0.25</td><td>0.25</td><td>0.143(3)</td><td>1</td><td>1^a</td></tr>
<tr><td>N1</td><td>2c</td><td>0.75</td><td>0.75</td><td>0.367(8)</td><td>0.84(4)</td><td>3^a</td></tr>
<tr><td>K1</td><td>2c</td><td>0.75</td><td>0.75</td><td>0.367(8)</td><td>0.16(4)</td><td>3^a</td></tr>
<tr><td>K2</td><td>2b</td><td>0.75</td><td>0.25</td><td>0.5</td><td>0.16(3)</td><td>3^a</td></tr>
</table>

<table>
<tr><th colspan="7">Product phase at t = 60 minutes</th></tr>
<tr><td colspan="2">Space group</td><td colspan="2">$P4/nmm$</td><td colspan="2">origin choice</td><td>2</td></tr>
<tr><td colspan="2">a / Å</td><td colspan="2">3.8286(5)</td><td colspan="2">c / Å</td><td>10.107(2)</td></tr>
<tr><td colspan="2">R_{wp} / %</td><td colspan="2">1.00</td><td colspan="2">Volume / Å^3</td><td>148.49(5)</td></tr>
<tr><td>atom</td><td>site</td><td>x</td><td>y</td><td>z</td><td>occupancy</td><td>Beq / Å^2</td></tr>
<tr><td>Fe1</td><td>2a</td><td>0.75</td><td>0.25</td><td>0</td><td>1</td><td>1^a</td></tr>
<tr><td>Se1</td><td>2c</td><td>0.25</td><td>0.25</td><td>0.1672(6)</td><td>1</td><td>1^a</td></tr>
<tr><td>N1</td><td>2c</td><td>0.75</td><td>0.75</td><td>0.408(2)</td><td>0.72(4)</td><td>3^a</td></tr>
<tr><td>K1</td><td>2c</td><td>0.75</td><td>0.75</td><td>0.408(2)</td><td>0.28(4)</td><td>3^a</td></tr>
<tr><td>K2</td><td>2b</td><td>0.75</td><td>0.25</td><td>0.5</td><td>0.00(1)</td><td>3^a</td></tr>
</table>

<table>
<tr><th colspan="7">poorly-crystalline intermediate at t = 60 minutes</th></tr>
<tr><td colspan="2">Space group</td><td colspan="2">$P4/nmm$</td><td colspan="2">origin choice</td><td>2</td></tr>
<tr><td colspan="2">a / Å</td><td colspan="2">3.813(9)</td><td colspan="2">c / Å</td><td>10.75(5)</td></tr>
<tr><td colspan="2">R_{wp} / %</td><td colspan="2">1.00</td><td colspan="2">Volume / Å^3</td><td>156.3(6)</td></tr>
<tr><td>atom</td><td>site</td><td>x</td><td>y</td><td>z</td><td>occupancy</td><td>Beq / Å^2</td></tr>
<tr><td>Fe1</td><td>2a</td><td>0.75</td><td>0.25</td><td>0</td><td>1</td><td>5^a</td></tr>
<tr><td>Se1</td><td>2c</td><td>0.25</td><td>0.25</td><td>0.15</td><td>1</td><td>5^a</td></tr>
<tr><td>N1</td><td>2c</td><td>0.75</td><td>0.75</td><td>0.405</td><td>0.9</td><td>5^a</td></tr>
<tr><td>K1</td><td>2c</td><td>0.75</td><td>0.75</td><td>0.405</td><td>0.1</td><td>5^a</td></tr>
<tr><td>K2</td><td>2b</td><td>0.75</td><td>0.25</td><td>0.5</td><td>0.1</td><td>5^a</td></tr>
</table>

IX. Rietveld refinement against neutron powder diffraction data for ammonia-poor potassium intercalated iron selenide

All fits to the neutron diffraction patterns from banks 1-6 of the GEM instrument at ISIS neutron source for $K_{0.3}(ND_{2.6(4)})_{0.14(2)}FeSe$, corresponding to Figure 5.15 and Table 5.8.

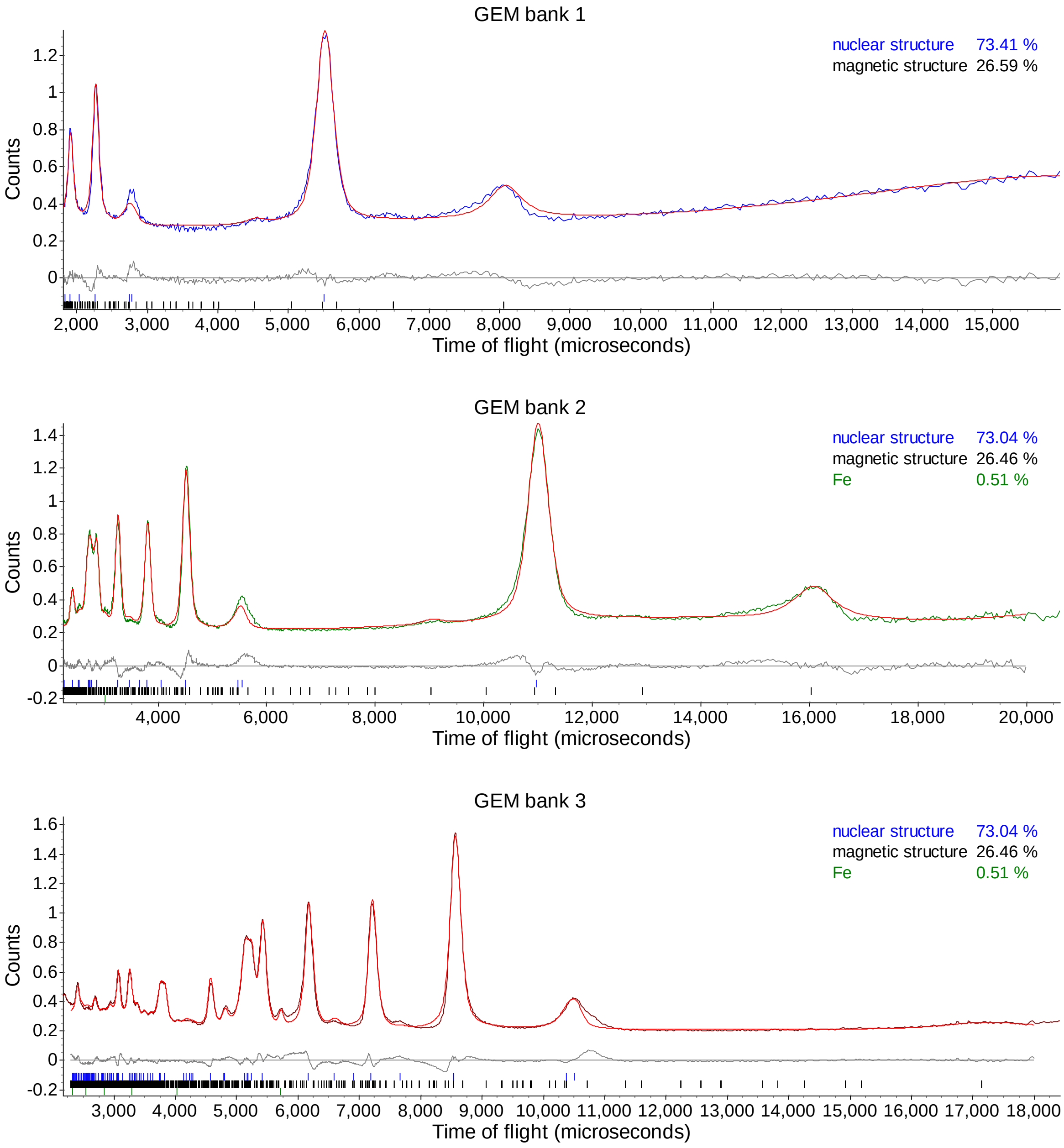

Figure IX.i Rietveld refinement against powder neutron diffraction patterns of $K_{0.3}(ND_{2.6(4)})_{0.14(2)}FeSe$.

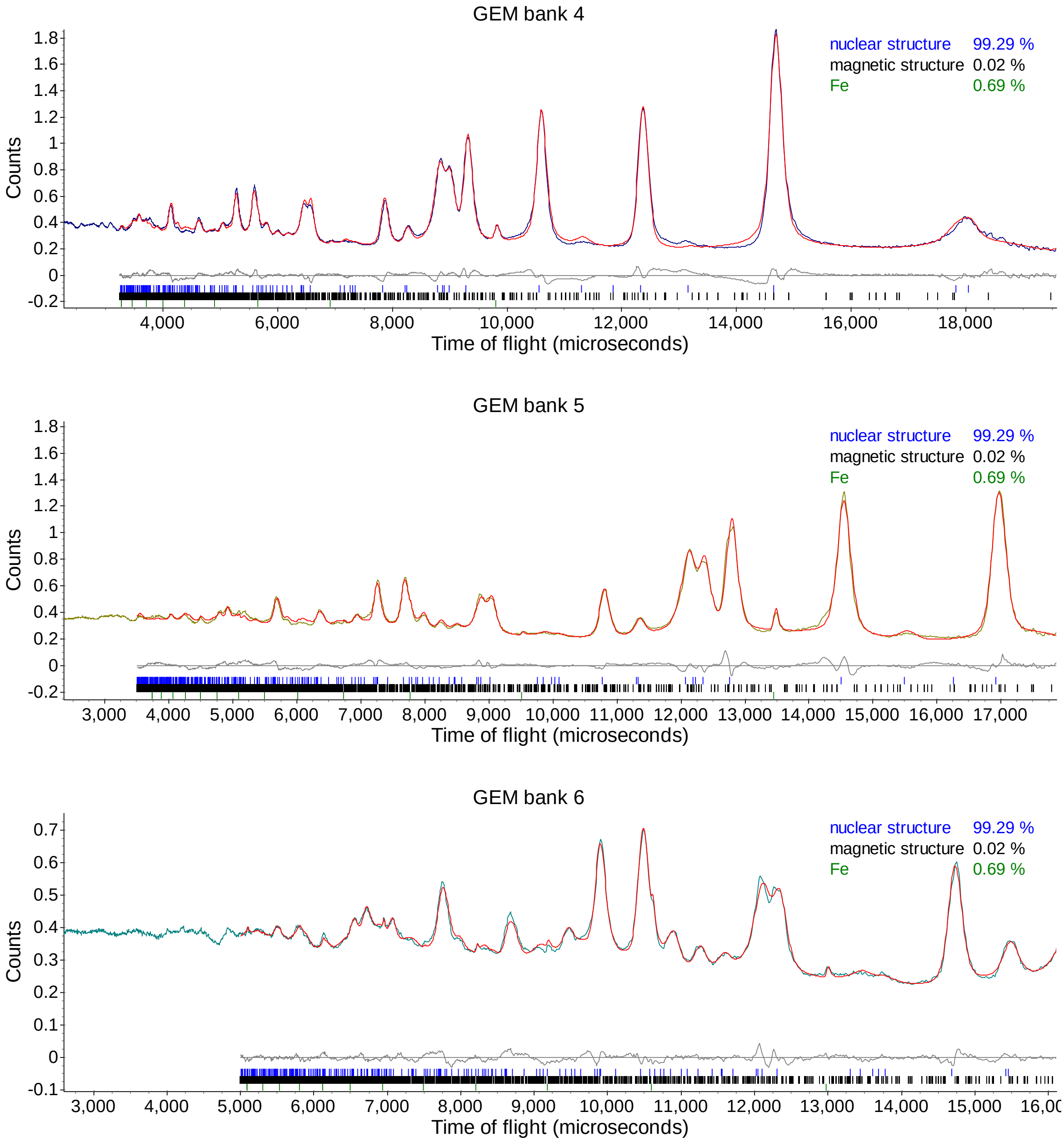

Figure IX.ii Rietveld refinement against powder neutron diffraction patterns of $K_{0.3}(ND_{2.6(4)})_{0.14(2)}FeSe$ continued.

All fits to the neutron diffraction patterns from banks 1-6 of the GEM instrument at ISIS neutron source for $K_{0.15}(ND_{2.9(3)})_{0.35(3)}FeSe$, corresponding to Figure 5.16 and Table 5.10.

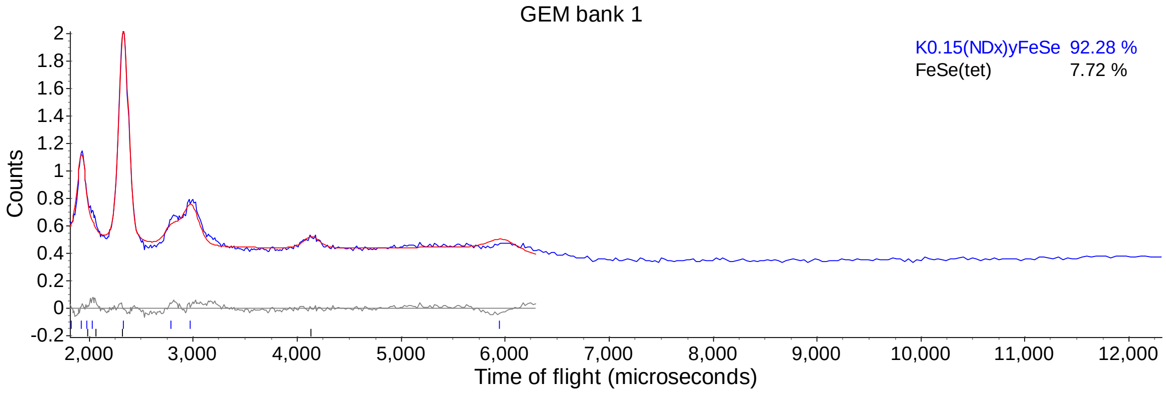

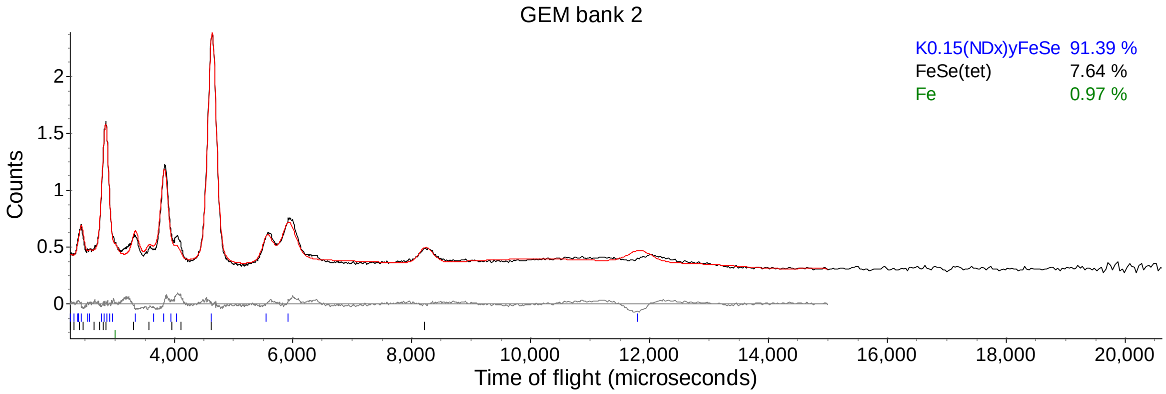

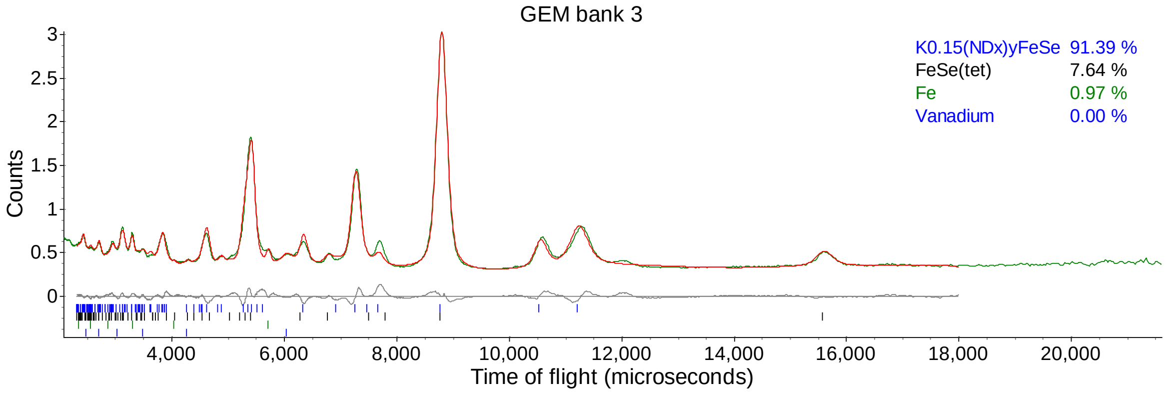

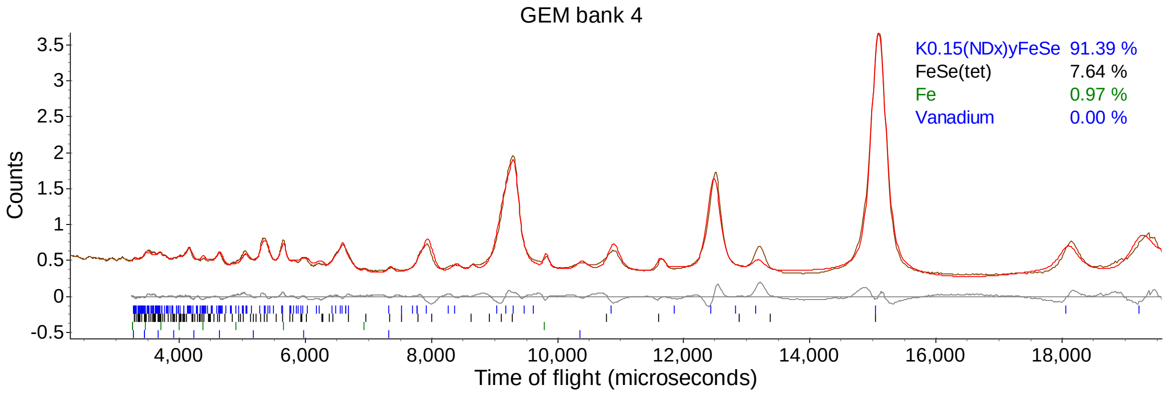

Figure IX.iii Rietveld refinement against powder neutron diffraction patterns of $K_{0.15}(ND_{2.9(3)})_{0.35(3)}FeSe$.

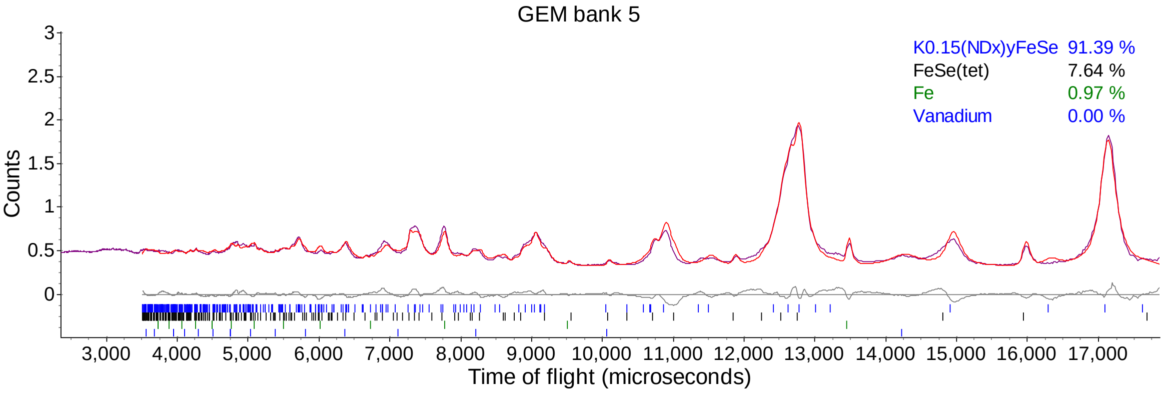

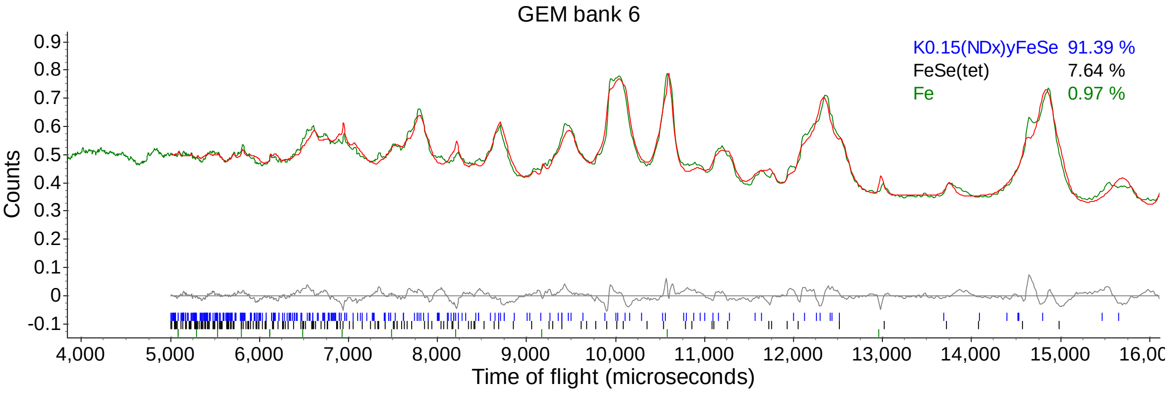

Figure IX.iv Rietveld refinement against powder neutron diffraction patterns of $K_{0.15}(ND_{2.9(3)})_{0.35(3)}FeSe$ continued.

X. Rietveld refinement parameters for the annealed potassium and ammonia intercalates of iron selenide.

Table X.i Rietveld refined structure of the product of a 0.5 $K_{(NH3)}$ + FeSe reaction after annealing at 400 °C, corresponding to the top panel of Figure 5.25.

<table>
<tr><td colspan="3">Refined formula</td><td colspan="3">$K_{0.99(1)}Fe_{1.64(1)}Se_2$</td></tr>
<tr><td colspan="2">space group</td><td colspan="2"><i>I</i>4/<i>m</i></td><td>Temperature / K</td><td>295</td></tr>
<tr><td colspan="2"><i>a</i> / Å</td><td colspan="2">8.7602(2)</td><td><i>c</i> / Å</td><td>14.048(1)</td></tr>
<tr><td colspan="2"><i>Volume</i> / Å^3</td><td colspan="2">1078.05(5)</td><td>R_{wp} / %</td><td>1.31</td></tr>
<tr><td>atom</td><td>site</td><td><i>x</i></td><td><i>y</i></td><td><i>z</i></td><td>Occupancy</td></tr>
<tr><td>K1</td><td>8<i>h</i></td><td>0.815(3)</td><td>0.371(2)</td><td>0.5</td><td>0.98(4)</td></tr>
<tr><td>K2</td><td>2<i>b</i></td><td>0</td><td>0</td><td>0.25</td><td>0.99(2)</td></tr>
<tr><td>Fe1</td><td>16<i>i</i></td><td>0.304(1)</td><td>0.415(1)</td><td>0.25</td><td>0.886(7)</td></tr>
<tr><td>Fe2</td><td>4<i>d</i></td><td>0</td><td>0</td><td>0.25</td><td>0.56(2)</td></tr>
<tr><td>Se2</td><td>16<i>i</i></td><td>0.1016(9)</td><td>0.2881(8)</td><td>0.3562(3)</td><td>1</td></tr>
<tr><td>Se1</td><td>4<i>e</i></td><td>0</td><td>0</td><td>0.139(1)</td><td>1</td></tr>
</table>

Table X.ii Rietveld refined structure of the product of a 0.3 $K_{(NH3)}$ + FeSe reaction after annealing at 400 °C, corresponding to the middle panel of Figure 5.25.

<table>
<tr><td colspan="3">Refined formula</td><td colspan="3">$K_{0.66(2)}Fe_{1.66(2)}Se_2$</td></tr>
<tr><td colspan="2">space group</td><td colspan="2"><i>I</i>4/<i>m</i></td><td>Temperature / K</td><td>400</td></tr>
<tr><td colspan="2"><i>a</i> / Å</td><td colspan="2">8.76869(1)</td><td><i>c</i> / Å</td><td>14.3633(3)</td></tr>
<tr><td colspan="2"><i>Volume</i> / Å^3</td><td colspan="2">1104.38(3)</td><td>R_{wp} / %</td><td>1.06</td></tr>
<tr><td>atom</td><td>site</td><td><i>x</i></td><td><i>y</i></td><td><i>z</i></td><td>Occupancy</td></tr>
<tr><td>K1</td><td>8<i>h</i></td><td>0.791(6)</td><td>0.437(3)</td><td>0.5</td><td>0.65(1)</td></tr>
<tr><td>K2</td><td>2<i>b</i></td><td>0</td><td>0</td><td>0.25</td><td>0.71(5)</td></tr>
<tr><td>Fe1</td><td>16<i>i</i></td><td>0.306(2)</td><td>0.395(3)</td><td>0.25</td><td>0.838(7)</td></tr>
<tr><td>Fe2</td><td>4<i>d</i></td><td>0</td><td>0</td><td>0.25</td><td>0.79(3)</td></tr>
<tr><td>Se2</td><td>16<i>i</i></td><td>0.095(1)</td><td>0.303(2)</td><td>0.3521(3)</td><td>1</td></tr>
<tr><td>Se1</td><td>4<i>e</i></td><td>0</td><td>0</td><td>0.142(1)</td><td>1</td></tr>
</table>

Table X.iii Rietveld refined structure of the product of a 0.15 $K_{(NH3)}$ + FeSe reaction after annealing at 400 °C, corresponding to the bottom panel of Figure 5.25.

<table>
<tr><td colspan="3">Refined formula</td><td colspan="3">$K_{0.54(3)}Fe_{1.58(3)}Se_2$</td></tr>
<tr><td colspan="2">space group</td><td colspan="2"><i>I</i>4/<i>m</i></td><td>Temperature / K</td><td>295</td></tr>
<tr><td colspan="2"><i>a</i> / Å</td><td colspan="2">8.6712(3)</td><td><i>c</i> / Å</td><td>14.173(1)</td></tr>
<tr><td colspan="2"><i>Volume</i> / Å^3</td><td colspan="2">106.7(1)</td><td>R_{wp} / %</td><td>0.81</td></tr>
<tr><td>atom</td><td>site</td><td><i>x</i></td><td><i>y</i></td><td><i>z</i></td><td>Occupancy</td></tr>
<tr><td>K1</td><td>8<i>h</i></td><td>0.794(7)</td><td>0.387(6)</td><td>0.5</td><td>0.61(4)</td></tr>
<tr><td>K2</td><td>2<i>b</i></td><td>0</td><td>0</td><td>0.25</td><td>0.23(8)</td></tr>
<tr><td>Fe1</td><td>16<i>i</i></td><td>0.324(3)</td><td>0.401(3)</td><td>0.25</td><td>0.81(3)</td></tr>
<tr><td>Fe2</td><td>4<i>d</i></td><td>0</td><td>0</td><td>0.25</td><td>0.72(3)</td></tr>
<tr><td>Se2</td><td>16<i>i</i></td><td>0.078(1)</td><td>0.293(2)</td><td>0.3561(5)</td><td>1</td></tr>
<tr><td>Se1</td><td>4<i>e</i></td><td>0</td><td>0</td><td>0.149(2)</td><td>1</td></tr>
</table>

XI. Comparison of CaFeSeO samples

Comparison of laboratory X-ray diffraction patterns (normalised intensity) for the two samples analysed for the investigations of CaFeSeO in chapter 6. The blue pattern of SXC195 was taken on a spinning flat plate in the open air using the Empyrean diffractometer and the red pattern of SXC223 was taken in under argon in an air-tight sample holder using the primary monochromated X-pert diffractometer (appendix I).

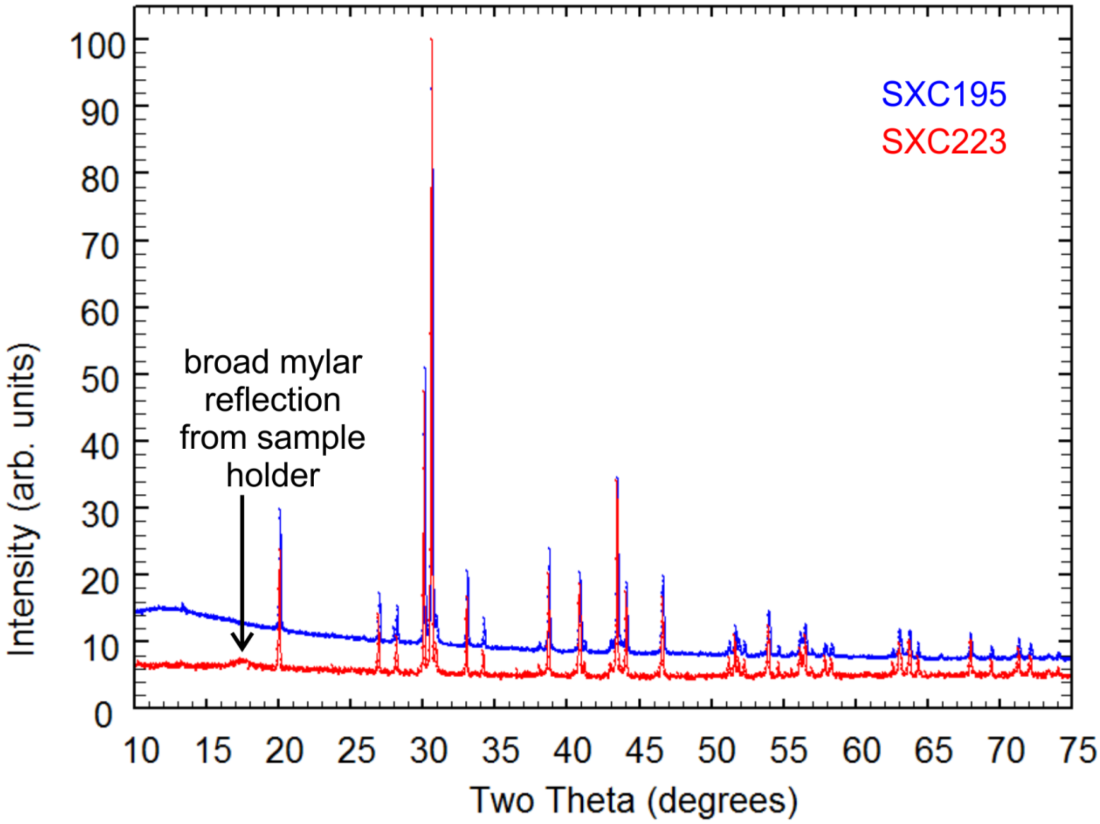

Figure XI.i comparison of the laboratory X-ray diffraction patterns (λ = 1.54056 Å) of two, separately synthesised CaFeSeO samples that were reported in the main document.

XII. CaFeSeO 100:70:30:0 vacancy ordering model

Rietveld refinement against powder neutron diffraction data for CaFeSeO (SXC223) taken on the WISH diffractometer. The model used is the same as described in 6.5, page 193.

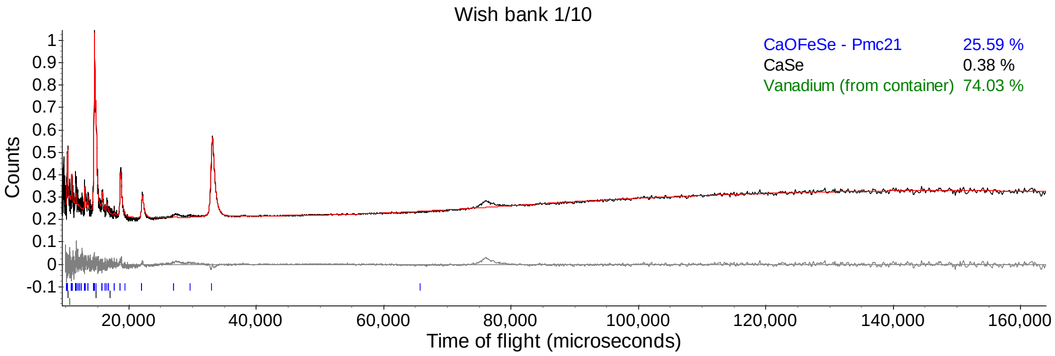
Wish bank 1/10

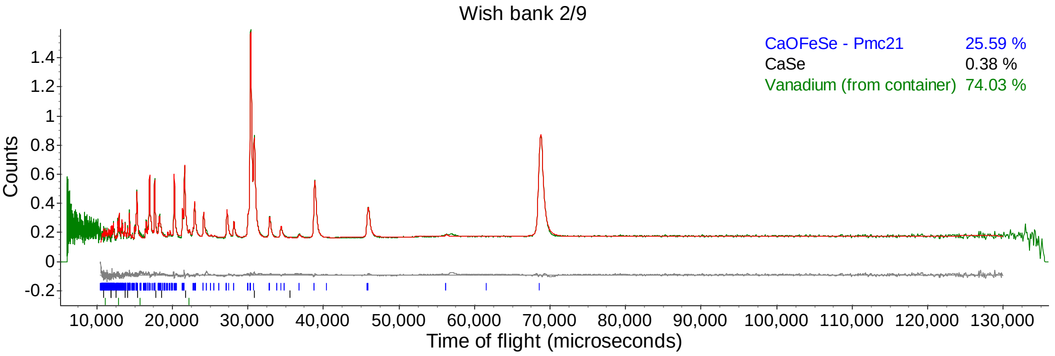
Wish bank 2/9

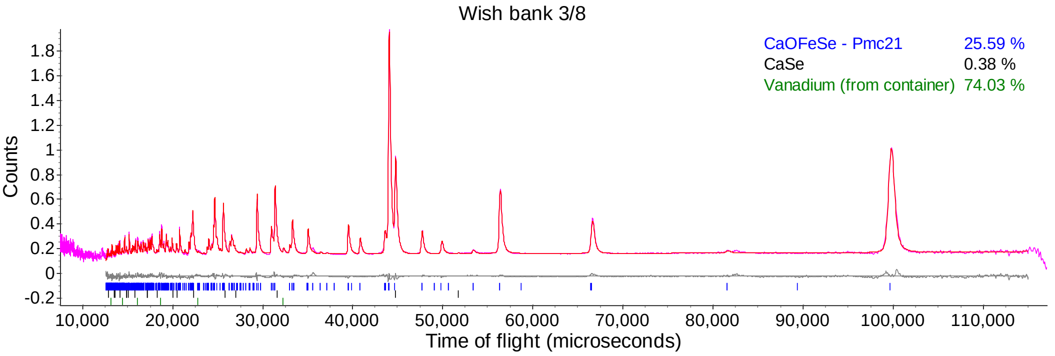
Wish bank 3/8

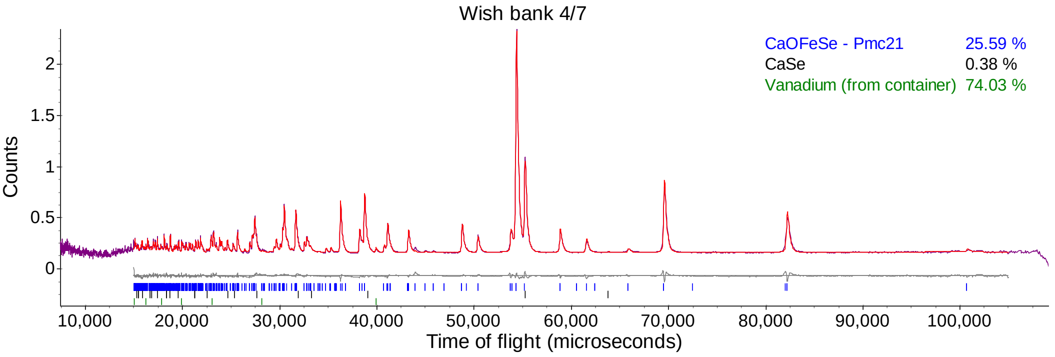
Wish bank 4/7

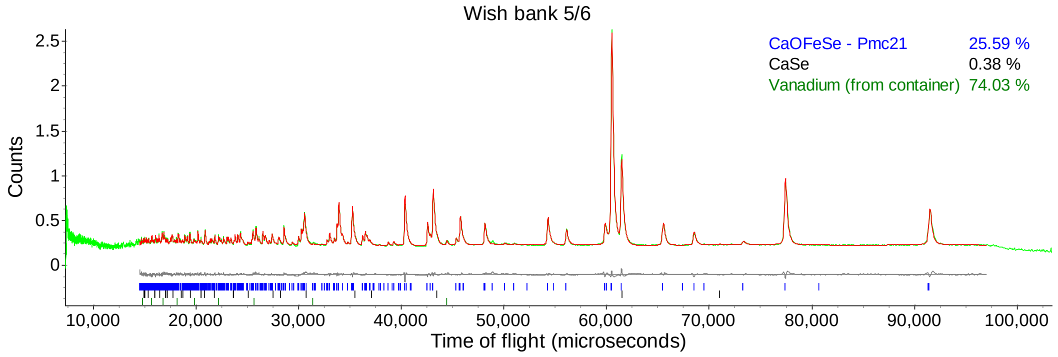

Figure XII.i Rietveld refinement against powder neutron diffraction patterns of CaFeSeO using a Pmc21 unit cell

Table XII.i Parameters for and obtained from the Rietveld refinement shown in Figure XII.i.

Instrument	WISH	**Temperature /K**	180
Sample	SXC223	**Space group**	$Pmc2_1$
R_{wp} / %	3.55	**model name**	100:70:30:0
a / Å	3.89045(8)	**b / Å**	13.2139(4)
c / Å	5.9256(1)	**V / Å^3**	304.63(2)

Table XII.ii Atomic site information obtained from the Rietveld refinement shown in Figure XII.i.

atom	**site**	**x**	**Y**	**z**	**Occupancy**
Se1	2*a*	0	0.6539(1)	0.60255	1
Se2	2*b*	0.5	0.1539(1)^a	0.60255^a	1
Ca1	2*b*	0.5	0.6694(1)	0.1071(6)	1
Ca2	2*a*	0	0.1694(1)^a	0.1071(6)^a	1
Fe1	2*b*	0.5	0.0448(1)	0.2435(4)	0.72(2)
Fe2	2*a*	0	0.5448(1)^a	0.2435(4)	1.00(2)
Fe3	2*b*	0.5	0.9552(1)^a	0.456(2)	0.28(2)
Fe4	2*a*	0	0.4552(1)^a	0.456(2)	0.00(2)
O1	2*b*	0.5	0.0753(1)	0.0630(5)	0.72(2)^b
O2	2*a*	0	0.5753(1)	0.0630(5)	1.00(2)^b
O3	2*b*	0.5	0.0753(1)	0.145(4)	0.28(2)^b
O4	2*a*	0	0.5753(1)	0.145(4)	0.00(2)^b

Table XII.iii Thermal displacements obtained from the Rietveld refinement shown in Figure XII.i.

atom	**U_{11} / Å^2 × 100**	**U_{22} / Å^2 × 100**	**U_{33} / Å^2 × 100**	**U_{23} / Å^2 × 100**
Se1	0.74(9)	0.44(9)	0.96(9)	-0.1(4)
Se2	0.74(9)	0.44(9)	0.96(9)	-0.1(4)
Ca1	1.2(2)	0.0(1)	0.1(1)	0.11(5)
Ca2	1.2(2)	0.0(1)	0.1(1)	0.11(5)
Fe1	1.1(1)	0.25(9)	0.18(6)	0.64(9)
Fe2	1.1(1)	0.25(9)	0.18(6)	0.64(9)
Fe3	1.2(5)	1.2(5)	1.2(5)	0
Fe4	1.2(5)	1.2(5)	1.2(5)	0
O1	1.6(2)	0.2(2)	0.3(2)	0.0(1)
O2	1.6(2)	0.2(2)	0.3(2)	0.0(1)
O3	3.9(18)	3.9(18)	3.9(18)	0
O4	3.9(18)	3.9(18)	3.9(18)	0

XIII. GEM and Polaris diffraction patterns for CaFeSeO

The following diffraction patterns and Rietveld fits correspond to those shown in section 6.6.1, Figure 6.12, and Table 6.1. A peak splitting occurred in banks 1, 2, and 3 of the Polaris data from a mis-centring of the sample in the beam, which caused different path lengths for the scattered neutrons from the sample to different parts of the detector banks.

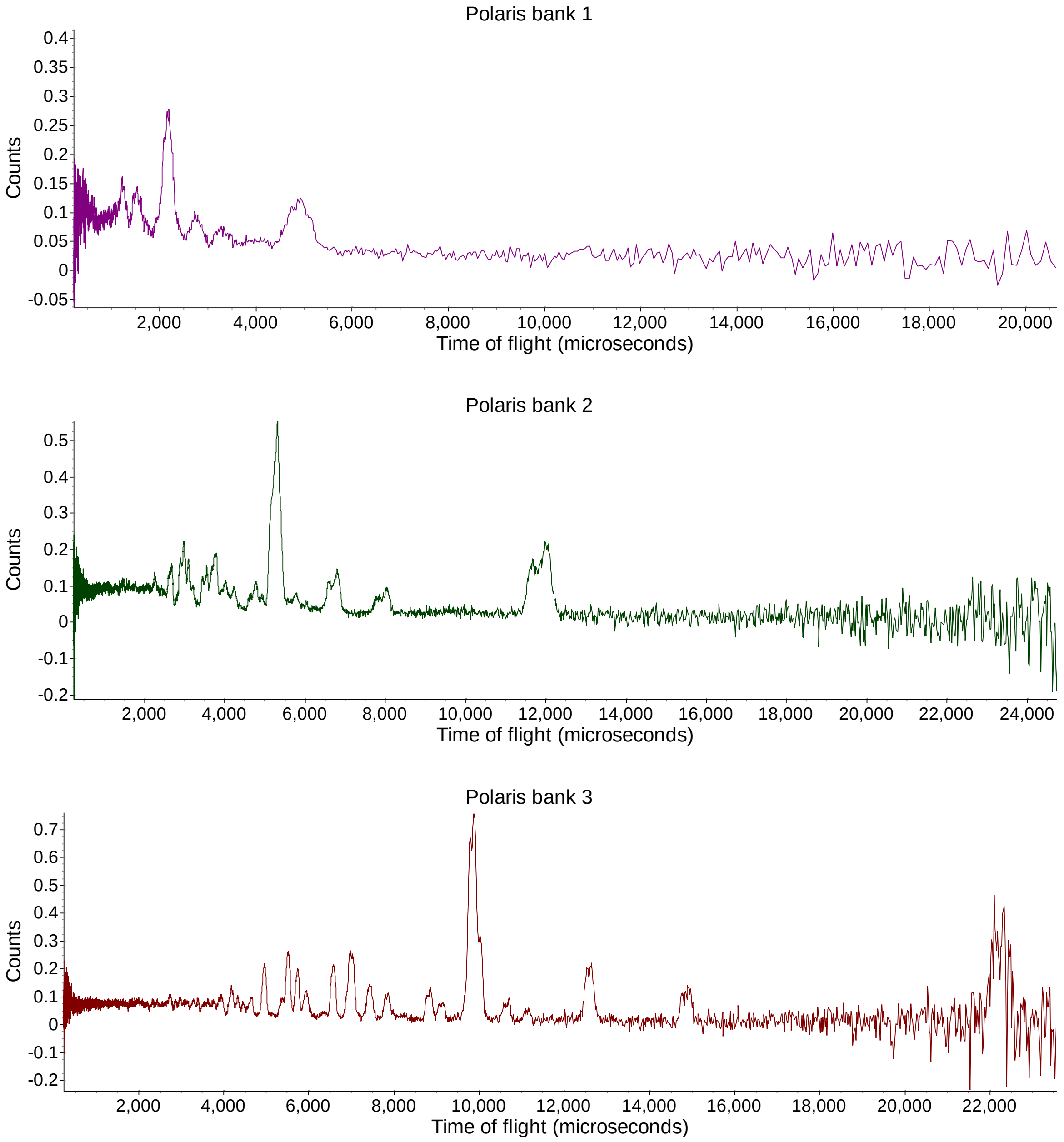

Figure XIII.i Powder neutron diffraction patterns of CaFeSeO (SXC195) showing a peak splitting from a sample misalignment.

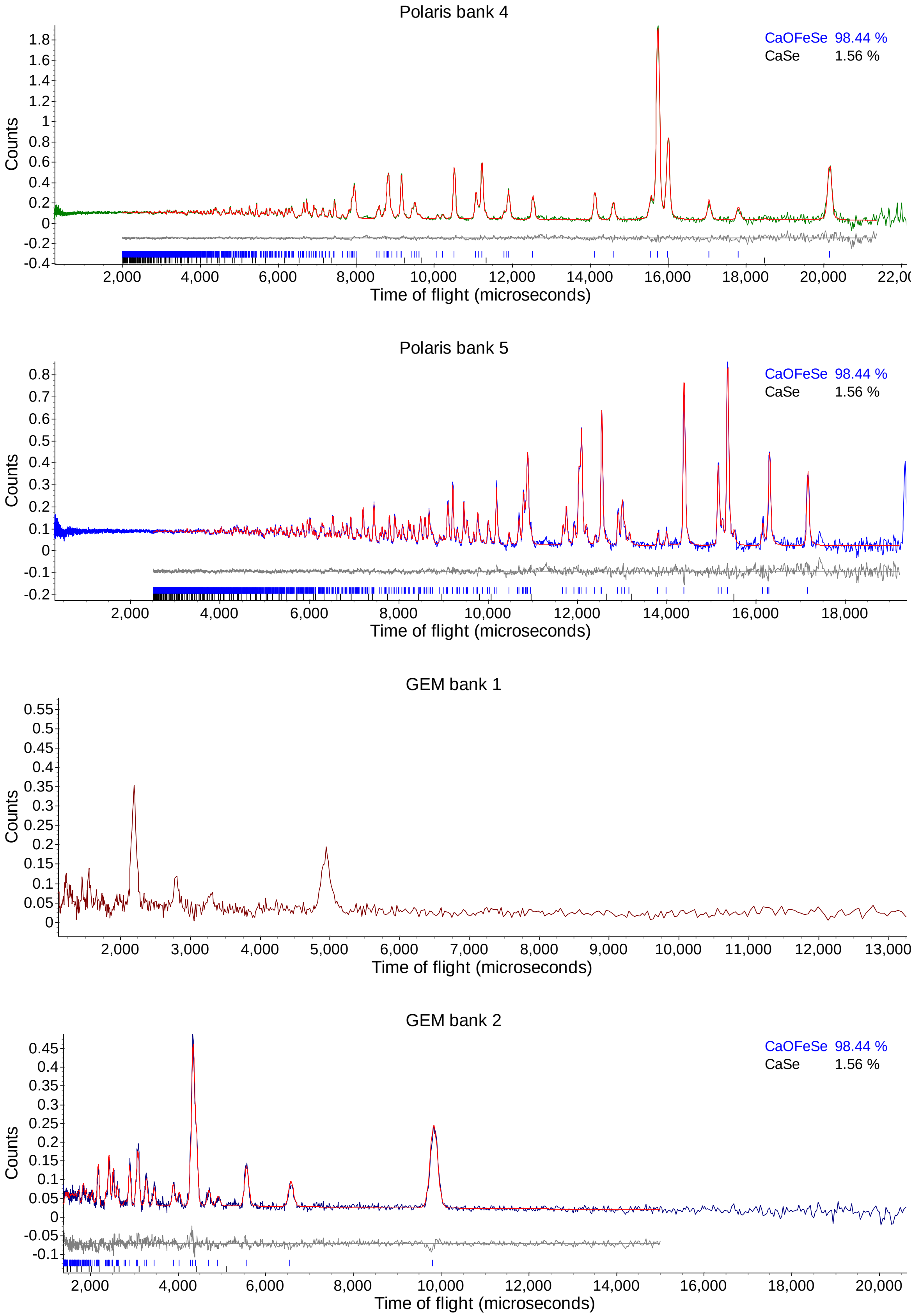

Figure XIII.ii Rietveld refinement against Powder neutron diffraction patterns of CaFeSeO (SXC195) not showing any sample misalignment. GEM bank 1 is not refined against owing to its low signal-to-noise.

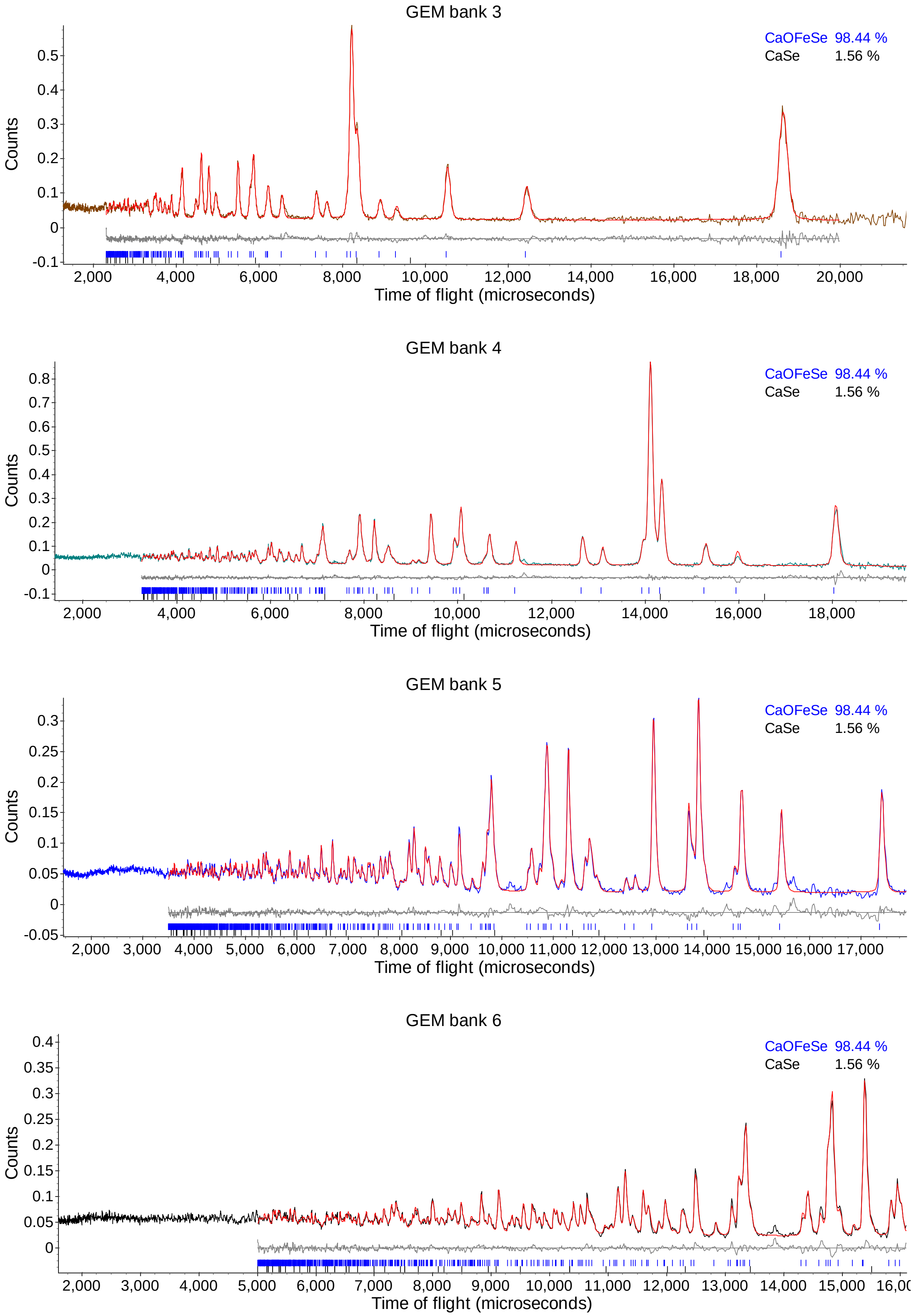

Figure XIII.iii Rietveld refinement against Powder neutron diffraction patterns of CaFeSeO (SXC195) not showing any sample misalignment continued.

XIV. Comparison of refinements against neutron and X-ray data for CaFeSeO

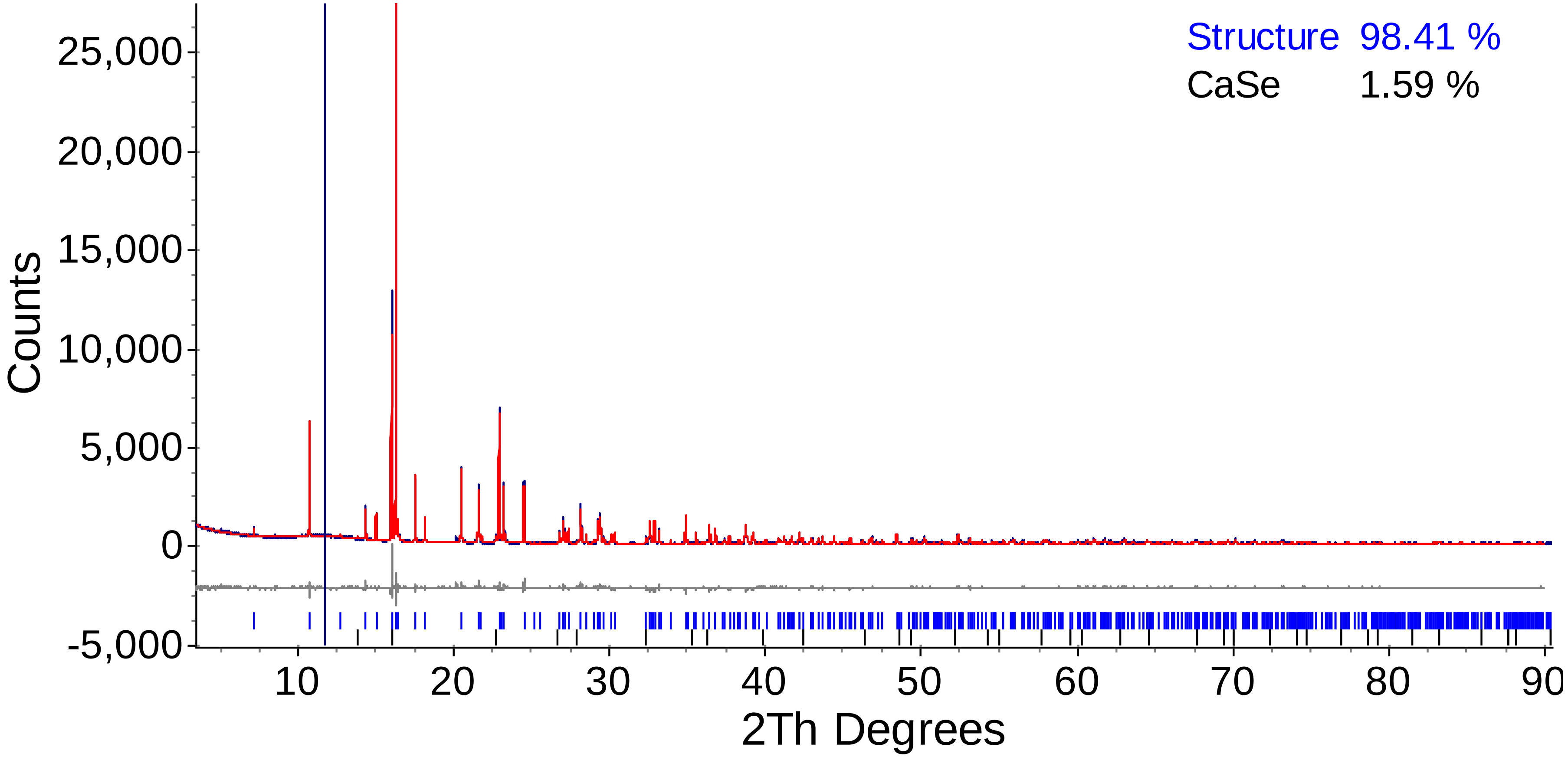

Figure XIV.i Rietveld refinement of the CaFeSeO model in *Cmc*2_1 symmetry, corresponding to the model used in section 6.6.1. The model is applied against X-ray powder diffraction data from the I11 instrument at Diamond Light Source, which is in good agreement with the neutron diffraction model. The vertical blue line marks a broad (FWHM ~5 °), Gaussian peak that has been inserted to model a feature in the background.

Table XIV.i A comparison of refined parameters for fits to powder X-ray and neutron diffraction data using the same model in *Cmc*2$_1$ symmetry.

Instrument	GEM, Polaris	I11
R_{wp} / %	7.80	7.674
χ^2 / %	-	1.96
a / Å	3.8916(1)	3.89663(2)
b / Å	13.1952(5)	13.2212(7)
c / Å	5.9266(2)	5.93634(2)
Fe1-Se / Å	2.575(2)	2.577(1)
Fe2-Se / Å	2.50(1)	2.52(1)
Fe1-O1 / Å	1.902(4), 1.943(6)	1.87(1), 1.98(2)
Fe2-O2 / Å	1.9(1), 1.98(6)	1.9(1), 2.0(2)
Ca-Se/ Å	2.944(4), 3.041(2)	2.921(3), 3.043(1)
Ca-O1 / Å	2.316(2)	2.330(3)
Ca-O2/ Å	2.31(1)	2.32(1)

Table XIV.ii Structural parameters for CaFeSeO from Rietveld refinement against the I11 diffraction data. These parameters compare well with those obtained by refinement of the neutron diffraction data given in the main text in Table 6.2.

atom	site	*x*	*y*	*z*	Occupancy
Se	4*a*	0	0.65413(5)	0.60255	1
Ca	4*a*	0.5	0.66908(8)	0.1115(5)	1
Fe1	4*a*	0.5	0.4564(1)	0.2440(3)	0.903(3)
Fe2	4*a*	0	0.551(1)	0.462(3)	0.078(3)
O1	4*a*	0.5	0.5742(3)	0.070(3)	0.87(14)
O2	4*a*	0.5	0.5742(3)	0.12(3)	0.16(13)

Table XIV.iii Thermal displacement parameters for atoms in Table XIV.ii. Correlation of these displacement values to the samples absorption and an incomplete absorption correction leads to several values are anomalously close to zero.

atom	U_{11} / Å^2 × 100	U_{22} / Å^2 × 100	U_{33} / Å^2 × 100	U_{23} / Å^2 × 100
Se	0.06(3)	0.45(4)	0.00(3)	0.15(4)
Ca	0.00(5)	0.00(6)	0.00(6)	0.46(9)
Fe1	0.20(6)	0.26(7)	0.19(6)	0.30(5)
Fe2	0.2(4)	0.2(4)	0.2(4)	0
O1	0.0(5)	1.6(6)	0.0(6)	2.3(4)
O2	3(3)	3(3)	3(3)	0